RAFT Polymerisation using 2-(*N*-acryloyloxy)ethyl Pyrrolidone in Aqueous Media

Oliver Johnathan Deane

Department of Chemistry
The University of Sheffield

Submitted to the University of Sheffield in fulfilment of the requirements for the award of Doctor of Philosophy

February 2021

Declaration

The work described in this thesis was undertaken at the University of Sheffield under the supervision of Professor Steven P. Armes between October 2016 and February 2021 and has not been submitted, either wholly or in part, for this or any other degree. All the work is the original work of the author, except where acknowledged.

Signature: ______________________________

Oliver Johnathan Deane

February 2021

Acknowledgments

I would like to thank Prof Steve Armes for giving me the opportunity to undertake my PhD within his group. I am extremely grateful for all the support, enthusiasm, and the countless number of hours you have given towards my work and ideas. I feel extremely fortunate to have been given the chance to present at a number of conferences, all of which were unforgettable experiences. Your help and guidance over the last four years has not only improved my writing and research abilities but has also made this PhD extremely enjoyable. However, I am not sure about the nicknames though…

I would like to thank the EPSRC and Ashland Global Specialty Chemicals Inc for funding my PhD. In particular, I would like to thank Osama Musa and Alan Fernyhough for the many interesting discussions and for ensuring that I was provided with litres of NAEP. This Thesis would look a lot different (and be significantly shorter) if I had to carry on synthesising my own. Furthermore, thank you for giving the opportunity to perform a 3-month placement at your R&D facility in Bradford.

My PhD experience has been extremely improved by a number of amazing University of Sheffield staff members. I would like to thank Svet and Chris for all their help and discussions. I would like to thank Rob for the time he gave me setting up the new DSC instrument. I would like to thank Sandra for all of her time, numerous discussions and the impeccable running and maintenance of the NMR spectrometers. I would like to thank Denise and Louise for all of the laughs (excluding the Stagecoach jokes) and for going above and beyond to keep everything running smoothly. I would also like to thank Nick and Sharron in stores who have been extremely friendly and helpful.

I have met, and hope to stay in contact, with a number of great people who have improved the time I have spent in the Armes group. Erik, you are a fantastic scientist and — as the only person that would talk to me about my English grammar books — a great scholar. James Jennings, I always enjoyed working with you and you never failed to teach me something new. See you in Austria for the F1. Last (and almost certainly least), Dr Joseph Lovett (AKA Dr Cheese Bucket, AKA Dr A-Little-Bit-of-That) the time we spent together in the Armes group and the times staying up all night were undoubtedly some of my favourite times during my PhD. I will never forget the straight-arm Eurovision slap and don't think I will ever be the same.

Mum and Dad, thank you for everything. I am sure if you asked a teenaged Olly what he would be doing at the age of 27, he could not have imagined that he would still be in school! I could not have done this without you. Jess and Max, thank you for all the encouragement and support, it has kept me going during the harder times, even if you have no idea what I actually do! And thank you Nan for always listening to me on the phone even though I do not call you enough. Although living in the North has meant that I have not seen you all as much as I would have wanted, I have always felt you were never more than a phone call away. I would also like to thank all the Gibsons for being so friendly and welcoming and providing me so many great memories over the last four years. I feel so lucky to have met you and will be forever smug about the Fort William scarf present.

Finally, I would like to thank Reb. The early(ish) morning workouts and the late night discussions (or slurs) have made this PhD something I never thought it could be. The experiences we have had together have defined the person I am now and inspire me for the future to come. Thank you.

Publications

Primary Publications:

(1) Deane, O. J.; Lovett, J. R.; Musa, O. M.; Fernyhough, A. and Armes, S. P. ‘Synthesis of Well-Defined Pyrrolidone-Based Homopolymers and Stimulus-Responsive Diblock Copolymers via RAFT Aqueous Solution Polymerization of 2-(N-Acryloyloxy)ethylpyrrolidone’ Macromolecules 2018, 51, 7756−7766

(2) Deane, O. J.; Musa, O. M.; Fernyhough, A. and Armes, S. P. ‘Synthesis and Characterization of Waterborne Pyrrolidone-Functional Diblock Copolymer Nanoparticles Prepared via Surfactant-free RAFT Emulsion Polymerization’ Macromolecules 2020, 53, 4, 1422–1434

(3) Deane, O. J.; Jamali, M.; Musa, O. M.; Fernyhough, A. and Armes, S. P. ‘Synthesis and Characterisation of All-Acrylic Tetrablock Copolymer Nanoparticles via One-Pot RAFT Emulsion Polymerisation’ manuscript in *preparation*

(4) Deane, O. J.; Musa, O. M.; Fernyhough, A. and Armes, S. P. ‘Synthesis and Aqueous Solution Properties of Shape-Shifting Stimulus-Responsive Diblock Copolymer Nano-Objects’, *Chem. Sci.*, submitted for publication (2021)

(5) Deane, O. J.; Jennings, J. and Armes, S. P. ‘Thermoreversible Diblock Copolymer Nano-Objects via RAFT Aqueous Dispersion Polymerization of 4-Hydroxybutyl Acrylate’, *J. Am. Chem. Soc*, submitted for publication (2021)

Other Publications:

(1) Jennings, J.; Cornel, E. J.; Derry, M. J.; Beattie, D. L.; Rymaruk, M. J.; Deane, O. J.; Ryan, A. J.; and Armes, S. P. ‘Synthesis of High χ–Low *N* Diblock Copolymers by Polymerization-Induced Self-Assembly’ Angew. Chem. 2020, 132, 10940-10945

Patents:

(1) Deane, O. J; Musa, O. M.; Armes, S. P.; Fernyhough A.; Gibson, R. R. ‘Methods of synthesis of homopolymers and non-homopolymers comprising repeating units derived from monomers comprising lactam and acryloyl moieties in an aqueous medium’ US20200407470A1, 2020

Conferences

June 2017	*Poster Presentation* at the Young Researchers Meeting, Edinburgh, UK
July 2018	*Poster Presentation* at the Young Researchers Meeting, Dublin, UK
December 2018	*Poster Presentation* at the 2nd NSFC-RSC Symposium on Novel Polymer Synthesis to Solve Tomorrow's Problems, Warwick, UK
April 2019	*Oral Presentation* at the 13th International Conference on Advanced Polymers via Macromolecular Engineering, Stellenbosch, SA
July 2019	*Oral Presentation* at Young Researchers Meeting, Kent, UK
August 2019	*Oral Presentation* at the 258th National Meeting & Exposition of the American Chemical Society, San Diego, USA
September 2019	*Oral Presentation* at the Institute of Physics: Physical aspects of polymer science 2019, Lincoln, UK

Abstract

This Thesis evaluates 2-(*N*-acryloyloxy)ethyl pyrrolidone (NAEP) for use in a range of reversible addition-fragmentation chain transfer (RAFT)-mediated aqueous polymerisation-induced self-assembly (PISA) formulations. Initially, the RAFT aqueous solution polymerisation of NAEP was studied. A potassium persulfate and ascorbic acid initiator system enabled high NAEP conversions (< 99%) to be reached with 10 min whilst achieving narrow molecular weight distributions (M_w/M_n < 1.3). 2-Hydroxyethyl acrylate (HEA), oligo(ethylene glycol) methyl ether acrylate (OEGA) and *N*-isopropylacrylamide (NIPAM) were chain-extended from $PNAEP_x$ precursors via RAFT aqueous solution polymerisation. The latter case yielded thermoresponsive polymers that self-assembled into spherical micelles above the LCST of the PNIPAM block, as evidenced by dynamic light scattering (DLS) studies. Finally, the RAFT solution polymerisation of NAEP using a poly(2-(diethylamino)ethyl methacrylate) (PDEA) precursor produced soluble diblock copolymers that self-assembled when the dispersion pH was raised above the pK_a of the PDEA block.

PNAEP precursors were then assessed as new non-ionic stabiliser blocks for the RAFT emulsion polymerisation of styrene, *n*-butyl acrylate (nBA), or statistical mixtures thereof. In each case, PNAEP enabled the production of kinetically-trapped spheres in less than 60 min under optimised conditions. DLS studies indicated that the final z-average diameter could be tuned by varying the final DP. Differential scanning calorimetry (DSC) analysis indicated that the statistical copolymers exhibited intermediate glass transition temperatures (T_g) compared to the two respective homopolymers resulting in highly transparent and non-tacky films when cast at room temperature.

Thermoplastic elastomer multiblock copolymer nanoparticles were synthesised via one-pot sequential RAFT aqueous emulsion polymerisation of nBA and *t*-butyl acrylate (tBA) using a PNAEP precursor formed *in situ*. DSC studies indicated the difference in their molecular structures resulted in significantly different T_g values. Small angle X-ray scattering (SAXS) indicated the two blocks underwent microphase separation into lamellae sheets of PnBA and PtBA domains. The all-acrylic nature of this formulation enabled transparent films to be cast at room temperature that become more elastic as the PnBA content was increased.

Finally, thermoresponsive diblock copolymer nano-objects were synthesised via RAFT aqueous dispersion polymerisation of 4-hydroxybutyl acrylate (HBA) at 30 °C using a one-pot protocol. Rheological studies indicated that the critical temperature corresponding to sphere-to-worm, worm-to-vesicle and vesicle-to-lamellae transitions could be tuned by adjusting the PHBA DP. Glutaraldehyde was used to covalently stabilise these nano-objects enabling transmission electron microscopy (TEM) studies the construction of a pseudo-phase diagram. Aqueous electrophoresis, DLS and TEM studies confirmed that raising the dispersion pH above the pK_a of the terminal carboxylic acid group located on the PNAEP chains was sufficient to increase the degree of hydration of the PHBA chains which induced a rapid and reversible vesicle-to-sphere transition.

Abbreviations

AIBN	2,2’-Azobis(2-methylpropionitrile)
AsAc	Ascorbic acid
ARGET	Activators regenerated by electron transfer
ATRP	Atom transfer radical polymerisation
CGC	Critical gelation concentration
CMC	Critical micelle concentration
CRP	Controlled radical polymerisation
CTA	Chain transfer agent
DDMAT	2-(Dodecylthiocarbonothioylthio)-2-methylpropionic acid
DLS	Dynamic light scattering
DP	Degree of polymerisation
DSC	Differential scanning calorimetry
D_k	Kinetic chain length
FRP	Free radical polymerisation
G’	Storage modulus
G’’	Loss modulus
GA	Glutaraldehyde
GPC	Gel permeation chromatography
ICAR	Initiators for continuous activator regeneration
k_p	Propagation rate constant
k_t	Termination rate constant
k_rec	Termination by combination rate constant
k_disp	Termination by disproportionation rate constant
KPS	Potassium persulfate
LAM	Less activated monomer
LAP	Living anionic polymerisation
LCST	Lower critical solution temperature
Macro-CTA	Macromolecular chain transfer agent
MAM	More activated monomer
M_n	Number-average molecular weight
M_p	Peak molecular weight
M_w	Weight-average molecular weight
MW	Molecular weight

MWD	Molecular weight distribution
NMP	Nitroxide-mediated polymerisation
NVC	*N*-vinylcarbazole
P	Packing parameter
PAA	Poly(acrylic acid)
PAM	Poly(acrylamide)
PnBA	Poly(*n*-butyl acrylate)
PBzMA	Poly(benzyl methacrylate)
PDAAM	Poly(diacetone acrylamide)
PDEGMA	Poly(di(ethylene glycol) methyl ether methacrylate)
PDEA	Poly(2-(dieethylamino)ethyl methacrylate)
PDMAC	Poly(*N*,*N*-dimethyl acrylamide)
PEG	Poly(ethylene glycol)
PEGA	Poly(ethylene glycol) methyl ether acrylate
PETTC	4-Cyano-4-(2-phenylethanesulfanylthiocarbonyl)sulfanyl pentanoic acid
PGMA	Poly(glycerol monomethacrylate)
PGlyMA	Poly(glycidyl methacrylate)
PHBA	Poly(4-hydroxybutyl acrylate)
PHBMA	Poly(2-hydroxybutyl methacrylate)
PHEA	Poly(2-hydroxyethyl acrylate)
PHPMA	Poly(2-hydroxypropyl methacrylate)
PHPMAC	Poly(*N*-(2-hydroxypropyl) methacrylamide)
PISA	Polymerisation-induced self-assembly
pK_a	Acid dissociation constant
PMAA	Poly(methacrylic acid)
PMA	Poly(methyl acrylate)
PMEA	Poly(2-methoxyethyl acrylate)
PMMA	Poly(methyl methacrylate)
PMOEMA	Poly(2-methoxyethyl methacrylate)
PMPC	Poly(2-(methacyloyloxy)ethylphosphorylcholine)
PNAEP	Poly(*N*-(2-acryloyloxy)ethyl pyrrolidone)
PNMEP	Poly(*N*-(2-methacryloyloxy)ethyl pyrrolidone)
PNAM	Poly(*N*-acryloylmorpholine)
PNIPAM	Poly(*N*-isopropylacrylamide)
PNVP	Poly(*N*-vinylpyrrolidone)

POEGA	Poly(oligo(ethylene oxide) methyl ether acrylate)
PRE	Persistent radical effect
PS	Polystyrene
PVA	Poly(vinyl alcohol)
RAFT	Reversible addition-fragmentation chain transfer
RDRP	Reversible deactivation radical polymerisation
R_{g}	Radius of gyration
R_{poly}	Rate of polymerisation
SAXS	Small angle X-ray scattering
TEM	Transmission electron microscopy
T_{g}	Glass transition temperature
UCST	Upper critical solution temperature
UV-Vis	Ultraviolet-Visible
VA-044	2,2’ Azobis(2-(2-imidazolin-2-yl)propane)dihydrochloride
χ	Flory-Huggins parameter
^{1}H NMR	^{1}H nuclear magnetic resonance

Table of Contents

Chapter 1

Introduction

1.1 General Concepts in Polymer Science

Precisely 101 years ago Staudinger postulated that polymers were long-chain molecules of relatively high molecular weight (so-called macromolecules[1]) composed of many identical repeat units of small molecules (monomers).[2] This new concept laid the foundations for the field of polymer science and also explained various solution properties of well-known natural materials such as proteins, starch, cellulose and DNA. Moreover, it enabled the rational design of many new synthetic polymers with a remarkably diverse range of materials properties. Over the past century, synthetic polymers have become both ubiquitous and essential in modern life, with applications ranging from disposable plastic shopping bags, durable pipelines and weatherproof window frames to modern technologies such as organic semiconductors and light emitting materials, bullet-proof vests, artificial skin and drug delivery systems. Our understanding of polymer science has evolved significantly to enable such technologies. Prior to Staudinger's 'macromolecules' hypothesis, it was widely believed that the mass of a molecule was limited to the size of its crystallographic unit (~600 Daltons). Colloidal dispersions of naturally-occurring polymers (e.g. natural rubber) were considered to be composed of aggregates held together by non-covalent interactions arising from π-π interactions between unsaturated double bonds, rather than long-chain molecules with molecular weights that could exceed one million Da. This prevailing viewpoint was challenged in 1920 when Staudinger reported several examples of reactions – polymerisations – that formed high molecular weight molecules by linking together many small molecules.[2] Staudinger went on to hydrogenate natural rubber (thus preventing the postulated π-π interactions) and demonstrate that the elastic properties of the product were comparable to those of the starting material. However, it was not until Svedberg invented the ultracentrifuge in 1923 that pure substances from colloidal dispersions could be isolated.[3] In some cases, molecular weights were in the range of millions of Daltons but it still took some years before the scientific community finally accepted Staudinger's radical concept of 'macromolecules'. Nevertheless, by the late 1920s the fledgling field of polymer science had been embraced by many industrial companies. In 1929, Carothers (an industrial chemist working at DuPont) had categorised polymers as either condensation or addition depending on structural differences between the polymer and its monomer(s).[4] Condensation polymers are synthesised by reactions that typically eliminate a small molecule (or 'condensate'). In contrast, addition polymers are formed without any elimination and exhibit precisely the same chemical composition as the original monomer(s). However, as the number of known synthetic polymers expanded, inconsistencies were found in these definitions. In 1953, Flory outlined the formation and behaviour of polymers by developing new theories based on kinetics, thermodynamics and statistical mechanics.[5] Unlike Carothers, Flory classified polymerisations as either step-growth polymerizations or chain polymerisations. The latter proceed by the sequential addition of multiple monomers via a reactive centre. This behaviour is exemplified by free radical polymerisation, which will be further discussed in this Thesis.

The physical properties of polymers (such as mechanical strength, solubility and brittleness) often depend on their molecular weight.[6] Unlike small molecules, all synthetic polymers are polydisperse: they contain chains that differ markedly in their length so their molecular weight is not a single discrete value. The molecular weight of a polymer must therefore be described as an average molecular weight calculated from the molecular weights of all the individual chains within the sample.[7] Two common moments of a polymer's molecular weight distribution are the number-average molecular weight (M_n; Equation 1.1) and the weight-average molecular weight (M_w; Equation 1.2).

$$M_n = \frac{\sum N_i M_i}{\sum N_i} \tag{1.1}$$

$$M_w = \frac{\sum N_i M_i^2}{\sum N_i \, M_i} \tag{1.2}$$

Here M_i corresponds to the molecular weight of the monomer repeat unit and N_i is the number of chains. M_n is biased towards low molecular weight and hence is sensitive to residual monomer or solvent impurities. On the other hand, M_w is biased towards high molecular weight, so it is particularly sensitive to branching or cross-linking. M_w/M_n is often described as the polydispersity index, now more commonly known as the dispersity (Figure 1.1). Because M_w is always greater than M_n, M_w/M_n is always greater than unity for any molecular weight distribution of finite width (which is the case for all synthetic polymers). The M_w/M_n can be considered to be a crude measure of the width of the molecular weight distribution, with larger values indicating broader distributions.

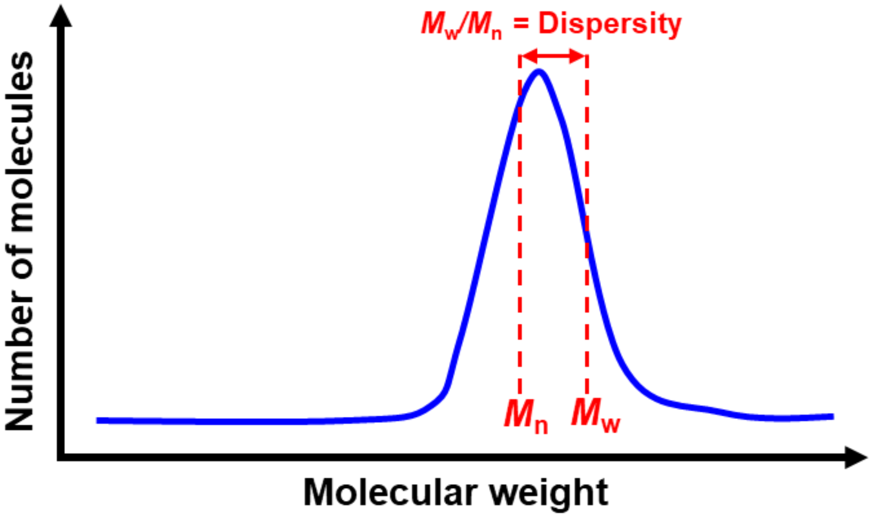

Figure 1.1. Schematic cartoon of a molecular weight distribution curve for a polymer indicating the number-average molecular weight (M_n) and weight-average molecular weight (M_w) and its dispersity (M_w/M_n).[8,9]

1.2 Polymerisation Techniques

1.2.1 Free Radical Polymerisation

Free radical polymerisation (FRP) is a type of chain polymerisation where radical-based active centres are typically generated by thermal degradation of a suitable initiator.[10] FRP is widely used in industry as it enables the convenient polymerisation of a wide range of vinyl monomers in many solvents. Moreover, FRP is relatively tolerant of monomer functionality and is insensitive to protic impurities.[9,11] Typically, FRP involves four fundamental steps: initiation, propagation, termination, and transfer (Figure 1.2).[11] The presence of molecularly-dissolved oxygen in the reaction mixture can lead to retardation (or even inhibition) of the polymerisation. This is because the growing polymer radical can react with oxygen to form a relatively unreactive peroxy-capped polymer chain, which significantly reduces the rate of propagation. Fortunately, this problem can be avoided either by degassing the reaction mixture with an inert gas (i.e. nitrogen or argon) or by using excess initiator that scavenges oxygen at the beginning of the reaction.

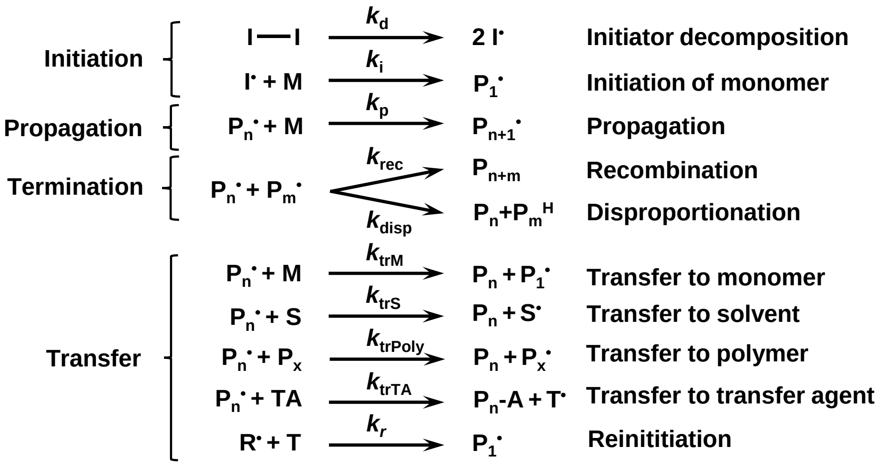

Figure 1.2. Reaction mechanism and associated rate constants for free radical polymerisation, which comprises four fundamental steps: initiation, propagation, termination and transfer.[11]

After homolytic cleavage of an initiator molecule, two primary radicals ($I^\bullet$) are produced. Formation of a new active centre ($P_1^\bullet$) occurs when one of these radicals reacts with a monomer unit (M) in the initiation step. The rate of initiator decomposition is relatively slow compared to the rate of formation of $P_1^\bullet$ (i.e. $k_d < k_i$) and hence is rate-limiting. This enables the overall rate of initiation (R_i) to be calculated (Equation 1.3).

$$R_i = \frac{\mathrm{d}[P_1^\bullet]}{dt} = 2k_d f[\mathrm{I}] \tag{1.3}$$

Here k_d is the rate constant for decomposition and f is the initiator efficiency (i.e., the ability of the primary radical to initiate a monomer). A numerical factor of two is required in Equation 1.3 because two radicals are produced by the thermal decomposition of each initiator molecule (I_2). Propagation involves the addition of multiple monomer units to $P_1^\bullet$ to produce polymer radicals ($P_n^\bullet$). If the rate constant for propagation (k_p) and termination (k_t) are assumed to be independent of the size of the growing polymer radicals, the rate equation can be expressed as shown in Equation 1.4.

$$R_p = \frac{\mathrm{d}[\mathrm{M}]}{dt} = k_p[P_n^\bullet][\mathrm{M}] \tag{1.4}$$

When two polymer radicals (e.g. $P_n^\bullet$ and $P_m^\bullet$) react with each other this is known as termination. This can occur via two distinct mechanisms: combination or disproportionation. Termination by combination involves two polymer radicals forming a single, longer dormant chain. Disproportionation occurs when one polymer radical abstracts a hydrogen atom from another polymer radical, resulting in two polymer chains with one containing an unsaturated chain-end. The relative levels of termination by combination or disproportionation can influence the dispersity and molecular weight of the final polymers.[7] The overall rate of termination (R_t; Equation 1.5) involves a composite rate constant for termination (k_t) that is equal to the sum of the rate constant for termination by combination (k_{rec}; Equation 1.6) and that for termination by disproportionation (k_{disp}; Equation 1.7).

$$R_t = k_t[P_n^\bullet]^2 \tag{1.5}$$

$$R_{rec} = k_{rec}[P_n^\bullet][P_m^\bullet] \tag{1.6}$$

$$R_{disp} = k_{disp}[P_n^\bullet][P_m^\bullet] \tag{1.7}$$

Polymer radicals can also react with monomer, solvent, dormant polymer chains or transfer agents via chain transfer reactions. These side reactions can result in cross-linking or branching, which can significantly affect the molecular weight and dispersity of the resulting polymer chains. Such chain transfer reactions are relatively fast and no radicals are destroyed, so the overall kinetics of polymerisation remains unchanged. Thus, the rate of polymerisation (R_{poly}) is only influenced by the initiation, propagation and termination steps and, to a good first approximation, can be equated to the rate of propagation. In principle, experimental quantification of the polymer radical concentration can be determined by electron spin resonance spectroscopy. However, in practice this is technically challenging. Fortunately, if the so-called steady-state approximation is valid, then $R_i \approx R_t$ and the concentration of polymer radicals (Equation 1.8) can be calculated by rearranging Equations 1.3 and 1.5.

$$[P_n^\bullet] = \sqrt{\frac{f k_d[I]}{k_t}} \tag{1.8}$$

Substituting Equation 1.8 into Equation 1.4 affords the overall rate of polymerisation (R_{poly}; Equation 1.9).

$$R_{poly} = k_p[\mathrm{M}]\sqrt{\frac{f k_d[I]}{k_t}} \tag{1.9}$$

If f is high, R_{poly} is proportional to both [M] and $[\mathrm{I}]^{1/2}$. However, if f is low then R_{poly} only depends on [M] and the rate is then proportional to $[\mathrm{M}]^{3/2}$.[7] In FRP, the reaction mixture can become viscous towards the end of the polymerisation. Thus, polymer radicals diffuse relatively slowly (which lowers k_t) compared to unreacted monomer; this causes a significant increase in R_{poly}, which is known as auto-acceleration.[7]

The average number of monomer units consumed per active radical centre (or the kinetic chain length, D_k) is equal to R_p divided by R_t and hence is proportional to [M] and $[I]^{-1/2}$ (Equation 1.10).

$$D_k = \frac{R_p}{R_t} = \frac{k_p[\mathrm{M}][P_n^\bullet]}{2k_t[P_n^\bullet]^2} = \frac{k_p[\mathrm{M}]}{2\sqrt{fk_dk_t[I]}} \tag{1.10}$$

Thus, to grow long polymer chains (high D_k), both high monomer and low radical concentrations are required. This is because the rate of termination is much faster than that of propagation ($k_t > 10^8$ M^{-1} s^{-1} vs. $k_p \approx 10^2$-10^4 M^{-1} s^{-1})[12] and R_t is second-order with respect to the radical concentration (Equation 1.5), whereas R_p is only first-order (Equation 1.4). The mean degree of polymerisation (DP) can be readily calculated if termination occurs exclusively by combination (Equation 1.11) or disproportionation (Equation 1.12).

$$DP = 2D_k \tag{1.11}$$

$$DP = D_k \tag{1.12}$$

However, if neither termination mechanism dominates then the DP is equal to the average number of reacted monomers per inactive polymer chain. Assuming steady-state conditions, the mean DP can be calculated as the ratio between the rate of monomer consumption (R_p) and the rate of formation of inactive polymer ($R_{inac,poly}$). In FRP, $R_{inac,poly}$ is a result of combination, disproportionation of chain radicals and chain transfer to solvent (S) and monomer (M) (see Equation 1.13).

$$R_{\mathrm{inac,poly}} = k_{trM}[P_n^\bullet][\mathrm{M}] + k_{trS}[P_n^\bullet][S] + (\frac{k_{rec}}{2} + k_{disp})[P_n^\bullet]^2 \tag{1.13}$$

Combining this expression with equation 1.04, the DP can be calculated (Equation 1.14) and inverted (Equation 1.15).

$$DP = \frac{k_p[P_n^\bullet][\mathrm{M}]}{k_{trM}[P_n^\bullet][\mathrm{M}] + k_{trS}[P_n^\bullet][S] + (\frac{k_{rec}}{2} + k_{disp})[P_n^\bullet]^2} \tag{1.14}$$

$$\frac{1}{DP} = \frac{k_{trM}}{k_p} + \frac{k_{trS}[S]}{k_p[M]} + \frac{[P_n^\bullet](\frac{k_{rec}}{2} + k_{dis})}{k_p[M]} \tag{1.15}$$

The average lifetime of a kinetic chain (τ; Equation 1.16) is equal to the polymer radical concentration divided by the rate of radical formation (Equation 1.17).

$$\tau = \frac{[P_n^\bullet]}{I} \tag{1.16}$$

$$I = (k_{rec} + k_{dis})[P_n^\bullet]^2 \tag{1.17}$$

Rearranging Equation 1.17 for $[P_n^\bullet]$ and then substituting into Equation 1.15 results in a final expression for DP (Equation 1.18).

$$\frac{1}{DP} = \frac{k_{trM}}{k_p} + \frac{k_{trS}[S]}{k_p[M]} + \frac{(\frac{k_{rec}}{2} + k_{dis})I^{\frac{1}{2}}}{(k_{rec} + k_{dis})^{\frac{1}{2}} k_p[M]} \tag{1.18}$$

Despite FRP being widely used in industry, it does not enable the preparation of well-defined, functional polymers with pre-determined DPs and complex architectures (e.g. block copolymers). For polymer science to be employed in many new high-tech applications, more sophisticated polymerisation techniques are required.

1.2.2 Living Anionic Polymerisation

In 1956 Szwarc *et al.* reported the synthesis of polystyrene chains in anhydrous THF via living anionic polymerisation (LAP).[13,14] LAP is a type of chain polymerisation that involves propagation of monomers with electron-withdrawing substituents *via* anionic active centres. These are generated by an anionic initiator (*n*-butyl lithium) that transfers an electron (or negatively charged group[5]) to a monomer to form an anionic monomer-initiator adduct. Such chain-ends are mutually repulsive and cannot react with each other. Furthermore, there is no mechanism for unimolecular termination, thus there is no intrinsic termination for such polymerisations. Unlike FRP, LAP is limited to certain vinyl monomers such as styrene, vinyl naphthalene, dienes, vinyl pyridine, (meth)acrylates, *N,N*-dialkyl acrylamides, (meth)acrylonitriles and cyclic monomers (such as, ethers, esters and siloxanes).[15] Furthermore, the rate of initiation is far greater than that of propagation (k_i >> k_p), so initiation is complete prior to any propagation. This results in the uniform growth of all polymer chains simultaneously (Figure 1.3).

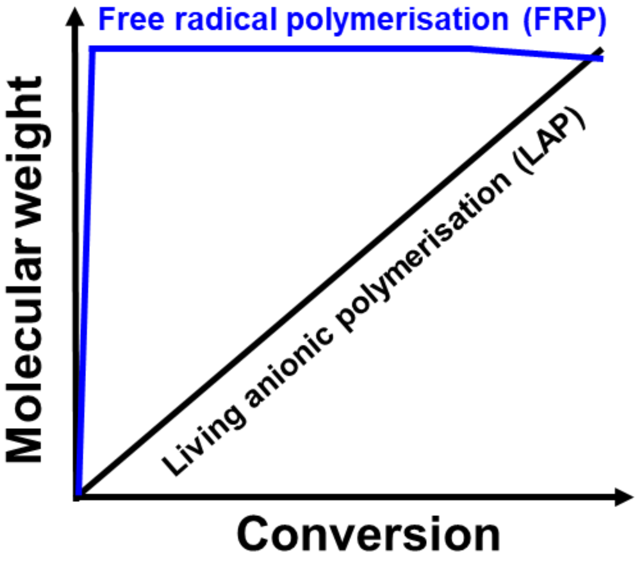

Figure 1.3. Evolution of polymer molecular weight (or DP) with monomer conversion for a typical free radical polymerisation (blue) and a living anionic polymerisation (black).

During LAP, the rate of polymerisation is equal to the rate of propagation because this is the rate-limiting step (Equation 1.19, where [P_n^-] is the concentration of propagating anionic chains). Integration of Equation 1.19 affords the integrated rate equation (Equation 1.20, where [M]$_0$ is the initial monomer concentration) and enables D_k to be calculated at any given time (Equation 1.21, where [I]$_0$ is the initiator concentration).

$$R_p = k_p[P_n^-][M] \tag{1.19}$$

$$[M] = [M]_0 e^{(-k_p[P_n^-]t)} \tag{1.20}$$

$$D_k = \frac{[M]_0 - [M]}{[I]_0} \tag{1.21}$$

If no transfer or branching side-reactions occur, LAP enables the facile production of polymers with pre-determined DPs by simply adjusting the initial molar concentration between [M]$_0$ and [I]$_0$ (Equation 1.22). Furthermore, once high monomer conversion has been achieved, addition of a suitable second monomer enables the formation of block copolymers. It is worth contrasting this situation with that of FRP, which does not provide access to either pre-determined DPs (see Equation 1.18) or well-defined block copolymers.

$$\mathrm{DP} = \frac{[M]_0}{[I]_0} \tag{1.22}$$

Due to the high nucleophilicity of the initiators used, LAP must be performed under rigorously anhydrous conditions because trace protic solvents (such as water or alcohols) can react with the active centre, leading to premature termination. However, *intentional* termination by addition of a suitable reagent, (e.g. water, methanol, CO_2 etc.) enables the introduction of specific end-groups. Despite these synthetic advantages, the restricted monomer palette and stringent synthesis conditions severely limit the scope of LAP. Nevertheless, companies such as Kraton Polymers use LAP on an industrial scale to produce thermoplastic elastomers,[16] viscosity modifiers, and diesel soot dispersants.[17] Other examples of living polymerisation include, living cationic polymerisation[18,19], ring-opening[20–22] and group transfer polymerisation[23,24], but these chemistries are beyond the scope of this Thesis.

1.2.3 Reversible Deactivation Radical Polymerisation

Since the 1990s there have been many important milestones in the synthesis of complex polymer architectures *via* reversible deactivation radical polymerisation (RDRP). This radical- based chemistry combines the high tolerance of monomer functionality associated with FRP with the excellent control offered by LAP. RDRP is sometimes described as 'pseudo-living' because termination is only suppressed relative to propagation, rather than eliminated. In the case of FRP, if $[P^\bullet]$ is reduced then the rate of termination is lowered relative to the rate of propagation since $k_p \propto [P^\bullet]$ and $k_t \propto [P^\bullet]^2$ (equation 1.04 and equation 1.05 respectively). In principle, a reduction in $[P^\bullet]$ can be achieved by either deactivating or reducing the reactivity of the polymer radicals, thus preventing radical coupling and producing a more controlled polymerisation. This approach relies on the rapid exchange of propagating polymer radicals between active and dormant states, which is achieved by the addition of a suitable moderating species. There are two types of equilibria, which are termed reversible deactivation/activation (Scheme 1.1a) and reversible transfer (Scheme 1.1b).[9,11,25]

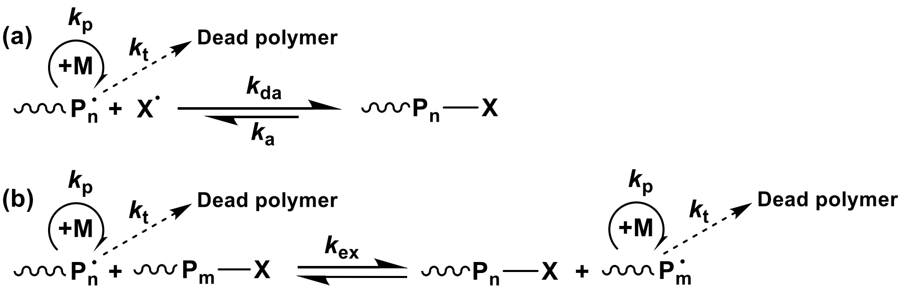

Scheme 1.1. Dynamic equilibria formed during RDRP: (a) reversible deactivation/activation and (b) reversible transfer.

The reversible deactivation/activation equilibrium is exploited in two widely-used RDRP techniques: nitroxide-mediated polymerisation (NMP) and atom transfer radical polymerisation (ATRP), which are both based on the persistent radical effect (Scheme 1.1a).[26] Here, an initiator is homolytically cleaved to yield a reactive radical and a stable/persistent radical ($X^{\bullet}$). The former species initiates polymerisation and all the polymer chains propagate at approximately the same rate. Importantly, the $X^{\bullet}$ radicals cannot react with themselves: instead they rapidly cap and deactivate the propagating chains ($P_n^{\bullet}$), where k_{da} is the rate of deactivation. This dormant species can be reactivated to enable propagation to continue, where k_a is the rate of activation. To achieve good living character and avoid termination, the equilibrium must lie in favour of the dormant species (i.e., $k_{da} > k_a$) in order to minimise [$P_n^{\bullet}$]. Termination results in an irreversible accumulation of $X^{\bullet}$, thus shifting the equilibrium towards capped polymer chains and reducing the rate of termination (k_t).

In contrast, CRPs involving reversible transfer (Scheme 1.1b) are not based on the persistent radical effect. Instead, an initiator is homolytically cleaved to form polymer radicals ($P_n^{\bullet}$). This mechanism more closely matches FRP, with pseudo-living character being achieved by introducing a transfer agent which enables rapid rates of exchange (k_{ex}) to be achieved between $P_n^{\bullet}$ and their dormant unreactive state. To achieve good control, the rate of transfer must be faster than that of propagation ($k_{ex} >> k_p$) and the concentration of the transfer agent should be significantly higher than the primary radical flux. This is the main basis for reversible addition-fragmentation chain transfer (RAFT) polymerisation, which will be discussed in more detail in section 1.2.3.3.

For both mechanisms shown in Scheme 1.1, the rate of exchange between an active and a dormant species is faster than the rate of propagation. This provides good control over the target DP and affords narrow molecular weight distributions (M_w/M_n < 1.30).[25] Furthermore, the ability to prepare well-defined block copolymers allows access to many types of copolymers with various architectures (Figure 1.4).[27,28]

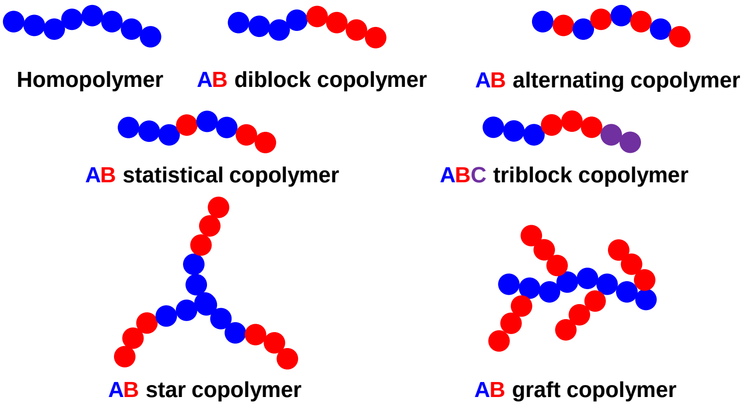

Figure 1.4. Schematic representation of the most common copolymer architectures.[27,28]

1.2.3.1 Nitroxide-Mediated Radical Polymerisation

After the discovery of stable nitroxide species,[29] many research groups employed them as irreversible radical traps to monitor reactions between initiators and radicals.[30] Early examples of nitroxide-mediated radical polymerisation (NMP) were reported by Druliner *et al.,* who used arylazaoxyl radicals to produce block copolymers with relatively broad molecular weight distributions via relatively slow polymerisations (compared to FRP).[31] In the mid-1990s, Georges *et al.*[32] and subsequently Hawker and co-workers[33] used 2,2,6,6-tetramethylpiperidinyloxy (TEMPO) for the synthesis of well-defined polystyrene via NMP. NMP follows a reversible deactivation/activation mechanism that relies on the persistent radical effect (see Scheme 1.1a). The persistent radicals are generated *via* homolytic cleavage of a relatively weak C-O bond (Scheme 1.2).

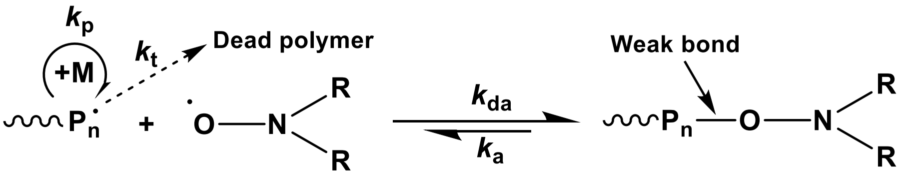

Scheme 1.2. Reversible termination equilibrium for NMP.

Early examples of NMP involved using conventional thermal initiators in the presence of a nitroxide species (i.e. TEMPO) that formed an alkoxyamine radical *in situ*.[32] Later, initiation was achieved using unimolecular alkoxyamines that formed both the nitroxide species that mediated the subsequent polymerisation and also the radical source.[34,35] The nitroxide radical then reacts with the growing polymer chain to produce a thermally labile alkoxyamine: fine-tuning the reaction temperature thus provides control over the polymerisation.

Compared to ATRP, NMP is an attractive technique to prepare well-defined polymers because of its relative simplicity. The nitroxide species used to mediate the polymerisation are not toxic (unlike the transition metal catalysts required for ATRP) nor malodorous (unlike the organosulfur compounds required for RAFT polymerisation). Thus, NMP-synthesised polymers can be used in various applications without any post-polymerisation purification steps. NMP can be conducted under heterogeneous conditions (e.g. emulsion or mini-emulsion polymerisation) and has enabled the synthesis of homopolymers[36–38], random copolymers[39], diblock copolymers[40–42] and cross-linked polymers[43,44] with relatively narrow molecular weight distributions.

Nevertheless, NMP is not as popular as ATRP or RAFT polymerisation. The synthesis of nitroxide initiators is a complex and labour-intensive process compared to that of RAFT and ATRP precursors. This explains why only a rather small number of nitroxides have become commercially available. Generally, NMP requires relatively high temperatures (> 120 °C) in order to achieve the desired equilibrium ($K_{eq} = k_a/k_{da}$ in Scheme 1.2) between the alkoxyamine species and the active radical.[32] In principle, this can be mitigated by weakening the P_n-O bond, which can be achieved by adjusting the electronic and steric nature of the nitroxide substituents in order to increase the number of propagating radicals (thus increasing K_{eq}).[45,46] However, this usually reduces the pseudo-living character of the polymerisation. Moreover, homopolymerisation of methacrylic monomers by NMP is problematic owing to slow recombination of nitroxides with sterically-hindered polymer radicals and disproportionation side-reactions between polymer radicals and nitroxides.[47–50] Recently, new nitroxides that improve the NMP of methacrylate monomers have been developed.[51–55] However, this limitation still severely restricts the use of NMP as a controlled polymerisation technique. In academic research, there is no doubt that ATRP and RAFT polymerisation have become preferred for the synthesis of functional block copolymers with tuneable structures, compositions, and complex architectures.

1.2.3.2 Atom Transfer Radical Polymerisation

In 1995, atom transfer radical polymerisation (ATRP) was independently developed by Sawamoto *et al.*[56] and Matyjaszewski's group.[57] ATRP enables the preparation of well-defined polymers using a wide range of vinyl monomers *via* a transition metal catalyst (Mt^n–L) that controls the rate of monomer (M) addition to the growing polymer chains (Scheme 1.3).[58] The most popular transition metal for ATRP is Cu but many other transition metals have also been reported, including Ti,[59] Fe,[60–64] Co,[65] Ni,[66–68] Mo,[69–71] Ru,[72–74] Rh,[75] Pd,[76] Re[77] and Os[78].

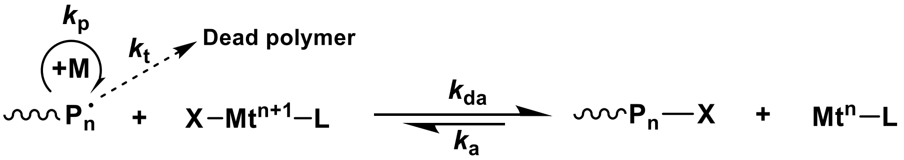

Scheme 1.3 The atom transfer radical polymerisation (ATRP) mechanism using a halogen capping agent (X; typically Cl or Br), a transition metal catalyst (Mt^n–L; with solubilising ligand L), an oxidised catalyst (X–Mt^{n+1}–L), an active radical ($P_n^{\bullet}$) and monomer (M).[57]

The mechanism of ATRP (Scheme 1.3) is based on an inner-sphere electron transfer process, whereby a halogen (X) is reversibly transferred from a dormant species (X–P_n) to a transition metal complex (Mt^n–L). The metal catalyst must be able to expand its coordination sphere and possess two readily accessible oxidation states (e.g. Cu^+ and Cu^{2+}). This reaction produces propagating radicals ($P_n^\bullet$) and the transition metal complex adopts its higher oxidation state (X–Mt^{n+1}–L). Propagation occurs via addition of multiple monomers at a propagation rate constant (k_p). The growing polymer radicals are deactivated by reaction with X–Mt^{n+1}–L, resulting in dormant halogen-capped polymer chains and regeneration of the transition metal complex. The rate of termination (k_t) is minimised *via* the persistent radical effect and the equilibrium is always shifted towards the dormant species (i.e $k_{da} >> k_a$).

The kinetics of ATRP depend on both the concentration of the persistent radical present (X–Mt^{n+1}–L) and the concentration of the transition metal catalyst (Mt^n–L). The mean DP of polymer chains prepared by ATRP is equal to the monomer concentration divided by the initiator concentration (see Equation 1.22) and is not affected by the catalyst concentration. The rate of polymerisation (R_p) is proportional to the initiator concentration and is also influenced by the reduced form of the transition metal complex divided by its oxidised form according to Equation 1.23.[12]

$$R_p = \frac{-d[M]}{dt} = k_p[M][P_n^\bullet] = \frac{k_p[M]K_{ATRP}[RX][(Mt^n - L)]}{[X - Mt^{n+1} - L]} \tag{1.23}$$

Here K_{ATRP} is the ATRP equilibrium constant (k_a/k_{da}) and [RX] is the concentration of halide initiator. Thus, according to Equation 1.23 the absolute amount of transition metal catalyst used for ATRP can be lowered without affecting the rate of polymerisation. However, the concentration of the oxidised metal complex significantly affects the molecular weight distribution of the final polymer (Equation 1.24).[79]

$$\frac{M_w}{M_n} = 1 + \frac{1}{DP_n} + \left(\frac{[RX]_0 k_p}{k_{da}[X - Mt^{n+1} - L]}\right)\left(\frac{2}{Conversion} - 1\right) \tag{1.24}$$

Equation 1.24 indicates that the dispersity (M_w/M_n) is reduced with increasing monomer conversion, increasing X–Mt^{n+1}–L concentrations and decreasing k_p/k_{da} ratio. This results in a significant disadvantage for conventional ATRP for which a near-stoichiometric amount of transition metal catalyst is required. Such transition metal complexes are problematic for biomedical applications owing to their toxicity. The removal of transition metal residues *via* post-polymerisation purification is feasible but both timeconsuming and costly, which reduces the viability of conducting ATRP on an industrial scale. Improved ATRP formulations have been devised to address this problem by ensuring that k_{da} values remain high, thus enabling relatively low concentrations of transition metal catalyst to be employed while maintaining the living character of the polymerisation. However, there is an intrinsic lower limit to the amount of transition metal catalyst that can be used because the X–Mt^{n+1}–L accumulates owing to unavoidable background termination.[80] The most successful examples of ATRP generate the air-sensitive transition metal catalyst at the start of the reaction. Such formulations include initiators for continuous activator regeneration (ICAR) and activators regenerated by electron transfer (ARGET). In ARGET, the transition metal catalyst is added to the reaction mixture in its oxidised state along with excess reducing agent, such as FDA-approved tin(II) 2-ethylhexanoate,[81] glucose and ascorbic acid,[82] phenol, [83] hydrazine and phenylhydrazine,[84] excess inexpensive ligands[85] and amines or nitrogen-containing monomers.[86] The reducing agent continuously regenerates the Mt^{n}–L complex from X–Mt^{n+1}–L species.[87] ICAR ATRP is similar to ARGET but thermal initiators act as a source of free radicals to continuously regenerate the Mt^{n}–L complex. Both techniques enable ATRP to be conducted using relatively low catalyst concentrations (typically 5-50 ppm) while maintaining narrow molecular weight distributions.[88,89]

1.2.3.3 Reversible Addition-Fragmentation Chain Transfer Polymerisation

Reversible addition-fragmentation chain transfer (RAFT) polymerisation was first reported in 1998 by the CSIRO group led by Moad, Rizzardo and Thang[90] and has subsequently become arguably the most versatile and robust CRP technique for the synthesis of complex polymer architectures (see Figure 1.3).[91–93] RAFT polymerisation controls the growth of polymers *via* a degenerative chain transfer process (Scheme 1.1b). Unlike NMP or ATRP, it does not rely on the persistent radical effect. Instead, control is achieved by addition of a suitable organosulfur RAFT chain transfer agent (CTA), which establishes an equilibrium between the active and dormant polymer radicals *via* rapid reversible chain transfer.[94] RAFT polymerisations can be optimised through judicious choice of the type of RAFT CTA (for which a generalised chemical structure is in Figure 1.5) and its Z and R substituents, but solubility must also be taken into consideration.[94] Examples of highly effective RAFT CTAs include dithioesters, trithiocarbonates, dithiocarbamates and xanthates.[94–96]

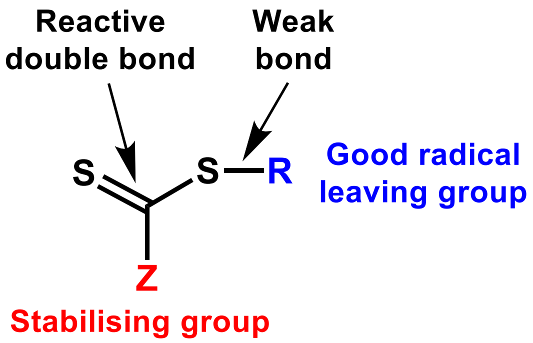

Figure 1.5. Generic chemical structure and key characteristics of a RAFT CTA showing its R and Z groups.

RAFT polymerisations are compatible with a wide range of functional vinyl monomers. Unlike NMP and ATRP, this chemistry can even be used to synthesise well-defined polymers from vinyl ester and vinyl amides such as vinyl acetate[97,98] or *N*-vinylpyrrolidone.[99] RAFT polymerisations can be performed in a wide range of solvents[100] and also under heterogenous dispersed conditions such as emulsion or suspension polymerisation.[101] One disadvantage of RAFT polymerisation is that the organosulfur-based RAFT end-groups are usually intrinsically coloured, malodorous and cytotoxic.[102–104] However, various methods have been developed to either modify or remove RAFT end-groups via thermolysis,[105] radical-induced reductions,[106] hetero-Diels-Alder reactions[107,108] and reactions with nucleophiles or reducing agents.[109–111]

The RAFT mechanism bears many similarities to that of FRP and rates of polymerisation are often comparable (Scheme 1.4).[91–93] However, depending on the type of CTA, monomer and other reaction conditions, the rate of polymerisation can sometimes be retarded.[94,112]

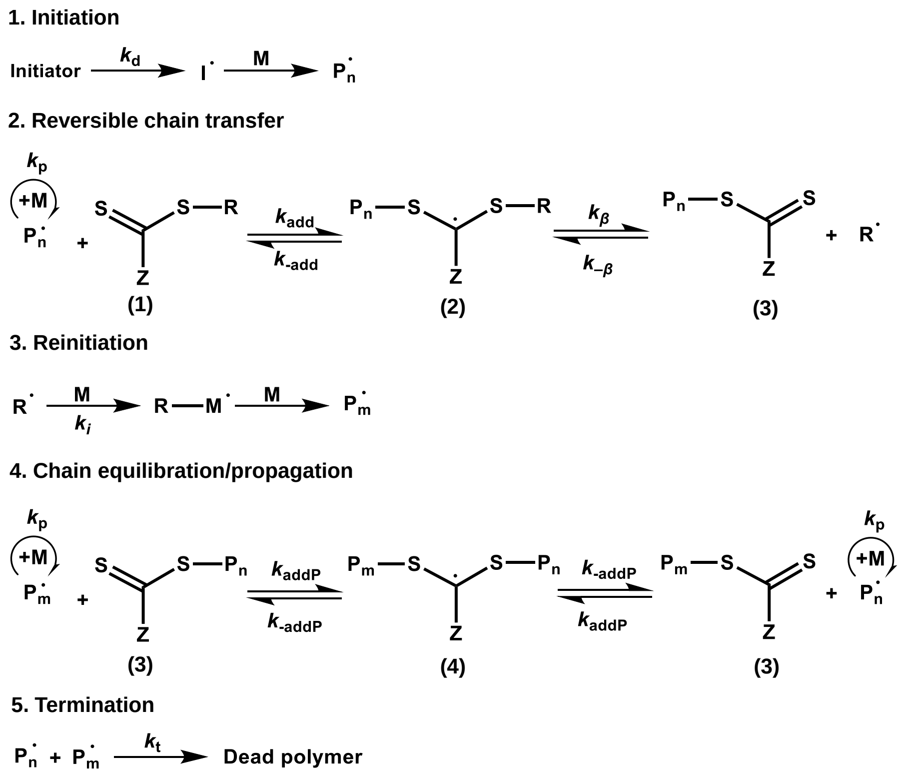

Scheme 1.4. The five main stages of a RAFT polymerisation: initiation, reversible chain transfer, re-initiation, chain equilibration/propagation and termination.[91–93]

Unlike NMR and ATRP, the sum of the RAFT CTA concentration and the concentration of initiator-derived radicals that go on to react with monomer affects the number of polymer chains that are formed and the mean DP of the final polymer at full monomer conversion (Equation 1.23). However, the number of chains containing initiator-derived fragments is usually negligible owing to the much higher CTA concentration compared to the initiator concentration (i.e. $[CTA]_0 >> 2f[I]_0$). Under these conditions, Equation 1.23 can be simplified, and the mean DP of the chains is simply equal to the monomer concentration divided by that of the RAFT CTA (Equation 1.24).

$$\mathrm{DP} = \frac{[M]_0}{([CTA]_0 + 2f[I]_0)} \tag{1.23}$$

$$\mathrm{DP} = \frac{[M]_0}{[CTA]_0} \tag{1.24}$$

RAFT polymerisation usually commences with homolytic cleavage of an initiator molecule via thermal degradation (see stage (i) in Scheme 1.4). These initiator-derived radicals react with monomer (M) to form first an initiator-monomer adduct ($P_1^\bullet$) and then propagating polymer radicals ($P_n^\bullet$). The RAFT CTA (1) then reacts with $P_n^\bullet$ to form a pre-equilibrium radical adduct (2). This adduct can undergo fragmentation via β-scission back to the original CTA or form a polymeric CTA precursor (3) and the eliminated RAFT agent-derived radical ($R^•$; see stage (ii) in Scheme 1.4). The stabilising Z group affects the rate of addition of a propagating radical to the CTA. Greater stabilisation favours the formation of the intermediate RAFT adducts during the equilibrium stages of a RAFT polymerisation (species 2 and 4 in Scheme 1.4). Furthermore, if the Z stabilising group contains electron-withdrawing groups or interacting adjacent heteroatoms (dithiocarbamates and xanthates), the reactivity of the C=S bond is either increased or reduced, respectively. The RAFT agent-derived radical ($R^•$) then re-initiates propagation via addition of further monomer (stage iii) to produce a second growing polymer chain ($P_m^•$). The R group must be a better leaving group than the propagating $P_n^•$ and $P_m^•$ species. Fragmentation of the R group can be increased using electrophilic and/or sterically hindered radicals. A rapid reversible equilibrium between the active and dormant (capped) states of $P_n^•$ and $P_m^•$ is set up in stage (iv) with the formation of an intermediate RAFT adduct (4). This ensures equal probability for propagation of each chain, resulting in a relatively narrow molecular weight distribution. During this rapid transfer, radicals are neither generated nor destroyed hence the overall rate of polymerisation is not influenced. The radical-radical reactions shown in stage (v) result in termination and the production of dead polymer chains; such background reaction result in pseudo-living character for RAFT polymerisations.

The type of CTA used to confer control over the polymerisation depends on the type of monomer. Moad and co-workers established guidelines that enable an appropriate RAFT CTA to be selected for a given monomer class depending on its activity (Figure 1.6).[91] More-activated monomers (MAMs) have a vinyl double bond that is conjugated to a carbonyl group [e.g., methyl methacrylate, (MMA), methyl acrylate, (MA), acrylamide (AM)], a nitrile group [e.g. acrylonitrile (AN)] or an aromatic group [e.g. styrene (S)]. Unlike NMP or ATRP, RAFT polymerisation of less-activated monomers (LAMs), whereby the vinyl group is adjacent to an unsaturated carbon or a heteroatom [such as vinyl acetate (VAc), *N*-vinylpyrrolidone (NVP) or *N*-vinylcarbazole (NVC)], can be well-controlled. Furthermore, acidic monomers can be polymerised in their unprotected forms, whereas ATRP normally requires protecting group chemistry (or the sodium salt form of the monomer).[113]

In particular, NVP is a commercially important example of a LAM. However, it offers only poor copolymerisability with other monomers, which limits its range of potential applications. Nevertheless, PNVP homopolymer is widely used as a highly versatile non-ionic water-soluble polymer with various commercial applications owing to the highly polar nature of the pyrrolidone ring (see Chapter 2).[114,115] Understanding the RAFT mechanism is critical for optimising the polymerisation of LAMs. In principle, this should enable well-defined pyrrolidone-based diblock copolymers to be prepared.

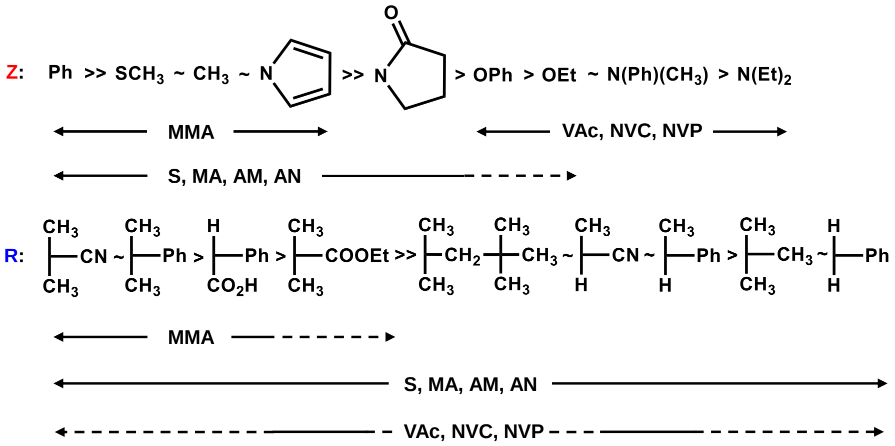

Figure 1.6. Guidelines for the appropriate selection of Z and R groups for the RAFT polymerisation of a given monomer class. For Z groups, fragmentation increases from left to right and the rate of addition is reduced. For R groups, the rates of fragmentation are reduced from left to right. Solid lines indicate good control, while dashed lines indicate reasonable control over the target molecular weight but poor control over the molecular weight distribution.[91]

The order in which different monomers are incorporated into a block copolymer during a RAFT polymerisation also must be considered. The monomer that is polymerised first serves as a polymeric R group (species 3 in Scheme 1.4) during the polymerisation of the second monomer. This polymeric R group must be a good homolytic leaving group and also must reinitiate polymerisation of the second monomer efficiently. This means that MAMs (e.g. methacrylates ~ methacrylamides ≫ styrenics ~ acrylates ~ acrylamides) must be polymerised before LAMs (e.g. N-vinylheteroaromatics > vinyl amides > vinyl esters) if well-defined diblock copolymer chains are desired. Furthermore, RAFT polymerisation of methacrylates or methacrylamides involves more stable tertiary propagating radicals that are also better leaving groups. This requires such monomers to be polymerised prior to monomers that produce secondary propagating radicals (e.g. styrenes, acrylates or acrylamides).[94] According to these guidelines, well-defined polymers can be synthesised *via* RAFT polymerisation of MAMs using dithioesters or trithiocarbonates, whereas the RAFT polymerisation of LAMS (such as NVP) requires dithiocarbamates or xanthates.[94,96] Thus the type of monomer dictates the choice of RAFT CTA.

Selection of appropriate Z and R groups is crucial for efficient RAFT polymerisations, failure to do so . For example, when dithioesters or trithiocarbonates are used to polymerise LAMs, inhibition and/or retardation occurs because the RAFT adducts (species 2 and 4 in Scheme 1.4) are relatively stable and $P_n^\bullet$ and $P_m^\bullet$ are poor leaving groups.[96] Similarly, when dithiocarbamates or xanthates are used to polymerise MAMs, retardation occurs because the CTA reactivity is lower than that of the monomer.[94]

The design of pH-responsive RAFT CTAs that switch between offering control for MAMs and LAMs respectively has enabled the synthesis of reasonably well-defined MAM-LAM block copolymers.[116] Moreover, the use of RAFT agents as 'photoiniferter' compounds (first reported by Otsu *et al.*)[117,118] have recently provided synthetical protocols to reverse this block order. Easterling and Sumerlin *et al*. have recently reported the synthesis of a poly(acrylamide)-poly(methacrylate) diblock copolymers *via* photoiniferter-mediated radical polymerisation.[119] Instead of RAFT adducts forming through addition-fragmentation, thiocarbonylthio photolysis of xanthate and dithiocarbamates-functional RAFT precursors led to the direct formation of leaving group macroradicals that cannot be generated via the addition−fragmentation mechanism (Figure 1.7). This relatively new method of polymerisation could enable various PNVP-based diblock copolymers to be designed. However, the synthesis of LAM-based block copolymers via photoiniferter chemistry is currently unexplored and is likely to be non-trivial.

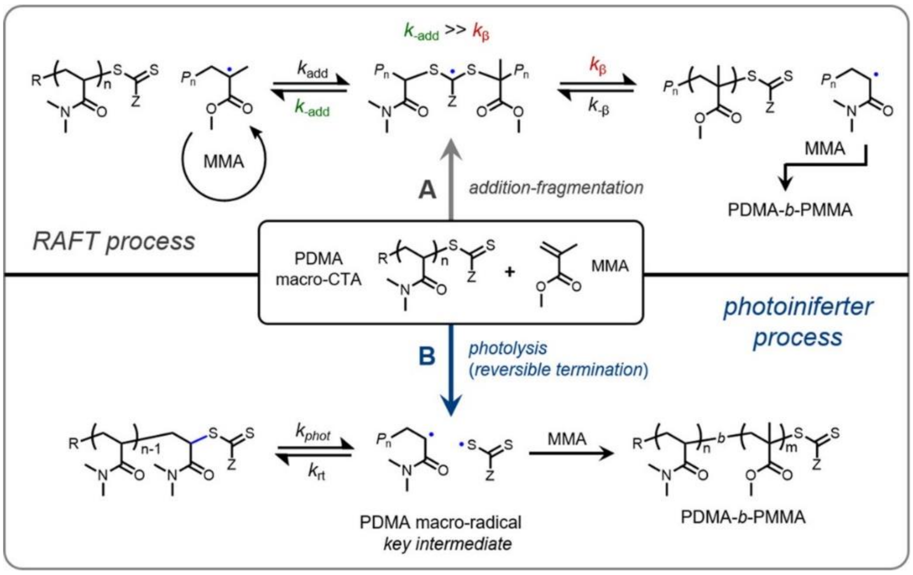

Figure 1.7. Possible mechanistic pathways for a poly(*N,N*-dimethylacrylamide) (PDMAc) RAFT precursor undergoing chain extension with methyl methacrylate (MMA) to produce a PDMAc-PMMA diblock copolymer through either RAFT polymerization (A) or photoiniferter polymerization (B).[119]

An alternative route to pyrrolidone-based diblock copolymers involves the polymerisation of more activated analogues of NVP (see Figure 1.8). Ashland optimised the multi-kilo synthesis of 2-(*N*-methacryloyloxy)ethylpyrrolidone (NMEP; see Figure 1.8) and its RAFT polymerisation was explored by Cunningham and co-workers.[120–122] High NMEP conversions were achieved when using a dithiobenzoate-based RAFT CTA or when conducting chain extensions of dithiobenzoate-capped poly(stearyl methacrylate) or poly(glycerol monomethacylate) precursors, with GPC analysis indicating relatively narrow molecular weight distributions for the resulting diblock copolymers ($M_w/M_n < 1.50$). However, the methacrylic group results in PNMEP exhibiting inverse-temperature solubility. Understandably, such behavior limits its use as an aqueous dispersant/stabiliser. However, it was exploited to prepare high molecular weight PNMEP polymers via a low-viscosity RAFT aqueous dispersion polymerisation route.[120] Ashland Inc have recently optimised the multi-kilo synthesis of 2-(*N*-acryloyloxy)ethylpyrrolidone (NAEP; see Figure 1.8). This monomer should possess similar copolymerisability to that of NMEP but the resulting PNAEP homopolymer should be significantly more hydrophilic with aqueous solubility properties similar to those of PNVP. Identifying and exploiting these properties is the main aim of this Thesis.

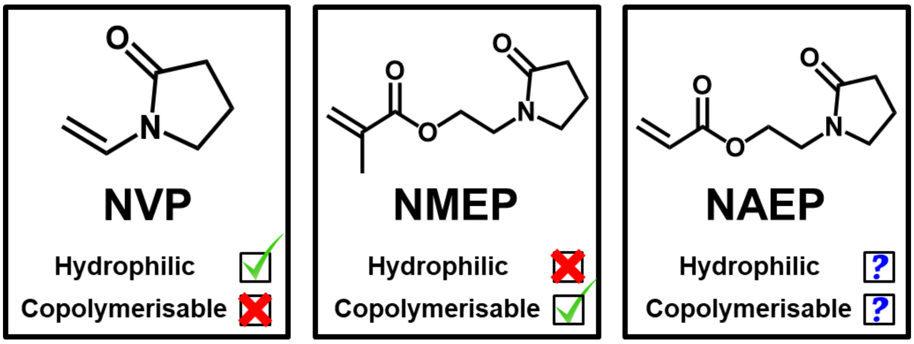

Figure 1.8. Chemical structures and physical properties of NVP and its (meth)acrylic analogues 2-(*N*-methacryloyloxy)ethylpyrrolidone (NMEP) and 2-(*N*-acryloyloxy)ethylpyrrolidone (NAEP), respectively.

1.3 Self-Assembly

1.3.1 Properties of Water and the Hydrophobic Effect

Water can be described as a ‘universal solvent’ owing to its ability to solubilise many types of ionic or polar solids.[123] This is achieved through the formation of hydrogen bonds between H_2O molecules and such solutes. Such non-covalent interactions are significantly stronger than classical van der Waals interactions (10-65 kJ mol^{-1} vs. 1 kJ mol^{-1}, respectively). It is often found that the solution pH and temperature can affect the solubility of solutes. However, if a solute cannot form hydrogen bonds then the H_2O

molecules that immediately surround it must give up at least one intermolecular hydrogen bond. To minimise the loss of enthalpy, water molecules reorient to form a cage-like structure[124,125] around the solute; this phenomenon is known as the hydrophobic effect.[126] Such molecular re-ordering is entropically unfavourable and increases as a function of the size of the hydrophobic solute. This explains why hydrophobic liquids such as oils are water-immiscible and hydrophobic solids do not dissolve in water. Moreover, if molecules possessing both hydrophobic and hydrophilic components (i.e. amphiphiles) are placed in water, the hydrophobic effect results in molecular reorientation to produce so-called micellar structures.

1.3.2 Self-Assembly of Surfactants: The Packing Parameter

Surfactants are examples of small-molecule amphiphiles that comprise a hydrophilic head-group and a hydrophobic tail. The hydrophobic tail drives aggregation to form micelles in aqueous solution.[127] The hydrophobic effect results in a hydrophobic core (composed of the surfactant tails) that is surrounded by the solvated hydrophilic head-groups. The formation of surfactant micelles involves a delicate balance between the attractive van der Waals interactions between neighbouring hydrophobic surfactant tails and the electrostatic repulsion between neighbouring hydrophilic head-groups. Such micellisation results in a highly dynamic equilibrium between individual surfactant molecules and their micellar aggregates (Figure 1.9).[128]

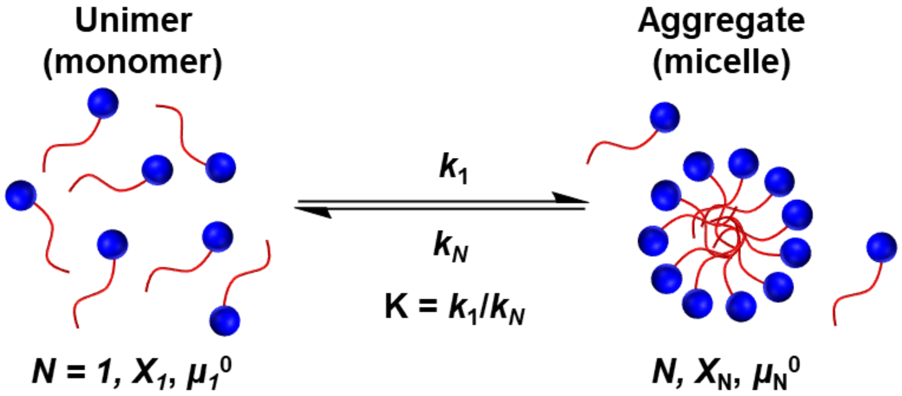

Figure 1.9. Schematic representation of the dynamic equilibrium between individual surfactant molecules (unimers) and their respective aggregates (micelles). Here N, X and μ denote the aggregation number, activity and chemical potential, respectively.

The equilibrium constant (K) between an aggregate and its unimer is equal to the rate constant of association (k_1) divided by the rate constant of dissociation (k_N). This leads to a mathematical expression involving the Boltzmann constant (k_B), absolute temperature (T), chemical potential of the aggregate in solution (μ_N^0; with an aggregation number N) and the chemical potential of a single surfactant molecule in solution (μ_1^0; Equation 1.25).[128]

$$K = \frac{k_1}{k_N} = e^{[-\frac{N(\mu_N^0 - \mu_1^0)}{k_B T}]} \tag{1.25}$$

According to the equilibrium shown in Figure 1.9, aggregation occurs when K is positive (i.e. if $k_1 > k_N$). For this to be true, Equation 1.25 indicates that the chemical potential of a single surfactant must be greater than that of the micellar aggregate that is formed ($\mu_1^0 > \mu_N^0$). Typically, the critical concentration at which aggregation occurs is known as the critical micelle concentration (CMC). When the surfactant concentration is increased well beyond the CMC, the aggregation number increases while the concentration of unimers remains relatively constant. The morphology of the micellar aggregates depends on the repulsion between neighbouring hydrophilic head-groups and the attraction of the hydrophobic chains at the hydrocarbon-water interface. Both interactions influence the area occupied per molecule (a_0). This can be described using the three contributions (transfer, interface and head in Equation 1.26) of Tanford's model for the standard free energy change per molecule on aggregation.[129]

$$\ln\left(X_{CMC}\right) = \left(\frac{\Delta\mu_N^0}{k_B T}\right) = \left\{\frac{\Delta\mu_N^0}{k_B T}\right\}_{Transfer} + \left\{\left(\frac{\sigma}{k_B T}\right)\mathrm{a}\right\}_{Interface} + \left\{\left(\frac{\alpha}{k_B T}\right)\frac{1}{a}\right\}_{Head} \tag{1.26}$$

The transfer term in Equation 1.26 makes a negative contribution corresponding to the transfer of the tail from bulk water to the centre of the aggregate. This depends on the chemistry of the surfactant tail but not on the shape or size of the aggregate. It affects the CMC (shown in Equation 1.26 in mole fraction units) but does not alter a_0. The interface term (Equation 1.26) is positive because a small area of the surfactant tail is still in contact with the water at the surface of the micelle. This can be calculated from the product of the interfacial free energy (σ) and the surface area per molecule of the aggregate core (a_0). As such, a reduction in this term corresponds to an increase in the aggregation number (N). The contribution from the surfactant head-group (Equation 1.26) is another unfavourable contribution representing the repulsive interactions between the head-groups within the micellar aggregate (α). Depending on the type of surfactant, this may involve steric interactions and/or electrostatic interactions (for ionic or zwitterionic surfactants). Repulsion between head-groups increases if the area *a* is reduced or the aggregation number *N* increases. This limits the growth of aggregates to a finite size.

Ultimately, lowering the interfacial energy by reducing the surface area and increasing the repulsive energy between head-groups as they are forced closer together results in a balance that dictates the final micelle morphology. A simple equation was proposed by Israelachvili to model the total surface energy (Equation 1.27).

$$\mu = \sigma a + \frac{K}{a_0} \tag{1.27}$$

Here μ is the chemical potential at the interface, *σ* is the interfacial energy between hydrocarbon tails in the aqueous phase, *a* is the surface area occupied per head-group and *K* is the proportionality constant for repulsion of head-groups. Differentiating Equation 1.27 with respect to head-group area, assuming equilibrium (i.e. dμ/da = 0) and solving for the optimal head-group area affords Equation 1.28.

$$a_0 = \left(\frac{K}{\sigma}\right)^{\frac{1}{2}} \tag{1.28}$$

Israelachvii et al. combined a_0 with the volume of the hydrocarbon chain (*v*) and the maximum effective chain length (l_c) to calculate the packing parameter (*P*), which is used to represent the curvature of the molecular aggregate (Equation 1.29).[127]

$$P = \frac{v}{a_0 l_c} \tag{1.29}$$

The simplest shape that an aggregate can form is a spherical micelle with a core radius (*R*) and mean aggregation number (*N*). Using simple geometric relationships, the volume (*V*) and the surface area of the core (A) can be calculated (Equations 1.30 and 1.31). Thus, *R* can be found (Equation 1.32).

$$V = Nv_0 = \frac{4\pi R^3}{3} \tag{1.30}$$

$$A = Na = 4\pi R^2 \tag{1.31}$$

$$R = \frac{3v_0}{a} \tag{1.32}$$

If the micelle cores comprise solely surfactant tails with no voids, then R cannot exceed l_c (i.e. $0 \leq R \leq l_c$). Substituting these limits for R into Equation 1.29, it is found that for spherical micelles, $0 \leq P \leq 1/3$ (Figure 1.9). Using similar geometric relationships for cylinders or bilayers, along with the constraint that one dimension of the aggregate cannot exceed l_c, the packing parameter can be calculated for a range of micelle morphologies (Figure 1.10).[129]

Variable	Sphere	Cylinder	Bilayer
Volume of core $V = gv_0$	$\frac{4\pi R^3}{3}$	πR^2	$2R$
Surface area of core $A = ga_0$	$4\pi R^2$	$2\pi R$	2
Area per molecule a_0	$\frac{3v_0}{R}$	$\frac{2v_0}{R}$	$\frac{v_0}{R}$
Packing Parameter $P = \frac{v_0}{a_0 l_c}$	$P \leq \frac{1}{3}$	$\frac{1}{3} < P \leq \frac{1}{2}$	$\frac{1}{2} < P \leq 1$

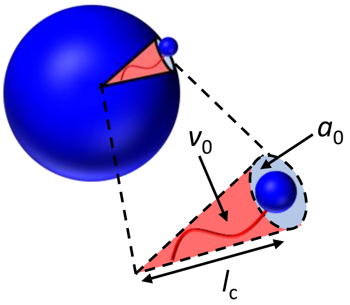

Figure 1.10. Schematic representation of the packing of surfactant molecules within a micellar aggregate, showing the two opposing forces of attraction between hydrophobic surfactant tails and repulsion between hydrophilic head-groups. The equation for the dimensionless packing parameter, *P*, and the characteristic ranges of *P* for spheres, cylindrical (worm-like) micelles and vesicles are stated.[129]

1.3.3 Self-Assembly of Diblock Copolymers

Self-assembly is not limited to surfactants but also applies to amphiphilic copolymers.[130–136] In particular, diblock copolymers typically undergo *microphase* separation – as opposed to macroscopic separation - owing to the covalent bond between the two chemically dissimilar (and hence enthalpically incompatible) blocks.[130,134,135] The phase adopted by such copolymers involves a subtle balance between enthalpic (Equation 1.33; where H, U, P and V represent the enthalpy, system energy, pressure, and volume, respectively) and entropic (S) parameters that lead to an overall negative Gibbs free energy (G) for the system (Equation 1.34).

$$H = U + PV \tag{1.33}$$

$$\Delta G_{mix} = \Delta H_{mix} - T\Delta S_{mix} \tag{1.34}$$

$$\frac{\Delta G_{mix}}{k_B T} = \left(\frac{\varphi_A ln\varphi_A}{N_A}\right) + \left(\frac{\varphi_B ln\varphi_B}{N_B}\right) + \varphi_A \varphi_B \chi_{AB} \tag{1.35}$$

In 1942 Flory[137] and Huggins[138] independently derived mathematical expressions for ΔG_{mix} when a homopolymer is mixed with a solvent (Equation 1.35). The extent of microphase separation for diblock copolymers in the solid state depends on three parameters: (i) the volume fraction of each block, (φ) (ii) the DP of the diblock copolymer (N) and (iii) the temperature-dependent Flory-Huggins parameter (χ_{AB}) which accounts for the enthalpic incompatibility between the two blocks (Equation 1.36).[130]

$$\chi_{AB} = \left(\frac{z}{k_B T}\right)\left[\varepsilon_{AB} - \frac{1}{2}(\varepsilon_{AA} - \varepsilon_{BB})\right] \tag{1.36}$$

Here z is the mean number of nearest neighbours per molecule, k_B is the Boltzmann constant, T is the temperature and ε_{AB}, ε_{AA} and ε_{BB} are the respective interaction energies between repeat units. For microphase separation to occur, net repulsion between the two blocks requires χ_{AB} to be positive. Furthermore, Equation 1.36 indicates that χ_{AB} is inversely proportional to temperature. This results in polymer mixtures exhibiting an order-disorder transition (ODT) at a critical temperature. In contrast, diblock copolymers can undergo order-order transitions (OOT). The degree of microphase separation exhibited by diblock copolymers is determined by the segregation product (χN). The strong segregation limit occurs when $\chi N > 100$, resulting in highly pure phases. The weak segregation limit involves poor segregation ($\chi N < 10$) where the system is close to its ODT. Self-consistent mean field (SC MF) theory has been used to predict the rich phase behaviour of diblock copolymers between these two limits and often agrees well with experimental data. Figure 1.11 shows that, on increasing relative volume fraction of block A (f_A) at a fixed χN (i.e. below the ODT), the OOT shifts from close-packed spheres, through to body-centered cubic spheres, hexagonally-packed cylinders, bicontinuous gyroids, and finally lamellae.[135,139]

Thermodynamic equations for the self-assembly of diblock copolymers in a given solvent require interaction parameters between each block and the solvent to be considered. This can make it difficult to predict the resulting phase behaviour.[140] Nevertheless, it is well-known that amphiphilic diblock copolymers undergo self-assembly in a solvent that is selective for one of the two blocks.[141–143] The solvophobic block is located within the micelle core, which is stabilised by a solvophilic corona formed by the other block. Kinetically stable structures can be formed as the unimer/aggregate exchange rate is much slower than that of surfactants.[144–150] Traditionally, diblock copolymer self-assembly has been achieved using post-polymerisation techniques such as direct dissolution, a solvent switch,[141,151,152] a pH switch[153–155] or thin film dehydration.[156] Unfortunately, such processes are limited to relatively low copolymer concentrations (typically < 1 % w/w), which severely restricts potential industrial applications for such nanostructured materials.

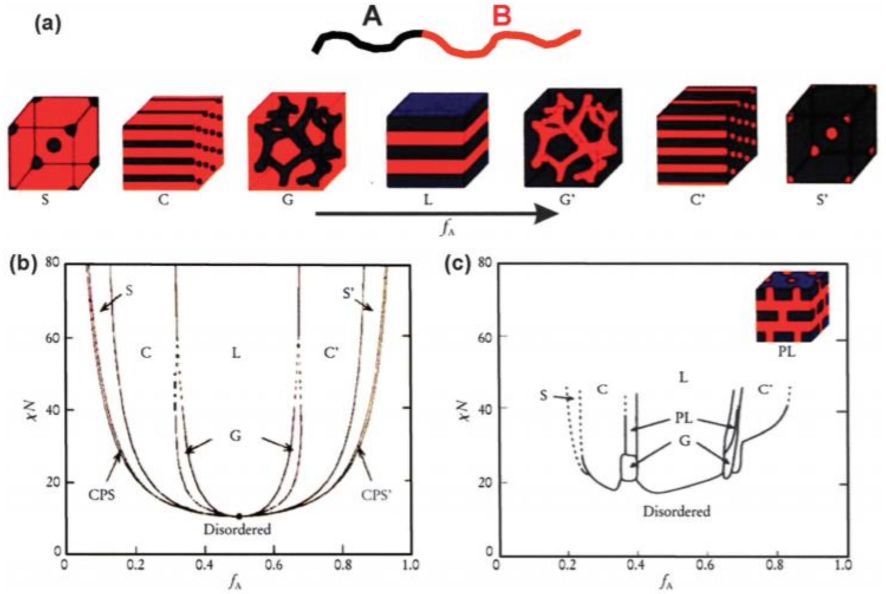

Figure 1.11. (a) Schematic illustration of various solid-state morphologies adopted by a series of AB diblock copolymers with an increasing volume fraction of component A (f_A). Here S and S' are body-centred-cubic spheres, C and C' are hexagonally-packed cyclinders, G and G' are gyroid phases and L represents lamellae. (b) Theoretical phase diagram for the same series of AB diblock copolymers as a function of f_A and the segregation product (χN), as predicted by self-consistent mean field theory. (c) Experimental phase diagram constructed for a series of polyisoprene-polystyrene (PI-PS) diblock copolymers where PI is the A block and PL denotes a perforated lamella phase.[135,139]

1.4 Latex Formation via Free Radical Polymerisation in Water

Over the past 75 years, the development of dispersion,[152,156] emulsion,[157–159] and precipitation[160–162] polymerisation has enabled the facile synthesis of monodisperse latex particles in water. An aqueous emulsion polymerisation formulation typically comprises a water-immiscible monomer (such as styrene), a water-soluble initiator, a surfactant and water.[163,164] Emulsion polymerisation is widely used in industry for the polymerisation of many vinyl monomers because water is a cheap, environmentally-friendly solvent that enables efficient removal of heat from the polymerisation. Moreover, the particulate form of the final polymer ensures a much lower viscosity compared to the equivalent soluble polymer chains. Consequently, emulsion polymerisation is utilised for the manufacture of paints, adhesives and coatings.[165] There are three stages during an emulsion polymerisation (intervals I, II and III; Figure 1.12).[158]

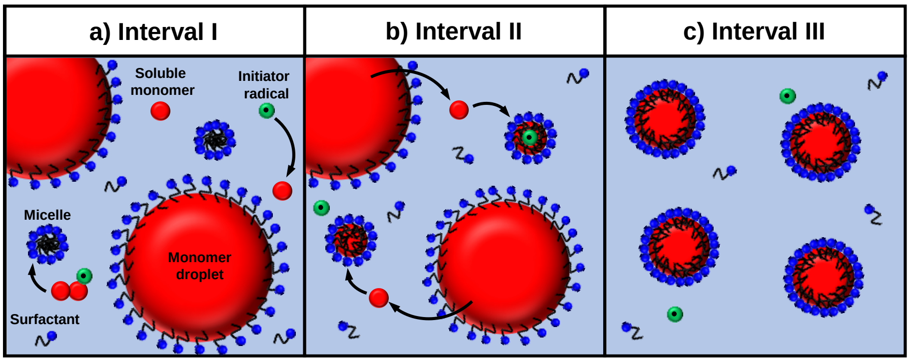

Figure 1.12. Schematic illustration of the main components and three stages (intervals I, II and III) of an *ab initio* aqueous emulsion polymerisation.[158]

Emulsion polymerisation requires efficient mechanical stirring of the reaction mixture to generate the micrometre-sized surfactant-stabilised monomer droplets within the aqueous solution. Despite its immiscibility with water, there is always a finite amount of dissolved monomer present in the aqueous continuous phase. Thermal decomposition of a water-soluble initiator results in the generation of radicals that either react with monomer solubilised within surfactant micelles (heterogeneous nucleation) or with the relatively small amount of monomer dissolved in the aqueous solution to form oligoradicals, which subsequently migrate into monomer-swollen surfactant micelles (homogeneous nucleation).[164,166] If the surfactant concentration is below its CMC during homogeneous nucleation, the oligoradicals become surface-active on reaching a critical DP and then associate with free surfactant molecules to produce nascent hybrid (mixed) micelles. When the surfactant concentration is above its CMC, the growing oligoradicals migrate into pre-existing surfactant micelles (Figure 1.12a). There are up to 10^8 surfactant micelles per monomer droplet. Thus, radical entry into these surfactant micelles is facilitated by their high surface area and number density relative to the much larger surfactant-stabilised monomer droplets. During interval I, the polymerisation rate increases because the local concentration of monomer is relatively high within the monomer-swollen micelles (Figure 1.12).[164,167] Once the monomer solubilised within these micelles has reacted, the rate of polymerisation is limited to the rate of monomer migration from the micrometre-sized monomer droplets into the micelles (interval II in Figure 1.12b). This results in a constant rate of polymerisation until the monomer droplet reservoirs become depleted and interval III begins (Figure 1.13). Entry of an additional radical into a micelle that already contains a growing polymer radical results in rapid termination (as $k_t >> k_p$). This monomer-swollen particle then remains dormant until a new radical enters and initiates a new polymer radical. As such, it can be assumed that all particles contain either one or zero radical species during the emulsion polymerisation. Moreover, as propagation is favoured over termination, relatively high molecular weight chains can be generated within short reaction times. This is known as Smith-Ewart kinetics and leads to copolymer films with superior mechanical properties for paints and coatings applications.[157]

A gradual reduction in the polymerisation rate is observed as the monomer concentration within the growing particles decreases (Figure 1.13).[167] Interval III ends when all monomer is consumed, and only colloidally stable latex particles remain.

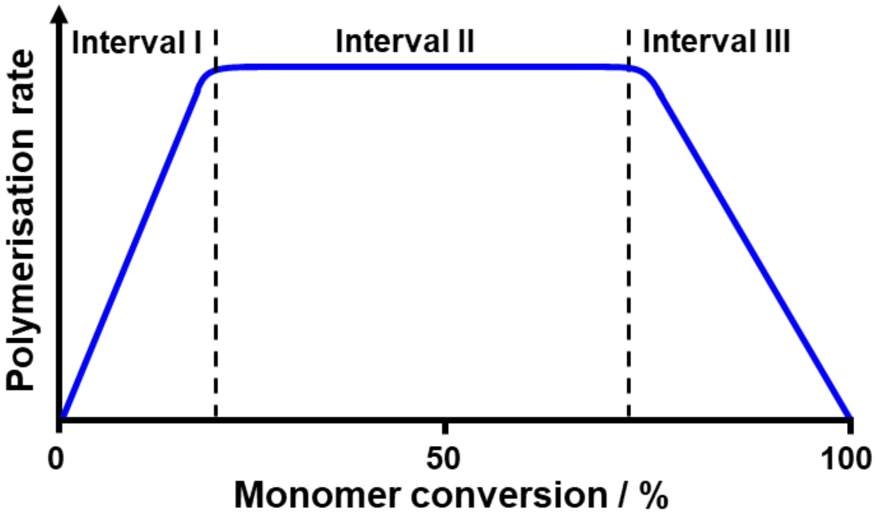

Figure 1.13. Rate of polymerisation versus monomer conversion for an emulsion polymerisation, illustrating intervals I, II and III.[167]

An alternative method for preparing monodisperse polymer latex particles via FRP involves dispersion polymerisation, which is a modified version of precipitation polymerisation (Figure 1.14).[152,159] Here, the polymerisation is conducted in the presence of a suitable polymeric stabiliser that is soluble in the reaction solution. The selection of an appropriate solvent is critical: it must be a good solvent for both the monomer (unlike aqueous emulsion polymerisation where the monomer is water-immiscible; see Figure 1.11) and the polymeric stabiliser, but a non-solvent for the target polymer. In 1962, scientists working at Imperial Chemical Industries (ICI) developed robust protocols for the preparation of sterically-stabilised (meth)acrylic- or styrene-based latex particles in non-polar media via FRP-mediated dispersion polymerisation.[168] Subsequently, Almog *et al.* reported dispersion polymerisations in alcohol to produce micron-sized polystyrene and poly(methyl methacrylate) latexes.[153] According to Kawaguchi and Ito, FRP-mediated dispersion polymerisation comprises six stages (Figure 1.14).[152]

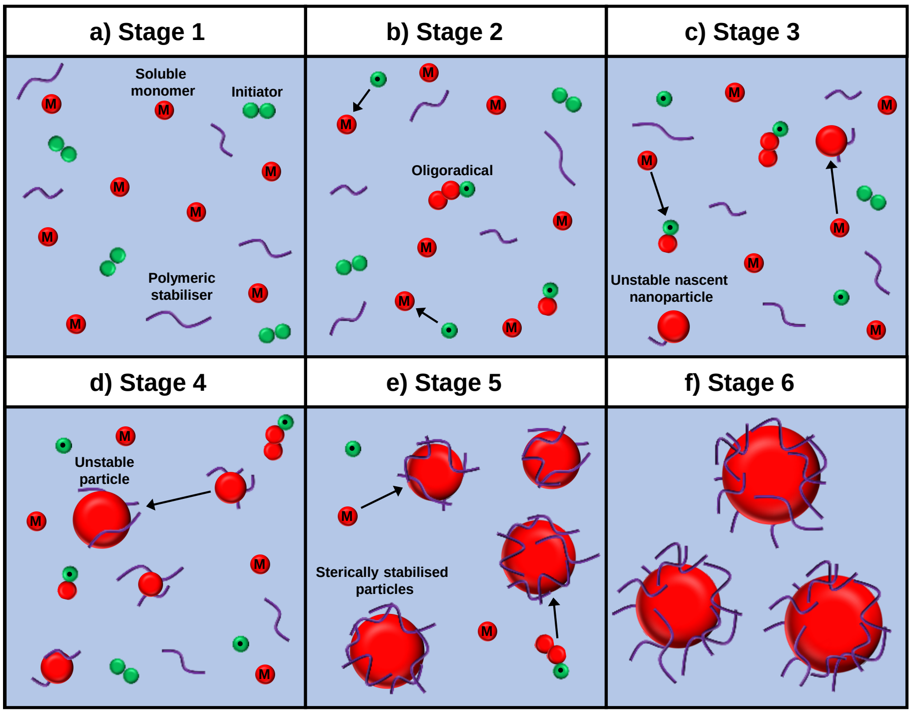

Figure 1.14. Schematic illustration describing the six stages (a-f) of FRP-mediated dispersion polymerisation.[152]

At the beginning of a dispersion polymerisation, all the components are molecularly dissolved into the continuous phase (stage 1; Figure 1.14a). Thermal activation of the initiator results in the formation of radicals, which react with the monomer to produce oligoradicals (stage 2; Figure 1.14b). These oligomers gradually become less soluble as they grow. At some critical DP, they precipitate and form nascent nanoparticles (stage 3; Figure 1.14c). These nanoparticles then aggregate (stage 4; Figure 1.14d) and simultaneous adsorption (or grafting) of the polymeric stabiliser leads to the formation of sterically-stabilised particles (stage 5; Figure 1.14e). After this point, no new particles are formed. Instead, the monomer-swollen particles continue to grow through diffusive capture of oligomers and further monomer (stage 5; Figure 1.14e). As the number of particles remain constant at this point, the final particle diameter simply depends on the amount of polymer that is produced via FRP.

The synthesis of various uniform latex particles *via* dispersion polymerisation in either non-polar or polar media has been well-documented.[153,154,169] Performing dispersion polymerisations in water offers important advantages such as high solids, low solution viscosity, an environmentally benign formulation and facile isolation of the final product. However, there are relatively few monomers that are both water-miscible and afford water-insoluble polymer chains, which is a prerequisite for an aqueous dispersion polymerisation. Early examples reported by Armes et al. include polypyrrole latexes synthesised in the presence of stabilisers such as PNVP,[170] poly(vinyl alcohol) (PVA),[170,171] poly(ethylene oxide)[171] and sodium dodecylbenzenesulfonate.[172] Later, Ali and co-workers prepared 100–1000 nm diameter poly(2-hydroxypropyl methacrylate) (PHPMA) latexes in the presence of either PNVP or sodium dodecylsulfate.[173]

There have been many reports focused on using NMP, ATRP or RAFT polymerisation to conduct aqueous emulsion or dispersion polymerisation syntheses.[112] Typically, this is achieved by using a suitable water-soluble polymer precursor as a steric stabiliser to prevent precipitation of the growing water-insoluble block. This approach is the basis of polymerisation-induced self-assembly (PISA), which is discussed in more detail in the following section. It enables the production of (multi)block copolymer nanoparticles via the controlled polymerisation of a wide range of functional vinyl monomers. In particular, RAFT-mediated PISA formulations provide convenient access to many block copolymer morphologies in the form of concentrated colloidal dispersions and the topic will be the focus of this Thesis.

1.5 Polymerisation-Induced Self-Assembly

Following Szwarc's introduction of living anionic polymerisation,[13] block copolymer self-assembly has been widely studied.[130–136] This led to the development of a number of post-polymerisation processing routes to produce block copolymer nanoparticles of various morphologies in dilute solution.[131,174–177] The limitations of such traditional self-assembly methods can be overcome by PISA.[178] The pseudo-living character of CRP is employed to prepare concentrated dispersions of block copolymer nanoparticles at up to 50% w/w solids with predictable morphologies.[179–185] During PISA, a solvophilic precursor block (or steric stabiliser) is first prepared and then subsequently chain-extended with a solvophobic block (core-forming block). In the case of a dispersion polymerisation formulation, each component is initially fully soluble and *in situ* self-assembly occurs when the growing solvophobic block reaches a critical DP (Figure 1.15). As the polymerisation continues, the relative volume fraction of the steric stabiliser block is gradually reduced relative to that of the core-forming block. This inevitably leads to a gradual increase in the geometric packing parameter, *P*, and this concept has been used to reproducibly target so-called higher order morphologies such as worms or vesicles, as well as the more common spheres (Figure 1.15).[179,180,186–199]

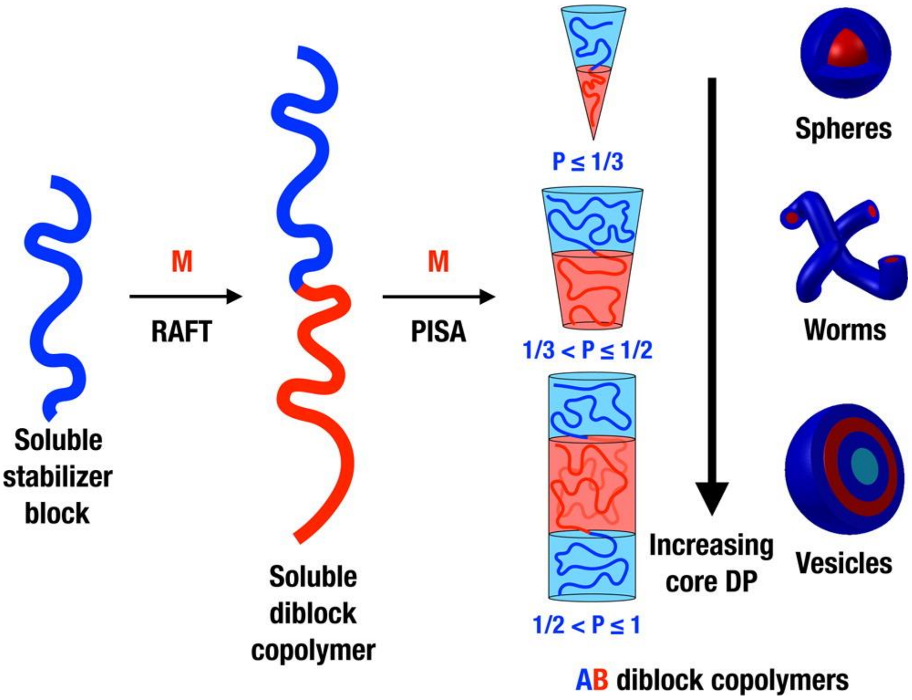

Figure 1.15. Schematic representation of the *in situ* formation of diblock copolymer nanoparticles prepared by PISA.[178]

The synthesis of nanoparticles *via* PISA has been performed using various CRP techniques.[200–205] However, RAFT polymerisation has become the most commonly used in the literature. This is because (i) various RAFT CTAs have become commercially available, (ii) this chemistry is applicable to a particularly wide range of monomers and (iii) it is compatible with many different solvents. RAFT-mediated PISA has been conducted in water,[179,206–208] alcohols,[209,210] *n*-alkanes,[194,211] mineral oil,[183] silicone oil,[212] CO_2,[213,214] and ionic liquids.[215] Water is a particularly attractive solvent for PISA syntheses because it is abundant, cost-effective, environmentally-friendly, non-flammable and has a relatively high heat capacity (which aids dissipation of the polymerisation exotherm). As such, PISA syntheses *via* RAFT aqueous emulsion polymerisation (where the second monomer is water-immiscible) or RAFT aqueous dispersion polymerisation (where the second monomer is water-miscible) have been widely examined for the rational design of many types of functional block copolymer nanoparticles.

1.5.1 PISA by RAFT A*b Initio* Emulsion Polymerisation

Early attempts to conduct heterogeneous polymerisations via RAFT chemistry were performed using pre-formed polymer particles as seeds.[216] Various technical problems were identified, including inhibition, substantially incomplete monomer conversions, poor colloidal stability and broad molecular weight distributions.[217,218]

Moreover, using seed particles required the use of acetone as a co-solvent, which is not ideal for industrial manufacture. Furthermore, the polymer seeds were prepared via FRP and thus broadened the overall molecular weight distribution. Small-molecule RAFT CTAs were employed in some of these early reports but usually with rather limited success.[217,219–223] The first example of a truly effective *ab initio* RAFT emulsion polymerisation was reported by Ferguson *et al.* in 2002.[224] A poly(acrylic acid) (PAA) precursor was chain-extended with *n*-butyl acrylate (nBA) under monomer-starved conditions (Figure 1.16).

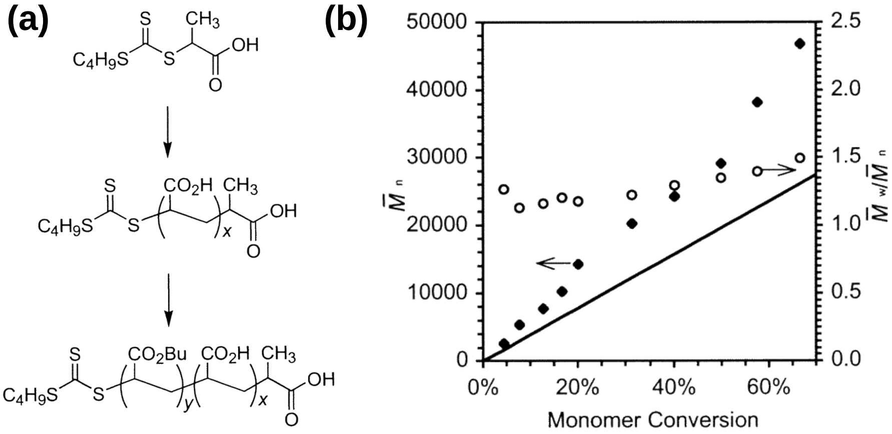

Figure 1.16. (a) Schematic representation for the synthesis of PAA-PnBA diblock copolymers via *ab initio* RAFT emulsion polymerisation and (b) GPC analysis of aliquots taken during the polymerisation of *n*BA using a PAA precursor (observed M_n (diamonds), M_w/M_n (circles) and calculated M_n (Full line).[224]

In 2005, the same research group expanded on this pioneering study and identifies key aspects that were essential for successful *ab initio* RAFT emulsion polymerisations.[225] The authors suggested that it was important to work under monomer-starved conditions so as to avoid the formation of monomer droplets. Otherwise, the macro-RAFT agent would act as an emulsifier and adsorb at the droplet surface, resulting in poor molecular weight control and broad particle size distributions.[225] Over the past 15 years, considerable effort has been devoted by many groups to develop robust RAFT *ab initio* emulsion polymerisation formulations to produce diblock copolymer nanoparticles using cationic,[226–228] anionic,[189,229–234] zwitterionic,[235,236] or non-ionic[182,237–239] RAFT-synthesised steric stabiliser blocks.[240,241]

Subsequently, experimental conditions were optimised to enable effective *ab initio* RAFT emulsion polymerisation under so-called ‘one-shot’ batch conditions (i.e. when all the monomer is present at the start of the reaction). Thus, Charleux and co-workers reported the first example of *ab initio* batch emulsion polymerisation of styrene or nBA in 2008.[242] A water-soluble poly(ethylene oxide)-based precursor was used as both the steric stabiliser and the RAFT agent for such syntheses (Figure 1.17). ^{1}H NMR studies indicated that 67% styrene conversion was obtained after 23 h at 80 °C and GPC analysis confirmed that good RAFT control was achieved when targeting relatively low molecular weight diblock copolymers (M_n = 12.2 kg mol^{-1}; M_w/M_n = 1.16). Much higher monomer conversion (> 96% within 4 h) was obtained for the RAFT emulsion polymerisation of nBA with GPC analysis again indicating good RAFT control (M_w/M_n = 1.21-1.26 when targeting M_n = 18.9-33.8 kg mol^{-1}). However, the block copolymer morphology was confined to kinetically-trapped spheres, with the final number of particles depending on the monomer/macro-RAFT agent molar ratio. Varying the latter parameter enabled the final particle size to be tuned between 200 and 510 nm while maintaining narrow particle size distributions.

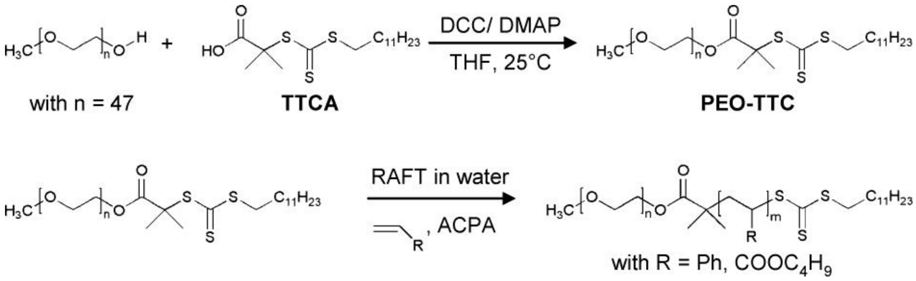

Figure 1.17. Two-step synthetic route reported by Charleux et al. for the *ab initio* RAFT emulsion polymerisation of styrene and/or *n*-butyl acrylate.[242] The first step involves the esterification of a monohydroxy-capped poly(ethylene oxide) precursor to produce a water-soluble macro-RAFT agent. The second step involves the *ab initio* RAFT emulsion polymerisation, which produced kinetically-trapped spheres.

Over the past five years, various RAFT aqueous emulsion polymerisation formulations have been reported in which essentially full monomer conversion has been achieved even when targeting relatively high molecular weights.[182,237,239] For example, Davis and co-workers reported the synthesis of ultrahigh molecular weight, low-dispersity polystyrene-based diblock copolymer nanoparticles (see Figure 1.18).[237]

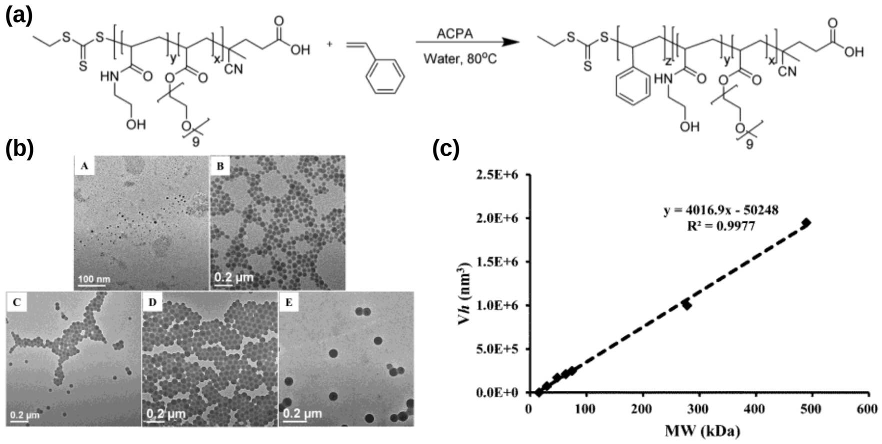

Figure 1.18. (a) Synthesis of P(PEGA-co-HEAA)-PS diblock copolymer nanoparticles *via* RAFT-mediated emulsion polymerization of styrene; (b) transmission electron microscopy (TEM) images of nanoparticles recorded during this polymerisation at various time points (A) 90 min, (B) 195 min, (C) 210 min, (D) 225 min and (E) 240 min; (c) linear relationship between the final nanoparticle volume (V_h) and M_n.[237]

A suitable soluble precursor was prepared via statistical copolymerisation of *N*-hydroxyethyl acrylamide (HEA) and poly(ethylene glycol) methyl ether acrylate (PEGA) using RAFT solution polymerisation. This macro-RAFT agent was then used to polymerise styrene while targeting DPs ranging from 1286 to 14577. Monomer conversions of 91-96% were achieved within 4 h while reasonably good RAFT control was maintained (M_w/M_n < 1.40). Again, DLS studies indicated that solely spherical nanoparticles were produced and a linear relationship was established between the nanoparticle volume and molecular weight. Armes *et al*. utilised a poly(glycerol monomethacrylate) (PGMA) precursor to conduct the RAFT emulsion polymerisation of benzyl methacrylate (BzMA) to produce diblock copolymer nanoparticles at up to 50% w/w solids within 6 h.[182] The mean particle diameter of the spherical nanoparticles was systematically varied from 20 to 193 nm by adjusting the target PBzMA DP between 50 and 1000 (Figure 1.19).

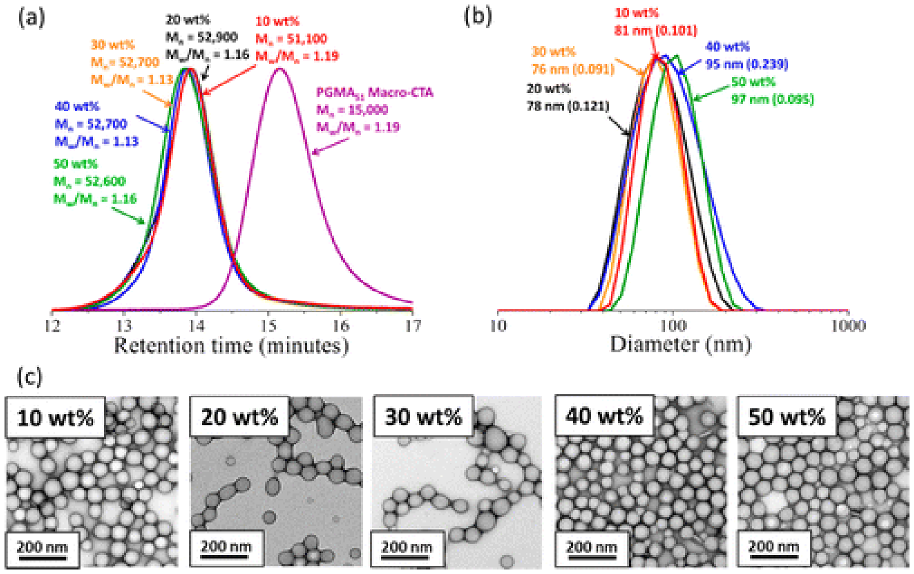

Figure 1.19. (a) DMF GPC curves obtained for five $PGMA_{51}$–$PBzMA_{250}$ diblock copolymers five prepared at 10 to 50% w/w solids and the $PGMA_{51}$ precursor used to mediate the RAFT aqueous emulsion polymerization of BzMA at 70 °C: (b) corresponding particle size distributions obtained by DLS studies of these five nanoparticle dispersions: (c) representative TEM images indicating spherical micelles were obtained in each case.[182]

A common observation for such RAFT emulsion polymerisation syntheses is the formation of *kinetically-trapped spheres*. In principle, the equilibrium copolymer morphology should depend on (i) the degree of stretching of the core-forming polymer block, (ii) repulsive interactions between adjacent stabiliser chains and (iii) the interfacial tension between the core-forming block and the solvent.[135,143] During RAFT emulsion polymerisation, kinetically-trapped spheres are often obtained owing to the restricted chain mobility for the core-forming block. This may arise because of its relatively high glass transition temperature (e.g. in the case of polystyrene) but another factor may be the relatively low degree of solvation by the unreacted monomer. This is because monomer mass transport from the monomer droplets to the growing nascent nanoparticles is likely to be limited by the relatively low solubility of monomers such as styrene or *n*-butyl acrylate in the aqueous continuous phase.[243] Early examples of *ab initio* RAFT emulsion polymerisation produced solely spherical nanoparticles. In at least some cases, this has been linked to strong electrostatic repulsions between highly anionic stabiliser blocks such as PMAA or PAA preventing sphere-sphere fusion, which is the critical first step on the path to worms and, ultimately, vesicles.[244] Nevertheless, there is now a sub-set of poorly-understood literature examples, initially by Charleux *et al.*,[231] and later by Hawkett et al.,[245] Davis et al.,[238] and D'Agosto et al.,[246] in which higher order morphologies have been obtained by RAFT-mediated emulsion polymerisation.[186,187,189,195]

For example, in 2010 Charleux et al. reported the RAFT statistical copolymerisation of AA with oligo(ethylene oxide) methyl ether acrylate (OEOA) in various molar proportions.[195] These copolymers were then used for the RAFT emulsion polymerisation of styrene to generate either spheres or examples of higher order morphologies (Figure 1.20).

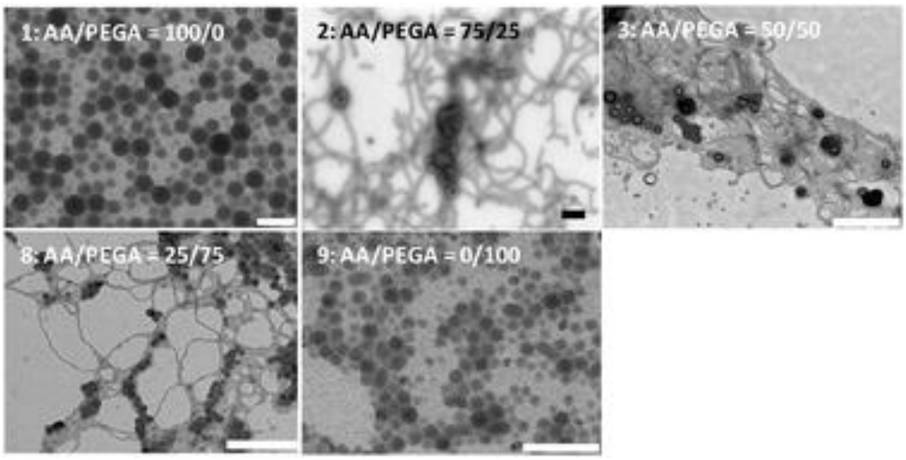

Figure 1.20. Representative TEM images of the various copolymer morphologies obtained from the RAFT emulsion polymerisation of styrene using a P(AA-*co*-OEGA) precursors with AA/OEGA molar ratios of (1) 100/0, (2) 75/25, (3) 50/50, (8) 25/75, (9) 0/100. Scale bars: (1) 100 nm, (2) 400 nm, (3) 500 nm, (8) 1 μm, (9) 200 nm.[195]

At sufficiently low solution pH, it is well-known that graft copolymers comprising a PMAA backbone and short PEG side-chains exhibit hydrogen bonding complexation behaviour.[247–249] Similar, albeit weaker, complexation is likely to occur between the AA units and OEGA side-chains in the P(AA-co-PEGA) stabiliser block. Moreover, incorporating the OEGA comonomer lowers the anionic charge density and hence reduces electrostatic repulsion between coronal chains compared to PAA homopolymer. This leads to a reduction in the effective volume fraction for the P(AA-co-PEGA) stabiliser block and so aids formation of higher order copolymer morphologies.[187] Subsequently, Charleux and co-workers reported the formation of higher order morphologies at pH 8 in the presence of added salt ($[NaHCO_3]_0$ = 40 mM), which screens the electrostatic repulsive forces.[189,195]

Recently, several research groups have identified specific reaction conditions that promote the formation of higher order morphologies during RAFT *ab initio* emulsion polymerisation. For example, D'Agosto *et al.* reported that the precise position of a minority comonomer within non-ionic steric stabiliser chains determined whether the synthesis of vesicles (as opposed to spheres) was feasible.[246] More specifically, PEGA was copolymerised with *N*-acryloylmorpholine (PNAM) such that it was present either at the beginning or the end of the stabiliser chains (Figure 1.21). Empirically, it was found that only the latter scenario promoted vesicle formation.

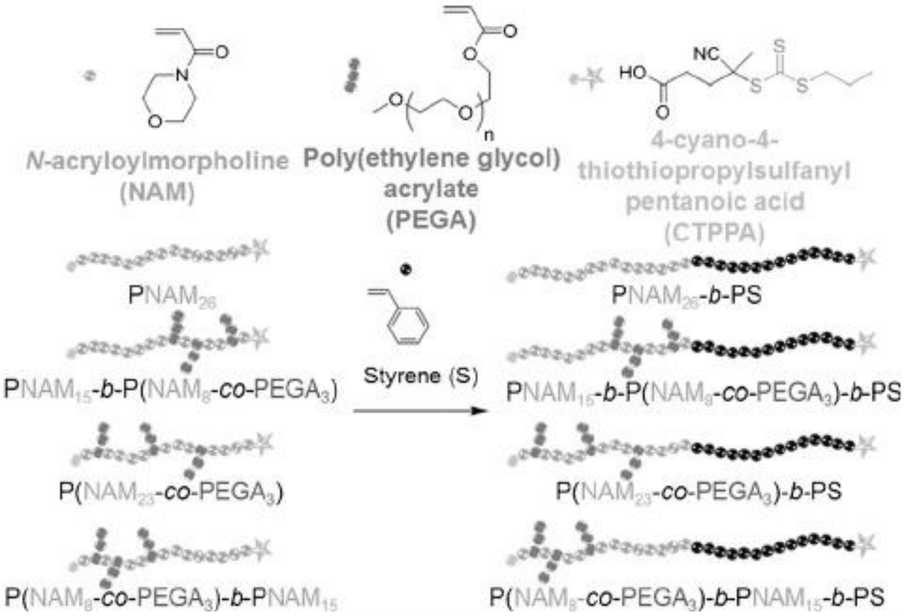

Figure 1.21. The *ab initio* RAFT aqueous emulsion polymerisation of styrene, as reported by D'Agosto *et al.*[246] The composition of the steric stabiliser precursors utilised affected the final diblock copolymer morphology.

In related work, Cockram and co-workers reported that the aqueous monomer solubility was a key parameter for promoting the formation of higher order morphologies, rather than kinetically-trapped spheres.[243,250,251] The RAFT aqueous emulsion polymerisation of 2-hydroxybutyl methacrylate (HBMA) produced unusual nanoparticles that exhibited a 'monkey nut' morphology.[243] The relatively high aqueous solubility of HBMA (20 g dm^{-3} at 70 °C) was suggested to allow its more efficient mass transport from the monomer droplets through the continuous phase to the growing diblock copolymer nanoparticles, thus providing greater chain mobility via enhanced monomer swelling. This hypothesis was supported by follow-up studies of the RAFT aqueous emulsion polymerisation of glycidyl methacrylate (GlyMA), which has comparable aqueous solubility to HBMA (24-25 g dm^{-3} at 80 °C).[250] This latter formulation provided access to well-defined worms via a facile one-pot formulation. Davis *et al*. reported that increasing hydrophobic character of the RAFT end-group enabled the formation of higher order morphologies for polystyrene-based nano-objects.[238] Thus, a carboxylic acid-based RAFT agent only enabled the preparation of kinetically-trapped spheres but its methyl ester analogue enabled the formation of higher order morphologies. This was attributed to a reduction in the effective interfacial area, thus increasing the packing parameter and producing a higher aggregation number. Increasing the initiator concentration was also beneficial: using a precursor/initiator molar ratio of 0.75 enabled the preparation of spheres, worms or vesicles, even when using the carboxylic acid-based RAFT agent.

Further research into understanding the key parameters that govern the formation of higher order morphologies via RAFT *ab initio* polymerisation is highly desirable. One major challenge is the formation of pure phases. Typically, mixed phases (typically either spheres/worms or worms/vesicles) are often produced and optimisation of both the stabiliser and core-forming block DPs and also the copolymer concentration is required to construct pseudo-phase diagrams. For example, Brotherton et al. recently investigated the RAFT *ab initio* polymerisation of 2-methoxyethyl methacrylate (MOEMA) using a PGMA precursor.[251] For this formulation, the relatively high aqueous solubility of MOEMA (19.6 g dm^{-3} at 70 °C) and systematic variation of the diblock copolymer composition and the copolymer concentration enabled the reproducible synthesis of spheres, worms or vesicles (Figure 1.22). Moreover, a bespoke stirrable reaction cell enabled *in situ* small angle X-ray scattering (SAXS) studies to be conducted when targeting vesicles (Figure 1.23).

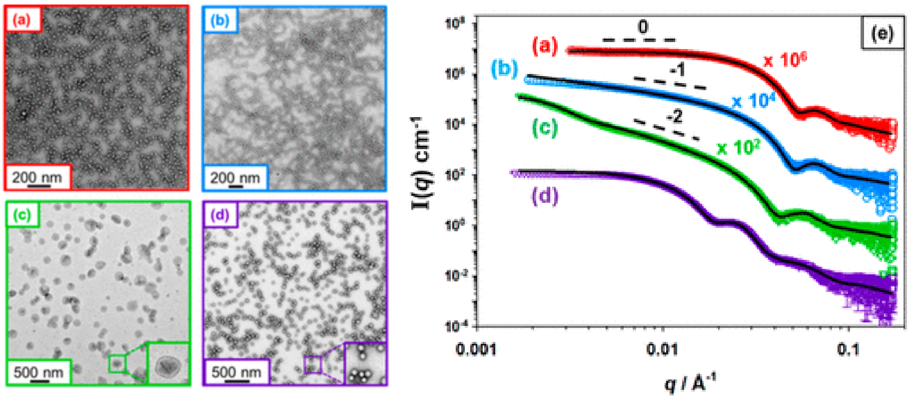

Figure 1.22. Representative TEM images of (a) $PGMA_{29}$-$PMOEMA_{38}$ spheres (red), (b) $PGMA_{29}$-$PMOEMA_{43}$ worms (blue), (c) large $PGMA_{29}$-$PMOEMA_{70}$ vesicles (green) and (d) relatively small $PGMA_{29}$-$PMOEMA_{84}$ vesicles (purple). Indicating that the water solubility of MOEMA enables the production of higher order morphologies (e) Corresponding SAXS patterns recorded for 1.0% w/w aqueous dispersion of the same four copolymer dispersions ((a)-(d). Black solid lines show the data fits obtained for each SAXS pattern using an appropriate spherical micelle, worm-like micelle, or vesicle model. Each low *q* gradient is consistent with the TEM images.[251]

It was found that the growing diblock copolymer chains initially formed spheres and the onset of micellar nucleation was identified. As the MOEMA polymerisation continued, the stochastic 1D fusion of multiple spheres then produced worms, and finally vesicles were produced towards the end of the polymerisation. However, SAXS analysis indicated that a pure worm phase was only obtained between PMOEMA DPs of 38 and 49.[251]

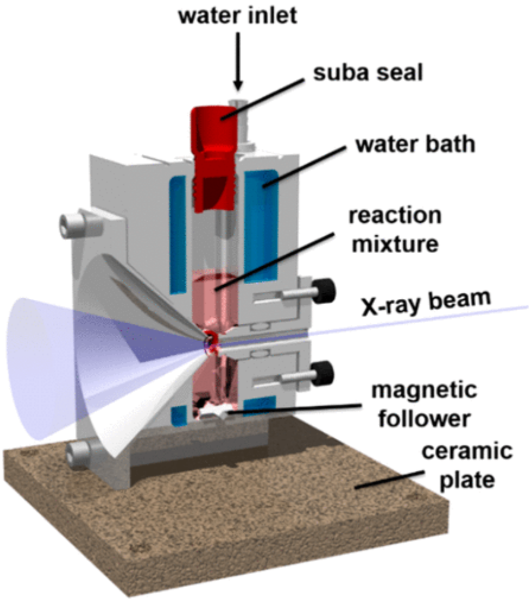

Figure 1.23. Schematic representation showing the cross-section of the stirrable reaction cell used by Brotherton et al. for *in situ* SAXS studies during RAFT aqueous emulsion polymerization of MOEMA at 70 °C. The reaction solution volume within this cell is approximately 2.0 mL.[251]

Recently, Rieger *et al*. has reported the facile production of block copolymer worms during RAFT emulsion polymerisation by introducing a bisurea motif into the RAFT agent.[252] This was used to form PDMAc precursors and hydrogen-bonding interactions within the core-forming block enabled the preparation of poly(2-methoxyethyl acrylate) (PMEA) worms over an unusually wide DP range (39-224) at a copolymer concentration of up to 28% w/w.

The development of RAFT *ab initio* emulsion polymerisation has enabled the production of various morphologies comprising well-defined block copolymer chains of relatively high molecular weight using various vinyl monomers. However, this approach is rather limited in some respects. For example, given the relatively hydrophobic character of the structure-directing block, such PISA formulations typically do not produce thermoresponsive block copolymer worms or vesicles.

1.5.2 PISA by RAFT Aqueous Dispersion Polymerisation

In 2007, An and Hawker *et al*. employed a PDMAc RAFT precursor for the polymerisation of *N*-isopropylacrylamide (NIPAM) in aqueous solution.[155] This water-soluble block acted as a steric stabiliser to prevent macroscopic precipitation of the diblock copolymer chains. Given that NIPAM is water-miscible, this was the first report of RAFT aqueous dispersion polymerisation as a route to nanoparticles, although this term was not actually used by the authors. Spherical nanoparticles were obtained at 70 °C, which is well above the lower critical solution temperature (LCST) of 32 °C for PNIPAM homopolymer.[253] These nanoparticles were cross-linked with bisacrylamide to avoid dissolution upon cooling, which results in colloidally stable thermoresponsive nanogels being formed at 20 °C (Figure 1.24).

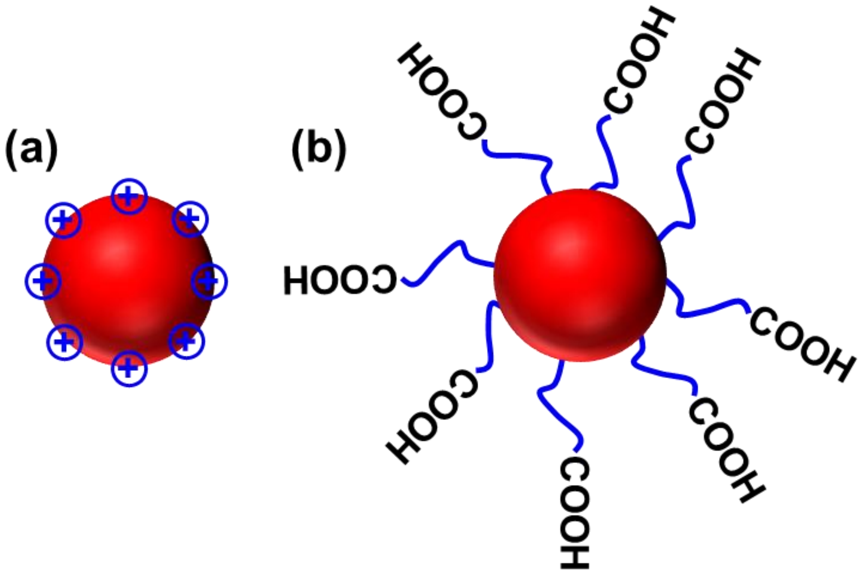

Figure 1.24. (a) Charge-stabilised nanogel formed by traditional free radical precipitation polymerization. (b) Novel core-shell nanoparticles formed by 'RAFT-mediated precipitation polymerization', which is actually best described as the RAFT aqueous dispersion (co)polymerisation of NIPAM with bisacrylamide.[155]

Zeta potential measurements performed on nanoparticles prepared with and without the PDMAc precursor indicated anionic character owing to the use of a carboxylic acid-functionalised RAFT agent for the preparation of the PDMAc precursor. At some critical PNIPAM DP, self-assembly occurred at 70 °C to form PNIPAM-core nanoparticles that were sterically stabilised by a corona of PDMAc chains (Figure 1.24). In principle, this approach should enable the facile production of a wide range of block copolymer nanoparticles by RAFT dispersion polymerisation. In practice, relatively few vinyl monomers are both water-miscible and form water-insoluble polymers when polymerised, which are the essential criteria required for an aqueous dispersion polymerisation. Apart from NIPAM,[155] suitable monomers include *N,N'*-diethylacrylamide (DEAA),[254] MEA,[255] HPMA,[179,192,244] HBMA,[256] diacetone acrylamide (DAAM),[257] and di(ethylene glycol) methyl ether methacrylate (DEGMA).[258]

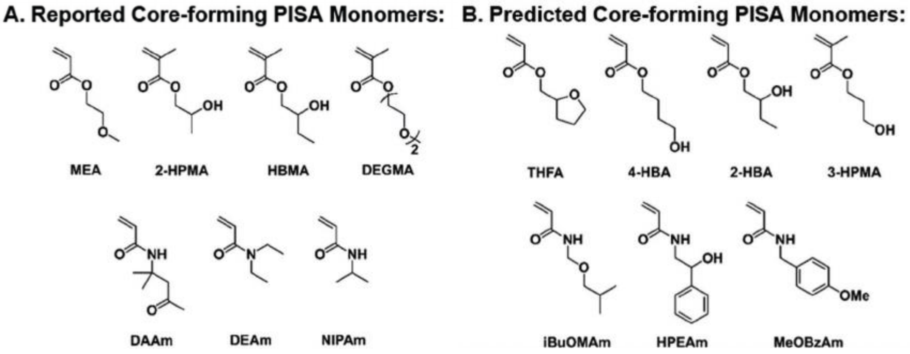

Figure 1.25. Suitable water-miscible vinyl monomers for use in RAFT aqueous dispersion polymerisation: (A) reported in the literature and (B) predicted by theory.[259]

Recently, O'Reilly *et al*. reported an *in silico* method to predict, based on the increase in hydrophobic character of the growing core-forming oligomers, whether a water-miscible monomer is suitable for RAFT aqueous dispersion polymerisation.[259] Octanol-water partition coefficients (LogP_{oct}) were used to assess hydrophobic character, which is a well-established method for predicting the aqueous solubility of hydrophobic drugs in the pharmaceutical industry.[260–262] This approach was used to predict five suitable vinyl monomers for RAFT aqueous dispersion polymerisation (Figure 1.25).

HPMA is the most widely used water-miscible monomer for the formation of diblock copolymer nanoparticles via RAFT aqueous dispersion polymerisation.[181,263–271] Typically, HPMA has been polymerised using various water-soluble steric stabiliser precursors such as PGMA,[179,192] poly(2-(methacryloyloxy)ethyl phosphorylcholine) (PMPC),[188] or PEG.[181] Such formulations were amongst the first to provide reliable access to worms or vesicles in aqueous media. Blanazs *et al*. conducted the RAFT aqueous dispersion polymerisation of HPMA using a $PGMA_{47}$ precursor at 70 °C.[244] ^1H NMR studies indicated that micellar nucleation occurred at around 46% conversion, corresponding to an instantaneous diblock copolymer composition of $PGMA_{47}$-$PHPMA_{92}$ (Figure 1.26).

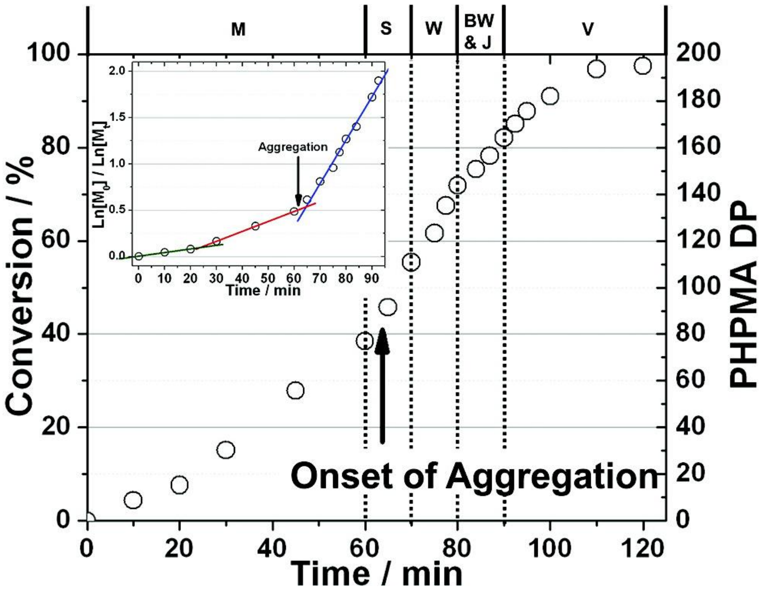

Figure 1.26. Kinetic data obtained for the RAFT aqueous dispersion polymerisation of HPMA when targeting G_{47}-H_{200} diblock copolymer vesicles at 70 °C and 10% w/v solids. The inset shows a semi-logarithmic plot for a sub-set of these data, which indicates a five-fold rate enhancement after micellar nucleation.[244]

DLS and TEM studies indicated that *in situ* self-assembly initially produced relatively small nascent nanoparticles of 20-30 nm diameter. Ingress of unreacted HPMA into these nanoparticles leads to a relatively high local monomer concentration, which leads to a much faster rate of polymerisation. ^{1}H NMR studies indicated a five-fold rate acceleration after micellar nucleation (Figure 1.26). Furthermore, this HPMA monomer plasticises the growing PHPMA chains, enhancing their mobility and promoting the stochastic 1D fusion of multiple spheres to form worms. As the polymerisation proceeds, the initially linear worms become increasingly branched and eventually ‘octopus-like’ structures are observed by TEM. Wrap up of such 2D structures produces ‘jellyfish’, which are hemi-vesicles with worms dangling as fronds from their periphery. The ‘jellyfish’ then anneal to form well-defined, polydisperse vesicles at high HPMA conversion (> 80 %; Figure 1.27). ^{1}H NMR studies indicated that this remarkable evolution in copolymer morphology is complete within 2 h at 70 °C. Furthermore, this was the first literature report to account for the evolution in copolymer morphology in terms of a gradual reduction in the packing parameter as a result of an increase in the core-forming block DP at a fixed stabiliser block DP (Figure 1.27).

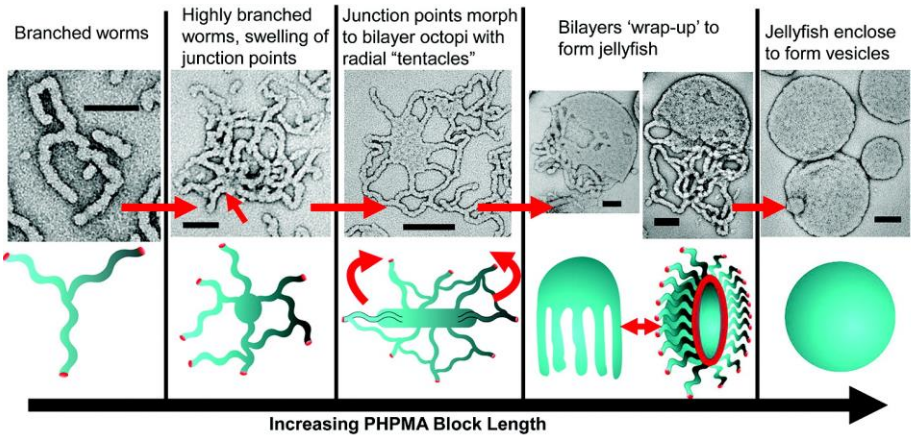

Figure 1.27. Representative TEM images recorded during the synthesis of $PGMA_{47}$-$PHPMA_{200}$ vesicles by RAFT aqueous dispersion polymerization of HPMA during as reported by Blanazs et al.[244] This resulted in a proposed mechanism for the worm-to-vesicle transition

Blanazs and co-workers constructed three pseudo-phase diagrams for a series of $PGMA_x$-$PHPMA_y$ diblock copolymer nano-objects where x = 47, 78 or 112.[179] Using a $PGMA_{112}$ precursor, access to higher order morphologies was restricted to copolymer concentrations above 20% w/w and no pure phases of worms or vesicles could be obtained (Figure 1.28a). At lower copolymer concentrations, only kinetically-trapped spheres were obtained. This was explained in terms of the highly effective steric stabilisation mechanism conferred by the relatively long $PGMA_{112}$ block. This impedes sphere-sphere fusion, which is the critical first step *en route* to higher order structures.

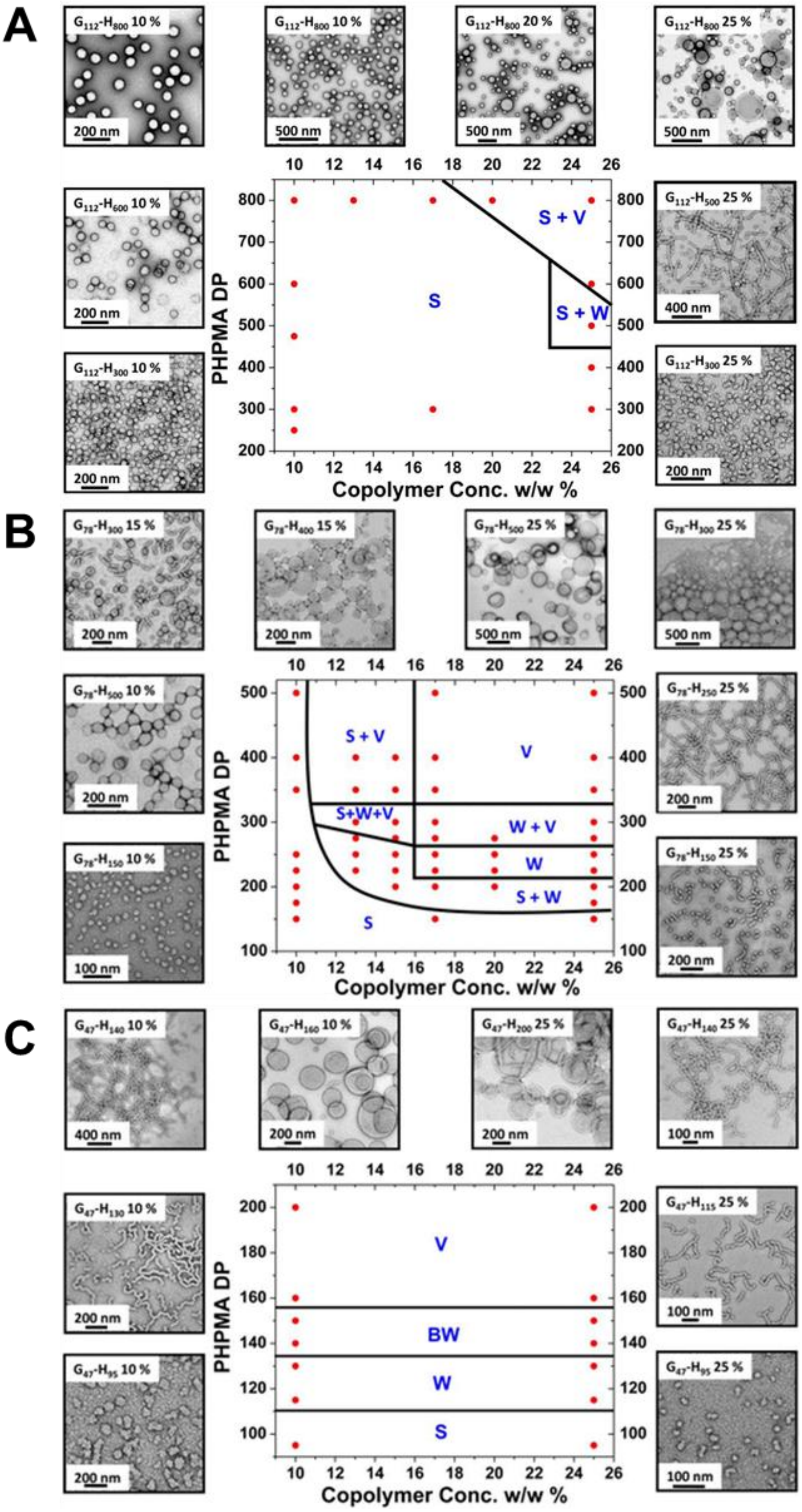

Figure 1.28. Representative TEM images and corresponding pseudo-phase diagrams constructed for a series of $PGMA_x$–$PHPMA_y$ diblock copolymer nano-objects (where x = (A) 112, (B) 78 and (C) 47, respectively) prepared by RAFT aqueous dispersion polymerisation of HPMA targeting copolymer concentrations of between 10 and 25% w/w. S = spherical micelles, W = worms, BW = branched worms, and V = vesicles.[179] These highlight the requirement for short stabiliser blocks (x < 78) to afford pure W and V phases.

In contrast, employing a shorter $PGMA_{78}$ precursor enabled the preparation of pure spheres, worms or vesicles at copolymer concentrations of 16-25% w/w (Figure 1.28b).[179] Moreover, when a $PGMA_{47}$ precursor was employed, there was no concentration dependence on the copolymer morphology: pure worms or vesicles could be prepared between 10% w/w and 25% w/w as the shorter PGMA stabiliser block conferred less effective steric stabilisation, hence allowing efficient sphere-sphere fusion to occur even under less favourable conditions (Figure 1.28c). Recently, a master phase diagram was published by Warren et al. that highlights how the respective DPs of each block influence the copolymer morphology for this $PGMA_x$-$PHPMA_y$ PISA formulation (Figure 1.29).[185] Such pseudo-phase diagrams are considered to be essential for the reproducible targeting of a desired copolymer morphology. This is particularly true for block copolymer worms, which usually occupy relatively narrow phase space.[207,272–274]

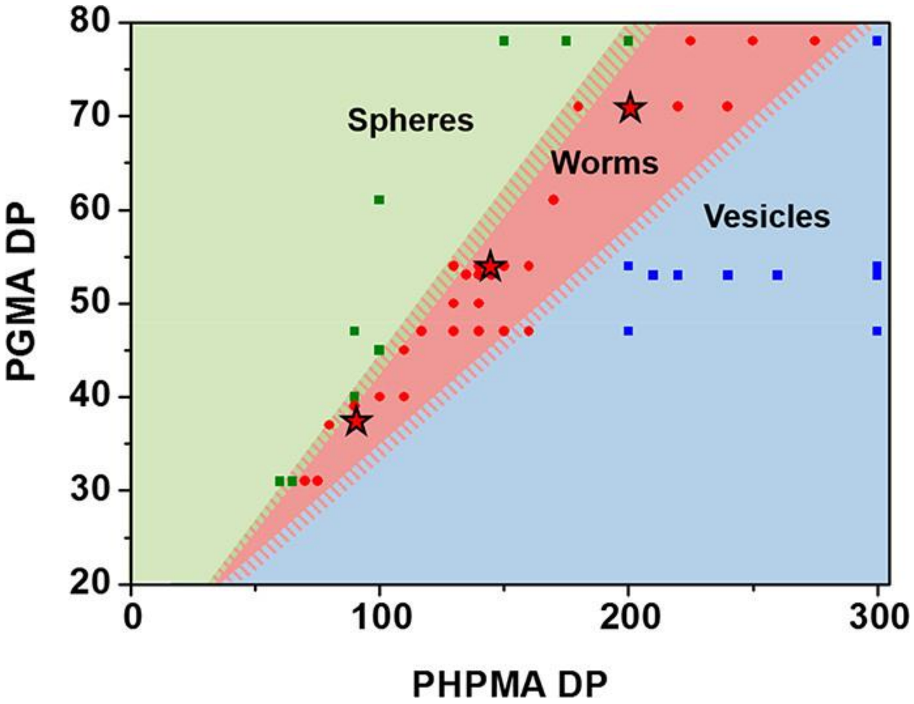

Figure 1.29. Master pseudo-phase diagram constructed for $PGMA_x$-$PHPMA_y$ diblock copolymer nano-objects to determine the precise copolymer composition corresponding to pure spheres (green), worms (red) or vesicles (blue). The morphologies were assigned at high HPMA conversions (> 95%) based on TEM studies. Shaded boundaries represent regions of uncertain morphology.[185]

Various potential applications had been reported for spheres and vesicles but the ability to produce PGMA-PHPMA diblock copolymer worms suggests new possibilities (see below). This is because such worms form soft, transparent free-standing gels in aqueous solution at 20 °C with typical storage moduli (G') of around 10^2 Pa at a copolymer concentration of 10% w/w. Tube inversion tests and gel rheology studies indicated that the critical gelation concentration is approximately 3-4% w/w.[275]

Initially, the gelation behaviour of the worms was suggested to be the result of inter-worm entanglements, which is the mechanism used to explain the gelation behaviour of small-molecule surfactant worms.[276,277] However, given their relatively short worm length it was postulated that the gelation behaviour of PGMA-PHPMA worms was perhaps more likely to be the result of multiple inter-worm contacts.[278,279] Recently, Lovett *et al.* examined the gelation behaviour of both PGMA_{56}-PHPMA_{155} worms (Figure 1.30b) and poly(methacrylic acid)-poly(styrene-*alt*-*N*-phenylmaleimide) (PMAA-P(S-*alt*-NMI)) worms (Figure 1.30b) to examine whether percolation theory could explain their gelation behaviour.[280] The former system comprised relatively long, flexible worms whereas the latter system produces relatively stiff, short worms, hence markedly different gelation behaviour was anticipated. In both cases, the experimental critical worm volume fraction (ϕ_c) required for gelation was determined from tube inversion experiments and rheological studies. Previously, Chatterjee had used mean field theory to show that ϕ_c could be estimated for polydisperse cylindrical rods with high aspect ratios (Equation 1.37).[281,282]

$$\phi_c = \left(\frac{R}{L_W}\right)\left(\frac{1+\frac{\sigma_R^2}{R^2}}{1+\frac{\sigma_R^2}{4R^2}}\right) \tag{1.37}$$

Here R is the number-average rod cross-sectional radius, L_W is the weight-average rod length and σ_R is the standard deviation of the rod cross-sectional radius. For populations of rods with properties similar to the block copolymer worms obtained by PISA (narrow cross-sectional worm radii, relatively high aspect ratios, and uncorrelated variations in the widths and lengths) σ_R tends to zero. Hence Equation 1.37 can be simplified to give Equation 1.38.

$$\phi_c = k\left(\frac{R}{L_W}\right) \tag{1.38}$$

This percolation theory was then used to calculate theoretical ϕ_c values for comparison to the experimental data. Obtaining R and L_w from SAXS studies, it was found that the experimental ϕ_c value determined for the relatively short, stiff PMAA-P(S-*alt*-NMI) worms agreed reasonably well (within 20%) with the theoretical ϕ_c value. This supported the hypothesis of the formation of a continuous 3D network of worms above the critical gelation concentration (CGC) owing solely to multiple inter-worm contacts. However, the theoretical and experimental ϕ_c values differed by a factor of two for the PGMA-PHPMA worms. This was rationalised in terms of their greater flexibility, which makes them less ‘rod-like’. It is perhaps also worth noting that the ‘multiple inter-worm contacts’ hypothesis also accounts for the gelation behaviour observed for crystalline cellulose nanorods.[283] In this case, the rigidity of such nanoparticles effectively excludes the possibility of an ‘inter-particle entanglements’ mechanism.

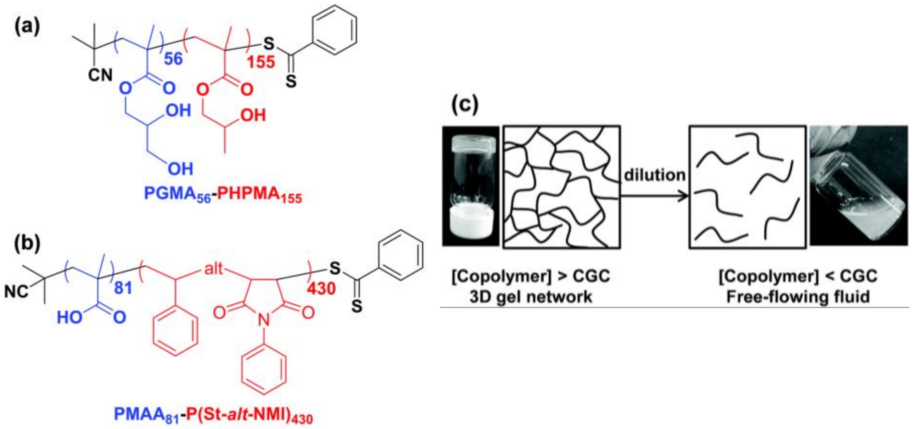

Figure 1.30. Chemical structures for (a) a $PGMA_{56}$–$PHPMA_{155}$ and (b) a $PMAA_{81}$-P(St-*alt*-NMI)$_{430}$ diblock copolymer dispersions prepared by RAFT dispersion polymerisation. (c) Schematic cartoon illustrating formation of a continuous 3D network above the critical gelation concentration (CGC) owing to multiple inter-worm contacts. Such inter-worm contacts are lost on dilution below the CGC, resulting in a free-flowing viscous dispersion of worms rather than a free-standing gel.[280]

It is well-known that PHPMA homopolymer is water-insoluble under all conditions.[173] However, when PHPMA chains are covalently linked to a second water-soluble block (e.g. PGMA), they exhibit unusual thermoresponsive behaviour (Figure 1.31a). It is well-known that PNIPAM, PDEAA or PMEA homopolymers exhibit inverse temperature-solubility behaviour: they are soluble in cold water but become insoluble in hot water.[155,254,255,258,284,285] In contrast, PHPMA always remains water-insoluble but its degree of (partial) plasticisation varies sufficiently with temperature to induce a change in morphology. More specifically, rheological studies indicate that *in situ* delegation occurs to form a free-flowing fluid when cooling PGMA-PHPMA worm gels from 20 to 5 °C (Figure 1.31b). TEM studies confirm that this is the result of a worm-to-sphere transition (Figure 1.31a). Variable temperature ^{1}H NMR studies indicate that the core-forming PHPMA block becomes significantly more hydrated at 5 °C. This is not sufficient for water solubility, but the resulting surface plasticization of the worms results in a reduction in the packing parameter, *P*, from a value that favours worms ($0.33 < P \leq 0.50$) to that favouring spheres

(P ≤ 0.33). The worm-to-sphere transition of a 10% w/w aqueous dispersion of PGMA$_{54}$-PHPMA$_{140}$ diblock copolymer was analysed using SAXS (Figure 1.31c). Comparing the gradient of the low *q* regime in an I(*q*) vs *q* plot confirmed that a transition from worms (low *q* gradient ~ –1) to spheres (low *q* gradient ~ 0) occurred upon cooling (Figure 1.31c).[286] SAXS analysis of two thermal cycles between 5 °C and 20 °C indicated excellent reversibility for this morphological transition in semi-concentrated aqueous solution. Importantly, rheology experiments indicated that the CGT could be tuned from 7 to 20 °C by varying the precise diblock copolymer composition, with longer PHPMA or shorter PGMA DPs each favouring lower CGTs.[287,288]

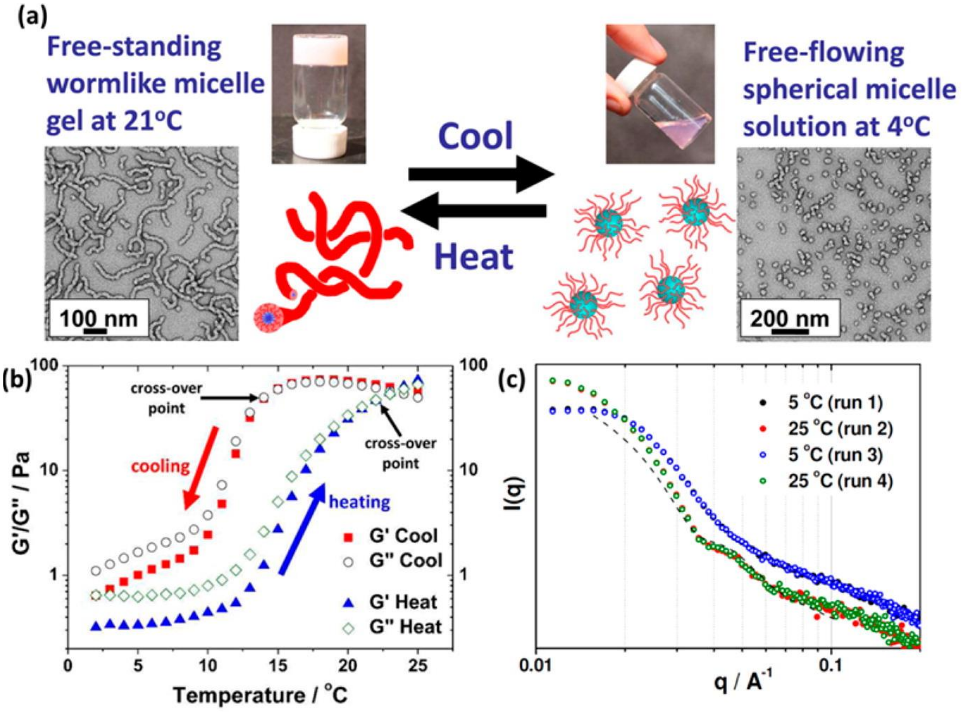

Figure 1.31. (a) Thermoresponsive aqueous solution behaviour of a 10% w/w aqueous dispersion of PGMA$_{54}$-PHPMA$_{140}$ diblock copolymer nano-objects. TEM studies of the corresponding dilute aqueous dispersion dried at either 21 or 4 °C indicate a thermoreversible worm-to-sphere transition. (b) Variation of storage (G′) and loss (G″, open symbols) moduli for a 10% w/w aqueous dispersion of PGMA$_{54}$-PHPMA$_{140}$ worms during cooling (red) and heating (blue) cycling at a rate of 1 °C min^{-1}. This indicated a 5 °C thermal hysteresis with worms reforming at 22 °C (cross-over point) (c) SAXS patterns recorded for a 10% w/w aqueous dispersion of PGMA$_{54}$-PHPMA$_{140}$ diblock copolymer nano-objects after two consecutive thermal cycles between 5 and 25 °C. These SAXS plots overlay almost perfectly, indicating excellent reversibility for this worm-to-sphere transition. The black dashed line shows a simulated SAXS pattern for long cylindrical rods.[286]

Blanazs *et al*. exploited the thermoresponsive behaviour of PGMA-PHPMA diblock copolymer worm gels for their facile sterilisation. In a proof-of-concept experiment, a 10% w/w $PGMA_{54}$-$PHPMA_{140}$ worm gel was combined with a fluorescently-labelled bacterium (Staphylococcus aureus; > 0.50 µm diameter). The worm gel was then cooled to 5 °C, resulting in the formation of relatively small diblock copolymer spheres of 30-50 nm diameter. This low-viscosity free-flowing aqueous dispersion was then passed through a 0.45 µm filter using a syringe and allowed to warm back up to 20 °C to reform the original worm gel. Fluorescence plate reader experiments indicated that this cold ultrafiltration step had removed all the relatively large bacteria from the worm gel. Subsequently, such thermoresponsive PGMA-PHPMA worm gels were shown to be highly biocompatible and evaluated as wholly synthetic 3D matrices for long-term cell culture studies.[289] Remarkably, it was also found that their hydroxyl functionality leads to stasis induction in embryonic human stem cell colonies.[290,291] Moreover, retrieval of stem cell colonies from the worm gel after two weeks at 37 °C led to the resumption of cell proliferation. This is a potentially important finding, because it could enable the long-term storage of human stem cells without loss of their pluripotency, which suggests their use as a cost-effective storage medium for the convenient global transportation of human stem cells.

In 2019, Ratcliffe *et al*. reported the first example of a *single* thermoresponsive amphiphilic diblock copolymer that can form spheres, worms or vesicles in aqueous solution simply by varying the temperature.[292] The hydrophilic steric stabiliser block was poly(*N*-(2-hydroxypropyl) methacrylamide) (PHPMAC) a well-known, highly biocompatible polymer that is ideally suited for use in biomedical applications.[293–296] PHPMA was used as the hydrophobic structure-directing block owing to its thermoresponsive character, with surface plasticisation enabling two phase boundaries to be crossed when varying the temperature over a relatively narrow range. For example, TEM, SAXS and rheology studies indicated that a $PHPMAC_{41}$-$PHPMA_{180}$ copolymer underwent a sphere-to-worm transition at 22 °C and exhibited a worm-to-vesicle transition at 50 °C.[292] However, significant hysteresis was observed: the worm-to-sphere transition occurred within 45 min, whereas the sphere-to-worm transition required several hours to occur. This was attributed to the former transition occurring via a dissociative mechanism (such as worm budding) while the latter involves a highly cooperative associative mechanism, whereby many spheres must fuse together to form the highly anisotropic worms. During the synthesis of this diblock copolymer via RAFT aqueous dispersion polymerisation, unreacted HPMA monomer plasticises the growing particles and hence facilitates the sphere-to-worm transition, enabling it to occur within a relatively short timescale (10-20 min). Moreover, numerical lattice computations were performed using the self-consistent field (SCF) theory developed by Scheutjens and Fleer.[297,298] Three interaction parameters (χ) were considered: χ_{HPMA-W}, $\chi_{HPMAC-HPMA}$ and $\chi_{HPMAC-W}$. $\chi_{HPMAC-HPMA}$ was set to be unity, which ensured inter-block segregation while $\chi_{HPMAC-W}$ was set at 0.48.[299] These numerical values ensured that SCF theory predicted the formation of colloidally stable diblock copolymer objects instead of macroscopic precipitation. The thermodynamically-preferred copolymer morphology could be identified at any given temperature as it corresponds to the lowest CMC, which can be expressed in terms of the Gibbs free energy of micellisation[300] (ΔG^{mic}; Equation 1.39).

$$\Delta G^{mic} = R\,T\,ln(CMC) \tag{1.39}$$

Using this approach, SCF calculations predicted that a PHPMAC$_{41}$-PHPMA$_{180}$ diblock copolymer should preferentially assume a spherical morphology when $0.70 < \chi_{HPMA-W} < 0.78$, form cylindrical (or worm-like) micelles when $0.78 < \chi_{HPMA-W} < 0.88$ and prefer to exist as vesicles when $\chi_{HPMA-W} > 0.88$ (see Figure 1.32).

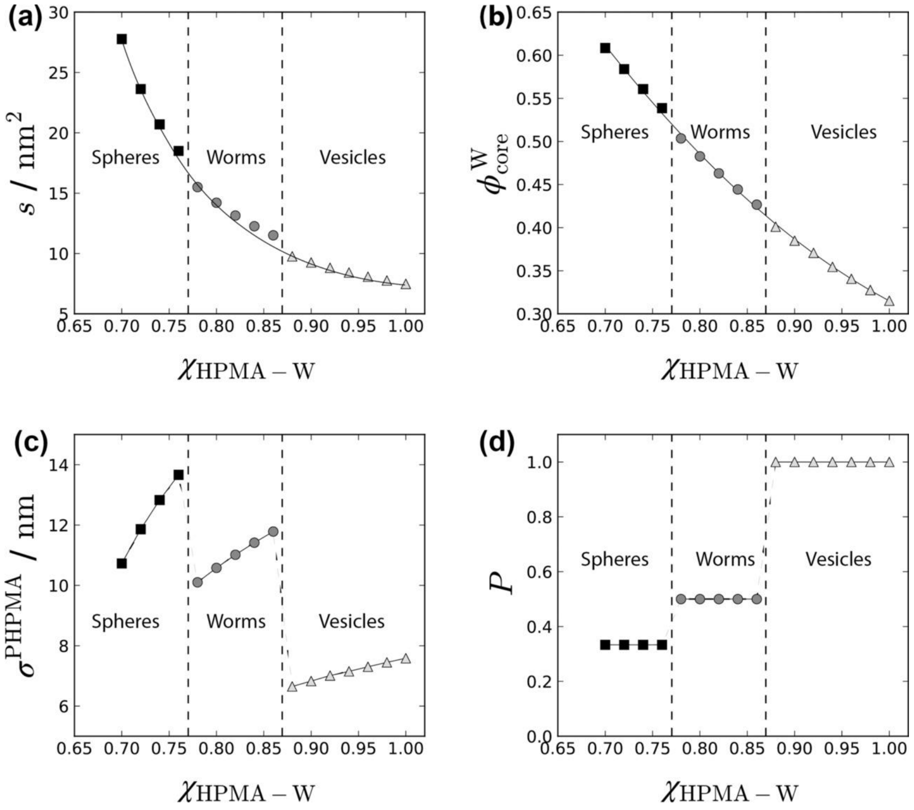

Figure 1.32. Variation of (a) the interfacial surface area per copolymer chain (*s*), (b) the mean water volume fraction associated with the hydrophobic structure-directing PHPMA block (ϕ^{W}_{core}), (c) the average end-to-end distance of the PHPMA block (σ^{PHPMA}) and (d) the packing parameter *P* as a function of χ_{HPMA-W}, as calculated for a PHPMAC$_{41}$-PHPMA$_{180}$ diblock copolymer. Dashed lines mark the locations of the sphere/worm and worm/vesicle boundaries.[292]

This enabled comparison between SCF theory and the experimentally-observed morphological transitions. The interfacial surface tension (γ) at the core-corona interface of the $PHPMAC_{41}$-$PHPMA_{180}$ diblock copolymer nano-objects can be estimated from $\chi_{HPMA\text{-}W}$ (Equation 1.40).[301,302]

$$\gamma \approx (\chi_{HPMA-W})^{\frac{1}{2}} \tag{1.40}$$

At 4 °C, SCF theory predicts that $\chi_{HPMA\text{-}W}$ is small, hence γ is also small and thus the equilibrium copolymer morphology has a relatively high interfacial surface area (*s;* Figure 1.32a). This results in weaker steric repulsion between the PHPMA chains, thus reducing the degree of chain stretching and hence favouring a spherical morphology (Figure 1.32c). An increase in γ at higher temperature results in a reduction in *s* (Figure 1.32a). This is achieved by expelling water molecules from the core (ϕ^{W}_{core}; Figure 1.32b), which causes a gradual increase in the end-to-end distance (σ^{PHPMA}; Figure 1.32c) of the core-forming chains. When a certain critical temperature is attained, the increase in σ^{PHPMA} causes chain stretching to become energetically unfavourable for a spherical morphology. Thus, a sphere-to-worm transition occurs at 22 °C, followed by a worm-to-vesicle transition at 50 °C. Such morphological transitions reduce σ^{PHPMA} and lead to a corresponding reduction in ΔG^{mic}. The change in *P* was also calculated and good agreement between calculated values and the literature was observed (see Figure 1.32d).[127]

More recently, Byard *et al*. reported the first example of a thermoresponsive diblock copolymer capable of crossing *three* phase boundaries to form spheres, worms, vesicles or lamellae in aqueous solution (Figure 1.33).[303] This remarkable phase behaviour was achieved using a poly(*N,N*-dimethylacrylamide)$_{56}$-poly(4-hydroxybutyl acrylate-*stat*-diacetone acrylamide)$_{264}$ ($PDMAc_{56}$–P(HBA-*stat*-DAAM)$_{264}$) diblock copolymer. TEM, oscillatory rheology experiments, shear-induced polarised light imaging and SAXS studies indicated that the sphere/worm and worm/vesicle morphological transitions were rapid and reversible even at 0.10% w/w (Figure 1.33). On the other hand, the lamellae/vesicle transition exhibited significant hysteresis as indicated by rheological experiments.

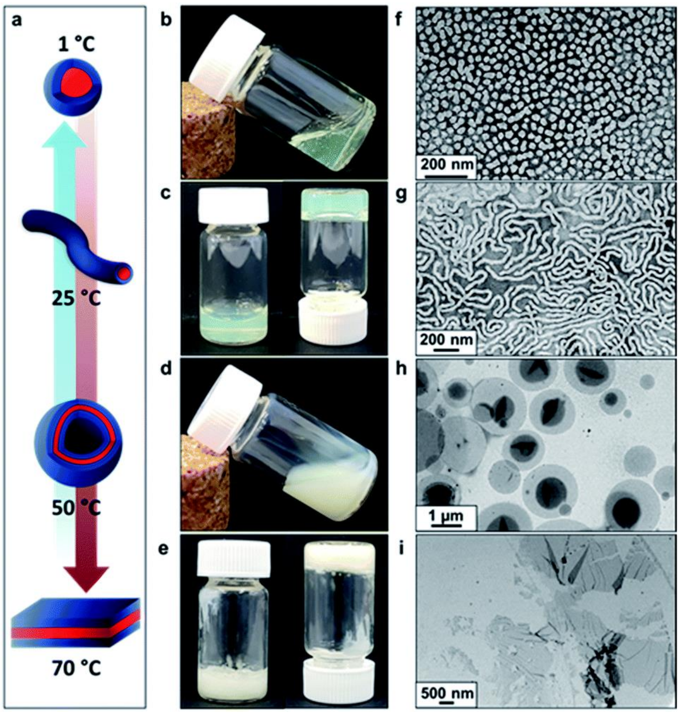

Figure 1.33. (a) Schematic representation of the thermoreversible morphological transitions for a single PDMAC$_{56}$–P(HBA-*stat*-DAAM)$_{264}$ diblock copolymer on varying the temperature from 1° to 70 °C. Digital images indicated significant changes in the physical appearance of the 20% w/w aqueous dispersion when the temperature was raised from (b) 1 °C, to 25°C, to (d) 50 °C and finally to (e) 70 °C. TEM images recorded for 0.10% w/w aqueous dispersions of the cross-linked (f) spheres (cross-linked at 1 °C), (g) worms (cross-linked at 25 °C), (h) vesicles (cross-linked at 50 °C) and (i) lamellae (cross-linked at 70 °C).[303]

Interestingly, despite HBA and HPMA being structural isomers, ^{1}H NMR studies indicate that they exhibit contrasting temperature-dependent hydration behaviour (Figure 1.34). As previously observed by Blanazs et al., the degree of (partial) hydration of the core-forming PHPMA block *increases* at lower temperature.[263] However, the degree of (partial) hydration of the core-forming PHBA block *decreases* at lower temperature (Figure 1.34).[303] Despite this complementary behaviour, in both cases it is observed that spheres are formed at relatively low temperature, worms at intermediate temperature and vesicles at high temperature. When PHPMA-based nano-objects are cooled, surface plasticisation leads to an effective increase in the volume fraction of the stabiliser block (and a concomitant reduction in the volume fraction of the core-forming block) as the HPMA repeat units located near the block junction become more hydrated. This accounts for the vesicle-to-worm and worm-to-sphere transitions that occur on lowering the solution temperature. However, this argument cannot account for the observed behaviour of the PHBA-based nano-objects.[303] Instead, the concept of *uniform* plasticisation is invoked in this case. This is not unreasonable given the significantly higher aqueous solubility of HBA monomer compared to HPMA monomer, because this suggests that PHBA homopolymer should be more weakly hydrophobic than PHPMA homopolymer. Thus, the entire length of the PHBA chains become more hydrated at higher temperature. This increases the effective volume fraction of this structure-directing block, which favours higher *P* values and hence explains the evolution from spheres to worms to vesicles (and ultimately lamellae) that is observed on heating. (Figure 1.34).

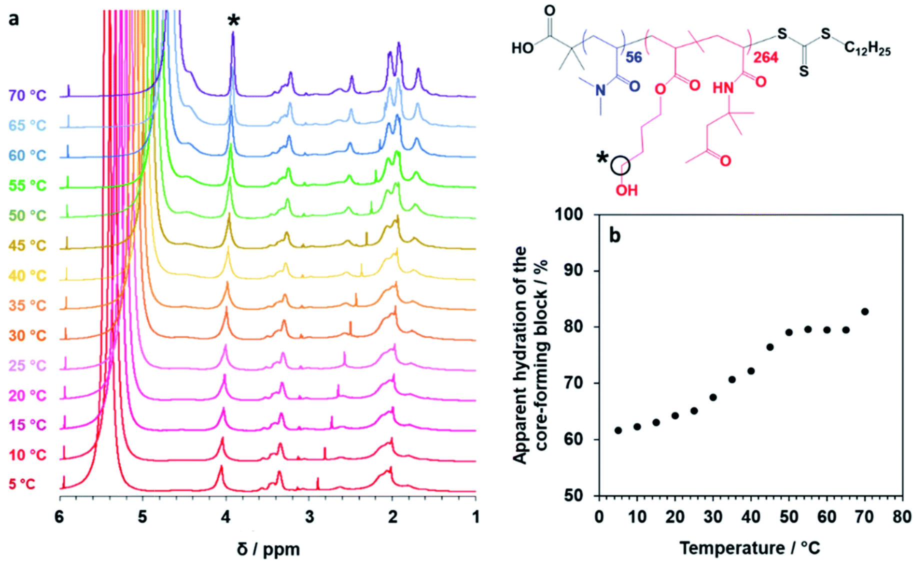

Figure 1.34. (a) Normalised partial ^{1}H NMR spectra when a linear 20% w/w aqueous PDMAc$_{56}$–P(HBA-*stat*-DAAM)$_{264}$ nano-object dispersion was warmed from 5 °C to 70 °C. (b) The apparent hydration of the PHBA block monitored using the two C$\underline{H_2}$–OH protons on the HBA residues (marked with an asterisk in the chemical structure) with 100% hydration corresponding to the PHBA DP identified by ^{1}H NMR spectroscopy studies of the molecularly-dissolved copolymer chains in CD$_3$OD. This ^{1}H NMR study indicated a gradual increase in hydration of PHBA with dispersion temperature.[303]

The ability to access each copolymer morphology solely by adjusting the solution temperature is expected to facilitate new theoretical studies of block copolymer self-assembly. Moreover, the rapid, reversible nature of such morphological transitions is expected to offer new applications for the *in situ* loading of vesicles with enzymes (or other actives), with subsequent release of the payload being achieved by simply lowering the solution temperature. In summary, the experimental observations made for PHPMA-based and PHBA-based nano-objects can be rationalised in terms of *surface* plasticisation and *uniform* plasticisation, respectively (Figure 1.35). However, such qualitative arguments may well require further refinement as we improve our understanding of the behaviour of such remarkable systems.

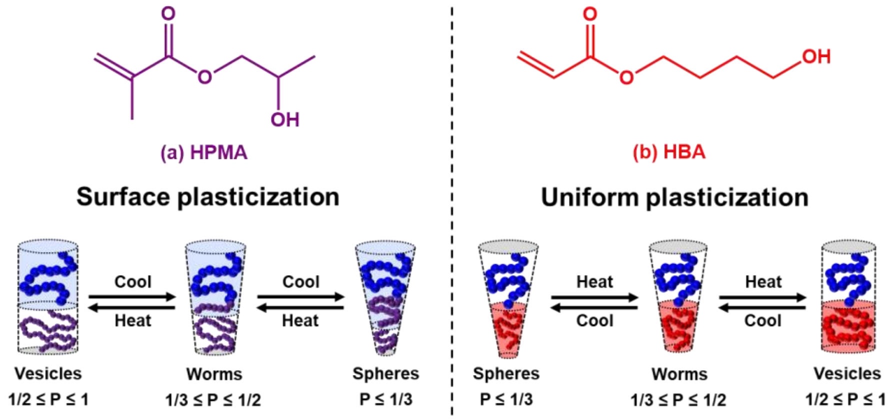

Figure 1.35. Schematic cartoon illustrating the two types of plasticisation postulated to occur when heating/cooling thermoresponsive diblock copolymer nano-objects if the structure-directing block is (a) PHPMA (*surface* plasticisation) and (b) PHBA (*uniform* plasticisation).

1.6 Thesis Outline

The focus of this Thesis is the evaluation of 2-(*N*-acryloyloxy)ethyl pyrrolidone (NAEP) for use in a range of RAFT-mediated aqueous PISA formulations. In Chapter 2, kinetic studies of the RAFT aqueous solution polymerisation of NAEP using either AIBN at 70 °C or a low-temperature redox initiator at 30 °C are undertaken. Using these findings, well-defined double-hydrophilic and/or stimulus-responsive PNAEP-based diblock copolymers are prepared via RAFT aqueous solution polymerisation and analysed by ^{1}H NMR, GPC and DLS. In Chapter 3, a trithiocarbonate-based PNAEP$_{67}$ precursor is employed as the steric stabiliser for the RAFT emulsion polymerisation of styrene, nBA, or statistical mixtures thereof. Several series of such diblock copolymers are prepared and analysed by ^{1}H NMR, GPC, DLS, TEM and differential scanning calorimetry (DSC) studies. The film formation behaviour of selected diblock copolymer nanoparticles is briefly explored. Chapter 4 involves the synthesis of new all-acrylic multiblock copolymer nanoparticles via one-pot sequential RAFT aqueous emulsion polymerisation of *n*BA and *t*-butyl acrylate (tBA) using PNAEP as a hydrophilic steric stabiliser block. DSC and SAXS studies are used to characterise the extent of microphase separation of the two isomeric blocks within transparent films that can be cast at room temperature. The thermoplastic elastomeric properties of PNAEP$_{85}$-PtBA$_{150}$-PnBA$_x$-PtBA$_{150}$ tetrablock copolymer (x = 200-700) films are briefly evaluated via tensile tests. Finally, Chapter 5 investigates the one-pot RAFT aqueous dispersion polymerisation of HBA at 30 °C using a PNAEP$_{85}$ precursor. The covalent stabilisation of these nano-objects using glutaraldehyde is demonstrated and optimised. TEM analysis of glutaraldehyde-fixed nano-objects and SAXS studies on linear nano-objects are used to construct a pseudo-phase diagram. The stimulus-responsive behaviour of these new nanoparticles is explored using ^{1}H NMR, DLS, SAXS and rheology.

1.7 References

1 A. W. A. D. McNaught, *IUPAC Compendium of Chemical Terminology*, Blackwell Scientific Publications, Oxford, 2nd edn., 1997.

2 H. Staudinger, *Berichte der Dtsch. Chem. Gesellschaft*, 1920, **53**, 1073–1085.

3 T. Svedberg and J. B. Nichols, *J. Am. Chem. Soc.*, 1923, **45**, 2910–2917.

4 W. H. Carothers, *J. Am. Chem. Soc.*, 1929, **51**, 2548–2559.

5 P. J. Flory, *Principles of Polymer Chemistry*, Cornell University Press, New York, 1953.

6 H. F. Brinson and L. C. Brinson, *Polymer Engineering Science and Viscoelasticity*, Springer, Boston, USA, 2008.

7 J. M. G. Cowie and V. Arrighi, *Polymers: Chemistry and Physics of Modern Materials, Third Edition*, CRC Press, Florida, USA, 2007.

8 R. O. Ebewele, *Polymer Science and Technology*, CRC Press, Florida, USA, 2000.

9 G. Odian, *Principles of Polymerization, 4th Edition*, Wiley, Hoboken, USA, 2004.

10 K. Matyjaszewski and T. P. Davis, *Handbook of Radical Polymerization*, John Wiley & Sons, Inc., Hoboken, NJ, USA, 2002.

11 K. Matyjaszewski, Y. Gnanou and L. Leibler, *Macromolecular Engineering*, Wiley, Weinheim, Germany, 2011, vol. 1.

12 W. A. Braunecker and K. Matyjaszewski, *Prog. Polym. Sci.*, 2007, **32**, 93–146.

13 M. Szwarc, M. Levy and R. Milkovich, *J. Am. Chem. Soc.*, 1956, **78**, 2656–2657.

14 M. Szwarc, *Nature*, 1956, **178**, 1168–1169.

15 K. Hong, D. Uhrig and J. W. Mays, *Curr. Opin. Solid State Mater. Sci.*, 1999, **4**, 531–538.

16 K. Knoll and N. Nießner, *Macromol. Symp.*, 1998, **132**, 231–243.

17 G. Holden, in *Applied Plastics Engineering Handbook*, William Andrew Publishing, Oxford, 2011, pp. 77–91.

18 T. Higashimura, M. Mitsuhashi and M. Sawamoto, *Macromolecules*, 1979, **12**, 178–182.

19 M. Miyamoto, M. Sawamoto and T. Higashimura, *Macromolecules*, 1984, **17**, 265–268.

20 R. R. Schrock, J. Feldman, L. F. Cannizzo and R. H. Grubbs, *Macromolecules*, 1987, **20**, 1169–1172.

21 C. W. Bielawski and R. H. Grubbs, *Prog. Polym. Sci.*, 2007, **32**, 1–29.

22 S. Varlas, J. C. Foster and R. K. O'Reilly, *Chem. Commun.*, 2019, **55**, 9066–9071.

23 O. W. Webster, W. R. Hertler, D. Y. Sogah, W. B. Farnham and T. V. RajanBabu, *J. Am. Chem. Soc.*, 1983, **105**, 5706–5708.

24 T. K. Georgiou, M. Vamvakaki, C. S. Patrickios, E. N. Yamasaki and L. A. Phylactou, *Biomacromolecules*, 2004, **5**, 2221–2229.

25 A. Goto and T. Fukuda, *Prog. Polym. Sci.*, 2004, **29**, 329–385.

26 H. Fischer, *Chem. Rev.*, 2001, **101**, 3581–3610.

27 P. C. Hiemenz and T. P. Lodge, *Polymer Chemistry - 2nd Edition*, CRC Press, New York, 2007.

28 K. Matyjaszewski, *Science*, 2011, **333**, 1104–1105.

29 O. Lebedev, M. Khidekel and GA Razuvaev, *Dokl. Akad. Nauk SSSR*, 1961, **140**, 1327.

30 E. G. Bagryanskaya and S. R. A. Marque, *Chem. Rev.*, 2014, **114**, 5011–5056.

31 J. D. Druliner, *Macromolecules*, 1991, **24**, 6079–6082.

32 R. P. N. Veregin, M. K. Georges, P. M. Kazmaier and G. K. Hamer, *Macromolecules*, 1993, **26**, 5316–5320.

33 C. J. Hawker, *J. Am. Chem. Soc.*, 1994, **116**, 11185–11186.

34 C. J. Hawker, *Acc. Chem. Res.*, 1997, **30**, 373–382.

35 C. J. Hawker, A. W. Bosman and E. Harth, *Chem. Rev.*, 2001, **101**, 3661–3688.

36 R. W. Simms, M. D. Hoidas and M. F. Cunningham, *Macromolecules*, 2008, **41**, 1076–1079.

37 M. N. Alam, P. B. Zetterlund and M. Okubo, *Polymer*, 2008, **49**, 3428–3435.

38 Y. Guo, J. Liu and P. B. Zetterlund, *Macromolecules*, 2010, **43**, 5914–5916.

39 M. E. Thomson, A. M. Manley, J. S. Ness, S. C. Schmidt and M. F. Cunningham, *Macromolecules*, 2010, **43**, 7958–7963.

40 C. Dire, S. Magnet, L. Couvreur and B. Charleux, *Macromolecules*, 2009, **42**, 95–103.

41 G. Delaittre and B. Charleux, *Macromolecules*, 2008, **41**, 2361–2367.

42 G. Delaittre, C. Dire, J. Rieger, J. L. Putaux and B. Charleux, *Chem. Commun.*, 2009, 2887–2889.

43 P. B. Zetterlund, M. N. Alam and M. Okubo, *Polym. J.*, 2008, **40**, 298–299.

44 P. B. Zetterlund, Y. Saka and M. Okubo, *Macromol. Chem. Phys.*, 2009, **210**, 140–149.

45 S. Miele, P. Nesvadba and A. Studer, *Macromolecules*, 2009, **42**, 2419–2427.

46 F. Chauvin, P. E. Dufils, D. Gigmes, Y. Guillaneuf, S. R. A. Marque, P. Tordo and D. Bertin, *Macromolecules*, 2006, **39**, 5238–5250.

47 B. Charleux, J. Nicolas and O. Guerret, *Macromolecules*, 2005, **38**, 5485–5492.

48 G. S. Ananchenko and H. Fischer, *J. Polym. Sci. Part A Polym. Chem.*, 2001, **39**, 3604–3621.

49 R. Mchale, F. Aldabbagh and P. B. Zetterlund, *J. Polym. Sci. Part A Polym. Chem.*, 2007, **45**, 2194–2203.

50 C. Dire, J. Belleney, J. Nicolas, D. Bertin, S. Magnet and B. Charleux, *J. Polym. Sci. Part A Polym. Chem.*, 2008, **46**, 6333–6345.

51 M. Edeleva, S. R. A. Marque, D. Bertin, D. Gigmes, Y. Guillaneuf, S. V. Morozov and E. G. Bagryanskaya, *J. Polym. Sci. Part A Polym. Chem.*, 2008, **46**, 6828–6842.

52 M. V. Edeleva, I. A. Kirilyuk, D. P. Zubenko, I. F. Zhurko, S. R. A. Marque, D. Gigmes, Y. Guillaneuf and E. G. Bagryanskaya, *J. Polym. Sci. Part A Polym. Chem.*, 2009, **47**, 6579–6595.

53 A. C. Greene and R. B. Grubbs, *Macromolecules*, 2009, **42**, 4388–4390.

54 A. C. Greene and R. B. Grubbs, *Macromolecules*, 2010, **43**, 10320–10325.

55 E. Bagryanskaya, D. Bertin, D. Gigmes, I. Kirilyuk, S. R. A. Marque, V. Reznikov, G. Roshchupkina, I. Zhurko and D. Zubenko, *Macromol. Chem. Phys.*, 2008, **209**, 1345–1357.

56 M. Kato, M. Kamigaito, M. Sawamoto and T. Higashimura, *Macromolecules*, 1995, **28**, 1721–1723.

57 J. S. Wang and K. Matyjaszewski, *J. Am. Chem. Soc.*, 1995, **117**, 5614–5615.

58 K. Matyjaszewski, *Adv. Mater.*, 2018, **30**, 1706441.

59 Y. A. Kabachii, S. Y. Kochev, I. V. Blagodatskikh and P. M. Valetskii, *Polym. Sci. - Ser. B*, 2003, **45**, 272–276.

60 I. Onishi, K.-Y. Baek, Y. Kotani, M. Kamigaito and M. Sawamoto, *J. Polym. Sci. Part A Polym. Chem.*, 2002, **40**, 2033–2043.

61 Y. Kotani, M. Kamigaito and M. Sawamoto, *Macromolecules*, 1999, **32**, 2420–2424.

62 K. Matyjaszewski, M. Wei, J. Xia and N. E. McDermott, *Macromolecules*, 1997, **30**, 8161–8164.

63 R. K. O'Reilly, V. C. Gibson, A. J. P. White and D. J. Williams, *Polyhedron*, 2004, **23**, 2921–2928.

64 M. Ishio, M. Katsube, M. Ouchi, M. Sawamoto and Y. Inoue, *Macromolecules*, 2009, **42**, 188–193.

65 B. Wang, Y. Zhuang, X. Luo, S. Xu and X. Zhou, *Macromolecules*, 2003, **36**, 9684–9686.

66 C. Granel, P. Dubios, R. Jérôme and P. Teyssié, *Macromolecules*, 1996, **29**, 8576–8582.

67 H. Uegaki, Y. Kotani, M. Kamigaito and M. Sawamoto, *Macromolecules*, 1998, **31**, 6756–6761.

68 H. Uegaki, M. Kamigaito and M. Sawamoto, *J. Polym. Sci. Part A Polym. Chem.*, 1999, **37**, 3003–3009.

69 J. A. M. Brandts, P. Van De Geijn, E. E. Van Faassen, J. Boersma and G. Van Koten, *J. Organomet. Chem.*, 1999, **584**, 246–253.

70 E. Le Grognec, J. Claverie and R. Poli, *J. Am. Chem. Soc.*, 2001, **123**, 9513–9524.

71 S. Maria, F. Stoffelbach, J. Mata, J. C. Daran, P. Richard and R. Poli, *J. Am. Chem. Soc.*, 2005, **127**, 5946–5956.

72 M. Kamigaito, Y. Watanabe, T. Ando and M. Sawamoto, *J. Am. Chem. Soc.*, 2002, **124**, 9994–9995.

73 T. Terashima, M. Ouchi, T. Ando and M. Sawamoto, *J. Polym. Sci. Part A Polym. Chem.*, 2010, **48**, 373–379.

74 H. Yoda, K. Nakatani, T. Terashima, M. Ouchi and M. Sawamoto, *Macromolecules*, 2010, **43**, 5595–5601.

75 V. Percec, B. Barboiu, A. Neumann, J. C. Ronda and M. Zhao, *Macromolecules*, 1996, **29**, 3665–3668.

76 P. Lecomte, I. Drapier, P. Dubois, P. Teyssié and R. Jérôme, *Macromolecules*, 1997, **30**, 7631–7633.

77 Y. Kotani, M. Kamigaito and M. Sawamoto, *Macromolecules*, 2000, **33**, 6746–6751.

78 W. A. Braunecker, Y. Itami and K. Matyjaszewski, *Macromolecules*, 2005, **38**, 9402–9404.

79 K. Matyjaszewski, *J. Macromol. Sci. - Pure Appl. Chem.*, 1997, **34**, 1785–1801.

80 A. Kajiwara and K. Matyjaszewski, *Macromol. Rapid Commun.*, 1998, **19**, 319–321.

81 W. Jakubowski and K. Matyjaszewski, *Angew. Chemie - Int. Ed.*, 2006, **45**, 4482–4486.

82 K. Min, H. Gao and K. Matyjaszewski, *Macromolecules*, 2007, **40**, 1789–1791.

83 Y. Gnanou and G. Hizal, *J. Polym. Sci. Part A Polym. Chem.*, 2004, **42**, 351–359.

84 K. Matyjaszewski, W. Jakubowski, K. Min, W. Tang, J. Huang, W. A. Braunecker and N. V. Tsarevsky, *Proc. Natl. Acad. Sci. U. S. A.*, 2006, **103**, 15309–15314.

85 Y. Kwak, A. J. D. Magenau and K. Matyjaszewski, *Macromolecules*, 2011, **44**, 811–819.

86 H. Dong and K. Matyjaszewski, *Macromolecules*, 2008, **41**, 6868–6870.

87 W. Jakubowski, K. Min and K. Matyjaszewski, *Macromolecules*, 2006, **39**, 39–45.

88 W. Tang, N. V. Tsarevsky and K. Matyjaszewski, *J. Am. Chem. Soc.*, 2006, **128**, 1598–1604.

89 P. Krys and K. Matyjaszewski, *Eur. Polym. J.*, 2017, **89**, 482–523.

90 J. Chiefari, Y. K. Chong, F. Ercole, J. Krstina, J. Jeffery, T. P. T. Le, R. T. A. Mayadunne, G. F. Meijs, C. L. Moad, G. Moad, E. Rizzardo and S. H. Thang, *Macromolecules*, 1998, **31**, 5559–5562.

91 G. Moad, E. Rizzardo and S. H. Thang, *Aust. J. Chem.*, 2006, **59**, 669–692.

92 G. Moad, E. Rizzardo and S. H. Thang, *Aust. J. Chem.*, 2009, **62**, 1402–1472.

93 G. Moad, E. Rizzardo and S. H. Thang, *Aust. J. Chem.*, 2012, **65**, 985–1076.

94 D. J. Keddie, *Chem. Soc. Rev.*, 2014, **43**, 496–505.

95 J. Rieger, *Macromol. Rapid Commun.*, 2015, **36**, 1458–1471.

96 S. Perrier, *Macromolecules*, 2017, **50**, 7433–7447.

97 S. Binauld, L. Delafresnaye, B. Charleux, F. D’Agosto and M. Lansalot, *Macromolecules*, 2014, **47**, 3461–3472.

98 P. Galanopoulo, P.-Y. Dugas, M. Lansalot and F. D’Agosto, *Polym. Chem.*, 2020, **11**, 3922–3930.

99 A. Guinaudeau, S. Mazières, D. J. Wilson and M. Destarac, *Polym. Chem.*, 2012, **3**, 81–84.

100 A. B. Lowe and C. L. McCormick, *Prog. Polym. Sci.*, 2007, **32**, 283–351.

101 P. B. Zetterlund, Y. Kagawa and M. Okubo, *Chem. Rev.*, 2008, **108**, 3747–3794.

102 S. Kato and M. Ishida, *Sulfur reports*, 1988, **8**, 155–312.

103 S. Z. Zard, *Aust. J. Chem.*, 2006, **59**, 663.

104 B. Quiclet-Sire and S. Z. Zard, in *Radicals in Synthesis II*, Springer-Verlag, Berlin/Heidelberg, 2006, vol. 264, pp. 201–236.

105 Y. K. Chong, G. Moad, E. Rizzardo and S. H. Thang, *Macromolecules*, 2007, **40**, 4446–4455.

106 K. L. Heredia, G. N. Grover, L. Tao and H. D. Maynard, *Macromolecules*, 2009, **42**, 2360–2367.

107 A. J. Inglis, S. Sinnwell, T. P. Davis, C. Barner-Kowollik and M. H. Stenzel, *Macromolecules*, 2008, **41**, 4120–4126.

108 S. Sinnwell, A. J. Inglis, T. P. Davis, M. H. Stenzel and C. Barner-Kowollik, *Chem. Commun.*, 2008, 2052.

109 Z. Wang, J. He, Y. Tao, L. Yang, H. Jiang and Y. Yang, *Macromolecules*, 2003, **36**, 7446–7452.

110 M.-F. Llauro, J. Loiseau, F. Boisson, F. Delolme, C. Ladavière and J. Claverie, *J. Polym. Sci. Part A Polym. Chem.*, 2004, **42**, 5439–5462.

111 C. W. Scales, A. J. Convertine and C. L. McCormick, *Biomacromolecules*, 2006, **7**, 1389–1392.

112 P. B. Zetterlund, S. C. Thickett, S. Perrier, E. Bourgeat-Lami and M. Lansalot, *Chem. Rev.*, 2015, **115**, 9745–9800.

113 E. J. Ashford, V. Naldi, R. O’Dell, N. C. Billingham and S. P. Armes, *Chem. Commun.*, 1999, **2**, 1285–1286.

114 F. Haaf, A. Sanner and F. Straub, *Polym. J.*, 1985, **17**, 143–152.

115 M. Teodorescu and M. Bercea, *Polym. Plast. Technol. Eng.*, 2015, **54**, 923–943.

116 D. J. Keddie, C. Guerrero-Sanchez, G. Moad, R. J. Mulder, E. Rizzardo and S. H. Thang, *Macromolecules*, 2012, **45**, 4205–4215.

117 T. Otsu and M. Yoshida, *Macromol. Rapid Commun.*, 1982, **3**, 127–132.

118 T. Otsu, *J. Polym. Sci. Part A Polym. Chem.*, 2000, **38**, 2121–2136.

119 C. P. Easterling, Y. Xia, J. Zhao, G. E. Fanucci and B. S. Sumerlin, *ACS Macro Lett.*, 2019, **8**, 1461–1466.

120 V. J. Cunningham, M. J. Derry, L. A. Fielding, O. M. Musa and S. P. Armes, *Macromolecules*, 2016, **49**, 4520–4533.

121 V. J. Cunningham, Y. Ning, S. P. Armes and O. M. Musa, *Polymer*, 2016, **106**, 189–199.

122 V. J. Cunningham, S. P. Armes and O. M. Musa, *Polym. Chem.*, 2016, **7**, 1882–1891.

123 L. Slade, H. Levine and D. S. Reid, *Crit. Rev. Food Sci. Nutr.*, 1991, **30**, 115–360.

124 D. Chandler, *Nature*, 2005, **437**, 640–647.

125 H. Schober, H. Itoh, A. Klapproth, V. Chihaia and W. F. Kuhs, *Eur. Phys. J. E* , 2003, **12**, 41–49.

126 C. Tanford, *Science*, 1978, **200**, 1012–1018.

127 J. N. Israelachvili, D. J. Mitchell and B. W. Ninham, *J. Chem. Soc. Faraday Trans. 2*, 1976, **72**, 1525–1568.

128 J. N. Israelachvili, *Intermolecular and Surface Forces*, Elsevier, San Diego, USA, 2011.

129 R. Nagarajan, *Langmuir*, 2002, **18**, 31–38.

130 F. S. Bates and G. H. Fredrickson, *Phys. Today*, 1999, **52**, 32–38.

131 D. E. Discher, *Science*, 2002, **297**, 967–973.

132 S. Jain and F. S. Bates, *Science*, 2003, **300**, 460.

133 P. Bhargava, J. X. Zheng, P. Li, R. P. Quirk, F. W. Harris and S. Z. D. Cheng, *Macromolecules*, 2006, **39**, 4880–4888.

134 M. C. Orilall and U. Wiesner, *Chem. Soc. Rev.*, 2011, **40**, 520–535.

135 Y. Mai and A. Eisenberg, *Chem. Soc. Rev.*, 2012, **41**, 5969.

136 L. Li, K. Raghupathi, C. Song, P. Prasad and S. Thayumanavan, *Chem. Commun.*, 2014, **50**, 13417–13432.

137 P. J. Flory, *J. Chem. Phys.*, 1942, **10**, 51–61.

138 M. L. Huggins, *J. Am. Chem. Soc.*, 1942, **64**, 1712–1719.

139 A. K. Khandpur, S. Förster, F. S. Bates, I. W. Hamley, A. J. Ryan, W. Bras, K. Almdal and K. Mortensen, *Macromolecules*, 1995, **28**, 8796–8806.

140 C. I. Huang and T. P. Lodge, *Macromolecules*, 1998, **31**, 3556–3565.

141 L. Zhang and A. Eisenberg, *Science*, 1995, **268**, 1728–1731.

142 K. Yu and A. Eisenberg, *Macromolecules*, 1996, **29**, 6359–6361.

143 H. Shen, L. Zhang and A. Eisenberg, *J. Phys. Chem. B*, 1997, **101**, 4697–4708.

144 L. Cantu, M. Corti and P. Salina, *J. Phys. Chem.*, 1991, **95**, 5981–5983.

145 W. A. Wan-Badhi, R. Palepu, D. M. Bloor, D. G. Hall and E. Wyn-Jones, *J. Phys. Chem.*, 1991, **95**, 6642–6647.

146 S. Kato, H. Nomura, R. Zieliński and S. Ikeda, *J. Colloid Interface Sci.*, 1991, **146**, 53–62.

147 M. Frindi, B. Michels and R. Zana, *J. Phys. Chem.*, 1992, **96**, 8137–8141.

148 J. Duhamel, A. Yekta, S. Ni, Y. Khaykin and M. A. Winnik, *Macromolecules*, 1993,

26, 6255–6260.

149 Y. Wang, C. M. Kausch, M. Chun, R. P. Quirk and W. L. Mattice, *Macromolecules*, 1995, **28**, 904–911.

150 S. Creutz, J. van Stam, S. Antoun, F. C. De Schryver and R. Jérôme, *Macromolecules*, 1997, **30**, 4078–4083.

151 A. J. Paine, Y. Deslandes, P. Gerroir and B. Henrissat, *J. Colloid Interface Sci.*, 1990, **138**, 170–181.

152 S. Kawaguchi and K. Ito, *Adv. Polym. Sci.*, 2005, **175**, 299–328.

153 Y. Almog and M. Levy, *J. Polym. Sci. Polym. Chem. Ed.*, 1981, **19**, 115–126.

154 Y. Almog, S. Reich and M. Levy, *Br. Polym. J.*, 1982, **14**, 131–136.

155 Z. An, Q. Shi, W. Tang, C.-K. Tsung, C. J. Hawker and G. D. Stucky, *J. Am. Chem. Soc.*, 2007, **129**, 14493–14499.

156 A. P. Richez, H. N. Yow, S. Biggs and O. J. Cayre, *Prog. Polym. Sci.*, 2013, **38**, 897–931.

157 W. V. Smith and R. H. Ewart, *J. Chem. Phys.*, 1948, **16**, 592–599.

158 W. D. Harkins, *J. Am. Chem. Soc.*, 1947, **69**, 1428–1444.

159 R. Arshady, *Colloid Polym. Sci.*, 1992, **270**, 717–732.

160 A. Pich and W. Richtering, in *Chemical Design of Responsive Microgels*, Springer, Berlin, Heidelberg, 2011, pp. 1–37.

161 G. L. Li, H. Möhwald and D. G. Shchukin, *Chem. Soc. Rev.*, 2013, **42**, 3628–3646.

162 L. I. Costa and G. Storti, *Kinetic Modeling of Precipitation and Dispersion Polymerizations*, Springer International Publishing, Cham, 2018, vol. 281.

163 J. M. Asua, *J. Polym. Sci. Part A Polym. Chem.*, 2004, **42**, 1025–1041.

164 S. C. Thickett and R. G. Gilbert, *Polymer.*, 2007, **48**, 6965–6991.

165 M. El-Aasser and P. A. Lovell, *Emulsion polymerization and emulsion polymers*, John Wiley and Sons, Chichester, 1998.

166 M. E. Adams, M. Trau, R. G. Gilbert, D. H. Napper and D. F. Sangster, *Aust. J. Chem.*, 1988, **41**, 1799–1813.

167 C. S. Chern, *Prog. Polym. Sci.*, 2006, **31**, 443–486.

168 United States Patent Office, 3095388, 1962.

169 F. L. Baines, S. Dionisio, N. C. Billingham and S. P. Armes, *Macromolecules*, 1996, **29**, 3096–3102.

170 S. P. Armes and B. Vincent, *J. Chem. Soc. Chem. Commun.*, 1987, 288–290.

171 S. P. Armes, M. Aldissi, G. C. Idzorek, P. W. Keaton, L. J. Rowton, G. L. Stradling, M. T. Collopy and D. B. McColl, *J. Colloid Interface Sci.*, 1991, **141**, 119–126.

172 C. DeArmitt and S. P. Armes, *Langmuir*, 1993, **9**, 652–654.

173 A. M. I. Ali, P. Pareek, L. Sewell, A. Schmid, S. Fujii, S. P. Armes and I. M. Shirley, *Soft Matter*, 2007, **3**, 1003–1013.

174 Z. Gao, S. K. Varshney, S. Wong and A. Eisenberg, *Macromolecules*, 1994, **27**, 7923–7927.

175 Y.-Y. Won, H. T. Davis and F. S. Bates, *Science*, 1999, **283**, 960–963.

176 P. Dalhaimer, A. J. Engler, R. Parthasarathy and D. E. Discher, *Biomacromolecules*, 2004, **5**, 1714–1719.

177 B. M. Discher, *Science*, 1999, **284**, 1143–1146.

178 S. L. Canning, G. N. Smith and S. P. Armes, *Macromolecules*, 2016, **49**, 1985–2001.

179 A. Blanazs, A. J. Ryan and S. P. Armes, *Macromolecules*, 2012, **45**, 5099–5107.

180 W. Zhao, G. Gody, S. Dong, P. B. Zetterlund and S. Perrier, *Polym. Chem.*, 2014, **5**, 6990–7003.

181 N. J. Warren, O. O. Mykhaylyk, D. Mahmood, A. J. Ryan and S. P. Armes, *J. Am. Chem. Soc.*, 2014, **136**, 1023–1033.

182 V. J. Cunningham, A. M. Alswieleh, K. L. Thompson, M. Williams, G. J. Leggett, S. P. Armes and O. M. Musa, *Macromolecules*, 2014, **47**, 5613–5623.

183 M. J. Derry, L. A. Fielding and S. P. Armes, *Polym. Chem.*, 2015, **6**, 3054–3062.

184 D. Zhou, S. Dong, R. P. Kuchel, S. Perrier and P. B. Zetterlund, *Polym. Chem.*, 2017, **8**, 3082–3089.

185 N. J. Warren, M. J. Derry, O. O. Mykhaylyk, J. R. Lovett, L. P. D. D. Ratcliffe, V. Ladmiral, A. Blanazs, L. A. Fielding and S. P. Armes, *Macromolecules*, 2018, **51**, 8357–8371.

186 X. Zhang, S. Boissé, W. Zhang, P. Beaunier, F. D'Agosto, J. Rieger and B. Charleux, *Macromolecules*, 2011, **44**, 4149–4158.

187 W. Zhang, F. D'Agosto, O. Boyron, J. Rieger and B. Charleux, *Macromolecules*, 2012, **45**, 4075–4084.

188 S. Sugihara, A. Blanazs, S. P. Armes, A. J. Ryan and A. L. Lewis, *J. Am. Chem. Soc.*, 2011, **133**, 15707–15713.

189 S. Boissé, J. Rieger, G. Pembouong, P. Beaunier and B. Charleux, *J. Polym. Sci. Part A Polym. Chem.*, 2011, **49**, 3346–3354.

190 W. M. Wan, X. L. Sun and C. Y. Pan, *Macromolecules*, 2009, **42**, 4950–4952.

191 W. M. Wan, C. Y. Hong and C. Y. Pan, *Chem. Commun.*, 2009, **0**, 5883–5885.

192 Y. Li and S. P. Armes, *Angew. Chemie Int. Ed.*, 2010, **49**, 4042–4046.

193 D. Zehm, L. P. D. Ratcliffe and S. P. Armes, *Macromolecules*, 2013, **46**, 128–139.

194 L. A. Fielding, M. J. Derry, V. Ladmiral, J. Rosselgong, A. M. Rodrigues, L. P. D. Ratcliffe, S. Sugihara and S. P. Armes, *Chem. Sci.*, 2013, **4**, 2081–2087.

195 S. Boissé, J. Rieger, K. Belal, A. Di-Cicco, P. Beaunier, M.-H. Li and B. Charleux, *Chem. Commun.*, 2010, **46**, 1950.

196 X. Zhang, J. Rieger and B. Charleux, *Polym. Chem.*, 2012, **3**, 1502–1509.

197 A. P. Lopez-Oliva, N. J. Warren, A. Rajkumar, O. O. Mykhaylyk, M. J. Derry, K. E. B. Doncom, M. J. Rymaruk and S. P. Armes, *Macromolecules*, 2015, **48**, 3547–

3555.

198 W. D. He, X. L. Sun, W. M. Wan and C. Y. Pan, *Macromolecules*, 2011, **44**, 3358–3365.

199 W. Cai, W. Wan, C. Hong, C. Huang and C. Pan, *Soft Matter*, 2010, **6**, 5554–5561.

200 G. Delaittre, J. Nicolas, C. Lefay, M. Save and B. Charleux, *Chem. Commun.*, 2005, 614–616.

201 S. Brusseau, F. Dagosto, S. Magnet, L. Couvreur, C. Chamignon and B. Charleux, *Macromolecules*, 2011, **44**, 5590–5598.

202 E. Groison, S. Brusseau, F. D'Agosto, S. Magnet, R. Inoubli, L. Couvreur and B. Charleux, *ACS Macro Lett.*, 2012, **1**, 47–51.

203 K. H. Kim, J. Kim and W. H. Jo, *Polymer*, 2005, **46**, 2836–2840.

204 S. Sugihara, K. Sugihara, S. P. Armes, H. Ahmad and A. L. Lewis, *Macromolecules*, 2010, **43**, 6321–6329.

205 S. Sugihara, S. P. Armes and A. L. Lewis, *Angew. Chemie Int. Ed.*, 2010, **49**, 3500–3503.

206 J. Tan, H. Sun, M. Yu, B. S. Sumerlin and L. Zhang, *ACS Macro Lett.*, 2015, **4**, 1249–1253.

207 S. J. Byard, M. Williams, B. E. McKenzie, A. Blanazs and S. P. Armes, *Macromolecules*, 2017, **50**, 1482–1493.

208 T. R. Guimarães, M. Khan, R. P. Kuchel, I. C. Morrow, H. Minami, G. Moad, S. Perrier and P. B. Zetterlund, *Macromolecules*, 2019, **52**, 2965–2974.

209 A. M. James, M. J. Derry, J. S. Train and R. Dawson, *Polym. Chem.*, 2019, **10**, 3879–3886.

210 R. R. Gibson, E. J. Cornel, O. M. Musa, A. Fernyhough and S. P. Armes, *Polym. Chem.*, 2020, **11**, 1785–1796.

211 M. J. Derry, L. A. Fielding and S. P. Armes, *Prog. Polym. Sci.*, 2016, **52**, 1–18.

212 M. J. Rymaruk, S. J. Hunter, C. T. O'Brien, S. L. Brown, C. N. Williams and S. P. Armes, *Macromolecules*, 2019, **52**, 2822–2832.

213 K. J. Thurecht, A. M. Gregory, W. Wang and S. M. Howdle, *Macromolecules*, 2007, **40**, 2965–2967.

214 M. Zong, K. J. Thurecht and S. M. Howdle, *Chem. Commun.*, 2008, 5942.

215 Q. Zhang and S. Zhu, *ACS Macro Lett.*, 2015, **4**, 755–758.

216 S. W. Prescott, M. J. Ballard, E. Rizzardo and R. G. Gilbert, *Macromolecules*, 2002, **35**, 5417–5425.

217 M. J. Monteiro, M. Hodgson and H. De Brouwer, *J. Polym. Sci. Part A Polym. Chem.*, 2000, **38**, 3864–3874.

218 S. W. Prescott, M. J. Ballard, E. Rizzardo and R. G. Gilbert, *Aust. J. Chem.*, 2002, **55**, 415–424.

219 I. Uzulina, S. Kanagasabapathy and J. Claverie, *Macromol. Symp.*, 2000, **150**, 33–38.

220 G. Moad, J. Chiefari, (Bill) Y?K Chong, J. Krstina, R. T. Mayadunne, A. Postma, E. Rizzardo and S. H. Thang, *Polym. Int.*, 2000, **49**, 993–1001.

221 M. J. Monteiro, M. Sjoberg, J. van der Vlist and C. M. Gottgens, *J. Polym. Sci. Part A Polym. Chem.*, 2000, **38**, 4206–4217.

222 D. Charmot, P. Corpart, H. Adam, S. Z. Zard, T. Biadatti and G. Bouhadir, *Macromol. Symp.*, 2000, **150**, 23–32.

223 M. J. Monteiro and H. de Brouwer, *Macromolecules*, 2001, **34**, 349–352.

224 C. J. Ferguson, R. J. Hughes, B. T. T. Pham, B. S. Hawkett, R. G. Gilbert, A. K. Serelis and C. H. Such, *Macromolecules*, 2002, **35**, 9243–9245.

225 C. J. Ferguson, R. J. Hughes, D. Nguyen, B. T. T. Pham, R. G. Gilbert, A. K. Serelis, C. H. Such and B. S. Hawkett, *Macromolecules*, 2005, **38**, 2191–2204.

226 L. Carlsson, A. Fall, I. Chaduc, L. Wågberg, B. Charleux, E. Malmström, F. D'Agosto, M. Lansalot and A. Carlmark, *Polym. Chem.*, 2014, **5**, 6076–6086.

227 L. Etchenausia, E. Deniau, A. Brûlet, J. Forcada and M. Save, *Macromolecules*, 2018, **51**, 2551–2563.

228 S. J. Stace, J. Vanderspikken, S. C. Howard, G. Li, B. W. Muir, C. M. Fellows, D. J. Keddie and G. Moad, *Polym. Chem.*, 2019, **10**, 5044–5051.

229 X. Wang, Y. Luo, B. Li and S. Zhu, *Macromolecules*, 2009, **42**, 6414–6421.

230 Y. Luo, X. Wang, Y. Zhu, B.-G. Li and S. Zhu, *Macromolecules*, 2010, **43**, 7472–7481.

231 I. Chaduc, W. Zhang, J. Rieger, M. Lansalot, F. D'Agosto and B. Charleux, *Macromol. Rapid Commun.*, 2011, **32**, 1270–1276.

232 I. Chaduc, A. Crepet, O. Boyron, B. Charleux, F. D'Agosto and M. Lansalot, *Macromolecules*, 2013, **46**, 6013–6023.

233 Y. Ning, L. A. Fielding, L. P. D. Ratcliffe, Y. W. Wang, F. C. Meldrum and S. P. Armes, *J. Am. Chem. Soc.*, 2016, **138**, 11734–11742.

234 G. K. K. Clothier, T. R. Guimarães, M. Khan, G. Moad, S. Perrier and P. B. Zetterlund, *ACS Macro Lett.*, 2019, **8**, 989–995.

235 H. Kitano, K. Tokuwa, H. Ueno, L. Li and Y. Saruwatari, *Colloid Polym. Sci.*, 2015, **293**, 2931–2939.

236 M. Sponchioni, P. Rodrigues Bassam, D. Moscatelli, P. Arosio and U. Capasso Palmiero, *Nanoscale*, 2019, **11**, 16582–16591.

237 N. P. Truong, M. V Dussert, M. R. Whittaker, J. F. Quinn and T. P. Davis, *Polym. Chem.*, 2015, **6**, 3865–3874.

238 S. Y. Khor, N. P. Truong, J. F. Quinn, M. R. Whittaker and T. P. Davis, *ACS Macro Lett.*, 2017, **6**, 1013–1019.

239 C. P. Jesson, V. J. Cunningham, M. J. Smallridge and S. P. Armes, *Macromolecules*, 2018, **51**, 3221–3232.

240 J. Jennings, G. He, S. M. Howdle and P. B. Zetterlund, *Chem. Soc. Rev.*, 2016, **45**, 5055–5084.

241 J. Zhou, H. Yao and J. Ma, *Polym. Chem.*, 2018, **9**, 2532–2561.

242 J. Rieger, F. Stoffelbach, C. Bui, D. Alaimo, C. Jérôme and B. Charleux, *Macromolecules*, 2008, **41**, 4065–4068.

243 A. A. Cockram, T. J. Neal, M. J. Derry, O. O. Mykhaylyk, N. S. J. Williams, M. W. Murray, S. N. Emmett and S. P. Armes, *Macromolecules*, 2017, **50**, 796–802.

244 A. Blanazs, J. Madsen, G. Battaglia, A. J. Ryan and S. P. Armes, *J. Am. Chem. Soc.*, 2011, **133**, 16581–16587.

245 B. T. T. Pham, D. Nguyen, V. T. Huynh, E. H. Pan, B. Shirodkar-Robinson, M. Carey, A. K. Serelis, G. G. Warr, T. Davey, C. H. Such and B. S. Hawkett, *Langmuir*, 2018, **34**, 4255–4263.

246 J. Lesage de la Haye, X. Zhang, I. Chaduc, F. Brunel, M. Lansalot and F. D'Agosto, *Angew. Chemie Int. Ed.*, 2016, **55**, 3739–3743.

247 A. M. Mathur, B. Drescher, A. B. Scranton and J. Klier, *Nature*, 1998, **392**, 367–370.

248 E. Tsuchida and K. Abe, *Interactions between macromolecules in solution and intermacromolecular complexes*, Springer-Verlag, Berlin, Germany, 2005.

249 V. A. Kabanov and I. M. Papisov, *Polym. Sci. U.S.S.R.*, 1979, **21**, 261–307.

250 F. L. Hatton, A. M. Park, Y. Zhang, G. D. Fuchs, C. K. Ober and S. P. Armes, *Polym. Chem.*, 2019, **10**, 194–200.

251 E. E. Brotherton, F. L. Hatton, A. A. Cockram, M. J. Derry, A. Czajka, E. J. Cornel, P. D. Topham, O. O. Mykhaylyk and S. P. Armes, *J. Am. Chem. Soc.*, 2019, **141**, 13664–13675.

252 G. Mellot, J. Guigner, L. Bouteiller, F. Stoffelbach and J. Rieger, *Angew. Chemie Int. Ed.*, 2019, **58**, 3173–3177.

253 Q. Zhang, C. Weber, U. S. Schubert and R. Hoogenboom, *Mater. Horizons*, 2017, **4**, 109–116.

254 C. Grazon, J. Rieger, N. Sanson and B. Charleux, *Soft Matter*, 2011, **7**, 3482–3490.

255 G. Liu, Q. Qiu, W. Shen and Z. An, *Macromolecules*, 2011, **44**, 5237–5245.

256 L. P. D. Ratcliffe, A. Blanazs, C. N. Williams, S. L. Brown and S. P. Armes, *Polym. Chem.*, 2014, **5**, 3643–3655.

257 Y. Jiang, N. Xu, J. Han, Q. Yu, L. Guo, P. Gao, X. Lu and Y. Cai, *Polym. Chem.*, 2015, **6**, 4955–4965.

258 W. Shen, Y. Chang, G. Liu, H. Wang, A. Cao and Z. An, *Macromolecules*, 2011, **44**, 2524–2530.

259 J. C. Foster, S. Varlas, B. Couturaud, J. R. Jones, R. Keogh, R. T. Mathers and R. K. O'Reilly, *Angew. Chemie Int. Ed.*, 2018, **57**, 15733–15737.

260 C. A. Lipinski, F. Lombardo, B. W. Dominy and P. J. Feeney, *Adv. Drug Deliv. Rev.*, 1997, **23**, 3–25.

261 A. K. Ghose, V. N. Viswanadhan and J. J. Wendoloski, *J. Phys. Chem. A*, 1998, **102**, 3762–3772.

262 A. A. Petrauskas and E. A. Kolovanov, *Perspect. Drug Discov. Des.*, 2000, **19**, 99–116.

263 A. Blanazs, R. Verber, O. O. Mykhaylyk, A. J. Ryan, J. Z. Heath, C. W. I. Douglas and S. P. Armes, *J. Am. Chem. Soc.*, 2012, **134**, 9741–9748.

264 J. R. Lovett, N. J. Warren, L. P. D. Ratcliffe, M. K. Kocik and S. P. Armes, *Angew. Chemie Int. Ed.*, 2015, **54**, 1279–1283.

265 L. D. Blackman, K. E. B. Doncom, M. I. Gibson and R. K. O'Reilly, *Polym. Chem.*, 2017, **8**, 2860–2871.

266 K. Ren and J. Perez-Mercader, *Polym. Chem.*, 2017, **8**, 3548–3552.

267 Q. Xu, Y. Zhang, X. Li, J. He, J. Tan and L. Zhang, *Polym. Chem.*, 2018, **9**, 4908–4916.

268 J. Tan, Q. Xu, Y. Zhang, C. Huang, X. Li, J. He and L. Zhang, *Macromolecules*, 2018, **51**, 7396–7406.

269 Y. Zhang, L. Yu, X. Dai, L. Zhang and J. Tan, *ACS Macro Lett.*, 2019, **8**, 1102–1109.

270 R. R. Gibson, S. P. Armes, O. M. Musa and A. Fernyhough, *Polym. Chem.*, 2019, **10**, 1312–1323.

271 S. M. North and S. P. Armes, *Polym. Chem.*, 2020, **11**, 2147–2156.

272 S. Jain and F. S. Bates, *Macromolecules*, 2004, **37**, 1511–1523.

273 X. Zhang, S. Boissé, C. Bui, P.-A. Albouy, A. Brûlet, M.-H. Li, J. Rieger and B. Charleux, *Soft Matter*, 2012, **8**, 1130–1141.

274 N. J. W. Penfold, J. R. Whatley and S. P. Armes, *Macromolecules*, 2019, **52**, 1653–1662.

275 R. Verber, A. Blanazs and S. P. Armes, *Soft Matter*, 2012, **8**, 9915–9922.

276 S. G. Jang, D. J. Audus, D. Klinger, D. V. Krogstad, B. J. Kim, A. Cameron, S. W. Kim, K. T. Delaney, S. M. Hur, K. L. Killops, G. H. Fredrickson, E. J. Kramer and C. J. Hawker, *J. Am. Chem. Soc.*, 2013, **135**, 6649–6657.

277 F. Stoffelbach, L. Tibiletti, J. Rieger and B. Charleux, *Macromolecules*, 2008, **41**, 7850–7856.

278 M E Cates, *J. Phys. Condens. Matter*, 1996, **8**, 9167–9176.

279 J. Madsen, S. P. Armes, K. Bertal, H. Lomas, S. MacNeil and A. L. Lewis, *Biomacromolecules*, 2008, **9**, 2265–2275.

280 J. R. Lovett, M. J. Derry, P. Yang, F. L. Hatton, N. J. Warren, P. W. Fowler and S. P. Armes, *Chem. Sci.*, 2018, **9**, 7138–7144.

281 A. P. Chatterjee, *J. Chem. Phys.*, 2010, **132**, 224905.

282 R. H. J. Otten and P. van der Schoot, *J. Chem. Phys.*, 2011, **134**, 094902.

283 K. R. Peddireddy, I. Capron, T. Nicolai and L. Benyahia, *Biomacromolecules*, 2016, **17**, 3298–3304.

284 B. Charleux, G. Delaittre, J. Rieger and F. D'Agosto, *Macromolecules*, 2012, **45**, 6753–6765.

285 G. Delaittre, M. Save and B. Charleux, *Macromol. Rapid Commun.*, 2007, **28**, 1528–1533.

286 N. J. Warren and S. P. Armes, *J. Am. Chem. Soc.*, 2014, **136**, 10174–10185.

287 V. J. Cunningham, L. P. D. Ratcliffe, A. Blanazs, N. J. Warren, A. J. Smith, O. O. Mykhaylyk and S. P. Armes, *Polym. Chem.*, 2014, **5**, 6307–6317.

288 J. R. Lovett, L. P. D. Ratcliffe, N. J. Warren, S. P. Armes, M. J. Smallridge, R. B. Cracknell and B. R. Saunders, *Macromolecules*, 2016, **49**, 2928–2941.

289 V. Frank, S. Kaufmann, R. Wright, P. Horn, H. Y. Yoshikawa, P. Wuchter, J. Madsen, A. L. Lewis, S. P. Armes, A. D. Ho and M. Tanaka, *Sci. Rep.*, 2016, **6**, 1–12.

290 I. Canton, N. J. Warren, A. Chahal, K. Amps, A. Wood, R. Weightman, E. Wang, H. Moore and S. P. Armes, *ACS Cent. Sci.*, 2016, **2**, 65–74.

291 M. Sponchioni, C. T. O'Brien, C. Borchers, E. Wang, M. N. Rivolta, N. J. W. Penfold, I. Canton and S. P. Armes, *Chem. Sci.*, 2020, **11**, 232–240.

292 L. P. D. Ratcliffe, M. J. Derry, A. Ianiro, R. Tuinier and S. P. Armes, *Angew. Chemie Int. Ed.*, 2019, **58**, 18964–18970.

293 P. Rejmanová, J. Labský and J. Kopeček, *Die Makromol. Chemie*, 1977, **178**, 2159–2168.

294 J. B. Lloyd, R. Duncan and M. K. Pratten, *Br. Polym. J.*, 1983, **15**, 158–159.

295 R. Duncan, L. W. Seymour, K. Ulbrich and J. Kopeček, *J. Bioact. Compat. Polym.*, 1988, **3**, 4–15.

296 R. Duncan and K. Ulbrich, *Makromol. Chemie. Macromol. Symp.*, 1993, **70**, 157–162.

297 P. N. Hurter, J. M. H. M. Scheutjens and T. A. Hatton, *Macromolecules*, 1993, **26**, 5592–5601.

298 G. J. Fleer, M. A. C. Stuart, J. M. H. M. Scheutjens, T. Cosgrove and B. Vincent, *Polymers at Interfaces*, Springer Netherlands, Dordrecht, 1998.

299 N. Orakdogen and O. Okay, *Polymer.*, 2006, **47**, 561–568.

300 J. Butt, H, K. Graf and M. Kappl, *Physics and Chemistry of Interfaces, 3rd Edition*, Wiley, 2013.

301 E. G. Kelley, T. P. Smart, A. J. Jackson, M. O. Sullivan and T. H. Epps, *Soft Matter*, 2011, **7**, 7094–7102.

302 E. B. Zhulina and O. V. Borisov, *Macromolecules*, 2012, **45**, 4429–4440.

303 S. J. Byard, C. T. O'Brien, M. J. Derry, M. Williams, O. O. Mykhaylyk, A. Blanazs and S. P. Armes, *Chem. Sci.*, 2020, **11**, 396–402.

Chapter 2

Synthesis of Well-Defined Pyrrolidone-Based Homopolymers and Stimulus-Responsive Diblock Copolymers via RAFT Aqueous Solution Polymerisation of 2-(*N*-acryloyloxy)ethyl Pyrrolidone

Reproduced in part with permission from:

O. J. Deane, J. R. Lovett, O. M. Musa, A. Fernyhough, and S. P. Armes, *Macromolecules* 2018, 51, 7756−7766

2.1 Introduction

Reppe reported the synthesis and polymerisation of NVP in 1954 (Scheme 2.1).[1] Since this pioneering work, PNVP has become a commercially important non-ionic water-soluble polymer with a wide range of commercial applications.[2,3] Its high dipole moment (4.06 D)[4] enables the efficient sequestration of many fugitive dyes and hence its widespread use as an anti-dye transfer agent in laundry formulations.[5,6] PNVP can also be utilised as a film-forming agent in various cosmetics such as mascara and hair sprays[7] and its excellent biocompatibility and relatively low cost has led to its use as an excipient in many drug formulations.[7,8] Bulk copolymerisation with other vinyl monomers enables the production of soft contact lenses[9] while the so-called 'popcorn' polymerisation of NVP produces cross-linked particles that can be used to clarify alcoholic beverages such as beer and wine.[10] PNVP can also be used as an emulsifier[11], as a dispersant for β-carotene[12] or a steric stabiliser for the preparation of conducting polymer nanoparticles.[13]

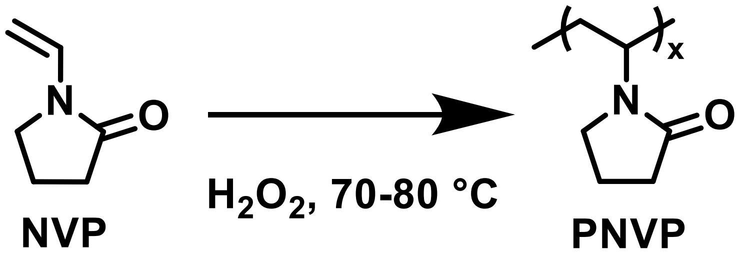

Scheme 2.1. Free radical polymerisation of *N*-vinylpyrrolidone to produce PNVP. Polymerisation is typically achieved through initiation with hydrogen peroxide.[2]

NVP is an example of a LAM. As discussed in Chapter 1, LAMs can be statistically copolymerised with comonomers such as vinyl acetate or acrylics. However, the copolymerisation of NVP with methacrylics or styrene is more problematic, with strongly non-ideal behaviour typically being observed.[14–17] Devasia and co-workers reported the first CRP of NVP utilising dithiocarbamate-mediated RAFT polymerisation (Scheme 2.2).[18] It was suggested that the highly polar lactam ring in NVP disrupts the catalyst-ligand structures formed in ATRP, resulting in uncontrolled polymerisation.[18]

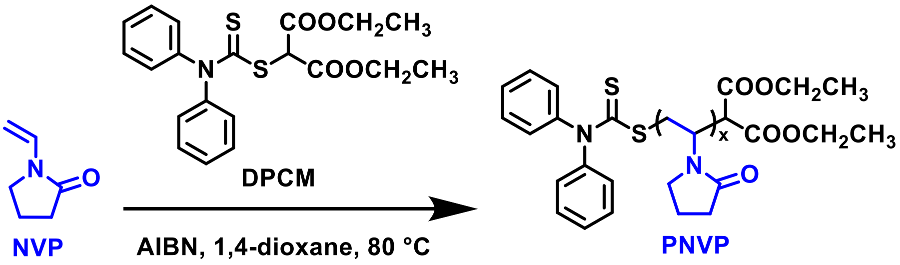

Scheme 2.2. Synthesis of PNVP *via* RAFT solution polymerisation of NVP in 1,4 dioxane at 80 °C using diphenyldithiocarbamate (DPCM) as the chain transfer agent and AIBN as the initiator.[18]

Gas chromatography studies indicated that 93% NVP conversion could be achieved within 44 h when using a [DPCM]/[AIBN] molar ratio of 0.50 at 80 °C.[18] This was attributed to a relatively low radical flux. GPC studies indicated a linear increase in PNVP molecular weight with NVP conversion. However, molecular weight distributions became noticeably broader above 50% conversion, indicating loss of RAFT control (Figure 2.1).

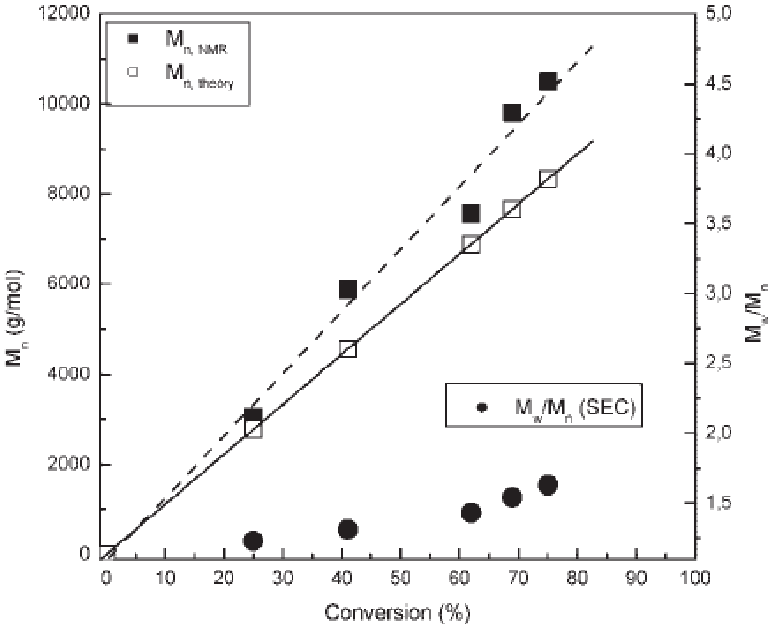

Figure 2.1. Evolution of M_n and M_w/M_n vs conversion for the RAFT aqueous solution polymerisation of NVP at 80 °C in 1,4 dioxane. (GPC eluent was a 4:1 H_2O/CH_3OH mixture containing 0.1 M $NaNO_3$; refractive index detector; calibration against a series of near-monodisperse poly(ethylene oxide) standards).[18]

As discussed in Chapter 1, water is an environmentally-friendly and cheap solvent and thus it is strongly preferred for industrial use. However, the RAFT aqueous solution polymerisation of NVP is best performed at low temperature to minimise *in situ* hydrolysis of the chain transfer agent.[19,20] This can result in a relatively slow rate of polymerisation[21] owing to retardation caused by either the initialisation period[22,23] or slow fragmentation of intermediate radicals.[24] However, the xanthate-mediated RAFT aqueous solution polymerisation of NVP is complicated by various side-reactions.[25] Furthermore, NVP is known to undergo side-reactions in acidic water resulting in unpolymerisable adducts (Scheme 2.3).[26]

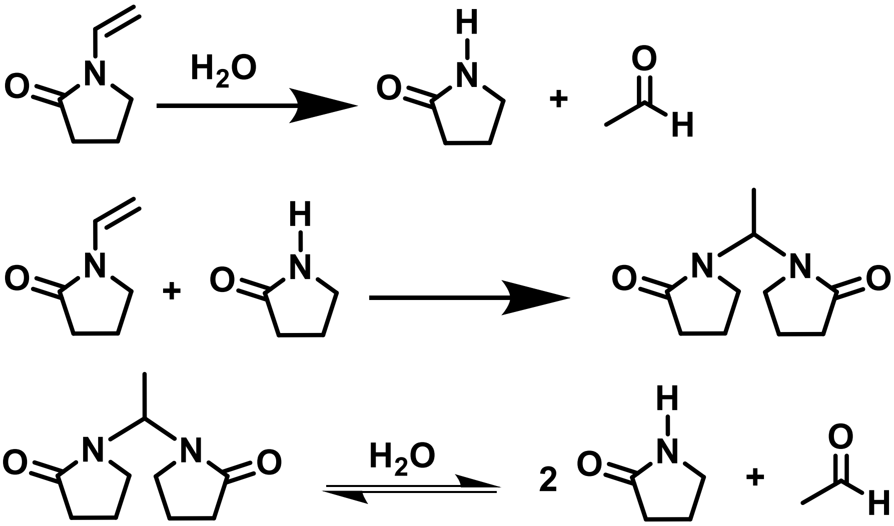

Scheme 2.3. Reactions of NVP and the resulting unpolymerisable adducts formed in acidic water.[26]

Pound *et al*. reported that a saturated NVP dimer was formed regardless of the presence or absence of RAFT agent or initiator.[25] Other by-products were obtained in the presence of various xanthates. Methyl-based by-products led to broader molecular weight distributions owing to facile abstraction of such labile protons. Furthermore, side reactions involving the NVP-xanthate adduct were also investigated. It was also reported that saturated products were formed after the elimination of the xanthate from NVP-adducts. This produced dead polymer chains that resulted in broader final PNVP molecular weight distributions.[25] Therefore, Pound *et al*. suggested using relatively low temperatures (< 60 °C) to minimise the formation of methylated species and also to reduce the elimination of xanthates from the dormant chain-end. Furthermore, it was suggested that water should be avoided for the RAFT polymerisation of NVP.[25]

Despite the unexpected side reactions of NVP in water (Scheme 2.3), there are various literature formulations for the RAFT aqueous solution polymerisation of NVP using either xanthates or dithiocarbamates which enable moderate monomer conversions to be achieved.[18,27,28] However, RAFT control is typically inferior to that achieved for (meth)acrylic monomers under optimised conditions, particularly for polymerisations performed in aqueous solution.[25,29–34] For example, Guinaudeau *et al*. reported the synthesis of PNVP-based double-hydrophilic diblock copolymers via RAFT/MADIX aqueous polymerisation by employing redox initiation at ambient temperature.[35,36] Using ascorbic acid led to the formation of *N*-(α-hydroxyethyl)pyrrolidone in acidic solution (i.e. the same by-product observed by Pound *et al.*[25]) but switching to sodium sulphite and mildly alkaline conditions (pH 9) prevented generation of this unwanted side-product (Figure 2.2).

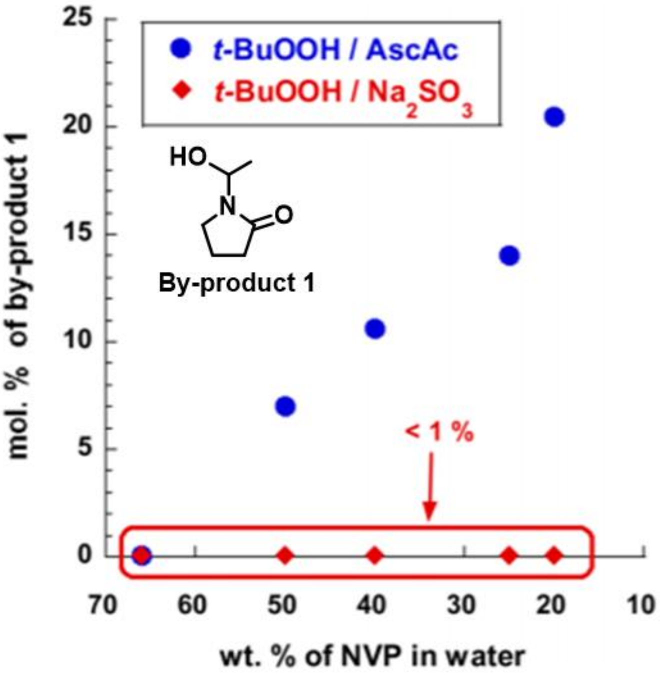

Figure 2.2. RAFT/MADIX aqueous solution polymerization of NVP performed at 25 °C using either *t*-BuOOH/AscAc (at pH 3) or *t*-BuOOH/Na_2SO_3 (at pH 9) as the redox initiator. Effect of dilution on the presence of the *N*-(α-hydroxyethyl)pyrrolidone by-product (by-product 1; see inset for chemical structure).[36]

Under optimised conditions, relatively good control was achieved for the RAFT homopolymerisation of NVP ($M_w/M_n < 1.20$). However, a self-blocking chain extension experiment led to a final M_w/M_n of 1.72, which suggests imperfect control (e.g. premature loss of RAFT end-groups). Nevertheless, the synthesis of PNVP-based double-hydrophilic diblock copolymers was achieved by preparing the other hydrophilic block first, followed by chain extension of this precursor via NVP polymerisation.

Notwithstanding these advances in the controlled polymerisation of NVP, a methacrylic analogue (2-(*N*-methacryloyloxy)ethyl pyrrolidone, NMEP) has been recently examined to address the copolymerisability problem. NMEP has been polymerised with good control using RAFT polymerisation by Cunningham and co-workers.[37–39] The resulting PNVP analogue, PNMEP has been used as a steric stabiliser block for the synthesis of diblock copolymer nano-objects via RAFT dispersion polymerisation of benzyl methacrylate in ethanol[37] and also as a core-forming block for RAFT dispersion polymerisation formulations conducted in *n*-dodecane.[39] However, PNMEP is significantly less hydrophilic than PNVP, exhibiting inverse temperature solubility in aqueous solution at around 55 °C in the high molecular weight limit.[40,41] Indeed, this property was exploited by Cunningham and co-workers to devise a RAFT aqueous dispersion polymerisation formulation in which the growing PNMEP chains formed the hydrated cores of sterically-stabilised nanoparticles at 70 °C (Figure 2.3).[38]

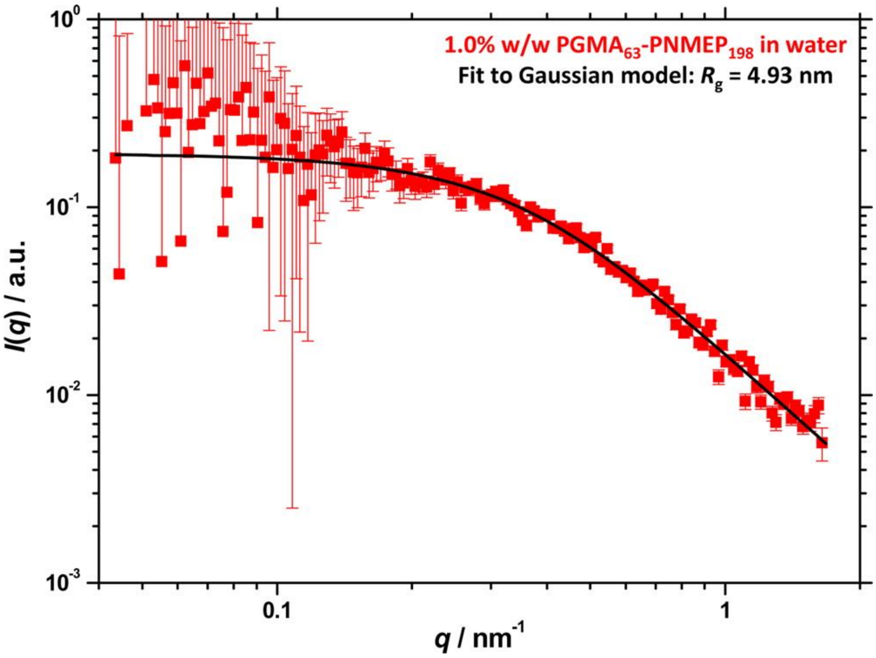

Figure 2.3. SAXS pattern (red squares) and corresponding data fit to a generalised Gaussian coil model (black line) for a 1.0% w/w aqueous dispersion of PGMA$_{63}$–PNMEP$_{198}$ diblock copolymer nanoparticles at 70 °C.[38]

In view of such observations, PNMEP was deemed to be unsuitable for use as a *stabiliser* block for either RAFT aqueous emulsion polymerisation or RAFT aqueous dispersion polymerisation because it did not confer sufficient steric stabilisation. Given this limitation, a more hydrophilic analogue of NVP was sought, with one obvious candidate being NAEP (see Figure 1.8 in Chapter 1).

In 2009 Shi *et al*. reported the RAFT aqueous solution homopolymerisation of NAEP *via* visible light irradiation at 25 °C using (2,4,6-trimethylbenzoyl)diphenylphosphine oxide as a photoinitiator.[42] This early example of photoinitiated RAFT polymerisation enabled the polymerisation to be started and stopped via periodic on-off irradiation.[42] Mild conditions were selected to ensure that chain transfer to polymer was suppressed and also to minimise hydrolysis of the trithiocarbonate-based RAFT agent. Good control over the molecular weight distribution was demonstrated ($M_w/M_n < 1.10$) but NAEP conversions did not exceed 77% (Figure 2.4a). ^{1}H NMR studies indicated a linear increase in M_n with NAEP conversion and targeting higher PNAEP DPs resulted in PNAEP homopolymers with higher final M_n values, as expected for optimised RAFT polymerisations (see Figure 2.4b). Presumably, the substantially incomplete conversions were due to the reaction being stopped after 45 min. However, ensuring high monomer conversion is crucial for commercial applications and the low conversions reported may have been the result of the mild conditions chosen for this RAFT polymerisation or required to avoid hydrolysis of the CTA employed. As such, an alternative initiation system that ensured both good RAFT control and high final NAEP conversions would be highly desirable.

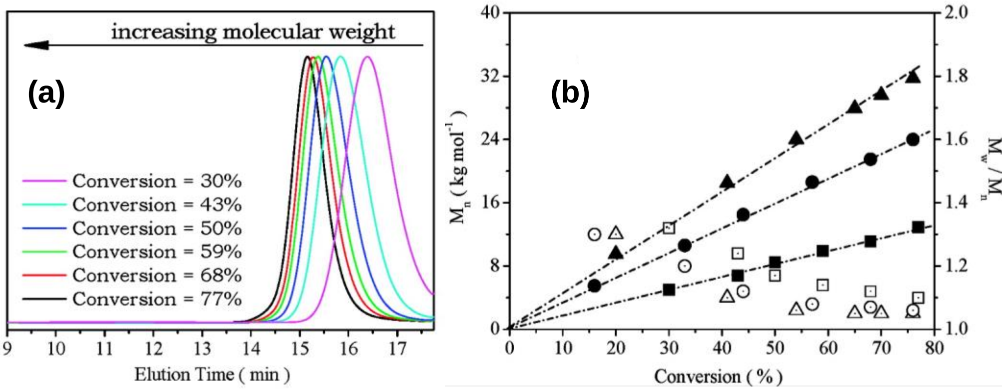

Figure 2.4. (a) GPC traces reported by Shi et al. for PNAEP homopolymers obtained at the stated intermediate conversions when targeting a final DP of 50 and (b) M_n (solid) and M_w/M_n (hollow) data obtained for PNAEP homopolymers (target DP = 150, 100, 50 for triangles, circles and squares, respectively) as a function of NAEP conversion.[43]

A PNAEP$_{34}$ homopolymer was then used as a precursor to mediate the RAFT aqueous solution polymerisation of either 2-hydroxyethyl acrylate (HEA) or OEGA via visible light irradiation at 25 °C. However, ^{1}H NMR studies indicated only 67% HEA conversion (target PHEA DP = 100) and 57% OEGA conversion (target POEGA DP = 50), respectively. During the RAFT solution polymerisation of HEA, GPC studies indicated that a high molecular weight shoulder appeared after 48% HEA conversion. This was attributed to traces of diacrylate impurities.[44,45] However, chain transfer to polymer may also have occurred.[46] GPC traces recorded for $PNAEP_{34}$-$POEGA_{29}$ diblock copolymers were highly symmetrical, indicating that well-defined diblock copolymers could be synthesised (albeit at relatively low OEGA conversions). In principle, an optimised protocol for the RAFT solution polymerisation of NAEP should enable near-monodisperse high molecular weight PNAEP homopolymers to be obtained at high monomer conversion. Furthermore, subsequent chain extension with appropriate comonomers should provide access to new stimulus-responsive diblock copolymers.[47–51]

Herein we report the efficient synthesis of a series of near-monodisperse homopolymers via RAFT aqueous solution polymerisation of NAEP using either a persulfate initiator at 30 °C (see Scheme 2.4a) or an azo initiator at 70 °C (see Scheme 2.4b). Optimised reaction conditions were then employed to prepare a series of new well-defined PNAEP-based diblock copolymers with high blocking efficiencies. The aqueous solution properties of selected stimulus-responsive copolymers are briefly explored.

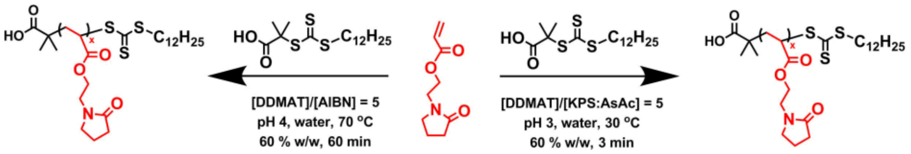

Scheme 2.4. Synthesis of PNAEP homopolymers by RAFT aqueous solution polymerisation of NAEP using a trithiocarbonate-based RAFT agent (DDMAT) and either (a) α,α′-azoisobutyronitrile (AIBN) initiator (b) a low-temperature redox initiator system based on a 1:1 molar ratio of potassium persulfate (KPS) and ascorbic acid (AsAc). A DDMAT/initiator molar ratio of 5.0 was employed for both formulations.

2.2 Experimental

2.2.1 Materials

N-(2-(Acryloyloxy)ethyl)pyrrolidone (NAEP; 95% purity) was kindly provided by Ashland Specialty Ingredients (Cherry Hill, NJ, USA) and was further purified through dilution with chloroform followed by sequential washes with 5% Na_2CO_3 solution, saturated NaCl solution and finally deionised water. Repeated washes with water were carried out until the NAEP solution was neutralised. The solution was then dried over anhydrous $MgSO_4$. All chemicals used for NAEP purification were purchased from Sigma-Aldrich UK and were used as received. 2-Hydroxyethyl acrylate (HEA) was purchased from Sigma-Aldrich UK and purified via twenty washes with n-hexane. Oligo(ethylene glycol) methyl ether acrylate (OEGA, $M_n \approx 454$ g mol^{-1}), 2-(diethylamino)ethyl methacrylate (DEA), ascorbic acid (AsAc), potassium persulfate (KPS), α,α′-azoisobutyronitrile (AIBN), 4,4'-azobis(4-cyanopentanoic acid) (ACVA; 99%) and 2-(dodecylthiocarbonothioylthio)-2-methylpropionic acid (DDMAT; 98%) were purchased from Sigma-Aldrich UK and was used as received. *N*-isopropylacrylamide (NIPAM; 97%) was purchased from Sigma-Aldrich UK and recrystallised from *n*-hexane twice before use. 4-Cyano-4-(2-phenylethanesulfanylthiocarbonyl)sulfanylpentanoic acid (PETTC) was prepared and purified as reported elsewhere.[52] MPETTC was then prepared from PETTC using a literature protocol.[53] d_4-Methanol and D_2O were purchased from Goss Scientific Instruments Ltd. (Cheshire, UK). All other solvents were purchased from Fisher Scientific (Loughborough, UK) and used as received. Deionised water was used for all experiments.

2.2.2 RAFT Solution Homopolymerisation of NAEP in Water at 70 °C

A typical protocol for the synthesis of a $PNAEP_{80}$ homopolymer is as follows: NAEP (1.00 g, 5.46 mmol), DDMAT RAFT agent (24.9 mg, 68.2 µmol; target DP = 80), deionised water (0.6847 g, corresponding to a 60% w/w solution), and AIBN (2.2 mg, 13.6 µmol; DDMAT/AIBN molar ratio = 5.0) were weighed into a 14 mL vial charged with a magnetic flea. This reaction vial was then placed in an ice bath and degassed with nitrogen for 30 min. Following this, the vial was then immersed in an oil bath set at 70 °C and the reaction solution was stirred for 50 min, resulting in a final monomer conversion of 99% as judged by ^1H NMR spectroscopy. ^1H NMR (in d_4-Methanol, δ): 1.6 (3H, CH_3 of methyl RAFT chain-end), 4.1-4.3 (160H, $COOCH_2CH_2$), 3.4-3.6 (320H, $COOCH_2C\underline{H_2}$, and $NCOC\underline{H_2}CH_2CH_2$), 1.3-2.5 (560H, $NCOCH_2C\underline{H_2}C\underline{H_2}$ and $C\underline{H_2}C\underline{H}COO$). DMF GPC analysis indicated an M_n of 13 300 g mol^{-1} and an M_w/M_n of 1.14 when calibrated against a series of near-monodisperse poly(methyl methacrylate) standards.

2.2.3 RAFT Solution Homopolymerisation of NAEP in Water at 30 °C

A typical protocol for the synthesis of a $PNAEP_{80}$ homopolymer is as follows: NAEP (1.00 g, 5.46 mmol), DDMAT RAFT agent (24.9 mg, 68.2 µmol; target DP = 80) and AsAc

(2.4 mg, 13.6 µmol; DDMAT/AsAc molar ratio = 5.0) were weighed into a 14 mL vial charged with a magnetic flea and degassed with nitrogen in an ice bath for 30 min (reaction solution 1). Deionised water (0.6873 g, corresponding to a 60% w/w solution), and KPS (3.7 mg, 13.6 µmol; DDMAT/KPS molar ratio = 5.0) were weighed into a separate 14 mL vial (reaction solution 2), sealed using a rubber septum and degassed with nitrogen in an ice bath for 30 min. After 30 min, the vial containing reaction solution 1 was immersed in an oil bath set at 30 °C. Following this, reaction solution 2 was added to this vial via a degassed syringe and needle to reaction solution 1 under nitrogen. The polymerisation was monitored for 5 min, resulting in a final monomer conversion of 99% as judged by ^{1}H NMR spectroscopy. ^{1}H NMR (in d_4-Methanol, δ): 1.6 (3H, CH_3 of methyl RAFT chain-end), 4.1-4.3 (160H, $COOCH_2CH_2$), 3.4-3.6 (320H, $COOCH_2C\underline{H_2}$, and $NCOC\underline{H_2}CH_2CH_2$), 1.3-2.5 (560H, $NCOCH_2C\underline{H_2}C\underline{H_2}$ and $C\underline{H_2}C\underline{H}COO$). DMF GPC analysis indicated an M_n of 12 300 g mol^{-1} and an M_w/M_n of 1.15 when calibrated against a series of near-monodisperse poly(methyl methacrylate) standards. Targeting mean DPs above 150 required reaction times of up to 60 min for high conversion.

2.2.4 Preparation of PNAEP$_x$ Macro-CTA

The typical protocol for the synthesis of a PNAEP$_{62}$ macro-CTA by RAFT aqueous solution polymerisation is as follows: NAEP (10.00 g, 54.6 mmol), DDMAT RAFT agent (199.0 mg, 0.5458 mmol; target DP = 100) and AsAc (1.0 mg, 5.5 µmmol) were weighed into a 14 mL vial charged with a magnetic flea (reaction solution 1). This reaction solution was then placed in an ice bath and degassed with nitrogen for 30 min. Deionised water (6.8010 g, 60% w/w), and KPS (1.5 mg, 5.5 µmol; DDMAT/KPS molar ratio = 100) were weighed into a second 14 mL vial (reaction solution 2) and degassed with nitrogen in an ice bath for 30 min. After 30 min, the vial containing reaction solution 1 was immersed in an oil bath set at 30 °C. Reaction solution 2 was then added via a degassed syringe and needle to reaction solution 1 under nitrogen. The polymerisation was allowed to proceed for 8 min before exposing the reaction solution to air and immersing the vial in an ice bath to quench the polymerisation. ^{1}H NMR analysis of the disappearance of vinyl signals at 5.9 and 6.4 ppm relative to the integrated four ethyl protons at 3.4-3.8 ppm assigned to PNAEP indicated a monomer conversion of 50%. The crude homopolymer was purified by precipitating into a ten-fold excess of diethyl ether. This purification protocol was repeated twice to give a PNAEP macro-CTA containing < 1% residual monomer. Its mean degree of polymerisation was calculated to be 62 as judged by ^{1}H NMR spectroscopy (comparison of the integral at 3.4-3.8 ppm (m, 4H) with that assigned to the methyl RAFT chain-end at 0.86−0.96 ppm (t, 3H). ^{1}H NMR (in d_4-Methanol, δ): 1.6 (3H, CH_3 of methyl RAFT chain-end), 4.1-4.3 (190H, $COOCH_2CH_2$), 3.4-3.6 (380H, $COOCH_2C\underline{H_2}$, and $NCOC\underline{H_2}CH_2CH_2$), 1.3-2.5 (665H, $NCOCH_2C\underline{H_2}C\underline{H_2}$ and $C\underline{H_2}C\underline{H}COO$). DMF GPC analysis indicated an M_n of 9 800 g mol^{-1} and an M_w/M_n of 1.25 when calibrated against a series of near-monodisperse poly(methyl methacrylate) standards. Other $PNAEP_x$ homopolymers were obtained by adjusting the NAEP/DDMAT molar ratio.

2.2.5 Synthesis of $PNAEP_{62}$−$PHEA_x$ Diblock Copolymers via RAFT Aqueous Solution Polymerisation of HEA at 30 °C

A typical protocol used for the synthesis of the $PNAEP_{62}$-$PHEA_{100}$ diblock copolymer was as follows: $PNAEP_{62}$ macro-CTA (0.250 g, 21.3 µmol), HEA (0.2476 g, 2.1324 mmol; target DP = 100) and AsAc (0.8 mg, 4.3 µmol; $PNAEP_{62}$ macro-CTA) were weighed into a 14 mL vial charged with a magnetic flea (reaction solution 1). This vial was immersed in an ice bath and the solution was degassed with nitrogen for 30 min. Deionised water (2.2306 g, corresponding to a 15% w/w solution) and KPS (1.2 mg, 4.3 µmol; $PNAEP_{62}$ macro-CTA/KPS molar ratio = 5.0) were weighed into a separate 14 mL vial (reaction solution 2) and degassed with nitrogen in an ice bath for 30 min. Reaction solution 1 was then immersed in an oil bath set at 30 °C. Reaction solution 2 was added to this vial via a degassed syringe and needle under nitrogen. The polymerisation was allowed to proceed for 18 h before being quenched by exposing the reaction solution to air and immersing the reaction vial in an ice bath. ^{1}H NMR studies indicated more than 99% conversion while DMF GPC analysis indicated a M_n of 29 400 g mol^{-1} and an M_w/M_n of 1.22 when calibrated against a series of near-monodisperse poly(methyl methacrylate) standards. Other diblock copolymer compositions were obtained by adjusting the HEA/$PNAEP_{62}$ molar ratio to target PHEA DPs of 50 to 400.

2.2.6 Synthesis of $PNAEP_{71}$−$POEGA_x$ Diblock Copolymers via RAFT Aqueous Solution Polymerisation of OEGA at 30 °C

A typical protocol used for the synthesis of the $PNAEP_{71}$-$POEGA_{40}$ diblock copolymer was as follows: $PNAEP_{71}$ macro-CTA (0.250 g, 21.3 µmol), OEGA (0.3872 g, 853 µmol; target DP = 40) and AsAc (0.8 mg, 4.3 µmol) were weighed into a 14 mL vial charged with a magnetic flea (reaction solution 1). This vial was placed in an ice bath and the solution was degassed with nitrogen for 30 min. Deionised water (2.3066 g, corresponding to a 20% w/w solution), and KPS (1.2 mg, 4.3 µmol; PNAEP71 macro-CTA/KPS molar ratio = 5.0) were weighed into a separate 14 mL vial (reaction solution 2) and degassed with nitrogen using an ice bath for 30 min. Reaction solution 1 was immersed in an oil bath set at 30 °C. Reaction solution 2 was then added to this vial via a degassed syringe and needle under nitrogen. ^{1}H NMR studies indicated more than 99% conversion while DMF GPC analysis indicated an M_n of 20 400 g mol^{-1} and an M_w/M_n of 1.27 when calibrated against a series of near-monodisperse poly(methyl methacrylate) standards. Other diblock copolymer compositions were obtained by adjusting the OEGA/PNAEP$_{71}$ macro-CTA molar ratio to give target POEGA DPs ranging from 50 to 400.

2.2.7 Synthesis of PNAEP$_{95}$−PNIPAM$_x$ Diblock Copolymers via RAFT Aqueous Solution Polymerisation of NIPAM at 22 °C using a PNEAP$_{95}$ Macro-CTA

A typical protocol used for the synthesis of the PNAEP$_{95}$−PNIPAM$_{100}$ diblock copolymer was as follows: PNAEP$_{95}$ macro-CTA (0.250 g, 14.1 µmol), NIPAM (0.159 g, 141 µmol; target DP = 100), and AsAc (0.50 mg, 2.8 µmol) were weighed into a 14 mL vial charged with a magnetic flea (reaction solution 1). This vial was placed in an ice bath, and the solution was degassed with nitrogen for 30 min. Deionised water (1.6393 g, corresponding to a 20% w/w solution) and KPS (0.76 mg, 2.8 µmol; PNAEP$_{95}$ macro-CTA/KPS molar ratio = 5.0) were weighed into a separate 14 mL vial (reaction solution 2) and degassed with nitrogen using an ice bath for 30 min. Reaction solution 1 was immersed in an oil bath set at 22 °C. Reaction solution 2 was then added to this vial via a degassed syringe and needle under nitrogen. ^{1}H NMR studies indicated more than 99% conversion while DMF GPC analysis yielded an M_n of 20 400 g mol^{-1} and an M_w/M_n of 1.21 when calibrated against a series of near-monodisperse poly(methyl methacrylate) standards. Other diblock copolymer compositions were obtained by adjusting the NIPAM/PNAEP$_{95}$ macro-CTA molar ratio to give target PNIPAM DPs ranging from 100 to 300.

2.2.8 Preparation of PDEA$_{99}$ Macro-CTA

A typical protocol used for the synthesis of the PDEA$_{99}$ homopolymer was as follows: DEA (10.00 g, 54.0 mmol), MPETTC RAFT agent (244.1 mg, 0.540 mmol; target

DP = 100), ACVA (50.4 mg, 180 μmol; MPETTC/ACVA molar ratio = 3.0), and THF (6.86 g, corresponding to a 60% w/w solution) were weighed into a 50 mL round-bottom flask charged with a magnetic flea. This flask was placed in an ice bath and degassed with nitrogen for 30 min before being immersed in an oil bath set at 70 °C. The polymerisation was allowed to proceed for 190 min, affording a monomer conversion of 95% as judged by ^{1}H NMR. The crude homopolymer was purified by precipitation into a ten-fold excess of mildly alkaline water (pH 10). This neutral PDEA homopolymer was then dried under vacuum before being protonated using an aqueous solution of 1.0 M HCl. The fully protonated PDEA homopolymer was isolated in its HCl salt via precipitation into a ten-fold excess of acetone. This homopolymer was then dried in a vacuum oven to afford a PDEA macro-CTA containing less than 1% residual monomer. Its mean degree of polymerisation was determined to be 99 by ^{1}H NMR spectroscopy. ^{1}H NMR (in D_2O, δ): 6.8-7.0 (5H, C_6H_5 of aromatic RAFT chain-end), 4.1-4.3 (199H, $COOC\underline{H_2}CH_2NH$), 3.2-3.5 (594H, $COOCH_2C\underline{H_2}NH(C\underline{H_2}CH_3)_2$), 1.3-1.5 (594H, $COOCH_2CH_2NH(CH_2C\underline{H_3})_2$). Chloroform GPC analysis indicated an M_n of 10 800 g mol^{-1} and an M_w/M_n of 1.24 when calibrated against a series of near-monodisperse poly(methyl methacrylate) standards.

2.2.9 Synthesis of PDEA$_{99}$−PNAEP$_y$ Diblock Copolymers via RAFT Aqueous Solution Polymerisation of NAEP at 30% w/w Solids using a PDEA$_{99}$ Macro-CTA at pH 2

A typical protocol used for the synthesis of the PDEA$_{99}$−PNAEP$_{100}$ diblock copolymer via RAFT aqueous solution polymerisation of NAEP was as follows: PDEA$_{99}$ macro-CTA (200 mg, 10.5 μmol), NAEP (190 mg, 1.054 mmol; target DP = 100), and AsAc (0.37 mg, 2.1 μmol) were weighed into a 14 mL vial charged with a magnetic flea (reaction solution 1). This vial was immersed in an ice bath and degassed with nitrogen for 30 min. Dilute aqueous HCl (0.001 M, 1.12 g) and KPS (57 mg, 2.1 μmol; PDEA$_{99}$ macro-CTA/KPS molar ratio = 5.0) were weighed into a separate 14 mL vial (reaction solution 2; final pH 2), which was immersed in an ice bath and degassed with nitrogen for 30 min. The vial containing reaction solution 1 was then immersed in an oil bath set at 30 °C. Reaction solution 2 was added to this vial using a degassed syringe/needle under nitrogen to afford a final solution at pH 2 targeting 30% w/w solids. ^{1}H NMR studies indicated that an NAEP conversion of 99% was achieved after 120 min. DMF GPC analysis indicated an M_n of 39 500 g mol^{-1} and an M_w/M_n of 1.27 when calibrated against a series of near-monodisperse poly(methyl methacrylate) standards.. Other diblock copolymer compositions were obtained by adjusting the NAEP/PDEA$_{99}$ macro-CTA molar ratio to give target PNAEP DPs ranging from 50 to 100.

2.2.10 Copolymer Characterisation

^{1}H NMR Spectroscopy. All ^{1}H NMR spectra were recorded in *d*$_4$-methanol using a 400 MHz Bruker AVANCE-400 spectrometer with 64 scans being averaged per spectrum.

Gel Permeation Chromatography. The molecular weights and dispersities of the homopolymers series and diblock copolymers were determined by using an Agilent 1260 Infinity set-up comprising two Polymer Laboratories PL gel 5 μm Mixed-C columns and a refractive index detector operating at 60 °C. The mobile phase was HPLC-grade DMF containing 10 mmol LiBr at a flow rate of 1.0 mL min^{-1}. Ten PMMA standards (M_n = 625 to 618 000 g mol^{-1}) were used for calibration. The molecular weight and dispersity of the PDEA$_{99}$ homopolymer was determined by using an Agilent 1260 Infinity set-up comprising two Polymer Laboratories PL gel 5 μm Mixed-C columns and a refractive index detector operating at 35 °C. The mobile phase was HPLC grade chloroform containing 0.25% v/v TEA at a flow rate of 1.0 mL min^{-1}. Ten near-monodisperse poly(methyl methacrylate) standards (PMMA; M_n = 625 to 618 000 g mol^{-1}) were used for calibration. The molecular weights and dispersities of the PDEA$_{99}$−PNAEP$_y$ diblock copolymers were determined by using an Agilent 1260 Infinity set-up comprising two Polymer Laboratories PL gel 5 μm Mixed-C columns and a refractive index detector operating at 60 °C. The mobile phase was HPLC-grade chloroform containing 0.25% v/v TEA and 10 mmol LiBr at a flow rate of 1.0 mL min^{-1}. Ten near-monodisperse poly(methyl methacrylate) standards (PMMA; M_n = 625 to 618 000 g mol^{-1}) were used for calibration.

Differential Scanning Calorimetry. Glass transition temperatures for four PNAEP homopolymers were determined using a Pyris 1 Perkin-Elmer differential scanning calorimeter operating over a temperature range from –30 to 70 °C at a rate of 10 °C min^{-1}. Each 10 mg sample was freeze-dried and subsequently dried for 24 h in a vacuum oven prior to analysis. Dried samples were hermetically sealed in a vented aluminium pan, and the instrument was calibrated for heat flow and temperature using both indium and zinc standards. Two heating−cooling cycles were performed: the first cycle ensured removal of residual water and the glass transition temperature was determined during the second cycle.

Visible Absorption Spectroscopy. Spectra were recorded from 400 to 800 nm for 1.0% w/w aqueous solutions of various PNAEP and PNMEP homopolymers between 20 and 80 °C at 5 °C increments using a Shimadzu UV-1800 spectrometer. A reduction in transmittance at 600 nm indicated the lower critical solution temperature (LCST) of the polymer, if applicable.

Dynamic Light Scattering. DLS studies were conducted using a Malvern Instruments Zetasizer Nano series instrument equipped with a 4 mW He−Ne laser (λ = 633 nm) and an avalanche photodiode detector. Scattered light was detected at 173°. Intensity-average hydrodynamic diameters were calculated via the Stokes−Einstein equation.

2.3 Results and Discussion

2.3.1 Synthesis and characterisation of PNAEP$_x$ precursors synthesised via RAFT aqueous solution polymerisation at 30 °C

RAFT polymerisations of methacrylic monomers are often more well-controlled compared to their acrylic counterparts, since the latter tend to undergo chain transfer to polymer.[54,55] In an attempt to optimise the RAFT homopolymerisation of NAEP in water, kinetic studies were conducted using a low temperature redox initiator at 30 °C or AIBN initiator at 70 °C (see Scheme 2.4 and Figure 2.6). In both cases, DDMAT was chosen as the trithiocarbonate-based CTA, and a mean DP of 200 was targeted. The *hydrophobic* DDMAT CTA is perhaps sub-optimal for aqueous systems but was chosen as it is commercially available and is one of the few CTAs synthesised on a multi-kilo scale. A relatively high NAEP concentration of 60% w/w was selected to solubilise the hydrophobic DDMAT. It was envisaged that the low-temperature redox initiator system would confer various benefits, including fewer side reactions, minimal induction periods, and greater RAFT control.[56]

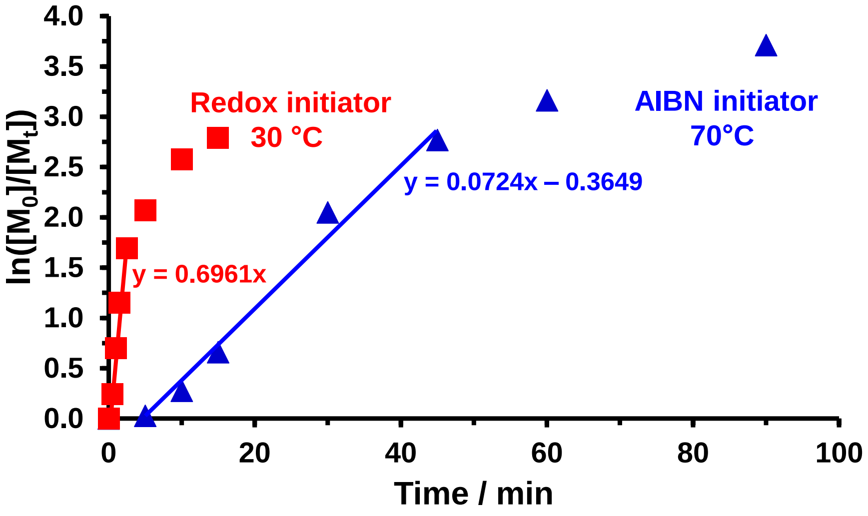

Figure 2.6. Semilogarithmic plots obtained for the RAFT aqueous solution polymerisation of NAEP using a DDMAT/initiator molar ratio of 5.0 where the initiator is either AIBN (triangles) at 70 °C or KPS/AsAc (squares) at 30 °C. Target degree of polymerisation = 200 at 60% w/w solids. Equations indicate the initial gradients associated with each plot, which are proportional to the respective initial rates. Clearly, there is almost an order of magnitude difference in the initial rate for these two RAFT aqueous solution polymerisation formulations.

Aliquots of each reaction mixture were taken at regular intervals, and monomer conversions were determined by ^{1}H NMR analysis. When using AIBN at 70 °C, more than 95% NAEP conversion was achieved within 60 min, despite a brief induction period. Remarkably, NAEP polymerisations conducted using the redox initiator at 30 °C proceeded to more than 90% conversion within just 5 min with no discernible induction period. Moreover, comparing the initial gradients of the linear regions of the respective semilogarithmic plots indicated that the rate of polymerisation at 30 °C was an order of magnitude faster than that at 70 °C (see Figure 2.6).

DMF GPC was used to monitor the evolution of molecular weight during the RAFT aqueous solution polymerisation of NAEP at either 30 °C or 70 °C (Figure 2.7). In both cases, relatively high dispersities (M_w/M_n > 1.30) were observed during the initial stages (below 40% conversion). Exotherms of up to 25 °C were observed during RAFT syntheses conducted at 30 °C (see Figure 2.8), and the polymerising solutions became highly viscous, with transparent yellow gels being obtained at high conversions when performing such syntheses at 60% w/w. Perhaps surprisingly, relatively low final dispersities (M_w/M_n < 1.20) were observed for both PNAEP$_{200}$ homopolymers, despite the much faster rate of polymerisation achieved at 30 °C.

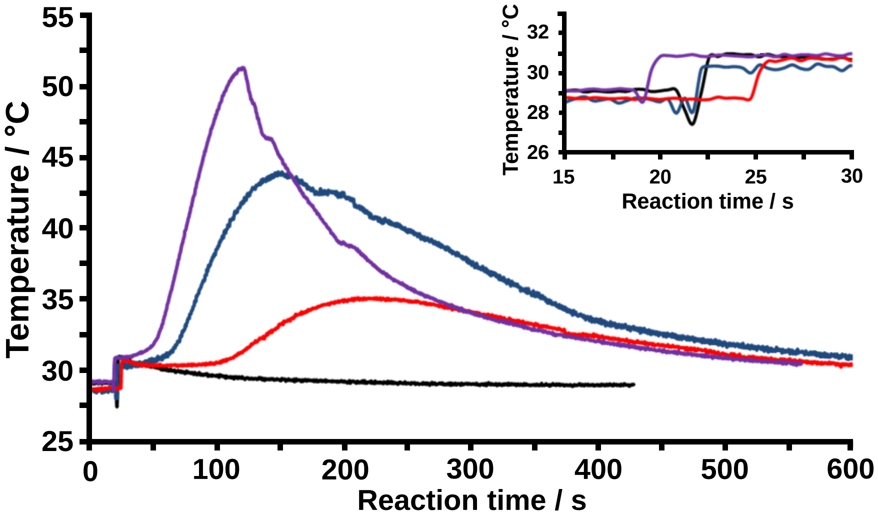

Figure 2.7. Temperature vs. reaction time plots for the RAFT aqueous homopolymerisation of NAEP targeting a DP of 200 using DDMAT/KPS molar ratios of 5.0 (purple), 50.0 (blue) and 100.0 (red). The black data set represents the control experiment where the two reaction solutions were added in the absence of any initiator. Inset shows the initial temperature change when the two reaction solutions were combined.

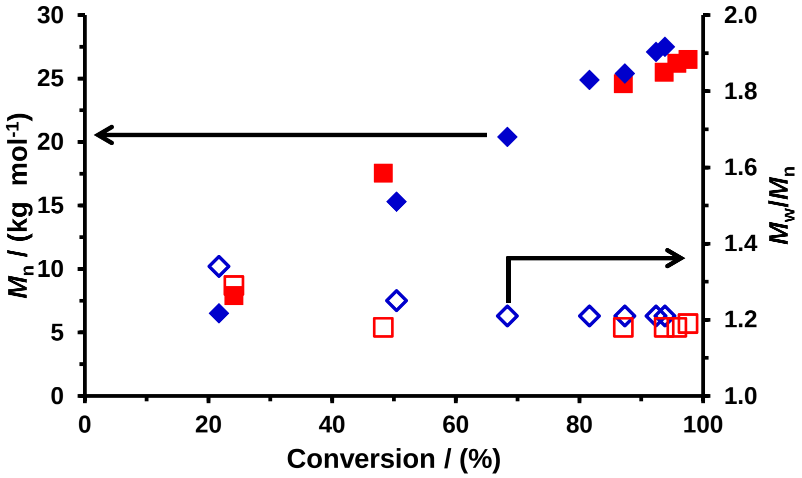

Figure 2.8. Evolution of M_n (filled symbols) and M_w/M_n (open symbols) vs conversion for the RAFT aqueous solution polymerisation of $PNAEP_{200}$ homopolymer at either 30 °C (diamonds) or 70 °C (squares). In both cases, the DDMAT/initiator molar ratio was 5.0 (GPC protocol: DMF eluent; refractive index detector; calibration against a series of near-monodisperse PMMA standards).

To examine whether the RAFT polymerisation of NAEP was well-controlled, a series of PNAEP homopolymers were prepared targeting a range of DPs using either

AIBN or the low-temperature redox initiator (see Table 2.1). A DDMAT/ initiator molar ratio of 5.0 was used for each of these homopolymerisations. DMF GPC analysis was used to determine the M_n and M_w/M_n values in each case. ^{1}H NMR analysis indicated that high NAEP conversions (≥ 98%) were achieved using either AIBN at 70 °C or the redox initiator at 30 °C when targeting PNAEP DPs of up to 120 or 400, respectively. These results represent a substantial improvement over the data previously reported by Shi et al., who reported 77% conversion within 35 min at 25 °C for the visible light-mediated RAFT aqueous solution polymerisation of NAEP at 50% w/w at pH 2.6.[33] DMF GPC analysis indicated that the M_n values for the final PNAEP$_x$ homopolymers increased linearly with the target DP, as expected. Moreover, monomodal GPC traces and narrow molecular weight distributions (M_w/M_n < 1.20) were observed in all cases (see Figure 2.9).

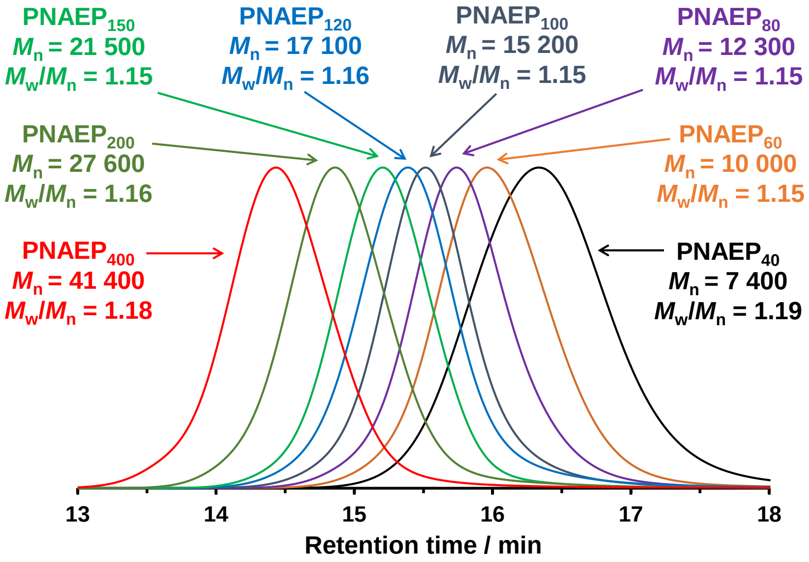

Figure 2.9. DMF GPC curves obtained for a series of PNAEP$_x$ homopolymers prepared via RAFT solution polymerisation of NAEP using KPS/AsAc redox initiator at 30 °C (calibrated against a series of near-monodisperse poly(methyl methacrylate) standards).

As discussed above for PNAEP syntheses targeting a DP of 200, the faster rate of polymerisation achieved at 30 °C did not adversely affect RAFT control over these polymerisations, with M_w/M_n remaining less than 1.20 up to DP 400. Thus, the low-temperature redox initiator route was adopted for all subsequent RAFT syntheses. When targeting DPs above 400, reaction solutions became very viscous when using 60% w/w NAEP, which led to significantly lower conversions (< 80%; see Table 2.1).

Recently, Cunningham and co-workers reported that PNMEP homopolymers exhibited inverse temperature solubility behaviour in aqueous solution.[38] The lower critical solution temperature (LCST) or cloud point can be monitored by turbidimetry. For example, a 1.0% w/w aqueous solution of PNMEP_{55} becomes turbid (i.e. has reduced transmittance) when heated to 62 °C (see Figure 2.10).[57] In striking contrast, a 1.0% w/w aqueous solution of PNAEP_{55} exhibits no LCST behaviour and remains fully water-soluble up to at least 90 °C (see Figure 2.10). Clearly, the acrylic analogue is significantly more hydrophilic, which is not unexpected. This is important because it means that such PNAEP_x homopolymers should enable the convenient preparation of a range of new double-hydrophilic pyrrolidone-based diblock copolymers in aqueous solution. This possibility is explored below.

Table 2.1. Summary of target PNAEP DP, conversions, molecular weights (M_n), and dispersities (M_w/M_n) obtained for PNAEP homopolymers prepared by RAFT aqueous solution polymerisation of NAEP at either 30 °C (low-temperature redox initiator) or 70 °C (AIBN) at 60% w/w solids.

Target PNAEP DP	Conversion / %	Temperature / °C	M_n / g mol^{-1}	M_w/M_n
PNAEP_{40}	99	70	7 600	1.13
PNAEP_{60}	99	70	11 200	1.13
PNAEP_{80}	99	70	13 300	1.14
PNAEP_{100}	99	70	15 700	1.19
PNAEP_{120}	99	70	19 300	1.15
PNAEP_{40}	99	30	7 400	1.19
PNAEP_{60}	99	30	10 000	1.15
PNAEP_{80}	99	30	12 300	1.15
PNAEP_{100}	98	30	15 200	1.15
PNAEP_{120}	98	30	17 100	1.16
PNAEP_{150}	99	30	21 500	1.15
PNAEP_{200}	99	30	27 600	1.16
PNAEP_{400}	99	30	41 400	1.18
PNAEP_{750}	75	30	74 600	1.26
PNAEP_{1000}	70	30	115 400	1.28

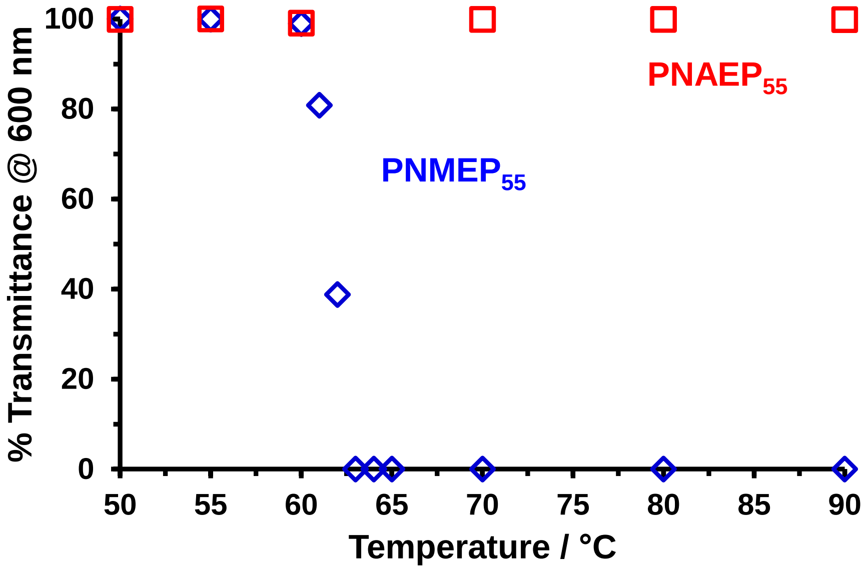

Figure 2.10. % Transmittance (at 600 nm) vs temperature plot recorded for a 1.0% w/w aqueous solution of a $PNMEP_{55}$ homopolymer (blue diamonds) compared to that for a 1.0% w/w aqueous solution of a $PNAEP_{55}$ homopolymer (red squares). $PNMEP_{55}$ has an LCST at 62 °C, whereas the more hydrophilic $PNAEP_{55}$ exhibits no discernible LCST behaviour over this temperature range.

Glass transition temperatures (T_g) for four $PNAEP_x$ homopolymers prepared via RAFT aqueous solution polymerisation of NAEP utilising the low-temperature redox initiator were determined using differential scanning calorimetry (DSC) for DPs ranging between 50 and 400. This technique indicated T_g values below room temperature for mean DPs of less than 400 (see Figure 2.11). A T_g of ~19.6 °C was obtained for a $PNAEP_{400}$ homopolymer, which appears to lie close to the T_g for the high molecular weight limit.[58] Such T_g values are significantly lower than those of PNMEP and suggest that the film-forming properties of PNAEP homopolymer at ambient temperature may be of potential commercial interest. Such films should couple the well-known highly biocompatible nature of PNVP films (which are used in numerous commercial applications such as, hair-care products and also as a main component of contact lenses)[59] and its non-ionic character to make effective anti-fouling films.[3]

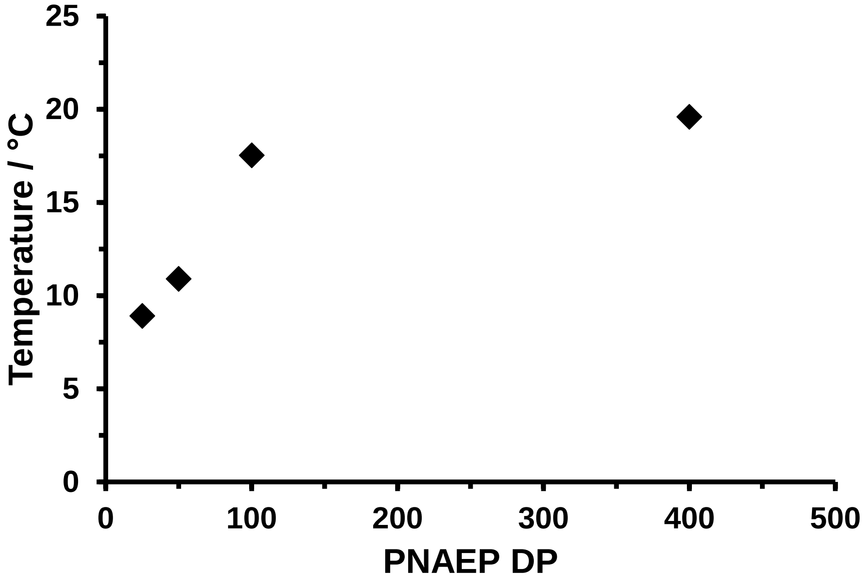

Figure 2.11. Variation of glass transition temperature with PNAEP DP for four $PNAEP_x$ homopolymers prepared via RAFT aqueous solution polymerisation of NAEP at 30 °C.

2.3.2 RAFT Aqueous Solution Polymerisation of either HEA or OEGA at 30 °C using a $PNAEP_x$ Macro-CTA.

A $PNAEP_{62}$ macro-CTA was prepared via RAFT aqueous solution polymerisation of NAEP at 30 °C using a DDMAT/KPS molar ratio of 100 and targeting a DP of 100. This much higher CTA/initiator molar ratio was selected in view of the relatively fast rate of polymerisation observed for a CTA/initiator molar ratio of 5.0 and was designed to ensure maximum RAFT end-group fidelity. The resulting macro-CTA was purified via successive precipitation into excess diethyl ether. ^1H NMR end-group analysis of the methyl proton signals assigned to the RAFT chain-ends indicated a mean DP of 62. Given the final NAEP conversion of 50%, this indicates a RAFT agent efficiency of 81%. DMF GPC analysis indicated an M_n of 9800 g mol^{-1} and a relatively narrow molecular weight distribution ($M_w/M_n < 1.25$). This $PNAEP_{62}$ macro-CTA was subsequently used to prepare a series of $PNAEP_{62}-PHEA_x$ diblock copolymers via RAFT aqueous solution polymerisation of HEA (see Scheme 2.5a) targeting PHEA DPs of between 50 and 400. A DDMAT/KPS molar ratio of 5.0 was used in all cases. ^1H NMR studies indicated that high HEA conversions (> 99%) were achieved within 18 h. Furthermore, DMF GPC analysis of the resulting $PNAEP_{62}-PHEA_x$ diblock copolymers indicated a linear increase in M_n with increasing PHEA DP (Figure 2.12a). Relatively low dispersities ($M_w/M_n < 1.35$) were obtained for all $PNAEP_{62}-PHEA_x$ diblock copolymers. Moreover, comparison with the GPC trace recorded for the PNAEP$_{62}$ macro-CTA confirmed high blocking efficiencies in each case.

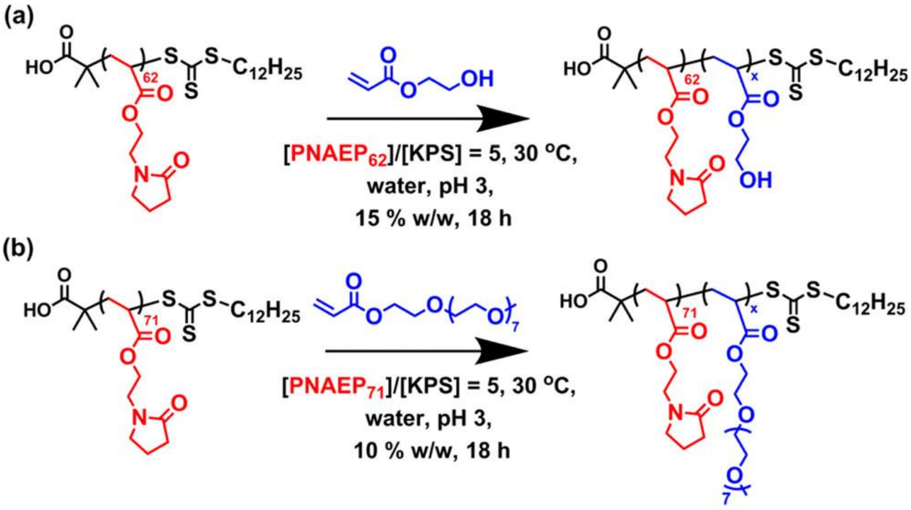

Scheme 2.5. Synthesis of (a) PNAEP$_{62}$−PHEA$_{x}$ diblock copolymers and (b) PNAEP$_{71}$−POEGA$_{x}$ diblock copolymers by RAFT aqueous solution polymerisation of either HEA or OEGA at 30 °C.

A second batch of PNAEP$_{71}$ macro-CTA was prepared via RAFT aqueous solution polymerisation using a similar protocol to that described above. In this case, ^{1}H NMR end-group analysis of the three methyl proton signals assigned to the RAFT chain end indicated a mean DP of 71 (59% conversion, CTA efficiency = 83%). DMF GPC analysis indicated an M_n of 11 200 g mol^{-1} and a M_w/M_n of 1.17. This PNAEP$_{71}$ macro-CTA was subsequently utilised for the RAFT aqueous solution polymerisation of OEGA, targeting POEGA DPs between 50 and 400 and using a DDMAT/KPS molar ratio of 5.0 (see Scheme 2.5b). OEGA conversions of at least 99% were achieved for all PNAEP$_{71}$−POEGA$_{x}$ diblock copolymers within 18 h at 30 °C, as judged by ^{1}H NMR. DMF GPC analyses of this series of PNAEP$_{71}$−POEGA$_{x}$ diblock copolymers indicated a monotonic increase in M_n with increasing POEGA DP, as expected. However, there is some discrepancy between the experimental and theoretical M_n values. Bearing in mind the brush-like nature of the POEGA block, this can be attributed to the PMMA standards used for GPC calibration. Nevertheless, relatively low dispersities (M_w/M_n < 1.30) were achieved for this PNAEP$_{71}$−POEGA$_{x}$ diblock copolymer series, which suggests good RAFT control. Moreover, comparison of the GPC traces obtained for these PNAEP$_{71}$−POEGA$_{x}$ diblock copolymers with that of the precursor PNAEP$_{71}$ macro-CTA indicated high blocking efficiencies (Figure 2.12b).

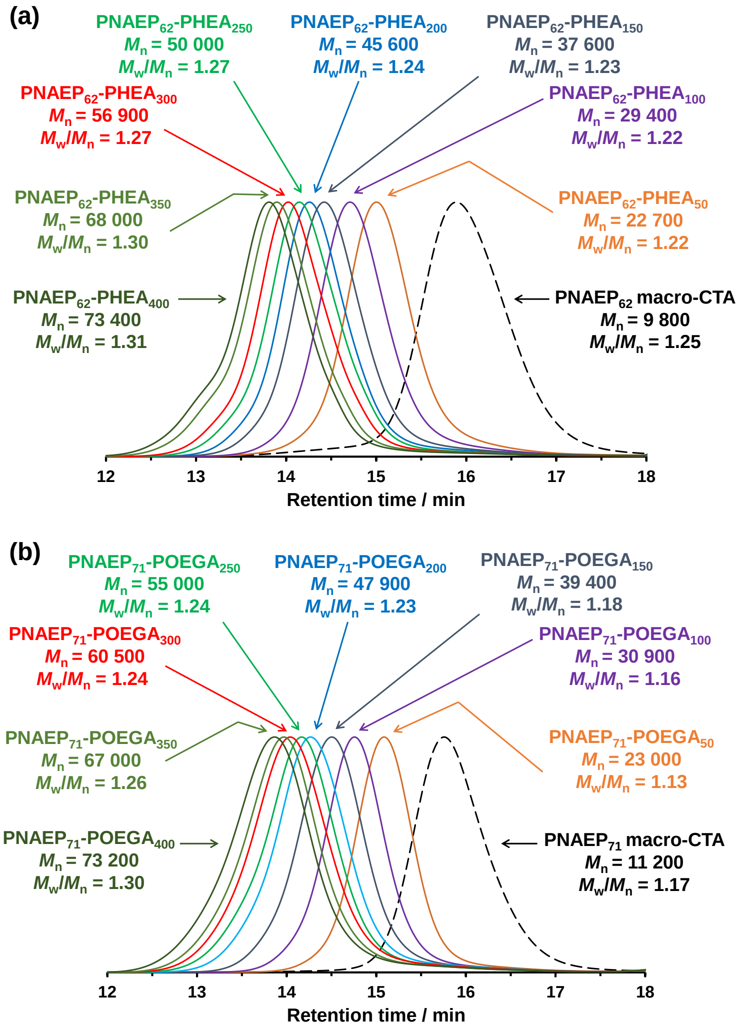

Figure 2.12. DMF GPC curves obtained for (a) a series of PNAEP$_{62}$−PHEA$_x$ diblock copolymers and the corresponding PNAEP$_{62}$ macro-CTA (dashed trace) and (b) a series of PNAEP$_{71}$−POEGA$_x$ diblock copolymers and the corresponding PNAEP$_{71}$ macro-CTA (dashed trace).

2.3.3 RAFT Aqueous Solution Polymerisation of NIPAM at 22 °C using a PNAEP$_{95}$ Macro-CTA.

A third batch of PNAEP$_{95}$ macro-CTA was prepared via RAFT aqueous solution polymerisation. In this case, ^{1}H NMR spectroscopy end-group analysis of the three methyl proton signals assigned to the RAFT chain-end indicated a mean DP of 95 (target DP = 150, 51% conversion, CTA efficiency = 81%). DMF GPC analysis indicated an M_n of 13 800 g mol^{-1} and a M_w/M_n of 1.21. This PNAEP$_{95}$ macro-CTA was subsequently utilised for the RAFT aqueous solution polymerisation of NIPAM, targeting PNIPAM DPs between 100 and 300 and using a PNAEP$_{95}$/KPS molar ratio of 5.0 (see Scheme 2.6). The RAFT polymerisation of NIPAM was conducted in an oil bath set to 22 °C, which is below the LCST of PNIPAM homopolymer.[60–63] NIPAM conversions of at least 99% were achieved for all $PNAEP_{95}-PNIPAM_x$ diblock copolymers within 1 h at this temperature, as judged by ^1H NMR studies conducted in D_2O.

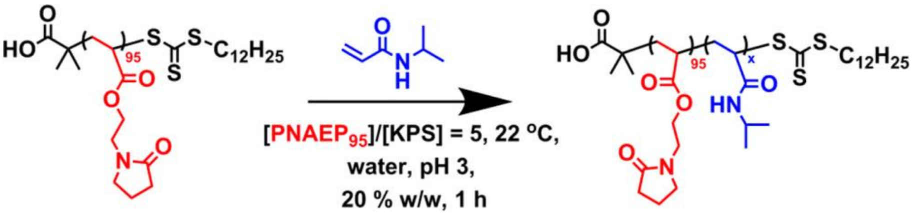

Scheme 2.6. Synthesis of a series of $PNAEP_{95}-PNIPAM_x$ diblock copolymers by RAFT aqueous solution polymerisation of NIPAM at 22 °C using a $PNAEP_{95}$ precursor. A low-temperature redox initiator (KPS/AsAc molar ratio = 1.0) was utilised and the $PNAEP_{95}$/initiator molar ratio was 5.0.

DMF GPC analysis of this series of $PNAEP_{95}-PNIPAM_x$ diblock copolymers indicated a monotonic increase in M_n with increasing PNIPAM DP. Relatively low dispersities ($M_w/M_n < 1.40$) were observed in all cases, indicating reasonably good RAFT control. Moreover, comparison of the GPC traces obtained for these $PNAEP_{95}-PNIPAM_x$ diblock copolymers with that of the corresponding $PNAEP_{95}$ macro-CTA indicated relatively high blocking efficiencies (Figure 2.13).

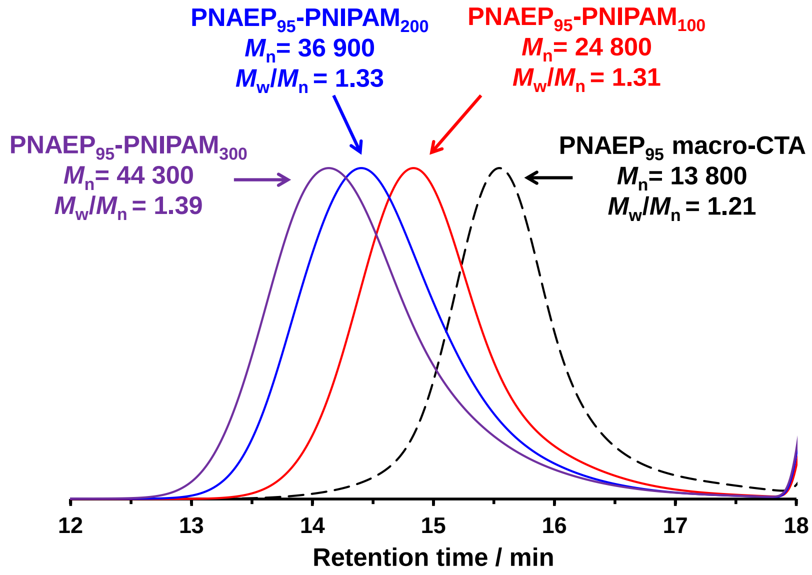

Figure 2.13. DMF GPC curves obtained for a series of three $PNAEP_{95}$−$PNIPAM_x$ diblock copolymers and the corresponding $PNAEP_{95}$ macro-CTA (dashed trace). The NIPAM conversion was more than 99% for each of the three diblock copolymers.

PNIPAM is a well-known thermoresponsive polymer that exhibits LCST behaviour in aqueous solution at around 32 °C.[60–63] Thus, proton signals assigned to the PNAEP and PNIPAM blocks are observed when inspecting a ^{1}H NMR spectrum recorded for the $PNAEP_{95}$−$PNIPAM_{200}$ diblock copolymer in D_2O at 20 °C (see Figure 2.14a). However, on heating this copolymer solution up to 50 °C, the PNIPAM chains become substantially desolvated. This leads to attenuation of all the PNIPAM signals (Figure 2.14b). On the other hand, all the PNAEP signals remain well-solvated under these conditions. Variable temperature ^{1}H NMR studies indicated that the two methyl signals assigned to the pendent isopropyl group of PNIPAM (labelled *d′* in Figure 2.14) become substantially attenuated between 34 and 36 °C (Figure 2.14c), suggesting reduced chain mobility owing to dehydration. These spectral changes are consistent with *in situ* self-assembly of the diblock copolymer chains to form PNIPAM-core micelles.

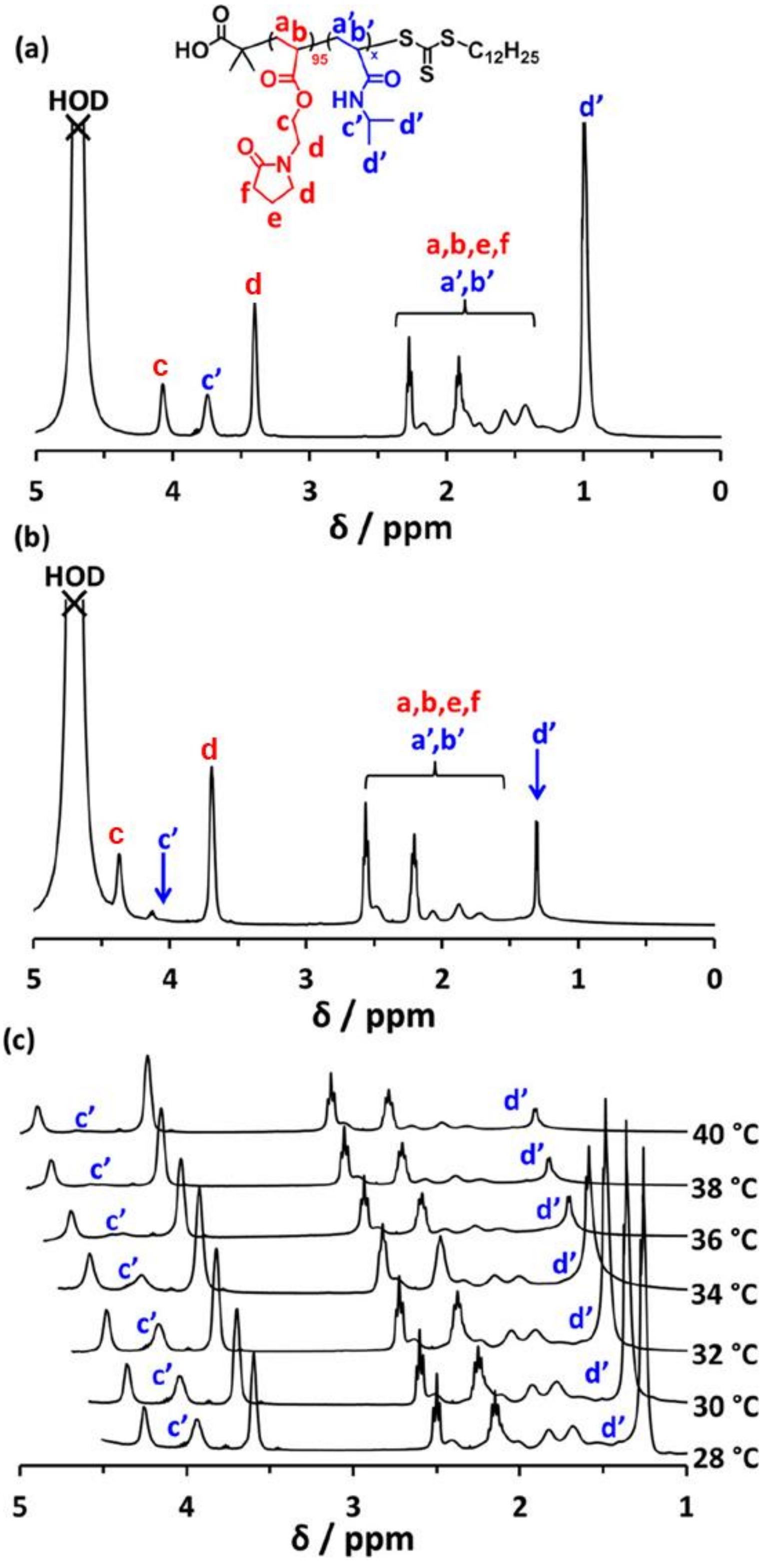

Figure 2.14. ^{1}H NMR spectra recorded for a $PNAEP_{95}$−$PNIPAM_{200}$ diblock copolymer in D_2O at (a) 20 °C (upper spectrum), (b) 50 °C (middle spectrum), and (c) between 28 and 40 °C.

DLS was utilised to gain further evidence for such micellar self-assembly. A 0.10% w/w $PNAEP_{95}-PNIPAM_{200}$ solution was monitored between 25 and 50 °C. The weak light scattering, and relatively small hydrodynamic diameter observed at 25 °C indicated that this copolymer existed as molecularly dissolved chains at this temperature (see Figure 2.15). On heating this copolymer solution, relatively large, ill-defined aggregates are obtained at around 35 °C, before well-defined near-monodisperse spherical nanoparticles (*z*-average diameter = 51 nm; PDI = 0.006) are formed above ~40 °C, which is in good agreement with the variable temperature ^1H NMR spectra shown in Figure 2.14c. Similar examples of so-called anomalous micellisation have been reported in the literature.[62,64–66] In at least some cases, such observations have been attributed to homopolymer contamination by the more hydrophobic block.[62] At first sight, this hypothesis does not seem to be applicable in the present case because the PNAEP precursor block is more hydrophilic than the PNIPAM block. However, in principle, the RAFT mechanism can generate a low level of PNIPAM homopolymer impurity (in this case (i.e. at a $PNAEP_{95}$]/[KPS] molar ratio of 5.0) a theoretical maximum of 17% dead chains could be generated)[67] so this possible explanation cannot be excluded.

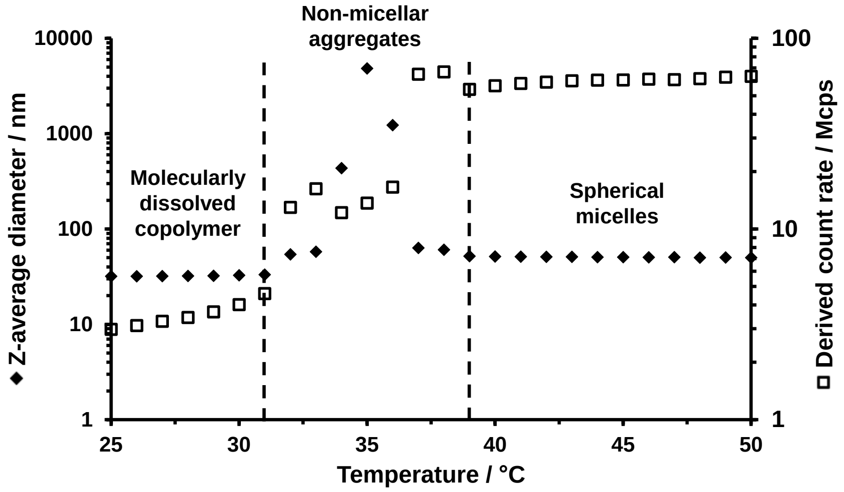

Figure 2.15. Variable temperature DLS studies of a 0.10% w/w aqueous solution of a $PNAEP_{95}-PNIPAM_{200}$ diblock copolymer at pH 3. Molecularly dissolved copolymer chains are obtained at 25 °C, anomalous micellisation occurs at around 35 °C, and well-defined, near-monodisperse micelles are formed above 40 °C. Such self-assembly is driven by the well-known thermoresponsive nature of the PNIPAM block, which exhibits inverse temperature solubility behaviour.

2.3.4 RAFT Aqueous Solution Polymerisation of NAEP at 30 °C using a $PDEA_{99}$ Macro-CTA.

A PDEA macro-CTA (target DP = 100) was prepared via RAFT solution polymerisation of DEA in THF at 70 °C using MPETTC (see Scheme 2.7a). MPETTC was chosen for its amine chemistry that will become protonated below its pK_a increasing its hydrophilicity. This precursor was purified via successive precipitation into a ten-fold excess of alkaline aqueous solution (pH 10) to afford a yellow gum, which was dried under vacuum before being dissolved in its protonated form using 1.0 M aqueous HCl. The resulting PDEA hydrochloride salt was isolated via precipitation into a ten-fold excess of acetone to yield a yellow powder. ^{1}H NMR studies indicated negligible residual monomer (< 1%), while end-group analysis based on the aromatic proton signals assigned to the MPETTC RAFT chain-ends indicated a mean DP of 99. Chloroform GPC analysis indicated a monomodal trace with an M_n of 10 800 g mol^{-1} and an M_w/M_n of 1.24 (see Table 2.2).

Table 2.2. Summary of molecular weight data, *z*-average diameters and DLS polydispersities (PDI) obtained for four $PDEA_{99}$-$PNAEP_y$ diblock copolymers prepared by RAFT aqueous solution polymerisation of NAEP at 30 °C (redox initiator at pH 2) at 30% w/w solids. The molecular weight data obtained for the $PDEA_{99}$ precursor prepared via RAFT solution polymerisation of DEA in THF at 70 °C using AIBN initiator at 60% w/w solids is included for comparison.

Polymer Composition	M_n / g mol^{-1}	M_w/M_n	Z-average diameter / nm	PDI
$PDEA_{99}$ macro-CTA	10 800[a]	1.24[a]	--	--
$PDEA_{99}$-$PNAEP_{50}$	19 100[b]	1.17[b]	99	0.07
$PDEA_{99}$-$PNAEP_{60}$	22 700[b]	1.16[b]	78	0.08
$PDEA_{99}$-$PNAEP_{75}$	27 900[b]	1.15[b]	55	0.07
$PDEA_{99}$-$PNAEP_{100}$	39 500[b]	1.27[b]	42	0.13

[a] Determined by chloroform (+ 0.25 v/v % TEA) GPC against a series of near-monodisperse PMMA calibration standards using a refractive index detector.

[b] Determined by DMF (+ 0.25 v/v % TEA) GPC against a series of near-monodisperse PMMA calibration standards using a refractive index detector.

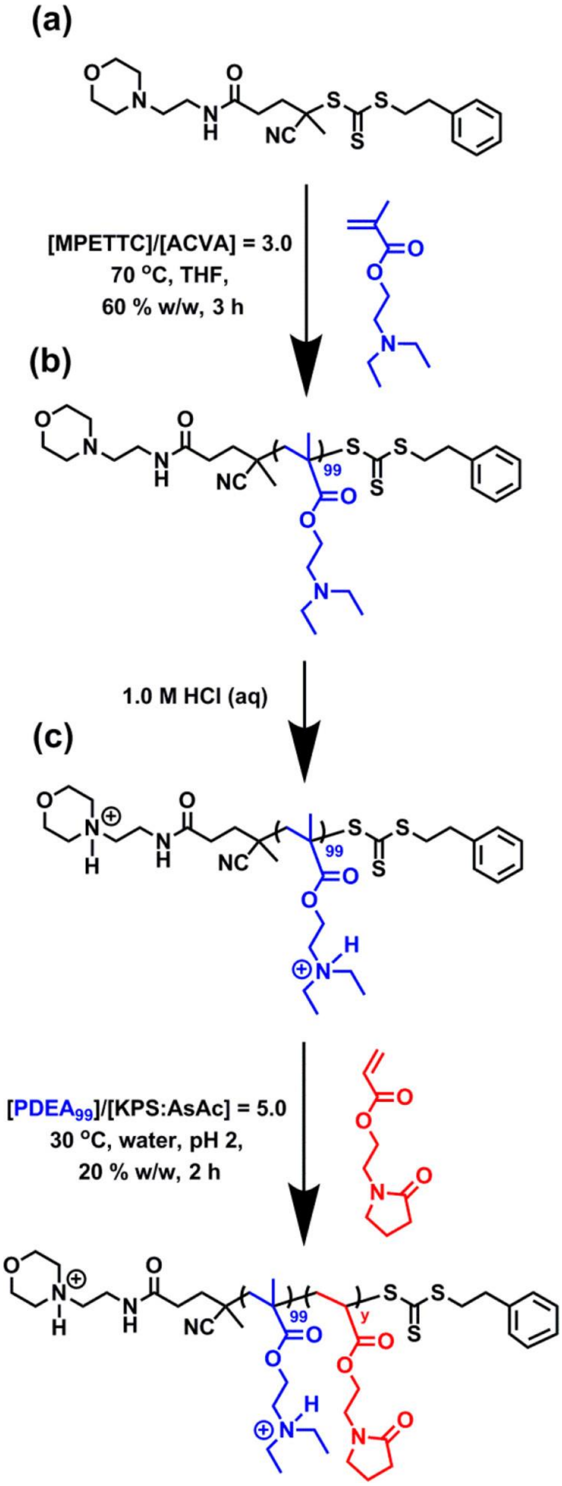

Scheme 2.7. Synthesis of (a) a $PDEA_{99}$ homopolymer by RAFT aqueous solution polymerisation of DEA at 70 °C in THF using a morpholine-based RAFT CTA; (b) Protonation of the $PDEA_{99}$ homopolymer precursor using 1.0 M HCl; (c) Synthesis of $PDEA_{99}$−$PNAEP_y$ diblock copolymers by RAFT aqueous solution polymerisation of NAEP at 30 °C using a protonated water-soluble $PDEA_{99}$ precursor and a macro-CTA/initiator molar ratio of 5.0 (KPS/AsAc molar ratio = 1.0)

This PDEA$_{99}$ macro-CTA was then utilised for the RAFT aqueous solution polymerisation of NAEP targeting a PNAEP DP of 50 to 100, as depicted in Scheme 2.7b. These syntheses were conducted in acidic aqueous solution to ensure that both blocks were fully water-soluble (with the protonated PDEA block being present in its cationic polyelectrolyte form, see Scheme 2.7c). ^{1}H NMR studies confirmed that high NAEP conversions (> 99%) were achieved in each case. Inspecting Table 2.2, DMF GPC analysis of this series of PDEA$_{99}$−PNAEP$_y$ diblock copolymers confirms that higher M_n values are obtained on increasing the target PNAEP DP from 50 to 100. A relatively low dispersity (M_w/M_n < 1.30) was observed for each PDEA$_{99}$−PNAEP$_y$ diblock copolymer, as expected. ^{1}H NMR studies were conducted on a PDEA$_{99}$−PNAEP$_{75}$ diblock copolymer in acidic aqueous solution (0.001 M DCl in D_2O, or pH 3; see Figure 2.16a).

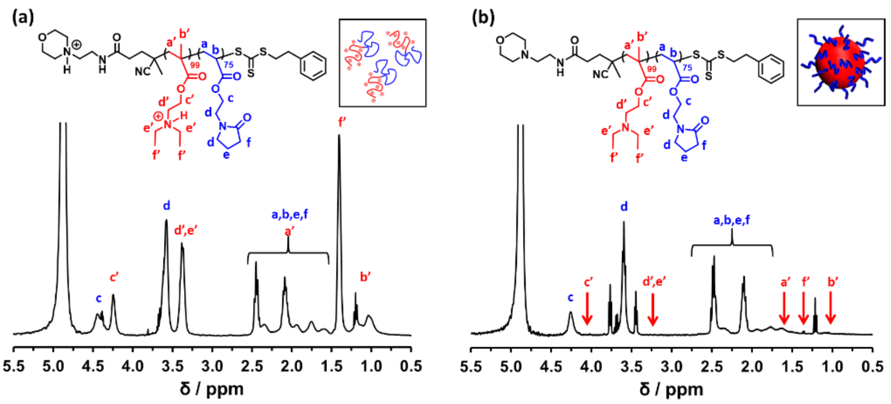

Figure 2.16. ^{1}H NMR spectra recorded for a PDEA$_{99}$−PNAEP$_{75}$ diblock copolymer at 25 °C: (a) in DCl/D_2O at pH 3 and (b) in NaOD/D_2O at pH 10. The inset is a schematic representation of (a) soluble PDEA$_{99}$−PNAEP$_{75}$ diblock copolymers at pH 3 and (b) PDEA-core micelles with the PNAEP chains acting as the stabiliser block at pH 10.

Under such conditions, all the tertiary amine groups in the PDEA block are protonated, and hence both blocks are fully solvated. Thus, all the expected ^{1}H NMR signals for both blocks are visible under such conditions (see Figure 2.16a). In particular, the six pendent methyl protons associated with the PDEA block are prominent between 1.20 and 1.50 ppm. On addition of sufficient NaOD, the PDEA$_x$ block (pK_a ~ 7.3) becomes completely deprotonated and hence hydrophobic.[68] This drives *in situ* self-assembly to form PDEA-core micelles with the PNAEP chains acting as the stabiliser block. Accordingly, the ^{1}H NMR signals associated with the de-solvated PDEA block are no longer visible (Figure 2.16b). The *z*-average micelle diameter is reduced from 100 to 40 nm for four PDEA$_{99}$−PNAEP$_y$ diblock copolymers as the DP (y) of the PNAEP block is increased from 50 to 100 (see Figure 2.17). This indicates lower micelle aggregation numbers when using longer stabiliser blocks, which is consistent with well-known theories of micellisation reported in the literature.[69,70]

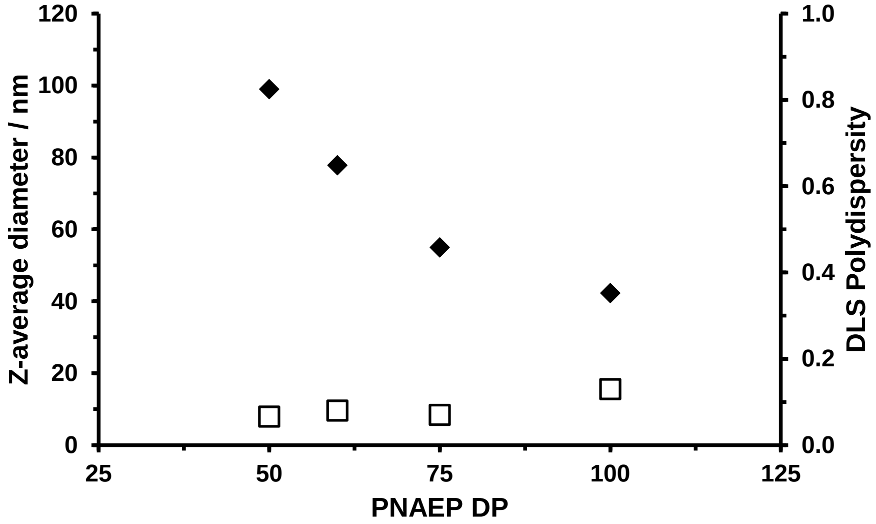

Figure 2.17. DLS studies for four PDEA$_{99}$−PNAEP$_y$ diblock copolymers (where y = 50−100) in dilute aqueous solution (0.1% w/w) at pH 10.

2.4 Conclusions

Water is an environmentally-friendly and cheap solvent and thus it is strongly preferred for industrial use. Accordingly, the RAFT aqueous solution polymerisation of NAEP using a trithiocarbonate-based CTA (DDMAT) enabled the preparation of a series of PNAEP$_x$ homopolymers with mean degrees of polymerisation varying from 40 to 400. Substituting a typical azo initiator for a low temperature redox initiator enabled the reaction temperature to be lowered from 70 to 30 °C while also reducing the reaction time from 60 to 5 min. GPC analyses indicated well-controlled RAFT polymerisations under these conditions (M_w/M_n ~ 1.20). Unlike the PNMEP homopolymers reported previously, these PNAEP$_x$ homopolymers do not possess LCST behaviour as judged by turbidimetry studies, which indicates that they are significantly more hydrophilic. High monomer conversions (≥ 99%) were obtained when targeting mean DPs between 40 and 400 at 60% w/w NAEP. DSC analysis indicated that PNAEP homopolymers with DPs of up to 400 exhibited glass transition temperatures below ambient temperature.

Using such trithiocarbonate-terminated PNAEP homopolymers as precursors, two series of PNAEP$_{62}$−PHEA$_x$ and PNAEP$_{71}$−POEGA$_x$ diblock copolymers were prepared via

RAFT aqueous solution polymerisation of either HEA or OEGA, respectively. High monomer conversions (≥ 99%) were achieved when targeting mean DPs between 50 and 400. DMF GPC analysis confirmed that relatively low dispersities ($M_w/M_n \leq 1.35$) and high blocking efficiencies were obtained for these two all-acrylic formulations, with monomodal GPC traces suggesting reasonably good RAFT control.

Two new classes of stimulus-responsive PNAEP-based diblock copolymers were also prepared. A series of thermoresponsive PNAEP_{95}−PNIPAM_x diblock copolymers were prepared via RAFT aqueous solution polymerisation of NIPAM at 22 °C, which is below the LCST of the PNIPAM block. Variable temperature DLS studies indicated the presence of relatively large, non-micellar aggregates between 32 and 39 °C prior to the formation of well-defined PNIPAM-core spherical micelles above 42 °C (51 nm; PDI = 0.006). Variable temperature ^{1}H NMR studies indicated that such self-assembly was accompanied by substantial desolvation of the PNIPAM block, as expected. Finally, a PDEA_{99} macro-CTA was chain-extended via RAFT aqueous solution polymerisation of NAEP at 30 °C. ^{1}H NMR studies confirmed that high conversions (≥ 99%) were achieved when targeting mean DPs of 50−100 and GPC studies indicated good RAFT control and low final dispersities ($M_w/M_n \leq 1.30$) in each case. Such PDEA_{99}−PNAEP_y diblock copolymers exhibited pH-responsive behaviour in aqueous solution. Molecular dissolution occurred at low pH, but spherical micelles comprising deprotonated PDEA cores were obtained at pH 10. DLS studies indicated that increasing the PNAEP DP led to a significant reduction in the *z*-average diameter for this series of PDEA_{99}−PNAEP_x diblock copolymers.

2.5 References

1 W. Reppe, *Angew. Chemie*, 1953, **65**, 577–578.

2 F. Haaf, A. Sanner and F. Straub, *Polym. J.*, 1985, **17**, 143–152.

3 M. Teodorescu and M. Bercea, *Polym. Plast. Technol. Eng.*, 2015, **54**, 923–943.

4 C. M. Lee and W. D. Kumler, *J. Am. Chem. Soc.*, 1961, **83**, 4593–4596.

5 H. Einaga and M. Harada, *Langmuir*, 2005, **21**, 2578–2584.

6 H. Tsunoyama, H. Sakurai, Y. Negishi and T. Tsukuda, *J. Am. Chem. Soc.*, 2005, **127**, 9374–9375.

7 J. Jiang, L. Zhu, L. Zhu, H. Zhang, B. Zhu and Y. Xu, *ACS Appl. Mater. Interfaces*, 2013, **5**, 12895–12904.

8 M. M. Faragalla, D. J. T. Hill and A. K. Whittaker, *Polym. Bull.*, 2002, **47**, 421–427.

9 S. Hosaka, A. Yamada, H. Tanzawa, T. Momose, H. Magatani and A. Nakajima, *J. Biomed. Mater. Res.*, 1980, **14**, 557–566.

10 F. Carli and F. Garbassi, *J. Pharm. Sci.*, 1985, **74**, 963–967.

11 R. Arshady, *Colloid Polym. Sci.*, 1992, **270**, 717–732.

12 V. Prosapio, E. Reverchon and I. De Marco, *Ind. Eng. Chem. Res.*, 2015, **54**, 11568–11575.

13 J. Stejskal, P. Kratochvíl and M. Helmstedt, *Langmuir*, 1996, **12**, 3389–3392.

14 T. P. Davis and M. B. Huglin, *Polymer*, 1990, **31**, 513–519.

15 G. Moad, E. Rizzardo and S. H. Thang, *Aust. J. Chem.*, 2006, **59**, 669–692.

16 G. Moad, E. Rizzardo and S. H. Thang, *Aust. J. Chem.*, 2009, **62**, 1402–1472.

17 G. Moad, E. Rizzardo and S. H. Thang, *Aust. J. Chem.*, 2012, **65**, 985–1076.

18 R. Devasia, R. L. Bindu, R. Borsali, N. Mougin and Y. Gnanou, *Macromol. Symp.*, 2005, **229**, 8–17.

19 D. B. Thomas, A. J. Convertine, L. J. Myrick, C. W. Scales, A. E. Smith, A. B. Lowe, Y. A. Vasilieva, N. Ayres and C. L. McCormick, *Macromolecules*, 2004, **37**, 8941–8950.

20 D. B. Thomas, A. J. Convertine, R. D. Hester, A. B. Lowe and C. L. McCormick, *Macromolecules*, 2004, **37**, 1735–1741.

21 A. B. Lowe and C. L. McCormick, *Prog. Polym. Sci.*, 2007, **32**, 283–351.

22 J. B. McLeary, J. M. McKenzie, M. P. Tonge, R. D. Sanderson and B. Klumperman, *Chem. Commun.*, 2004, **17**, 1950–51.

23 J. B. McLeary, F. M. Calitz, J. M. McKenzie, M. P. Tonge, R. D. Sanderson and B. Klumperman, *Macromolecules*, 2004, **37**, 2383–2394.

24 S. Perrier, C. Barner-Kowollik, J. F. Quinn, P. Vana and T. P. Davis, *Macromolecules*, 2002, **35**, 8300–8306.

25 G. Pound, Z. Eksteen, R. Pfukwa, J. M. McKenzie, R. F. M. Lange and B. Klumperman, *J. Polym. Sci. Part A Polym. Chem.*, 2008, **46**, 6575–6593.

26 J. W. Breitenbach, *J. Polym. Sci.*, 1957, **23**, 949–953.

27 P. W. Reader, R. Pfukwa, S. Jokonya, G. E. Arnott and B. Klumperman, *Polym. Chem.*, 2016, **7**, 6450–6456.

28 J. Giliomee, R. Pfukwa, N. P. Gule and B. Klumperman, *Polym. Chem.*, 2016, **7**, 1138–1146.

29 G. Pound, J. M. McKenzie, R. F. M. Lange and B. Klumperman, *Chem. Commun.*, 2008, **27**, 3193–3195.

30 D. J. Keddie, *Chem. Soc. Rev.*, 2014, **43**, 496–505.

31 S. J. Stace, G. Moad, C. M. Fellows and D. J. Keddie, *Polym. Chem.*, 2015, **6**, 7119–7126.

32 B. Panayiotis, P. Marinos and H. Nikos, *J. Polym. Sci. Part A Polym. Chem.*, 2006,

44, 659–665.

33 I. J. Johnson, E. Khosravi, O. M. Musa, R. E. Simnett and A. M. Eissa, *J. Polym. Sci. Part A Polym. Chem.*, 2015, **53**, 775–786.

34 C. L. McCormick and A. B. Lowe, *Acc. Chem. Res.*, 2004, **37**, 312–325.

35 A. Guinaudeau, S. Mazières, D. J. Wilson and M. Destarac, *Polym. Chem.*, 2012, **3**, 81–84.

36 A. Guinaudeau, O. Coutelier, A. Sandeau, S. Mazières, H. D. Nguyen Thi, V. Le Drogo, D. J. Wilson and M. Destarac, *Macromolecules*, 2014, **47**, 41–50.

37 V. J. Cunningham, Y. Ning, S. P. Armes and O. M. Musa, *Polymer*, 2016, **106**, 189–199.

38 V. J. Cunningham, M. J. Derry, L. A. Fielding, O. M. Musa and S. P. Armes, *Macromolecules*, 2016, **49**, 4520–4533.

39 V. J. Cunningham, S. P. Armes and O. M. Musa, *Polym. Chem.*, 2016, **7**, 1882–1891.

40 G. M. Iskander, L. E. Baker, D. E. Wiley and T. P. Davis, *Polymer.*, 1998, **39**, 4165–4169.

41 J. Deng, Y. Shi, W. Jiang, Y. Peng, L. Lu and Y. Cai, *Macromolecules*, 2008, **41**, 3007–3014.

42 Y. Shi, G. Liu, H. Gao, L. Lu and Y. Cai, *Macromolecules*, 2009, **42**, 3917–3926.

43 Z. An, Q. Shi, W. Tang, C.-K. Tsung, C. J. Hawker and G. D. Stucky, *J. Am. Chem. Soc.*, 2007, **129**, 14493–14499.

44 R. W. Lewis, R. A. Evans, N. Malic, K. Saito and N. R. Cameron, *Polym. Chem.*, 2018, **9**, 60–68.

45 J. Yeow and C. Boyer, *Adv. Sci.*, 2017, **4**, 1700137.

46 N. M. Ahmad, B. Charleux, C. Farcet, C. J. Ferguson, S. G. Gaynor, B. S. Hawkett, F. Heatley, B. Klumperman, D. Konkolewicz, P. A. Lovell, K. Matyjaszewski and R. Venkatesh, *Macromol. Rapid Commun.*, 2009, **30**, 2002–2021.

47 M. V. Deshmukh, A. A. Vaidya, M. G. Kulkarni, P. R. Rajamohanan and S. Ganapathy, *Polymer*, 2000, **41**, 7951–7960.

48 J. Xu, Z. Ge, Z. Zhu, S. Luo, H. Liu and S. Liu, *Macromolecules*, 2006, **39**, 8178–8185.

49 Z. Ge, Y. Cai, J. Yin, Z. Zhu, J. Rao and S. Liu, *Langmuir*, 2007, **23**, 1114–1122.

50 L. Liu, C. Wu, J. Zhang, M. Zhang, Y. Liu, X. Wang and G. Fu, *J. Polym. Sci. Part A Polym. Chem.*, 2008, **46**, 3294–3305.

51 G. Fundueanu, M. Constantin and P. Ascenzi, *Acta Biomater.*, 2009, **5**, 363–373.

52 E. R. Jones, M. Semsarilar, A. Blanazs and S. P. Armes, *Macromolecules*, 2012, **45**, 5091–5098.

53 N. J. W. Penfold, J. R. Lovett, N. J. Warren, P. Verstraete, J. Smets and S. P. Armes, *Polym. Chem.*, 2016, **7**, 79–88.

54 T. Junkers, S. P. S. Koo, T. P. Davis, M. H. Stenzel and C. Barner-Kowollik, *Macromolecules*, 2007, **40**, 8906–8912.

55 F. Heatley, P. A. Lovell and T. Yamashita, *Macromolecules*, 2001, **34**, 7636–7641.

56 G. S. Misra and U. D. N. Bajpai, *Prog. Polym. Sci.*, 1982, **8**, 61–131.

57 J. Sun, Y. Peng, Y. Chen, Y. Liu, J. Deng, L. Lu and Y. Cai, *Macromolecules*, 2010, **43**, 4041–4049.

58 R. F. Boyer, *Rubber Chem. Technol.*, 1963, **36**, 1303–1421.

59 GAF Corporation (New York, NY), US3914403, 1975.

60 M. Heskins and J. E. Guillet, *J. Macromol. Sci. Part A - Chem.*, 1968, **2**, 1441–1455.

61 B. R. Saunders and B. Vincent, *Adv. Colloid Interface Sci.*, 1999, **80**, 1–25.

62 T. P. Lodge, J. Bang, K. J. Hanley, J. Krocak, S. Dahlquist, B. Sujan and J. Ott, *Langmuir*, 2003, **19**, 2103–2109.

63 H. Liang, S. A. K, I. M. R, L. Xue, L. Zhenzhen and S. M. J, *J. Polym. Sci. Part A Polym. Chem.*, 2013, **51**, 3004–3020.

64 T. Zdeněk, S. Antonín, P. Vladimír and K. Pavel, *Die Makromol. Chemie*, 1977, **178**, 2743–2746.

65 Z. Zhou and B. Chu, *Macromolecules*, 1987, **20**, 3089–3091.

66 Y. Fukumine, K. Inomata, A. Takano and T. Nose, *Polymer.*, 2000, **41**, 5367–5374.

67 G. Moad, E. Rizzardo and S. H. Thang, *Polymer.*, 2008, **49**, 1079–1131.

68 V. Bütün, S. P. Armes and N. C. Billingham, *Polymer.*, 2001, **42**, 5993–6008.

69 S. L. Canning, T. J. Neal and S. P. Armes, *Macromolecules*, 2017, **50**, 6108–6116.

70 G. Moad, *Polym. Chem.*, 2017, **8**, 177–219.

Chapter 3

Synthesis and Characterisation of Waterborne Pyrrolidone-Functional Diblock Copolymer Nanoparticles Prepared via Surfactant-Free RAFT Emulsion Polymerisation

Reproduced in full with permission from:

O. J. Deane, O. M. Musa, A. Fernyhough, and S. P. Armes, *Macromolecules* 2020, 53, 1422−1434

3.1 Introduction

In principle, RAFT aqueous emulsion polymerisation combines the advantages of traditional emulsion polymerisation (fast polymerisation rate, high final monomer conversion, low solution viscosity, and a cost-effective, environmentally friendly solvent) with good control over the MWD and convenient introduction of functional end groups.[1–8] Moreover, the covalent bond between the stabiliser and the core-forming blocks leads to more effective and efficient stabilisation compared to that achieved for surfactant-stabilised latexes prepared by conventional emulsion polymerisation.[9] Such surfactant-free protocols should enable copolymer films to be prepared with superior transparency.[10] Anionic steric stabiliser blocks such as PMAA or PAA have been employed for various RAFT aqueous emulsion polymerisation formulations.[11–13] However, their polyelectrolytic character produces nanoparticles with pH-dependent colloidal stability.[14] In principle, using non-ionic steric stabiliser blocks eliminates this problem.[15–20] Steric stabilisation of polymer colloids can be explained using Flory-Krigbaum theory, which is closely related to the thermodynamic behaviour of polymers in solution (Figure 3.1).[21,22] As the particles approach one another, the surface-to-surface distance (see *D* in Figure 3.1a) is reduced until interpenetration of the two steric stabiliser layers (ϕ) occurs (see *d* in Figure 3.1b).

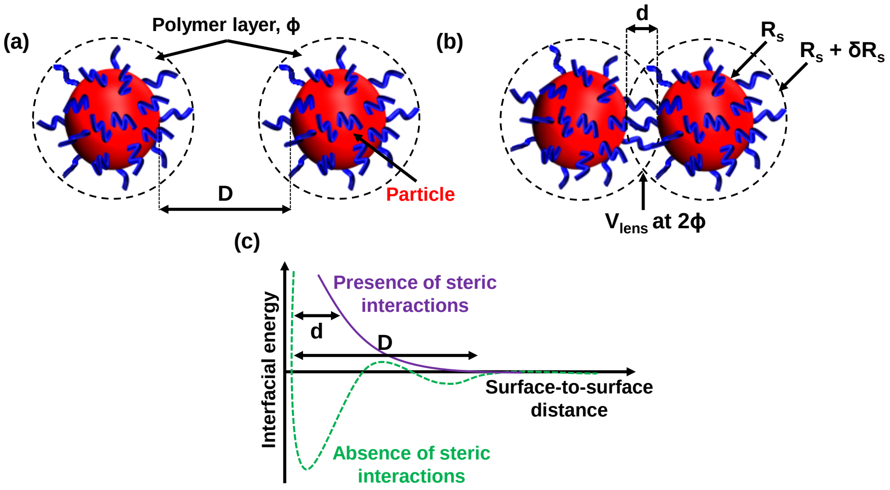

Figure 3.1. Schematic representation of the change in free energy of two sterically-stabilised colloidal particles as described by Flory-Krigbaum theory. [21,22]

When these two particles are sufficiently close, such interpenetration of the stabiliser chains leads to an effective local concentration of 2ϕ within the lens region (V_{lens}; Figure 3.1b). This results in an increase in the free energy of the system because intermingling of well-solvated polymer chains is both enthalpically and entropically unfavourable. The resulting increase in free energy for this pair of sterically-stabilised particles (Equation 3.1) is given by the product of V_{lens} (Equation 3.2) and the free energy change per unit volume (ΔG_{ov}; Equation 3.3).

$$\Delta G = \Delta G_{ov} V_{lens} \tag{3.1}$$

$$V_{lens} = \frac{2\pi}{3}\left(\delta R_s - \frac{D}{2}\right)^2 \left(3R_s + 2\delta R_s + \frac{D}{2}\right) \tag{3.2}$$

Where R_s is the core radius and δR_s is the outer shell radius (see Figure 3.1b).

$$\Delta G_{ov} = 2kt\left(\frac{\overline{V_2^2}}{\overline{V_1}V_d^2}\right)\left(\frac{1}{2} - \chi\right) \tag{3.3}$$

Where V_d is the volume occupied by a polymer coil, $\overline{V_1}$ is the solvent molar volume, $\overline{V_2}$ is the polymer molar volume, and χ is the interaction parameter for the system (see Equation 3.4).

$$\chi = \frac{z}{2kT}(2w_{12} - w_{11} - w_{22}) \tag{3.4}$$

Here z is the coordination number of a polymer segment (or solvent molecule), and w_{ij} is the energy of interaction between molecule i and j (when 1 denotes solvent molecules and 2 denotes polymer molecules). Importantly, this results in the χ parameter dictating the sign of ΔG_{ov}. When the polymer chains are immersed in a poor solvent, $\chi > 0.50$ and segment-segment interactions are more favourable than segment-solvent interactions. This results in flocculation rather than steric stabilisation. However, when the polymer chains are immersed in a good solvent, $\chi < 0.50$ and interpenetration of the steric stabiliser chains is unfavourable. This generates a strong steric repulsive force that ensures colloidal stabilisation.

A second contribution arises from the elastic interaction associated with the interpenetration of the steric stabiliser chains. Such intermingling restricts the degrees of freedom available to the polymer chains and hence lowers the configurational entropy (ΔS_{ov}; Equation 3.5), generating a repulsive force that approximately obeys Hooke's law.

$$\Delta S_{ov} = k_H d, where\ k_H = \frac{3kt}{nl^2} \tag{3.5}$$

Where *n* is the DP of the steric stabiliser chains and *l* is approximately the length of a monomer unit. This repulsive term is always positive and thus compression of such polymer chains is always entropically unfavourable.

In summary, Flory-Krigbaum theory accounts for the colloidal stability of sterically-stabilised particles when immersed in a good solvent for the steric stabiliser chains (Figure 3.1c). When immersed in a poor solvent, attractive interactions dominate initially leading to flocculation but repulsive forces can arise when the particles are further compressed (Figure 3.1c).

Historically, steric stabilisation was achieved by grafting polymer chains onto the surface of latex particles.[23–25] However, RAFT aqueous emulsion polymerisation using a soluble precursor enables the steric stabiliser chains to be covalently linked to the hydrophobic core block. This can produce exceptional tolerance towards added salt.[26] However, there are relatively few examples of non-ionic stabiliser blocks in the aqueous PISA literature.[16,18,27–33] According to Lansalot and Rieger, increasing the scope of RAFT aqueous emulsion polymerisation is expected to aid in the development of commercially relevant PISA protocols.[34] This deficiency is addressed in the current study.

There are only two reported examples of PNVP being used as a stabiliser block for RAFT aqueous emulsion polymerisation.[35,36] Binauld *et al.* prepared PNVP-stabilised nanoparticles *via* RAFT aqueous emulsion polymerisation of VAc (see Scheme 3.1). PNVP precursors were synthesised either in the bulk or in 1,4-dioxane using AIBN as the initiator at 80 °C.[36] This resulted in well-defined PNVP precursors within 7 h ($M_w/M_n < 1.40$, as determined by GPC). However, when NVP homopolymerisation was attempted in aqueous solution, a significantly slower rate of polymerisation was achieved (88% conversion after 24 h) and a somewhat broader final molecular weight distribution ($M_w/M_n = 1.60$). Importantly, ^{1}H NMR analysis indicated that NVP homopolymerisation in water under previously reported optimised conditions[37] (see Chapter 2.1) resulted in the formation of various hydrolysis degradation products. As such, PNVP precursors were prepared either in the bulk or in 1,4 dioxane for the RAFT emulsion polymerisation of VAc.

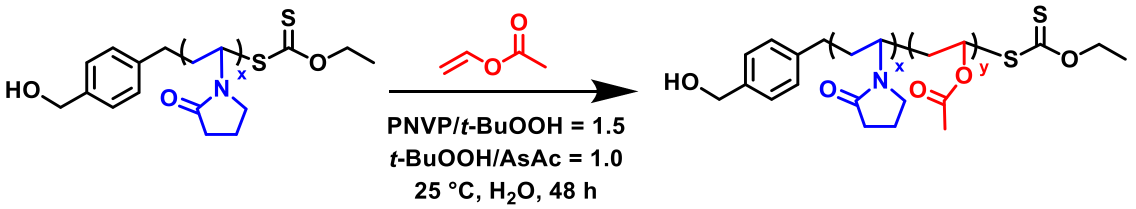

Scheme 3.1. RAFT aqueous emulsion polymerisation of VAc at 25 °C using a PNVP precursor.[36]

Gravimetric analysis indicated that conversions remained below 89% after 48 h when the RAFT emulsion polymerisation of VAc was performed at 25 °C. DMF GPC indicated broad molecular weight distributions for the final $PNVP_x$−$PVAc_y$ diblock copolymers ($M_w/M_n > 2.2$). Furthermore, the GPC traces indicated that a significant proportion of the water-soluble PNVP precursor did not participate in the VAc polymerisation and could be removed after centrifugation (Figure 3.2a and 3.2b). DLS and TEM analysis of a 0.1% w/w $PNVP_{33}$−$PVAc_y$ dispersion indicated the presence of near-monodisperse spherical nanoparticles (z-average diameter = 110-157 nm; DLS polydispersity = 0.02-0.11). Raising the polymerisation temperature from 25 °C to 35 °C reduced the polymerisation time to 5 h (final monomer conversion = 87%). However, this caused further hydrolysis of the xanthate chain-ends and resulted in the formation of larger, polydisperse nanoparticles (z-average diameter = 268 nm; DLS PDI = 0.30).[36] In principle, (meth)acrylic analogues of NVP should provide much better copolymerisability with a wide range of vinyl monomers, enabling the optimised PISA synthesis of well-defined pyrrolidone-based diblock copolymer nanoparticles in the form of concentrated aqueous dispersions.

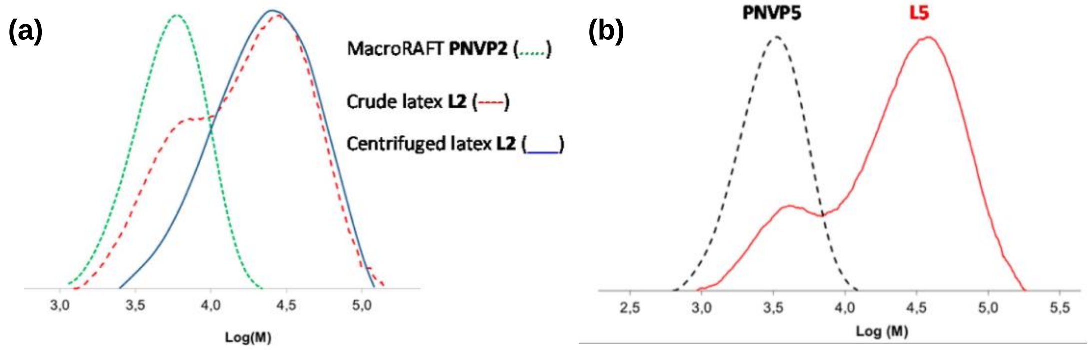

Figure 3.2. DMF GPC curves obtained for: (a) a PNVP macro-CTA prepared in 1,4 dioxane (dashed green trace), a $PNVP_{33}$−$PVAc_y$ (dashed red trace; L2) diblock copolymer prepared via RAFT aqueous emulsion polymerisation of VAc at 25 °C and the same diblock copolymer after centrifugation (blue solid trace); (b) a PNVP macro-CTA prepared in the bulk (dashed black trace) and a $PNVP_x$−$PVAc_y$ (solid red trace; L5) diblock copolymer prepared via RAFT aqueous emulsion polymerisation of VAc at 25 °C.

As discussed in Chapter 2, PNMEP homopolymer is significantly less hydrophilic than PNVP and exhibits LCST behaviour in aqueous solution. Indeed, Cunningham *et al.* exploited such inverse temperature solubility to prepare PNMEP−core diblock copolymer nanoparticles via RAFT aqueous dispersion polymerisation.[38] However, Gibson *et al.* recently prepared a series of PNMEP stabilisers with anionic carboxylate end-groups using an appropriate RAFT agent (see Figure 3.3a).[39] This minor modification was sufficient to eliminate the undesirable LCST behaviour (Figure 3.3b) and hence enable the synthesis of well-defined diblock copolymer spheres via aqueous PISA at pH 7 using PNMEP as an electrosteric stabiliser (Figure 3.3c).[39] Unfortunately, such nanoparticles became flocculated when the anionic character was removed or in the presence of relatively low levels of added salt. In principle, this colloidal instability problem can be addressed by replacing NMEP with its acrylic-analogue, NAEP, which is significantly more hydrophilic (see Chapter 2).[40]

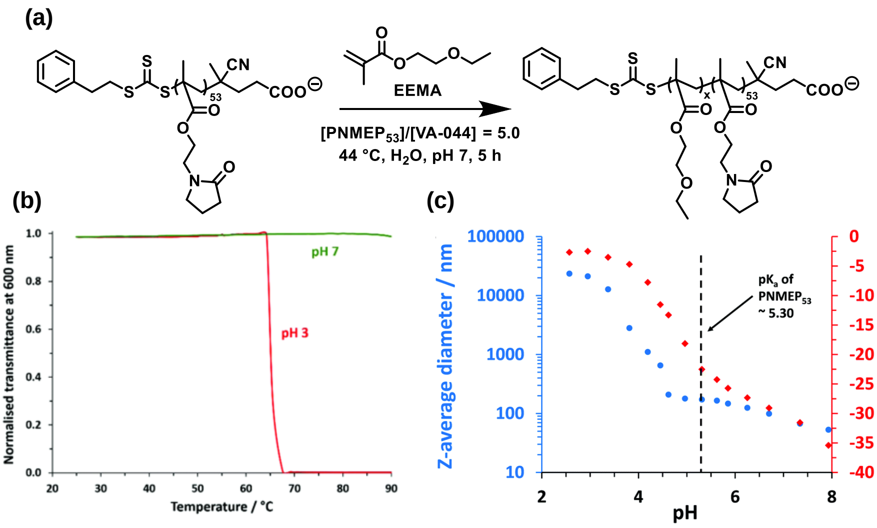

Figure 3.3. (a) Schematic representation of the synthesis of PNMEP$_{53}$-PEEMA$_x$ diblock copolymer nanoparticles by RAFT aqueous emulsion polymerisation of EEMA at 44 °C and pH 7. (b) Variation in transmittance at 600 nm with temperature for a PNMEP$_{53}$ homopolymer at either pH 3 (protonated carboxylic acid) or pH 7 (carboxylate end-group). (c) Variation in z-average diameter (blue circles) and zeta potential (red diamonds) with dispersion pH observed for a 0.01% w/w aqueous dispersion of spherical PNMEP$_{53}$-PEEMA$_{500}$ diblock copolymer nanoparticles.

Herein, we report the synthesis of well-defined PNAEP-based diblock copolymer spheres via RAFT aqueous emulsion polymerisation of either styrene or *n*-butyl acrylate (nBA) or statistical mixtures thereof. Polystyrene is a model high T_g polymer that has been well-studied as a structure-directing block in the context of PISA.[3,4,11,14,30,41–43] Polystyrene-based nanoparticles are readily imaged by TEM, which aids morphological assignment. In contrast, PnBA has a relatively low T_g (–54 °C) and can be considered to be a model film-forming polymer.[19,44,45] Statistical copolymerisation of these two comonomers enable the copolymer T_g to be tuned over a wide range, which is convenient for paints and coatings applications.[2,46,47] ^{1}H NMR spectroscopy was used to study the kinetics of optimised RAFT aqueous emulsion polymerisation formulations, while chloroform GPC was used to assess the evolution in molecular weight distribution. DSC was used to determine the T_g values for the resulting diblock copolymers. Finally, the transparency of selected diblock copolymer films was briefly explored using visible absorption spectroscopy.

3.2 Experimental

3.2.1 Materials.

NAEP was purified using the protocol outline in Chapter 2. Styrene, AsAc, KPS, DDMAT, and nBA were purchased from Sigma-Aldrich (Dorset, UK). 2,2-Azobis[2-(2-imidazolin-2-yl)propane]dihydrochloride (VA-044) was purchased from Wako (Japan) and used without further purification. $CDCl_3$ was purchased from Goss Scientific Instruments Ltd. (Cheshire, UK). All other solvents were purchased from Fisher Scientific (Loughborough, UK) and were used as received. Deionised water was used for all experiments.

3.2.2 Preparation of $PNAEP_{67}$ Macro-CTA.

The synthesis of PNAEP precursors by RAFT aqueous solution polymerisation has been previously discussed in detail in Chapter 2: NAEP (10.00 g, 54.6 mmol), DDMAT RAFT agent (199.0 mg, 0.546 mmol; target DP = 100), and AsAc (1.0 mg, 5.5 μmol) were weighed into a 14 mL vial charged with a magnetic flea (reaction solution 1). This reaction solution was then placed in an ice bath and degassed with nitrogen for 30 min. Deionised water (4.372 g, 70% w/w) and KPS (1.5 mg, 5.5 μmol; DDMAT/KPS molar ratio = 100) were weighed into a second 14 mL vial (reaction solution 2) and degassed with nitrogen in an ice bath for 30 min. After 30 min, the vial containing reaction solution 1 was immersed in an oil bath set at 30 °C. Reaction solution 2 was then added using a degassed syringe and needle to reaction solution 1 under nitrogen. The NAEP polymerisation was allowed to proceed for 8 min before being quenched via exposure to air and immersed in an ice bath. ^{1}H NMR analysis of the disappearance of vinyl signals at 5.9 and 6.4 ppm relative to the integrated four ethyl protons at 3.4−3.8 ppm assigned to PNAEP indicated a monomer conversion of 62%. The crude PNAEP homopolymer was purified by dialysis against water (72 h) using a 3500 molecular weight cut-off dialysis membrane (Fisher Scientific) to give a PNAEP chain transfer agent (CTA) containing less than 1% residual monomer. This precursor was then analysed by ^{1}H NMR and chloroform GPC. Its mean DP was calculated to be 67 as judged by ^{1}H NMR spectroscopy analysis in $CDCl_3$ [δ: 0.8-0.9 (3H, CH_3 of methyl RAFT chain-end), 4.1-4.3 (134H, $COOCH_2CH_2$), 3.4-3.7 (268H, $COOCH_2C\underline{H_2}$, and $NCOC\underline{H_2}CH_2CH_2$), 1.2-2.5 (469H, $NCOCH_2C\underline{H_2}C\underline{H_2}$ and $C\underline{H_2}C\underline{H}COO$)]. Chloroform GPC analysis indicated an M_n of 19.2 kg mol^{-1} and an M_w/M_n of 1.19 when compared to a series of near-monodisperse polystyrene standards.

3.2.3 Synthesis of $PNAEP_{67}$−PS_x Diblock Copolymer Nanoparticles via RAFT Aqueous Emulsion Polymerisation of Styrene at 80 °C.

A typical protocol used for the synthesis of a $PNAEP_{67}$-PS_{350} diblock copolymer was as follows: $PNAEP_{67}$ macro-CTA (0.185 g, 14.6 μmol), deionised water (2.880 g, corresponding to a 20% w/w solution), and VA-044 (1.580 mg, 4.9 μmol; $PNAEP_{67}$/VA-044 = 3.0) were weighed into a 10 mL round-bottom flask charged with a magnetic flea. NaOH (20 μL, 1 M) was added to raise the pH to 7.0. This flask was then immersed in an ice bath and the solution was degassed with nitrogen for 30 min. Styrene (1.0 g) was weighed into a separate 14 mL vial and degassed with nitrogen in an ice bath for 30 min. After 30 min, styrene (0.59 ml, 5.12 mmol; target DP = 350) was added to the flask using a degassed syringe and needle under nitrogen. The contents of the flask were then stirred vigorously to ensure thorough mixing and degassed for a further 5 min before being immersed in an oil bath set at 80 °C. The styrene polymerisation was allowed to proceed for 2 h before being quenched by exposing the reaction solution to air and immersing the reaction vial in an ice bath. ^{1}H NMR spectroscopy analysis of the disappearance of vinyl signals at 5.3 and 5.8 ppm (relative to the integrated five aromatic protons at 6.3−7.2 ppm assigned to styrene repeat units) indicated a final styrene conversion of 99%. ^{1}H NMR in $CDCl_3$ δ: 4.1-4.3 (134H, $COOC\underline{H_2}CH_2$ of $PNAEP_{67}$ precursor) compared against 6.3-7.3 (1750H, $C_6\underline{H_5}$ of styrene). Chloroform GPC analysis indicated an M_n of 46.6 kg mol^{-1} and an M_w/M_n of 1.28 when compared to a series of near-monodisperse polystyrene standards. Other target diblock copolymer compositions were obtained by adjusting the [styrene]/[$PNAEP_{67}$] molar ratio at a constant [$PNAEP_{67}$].

3.2.4 Synthesis of $PNAEP_{67}$−$PnBA_x$ Diblock Copolymer Nanoparticles via RAFT Aqueous Emulsion Polymerisation of nBA at 30 °C.

A typical protocol used for the synthesis of a $PNAEP_{67}$−$PnBA_{500}$ diblock copolymer was as follows: $PNAEP_{67}$ macro-CTA (0.185 g, 14.6 μmol), deionised water (4.501 g, corresponding to a 20% w/w solution), and KPS (1.320 mg, 4.9 μmol; $PNAEP_{67}$/KPS = 3.0) were weighed into a 10 mL round-bottom flask charged with a magnetic flea. HCl (10 μL, 0.2 M) was added to adjust the pH to 3.0. This flask was then immersed in an ice bath, and the solution was degassed with nitrogen for 30 min. nBA (1.500 g) was weighed into a separate 14 mL vial and degassed with nitrogen in an ice bath for 30 min. An AsAc stock solution (0.01% w/w) was weighed into a second 14 mL vial and degassed with nitrogen in an ice bath for 30 min. After 30 min, nBA (1.05 mL, 7.32 mmol; target DP = 500) was added to the flask using a degassed syringe and needle under nitrogen. The flask contents were then stirred vigorously to ensure thorough mixing and degassed for 5 min before being immersed in an oil bath set at 30 °C. After 1 min, AsAc (0.09 mL, 4.9 μmol; KPS/AsAc molar ratio = 1.0) was added to the flask. The nBA polymerisation was allowed to proceed for 1 h before being quenched by exposing the reaction solution to air and immersing the reaction vial in an ice bath. ^{1}H NMR spectroscopy analysis of the disappearance of vinyl signals at 5.8 and 6.1 ppm (relative to the integrated three protons at 0.9−1.0 ppm assigned to the pendant methyl group of nBA) indicated a final nBA conversion of 99%. %. ^{1}H NMR in $CDCl_3$ δ: 3.4-3.7 (268H, $COOCH_2C\underline{H_2}$, and $NCOC\underline{H_2}CH_2CH_2$) of $PNAEP_{67}$ precursor) compared against 0.9-1.0 (1500H, $COOCH_2CH_2CH_2C\underline{H_3}$ of nBA). Chloroform GPC analysis of this copolymer indicated an M_n of 86.6 kg mol^{-1} and an M_w/M_n of 1.56 when compared to a series of near-monodisperse polystyrene standards. Other diblock copolymer compositions were obtained by adjusting the [nBA]/[$PNAEP_{67}$] molar ratio at a constant [$PNAEP_{67}$].

3.2.5 Synthesis of $PNAEP_{67}$−P(S-*stat*-nBA)$_x$ Diblock Copolymer Nanoparticles via RAFT Aqueous Emulsion Polymerisation of styrene and nBA at 30 °C.

A typical protocol used for the synthesis of a $PNAEP_{67}$−P(S-*stat*-nBA)$_{400}$ diblock copolymer was as follows: $PNAEP_{67}$ macro-CTA (0.185 g, 14.6 μmol), deionised water

(3.472 g, corresponding to a 20% w/w solution), and KPS (1.320 mg, 4.9 μmol; $PNAEP_{67}$/KPS = 3.0) were weighed into a 10 mL round-bottom flask charged with a magnetic flea. HCl (10 μL, 0.2 M) was added to adjust the pH to 3.0. This flask was then immersed in an ice bath, and the solution was degassed with nitrogen for 30 min. nBA and styrene (1.500 g) were weighed into separate 14 mL vials and degassed with nitrogen in an ice bath for 30 min. An AsAc stock solution (0.01% w/w) was weighed into a second 14 mL vial and degassed with nitrogen in an ice bath for 30 min. After 30 min, styrene (0.34 mL, 2.97 mmol) and nBA (0.41 mL, 2.89 mmol; overall copolymer DP = 400, nBA content = 55% by mass) were added to the flask using a degassed syringe and needle under nitrogen. The flask contents were then stirred vigorously to ensure thorough mixing and degassed for 5 min before being immersed in an oil bath set at 30 °C. After 1 min, AsAc (0.09 mL, 4.9 μmol; KPS/AsAc molar ratio = 1.0) was added to the flask. The polymerisation was allowed to proceed for 3 h before being quenched by exposing the reaction solution to air and immersing the reaction vial in an ice bath. ^{1}H NMR spectroscopy analysis of the disappearance of vinyl signals at 5.8 and 6.1 ppm (relative to the integrated three protons at 0.8−1.0 ppm assigned to the pendant methyl group of nBA) and the vinyl signals at 5.3 and 5.8 ppm (relative to the integrated five aromatic protons at 6.5−7.2 ppm assigned to styrene repeat units) indicated a final comonomer conversion of 99%. ^{1}H NMR in $CDCl_3$ δ: 3.4-3.7 (268H, $COOCH_2C\underline{H_2}$, and $NCOC\underline{H_2}CH_2CH_2$) of $PNAEP_{67}$ precursor) compared against 6.3-7.3 (1015H, $C_6\underline{H_5}$ of styrene) and 0.9-1.0 (594H, $COOCH_2CH_2CH_2C\underline{H_3}$ of nBA). Chloroform GPC analysis of this copolymer indicated an M_n of 54.5 kg mol^{-1} and an M_w/M_n of 1.55 when compared to a series of near-monodisperse polystyrene standards. Other diblock copolymer compositions were obtained by adjusting the [(styrene + nBA)]/[$PNAEP_{67}$] molar ratio at a constant [$PNAEP_{67}$].

3.2.6 Copolymer Characterisation

^{1}H NMR Spectroscopy. All ^{1}H NMR spectra were recorded in $CDCl_3$ using a 400 MHz Bruker AVANCE-400 spectrometer with 64 scans being averaged per spectrum. Anhydrous $MgSO_4$ was used as a desiccant to remove water and hence enable molecular dissolution of each diblock copolymer.

Gel Permeation Chromatography. Copolymer molecular weights and dispersities were determined using an Agilent 1260 Infinity GPC system equipped with both refractive index and UV−visible detectors. Two Agilent PLgel 5 μm Mixed-C columns and a guard column were connected in series and maintained at 35 °C. High-performance liquid chromatography-grade chloroform containing 0.25% w/w triethylamine was used as the eluent, and the flow rate was set at 1.0 mL min^{-1}. The refractive index detector was used for the calculation of molecular weights and dispersities by calibration using a series of 10 near-monodisperse polystyrene standards (with the M_n values ranging from 370 to 2,520,000 g mol^{-1}).

Transmission Electron Microscopy. The as-prepared 20% w/w copolymer dispersions were diluted at 20 °C to generate 0.10% w/w aqueous dispersions. Copper/palladium TEM grids (Agar Scientific, UK) were coated in-house to produce thin films of amorphous carbon. These grids were then treated with a plasma glow discharge for 30 s to create a hydrophilic surface. One droplet of an aqueous diblock copolymer dispersion (20 μL; 0.10% w/w) was placed on a freshly treated grid for 1 min and then blotted with a filter paper to remove excess solution. To stain the deposited nanoparticles, an aqueous solution of uranyl formate (10 μL; 0.75% w/w) was placed on the sample-loaded grid via micropipette for 20 s and then carefully blotted to remove excess stain. Each grid was then dried using a vacuum hose. Imaging was performed using a Philips CM100 instrument operating at 100 kV and equipped with a Gatan 1k CCD camera.

Dynamic Light Scattering. Measurements were conducted at 25 °C using a Malvern Instruments Zetasizer Nano series instrument equipped with a 4 mW He−Ne laser (λ = 633 nm) and an avalanche photodiode detector. Scattered light was detected at 173°. Copolymer dispersions were diluted to 0.10% w/w prior to analysis. Intensity-average hydrodynamic diameters were averaged over three runs and calculated using the Stokes−Einstein equation.

Differential Scanning Calorimetry. DSC studies were performed using a TA Instruments Discovery DSC instrument equipped with TZero low-mass aluminium pans and vented lids. Copolymers (and homopolymers) were equilibrated above their T_g for 10 min before performing two consecutive thermal cycles at a rate of 10 °C min^{-1}. Two cycles were performed to minimise the thermal history of each sample.

Film Preparation and Visible Absorption Spectroscopy. Spin-coated copolymer films were prepared by depositing a 200 μL aliquot of a 20% w/w aqueous dispersion onto a glass slide mounted on a vacuum-free Ossila spin coater (initially rotating at 250 rpm, followed by rapid acceleration up to 3000 rpm for 15 min). For transmittance studies, films were prepared as described above, and their transparency was assessed by visible absorption spectroscopy using a PerkinElmer Lambda 25 spectrometer. The spectra were recorded from 200 to 800 nm at 2 nm intervals at a scan speed of 960 nm min^{-1}. Copolymer film thicknesses were measured using a micrometre screw gauge.

3.3 Results and Discussion

3.3.1 Synthesis of PNAEP$_{67}$–PS$_x$ Diblock Copolymer Nanoparticles via RAFT Aqueous Emulsion Polymerisation of Styrene at 80 °C

A PNAEP$_{67}$ macro-CTA was synthesised via RAFT solution polymerisation of NAEP in deionised water at 30 °C using DDMAT as the CTA and 1:1 KPS/AsAc as a low-temperature redox initiator pair at a [DDMAT]/[KPS] molar ratio of 100. In principle, the relatively low initiator concentration should reduce termination during the synthesis of the PNAEP macro-CTA, thus improving the blocking efficiency for its subsequent chain extension.[48] This PNAEP$_{67}$ macro-CTA was then chain-extended via RAFT aqueous emulsion polymerisation of styrene using VA-044 ([PNAEP$_{67}$]/[VA-044] molar ratio = 3.0) at 80 °C; see Scheme 3.2.

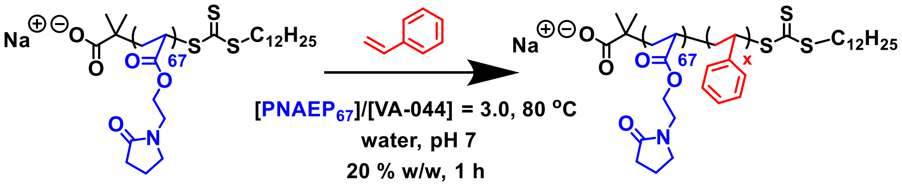

Scheme 3.2. Synthesis of PNAEP$_{67}$–PS$_x$ diblock copolymer nanoparticles via RAFT aqueous emulsion polymerisation of styrene at 80 °C using a [PNAEP$_{67}$]/[VA-044] molar ratio of 3.0.

The kinetics for the RAFT emulsion polymerisation of styrene at 80 °C was monitored for a target PNAEP$_{67}$–PS$_{350}$ diblock composition. Periodic sampling involved dilution of each aliquot extracted from the reaction mixture using $CDCl_3$, which is a good solvent for both the PNAEP and PS blocks. Anhydrous $MgSO_4$ was utilised as a desiccant to remove water in order to overcome this solvent's immiscibility with $CDCl_3$ and hence achieve molecular dissolution of the diblock copolymer chains. After quenching the polymerisation via dilution and cooling to 20 °C, each sample was analysed by ^{1}H NMR spectroscopy and chloroform GPC (Figure 3.4).

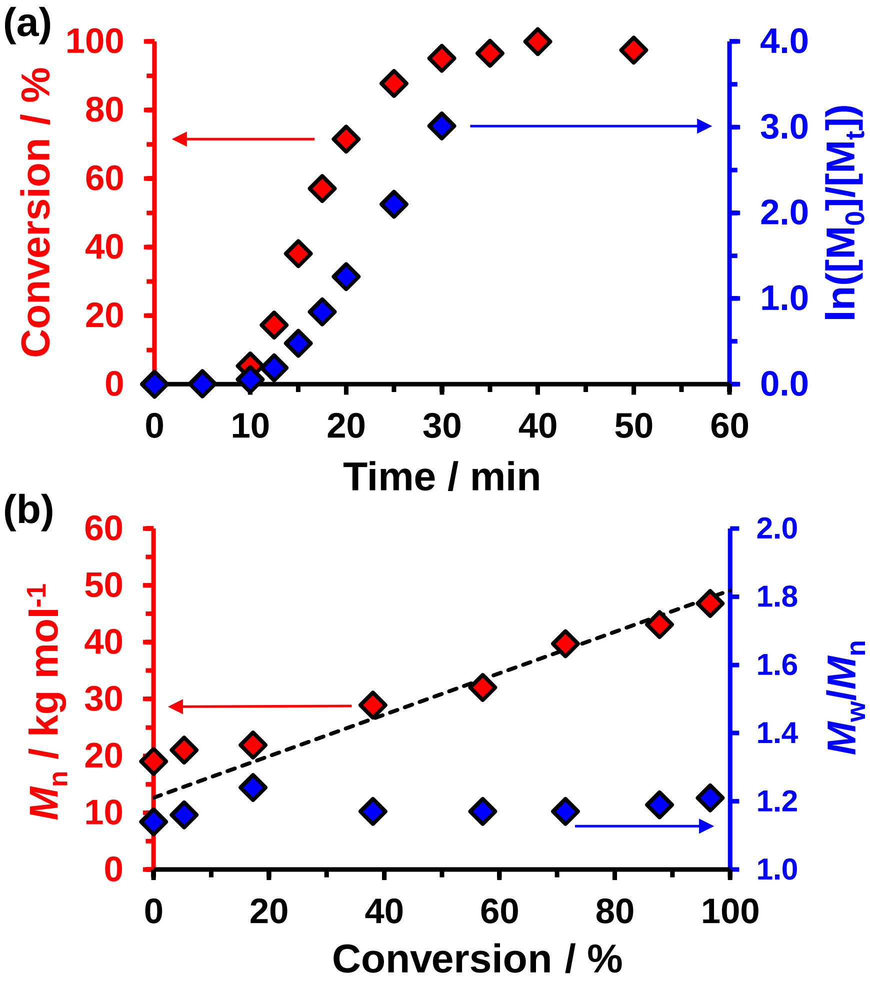

Figure 3.4. (a) Conversion vs time curve and the corresponding semilogarithmic plot determined by ^{1}H NMR spectroscopy during the RAFT aqueous emulsion polymerisation of styrene at 80 °C when targeting PNAEP$_{67}$−PS$_{350}$ diblock copolymer nanoparticles. Conditions: 20% w/w solids, [PNAEP$_{67}$]/[VA-044] molar ratio = 3.0. (b) Evolution of M_n and M_w/M_n against conversion determined by chloroform GPC using a series of near-monodisperse polystyrene calibration standards. The dashed line indicates the corresponding theoretical M_n values.

The former technique indicated that more than 95% conversion was achieved within 40 min. Furthermore, the semilogarithmic plot suggests that an approximate 30-fold increase in rate occurred between 10.0 and 12.5 min (Figure 3.4a), with the earlier time point corresponding to the onset of nanoparticle formation. This rate enhancement is well known for PISA syntheses and is attributed to micellar nucleation.[49–51] This hypothesis was confirmed via DLS analysis of aliquots taken from the reaction mixture (see Figure 3.5).

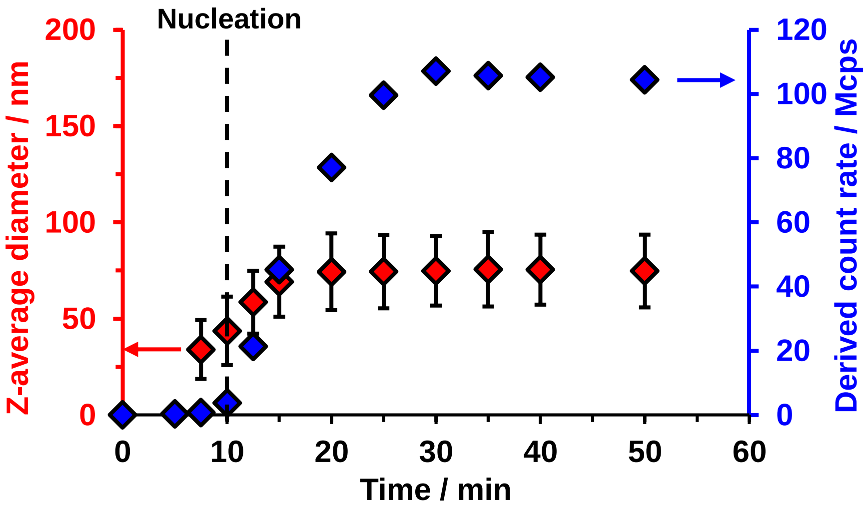

Figure 3.5. Evolution in *z*-average diameter and corresponding derived count rate (or scattered light intensity) over time as determined by DLS during the RAFT aqueous emulsion polymerisation of styrene at 80 °C and pH 7. Note: The first two data points have been omitted owing to very low derived count rates (0.5 Mcps) and relatively large *z*-average diameters (> 500 nm), which are attributed to low concentrations of relatively large styrene monomer droplets.

The growing PS chains become insoluble when they reach a critical DP, which drives *in situ* self-assembly to form nascent nanoparticles. For the present PISA formulation, this critical DP is around 24, which corresponds to just 8% conversion. Chaduc et al. performed the RAFT aqueous emulsion polymerisation of styrene at 80 °C using a PAA macro-CTA at pH 2.5−7.0.[14] Empirically, the optimum solution pH was found to be 2.5. However, the evolution in M_n and M_w/M_n did not display the expected living character when the styrene polymerisation was performed at pH 7 and induction periods of approximately 1 h were observed.[14] Moreover, a significant proportion of the initial PAA macro-CTA was consumed via at this higher pH, leading to higher-than-expected final M_n values.[14] In the present study, much shorter induction periods of around 10 min were observed at pH 7, which is attributed to the fact that VA-044 was employed at 80 °C. The 10 h half-life for this initiator is only 44 °C; so, the radical flux is relatively high at the reaction temperature, leading to rapid polymerisation even for the relatively low concentration of styrene that is dissolved in the aqueous phase (estimated to be 0.62 g dm^{-3} at 80 °C[52]). Unlike the observations made by Chaduc and co-workers, poor colloidal stability was observed for PISA syntheses conducted below pH 6. Acid titration studies indicated that the terminal carboxylic acid group on the PNAEP stabiliser chains has a pKa value of approximately 5.25 (see Figure 3.6a). Thus, maintaining colloidal stability during the PISA synthesis requires a relatively high degree of ionisation (>50%) of these acidic end-groups otherwise, macroscopic precipitation occurs. In this context, it is perhaps noteworthy that Gibson et al. recently reported similar observations when using carboxylic acid-functionalised PNMEP stabiliser blocks.[39] Presumably, the anionic character of the carboxylate end-groups confers additional (electrosteric) colloidal stability, which is sufficient to prevent nanoparticle aggregation. Perhaps surprisingly, lowering the solution pH from 8.9 to 2.1 did not induce colloidal instability for these PNAEP−PS nanoparticles after their initial synthesis (see Figure 3.6b).

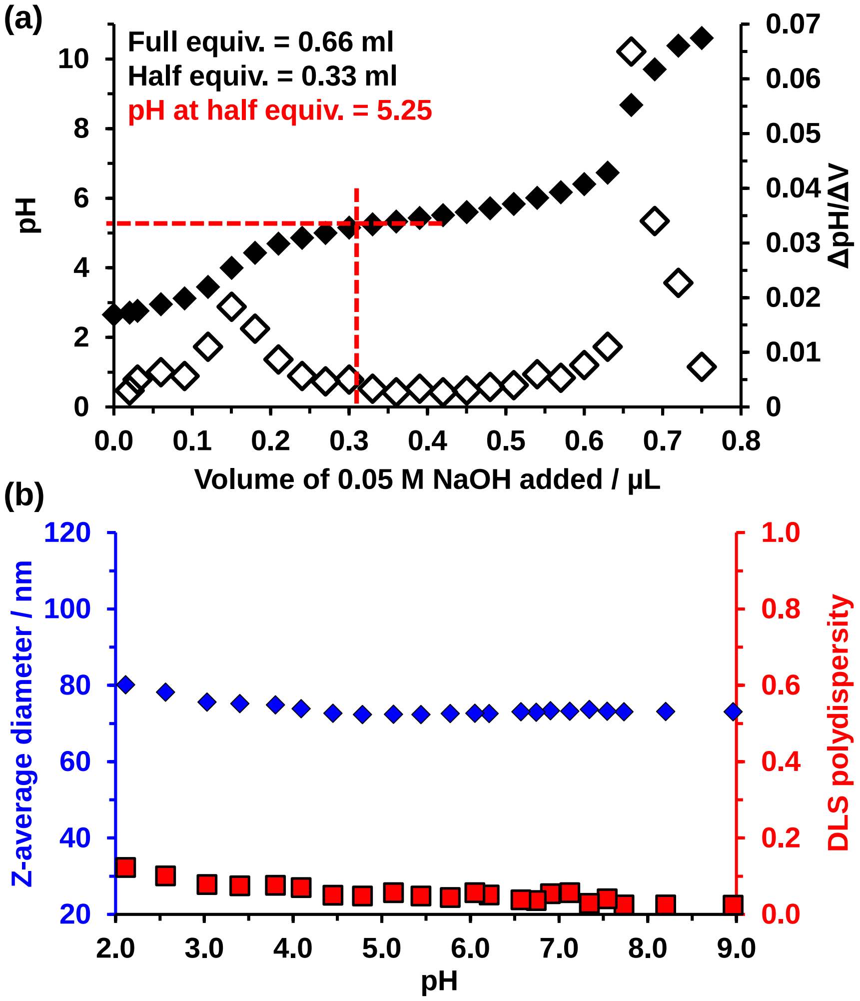

Figure 3.6. (a) Acid titration curve for a 20% w/w aqueous solution of HOOC-PNAEP$_{67}$ macro-CTA (carboxylic acid end-group pK_a ~ 5.25) and (b) Hydrodynamic diameter (and DLS polydispersity) vs. pH curves obtained for an 0.1% w/w aqueous dispersion of PNAEP$_{67}$-PS$_{250}$ nanoparticles synthesised by RAFT aqueous emulsion polymerisation of styrene at pH 7. All pH titrations were performed from high pH to low pH *via* addition of HCl.

When using a [PNAEP$_{67}$]/[VA-044] molar ratio of 3.0 and targeting a polystyrene DP of 350, chloroform GPC analysis indicated a linear evolution of molecular weight with conversion (see Figure 3.4b). Moreover, relatively low dispersities (M_w/M_n < 1.25) were maintained throughout the reaction. Both features are consistent with a well-controlled RAFT polymerisation. However, the experimental GPC data deviate significantly from the theoretical M_n values at low conversion. This discrepancy is likely to be a systematic error incurred by the use of polystyrene standards because much better agreement was observed at higher conversions as the growing diblock copolymer chains gradually became more polystyrene-rich. Four PNAEP$_{67}$−PS$_x$ diblock copolymers were prepared by targeting polystyrene DPs ranging between 100 and 1250, while maintaining the same 20% w/w solids concentration. More than 98% styrene conversion was achieved when targeting DPs of up to 700, with relatively narrow MWDs being maintained (M_w/M_n ≤ 1.30) (Figure 3.7).

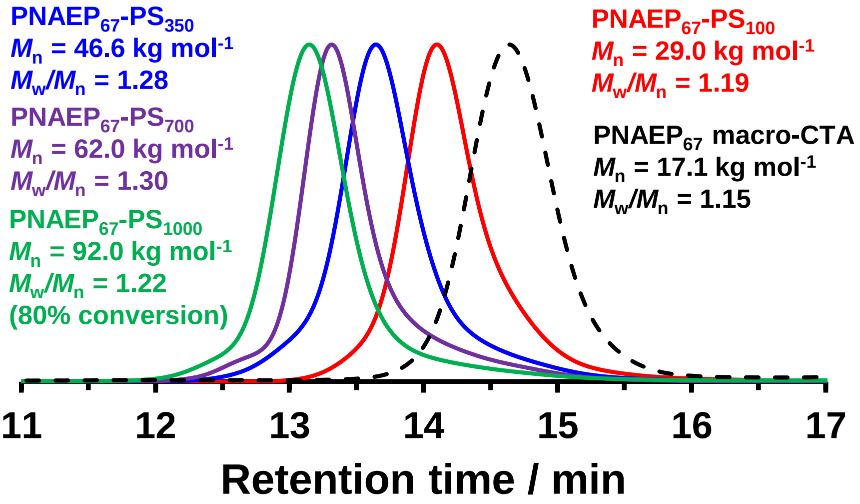

Figure 3.7. Chloroform GPC curves obtained for PNAEP$_{67}$−PS$_x$ diblock copolymers prepared at 20% w/w solids via RAFT aqueous emulsion polymerisation of styrene at 80 °C (where x = 100, 350, 700, or 1000). Molecular weight data are expressed relative to a series of near-monodisperse PS calibration standards. High conversions (<98%) are obtained when targeting PS DPs of up to 700, but only 80% conversion is achieved when targeting a PS DP of 1250 (green curve).

However, only 80% styrene conversion could be achieved when targeting a polystyrene DP of 1250. This is because such formulations require a relatively low concentration of the PNAEP$_{67}$ precursor and hence also the VA-044 initiator. Thus, the radical flux is significantly lower, which in turn affects the rate of polymerisation. Chloroform GPC analysis of the four PNAEP$_{67}$−PS$_x$ diblock copolymers shown in Figure

3.7 confirmed relatively high blocking efficiencies for the $PNAEP_{67}$ precursor and indicated a linear evolution in M_n when targeting longer PS block DPs. DLS was used to characterise dilute aqueous dispersions of the three $PNAEP_{67}-PS_x$ formulations for which 100% conversion was achieved (Figure 3.8).

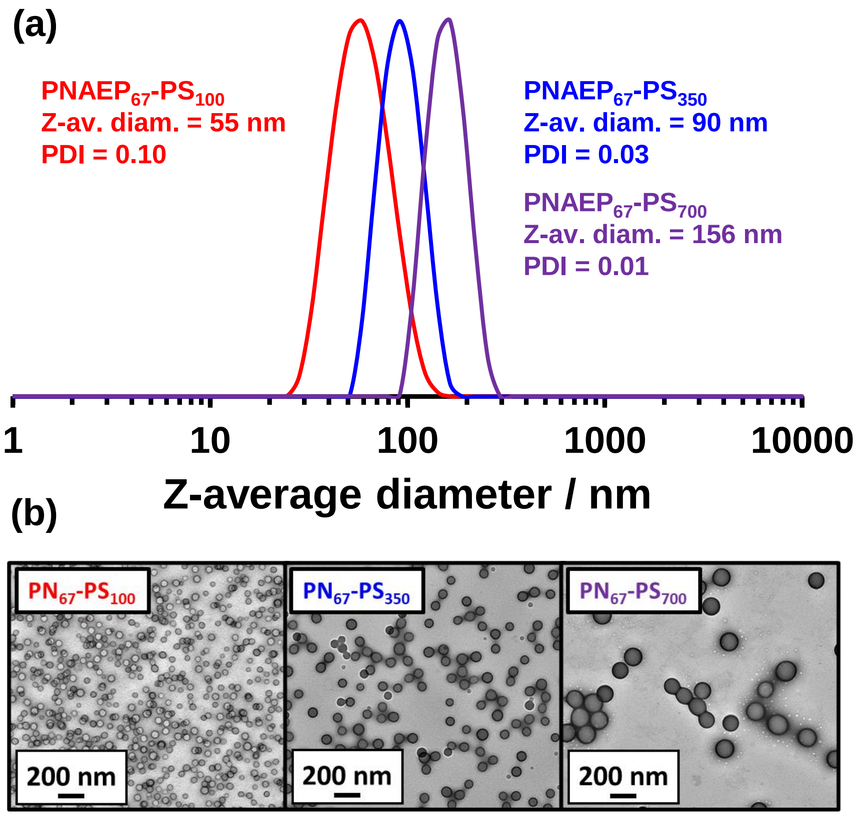

Figure 3.8. $PNAEP_{67}-PS_x$ diblock copolymer nanoparticles prepared at 20% w/w solids via RAFT aqueous emulsion polymerisation of styrene at 80 °C: (a) DLS particle size distributions obtained for x = 100, 350, and 700 (b) corresponding TEM images showing well-defined kinetically trapped spherical nanoparticles in each case.

For a fixed $PNAEP_{67}$ precursor, targeting higher PS DPs proved to be a highly convenient means of controlling the overall particle size. For example, amphiphilic $PNAEP_{67}-PS_{100}$ chains self-assembled to form nanoparticles with a mean hydrodynamic diameter of 55 nm, whereas $PNAEP_{67}-PS_{700}$ formed nanoparticles of 156 nm diameter. Moreover, relatively narrow particle size distributions were obtained (polydispersity index < 0.10). These DLS data were supported by TEM studies, which confirmed a well-defined spherical morphology in each case (Figure 3.8b). This suggests kinetically-trapped morphologies when targeting highly asymmetric diblock compositions such as $PNAEP_{67}-PS_{700}$.[53] Thus, the electrosteric stabilisation conferred by the $PNAEP_{67}$ stabiliser block is sufficient to prevent the stochastic 1D fusion of multiple spheres, which is a prerequisite for the production of so-called "higher order" morphologies such as worms or vesicles.[51,53,54] A range of diblock copolymer compositions and copolymer concentrations were explored, but in all cases only spherical morphologies were obtained (see Figure 3.9).

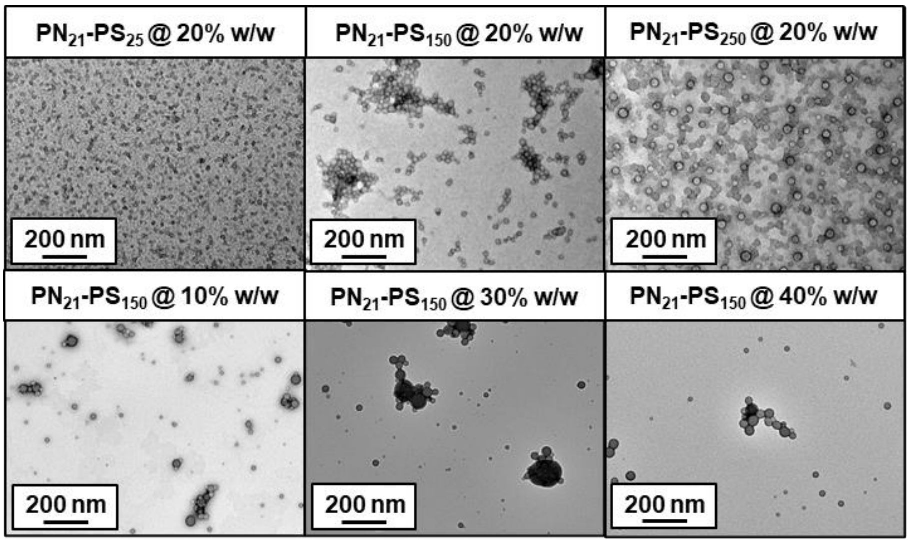

Figure 3.9. TEM images showing that kinetically-trapped spherical nanoparticles were obtained over a wide range of PN_{21}-PS_x diblock copolymer compositions and copolymer concentrations.

However, in at least some cases this restrictive paradigm can be overcome. For example, Hawkett and co-workers recently prepared polystyrene-based diblock copolymer vesicles via the RAFT aqueous emulsion polymerisation of styrene.[39] Currently, there is no convincing explanation for this rather puzzling aspect of aqueous PISA formulations, although incorporating oligo(ethylene glycol) (meth)acrylate comonomers does seem to be a useful, if rather empirical, approach for accessing worms and vesicles.[3,13,41,55]

3.3.2 Synthesis of $PNAEP_{67}$–$PnBA_x$ Diblock Copolymer Nanoparticles via RAFT Aqueous Emulsion Polymerisation of nBA at 30 °C

The same $PNAEP_{67}$ was also used for the RAFT aqueous emulsion polymerisation of nBA. It is well established that acrylic polymerisations undergo chain transfer to polymer and that this side reaction is more pronounced at higher temperatures (see Figure 3.10).[56–58]

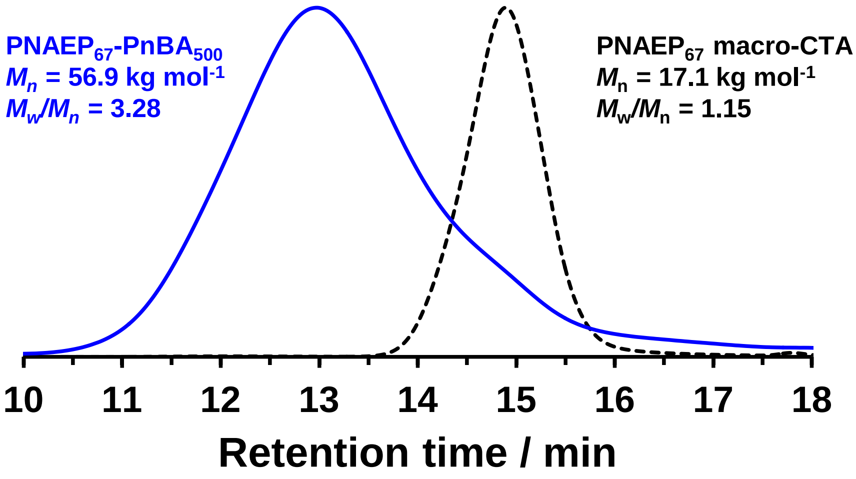

Figure 3.10. Chloroform GPC curves recorded for PNAEP$_{67}$-PnBA$_{500}$ diblock copolymers prepared at 20% w/w solids via RAFT aqueous emulsion polymerisation of nBA at 80 °C using VA-044 initiator at a [PNAEP$_{67}$]/[VA-044] molar ratio of 5.0. Molecular weight data are expressed relative to a series of near-monodisperse polystyrene calibration standards.

In view of this problem, a well-known low-temperature redox initiator couple[59–61] composed of KPS and AsAc was used to conduct the RAFT aqueous emulsion polymerisation of nBA at 30 °C in order to minimise the degree of branching (Scheme 3.3).

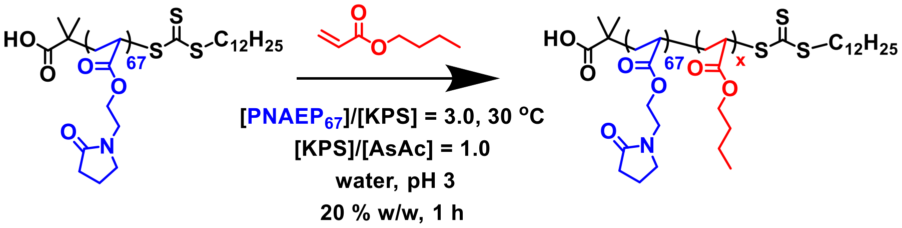

Scheme 3.3. Synthesis of PNAEP$_{67}$-PnBA$_x$ diblock copolymer nanoparticles via RAFT aqueous emulsion polymerisation of nBA at 30 °C targeting 20% w/w solids.

Representative kinetic data obtained for the RAFT aqueous emulsion polymerisation of nBA at 30 °C when targeting PNAEP$_{67}$−PnBA$_{500}$ diblock copolymer nanoparticles at 20% w/w solids are shown in Figure 3.11. Aliquots were taken from the polymerising reaction solution at regular time intervals prior to analysis by ^{1}H NMR spectroscopy. The nBA polymerisation proceeded after a relatively short induction period (5 min), after which an approximate 21-fold rate increase was observed, corresponding to 7% nBA conversion (Figure 3.11a). Moreover, visual inspection of the reaction mixture indicated that clarification of the initially milky emulsion occurred on the same time scale.

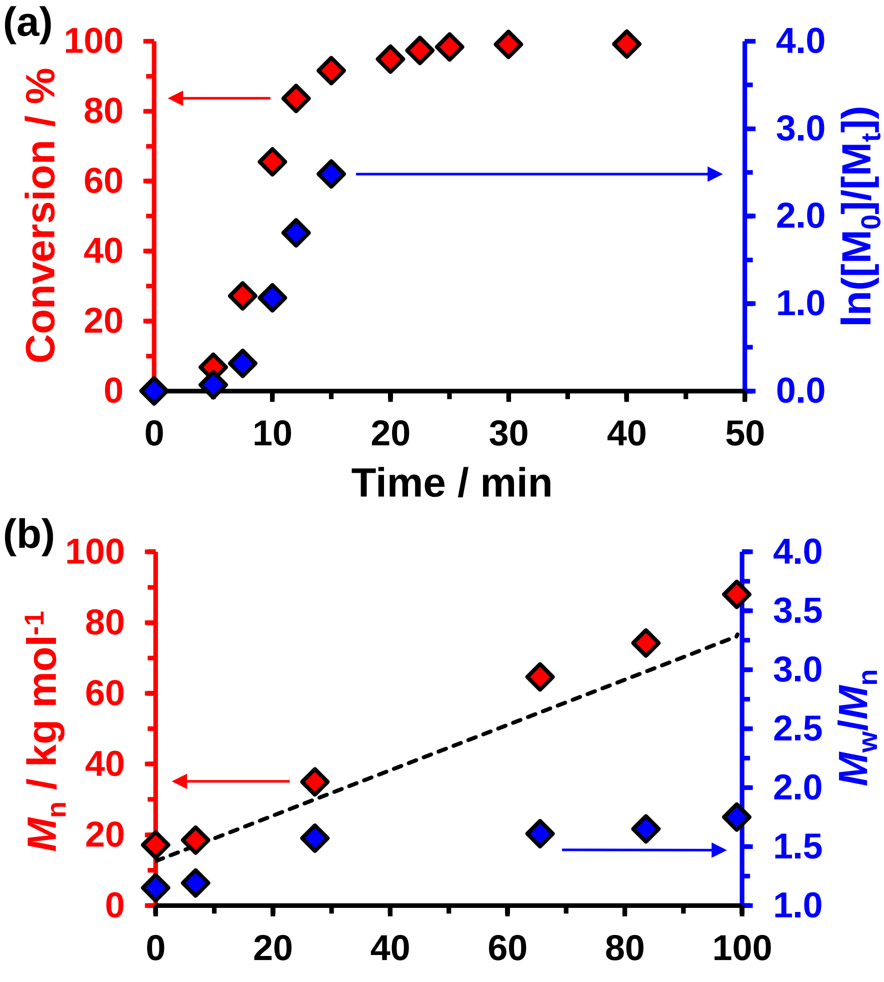

Figure 3.11. PISA synthesis of PNAEP$_{67}$−PnBA$_{500}$ nanoparticles at 20% w/w solids via RAFT aqueous emulsion polymerisation of nBA at 30 °C using a [PNAEP$_{67}$]/[KPS] molar ratio of 3.0: (a) conversion vs time curve and the corresponding semilogarithmic plot, as determined by ^{1}H NMR spectroscopy; (b) evolution of M_n and M_w/M_n against conversion determined by chloroform GPC using a series of near-monodisperse PS calibration standards.

DLS analysis of aliquots taken from the reaction mixture confirmed that this acceleration coincided with micellar nucleation (see Figure 3.12), for which the critical

PnBA DP is around 35. First-order kinetics were then observed up to 90% conversion, and more than 99% nBA conversion was achieved within 25 min at 30 °C.

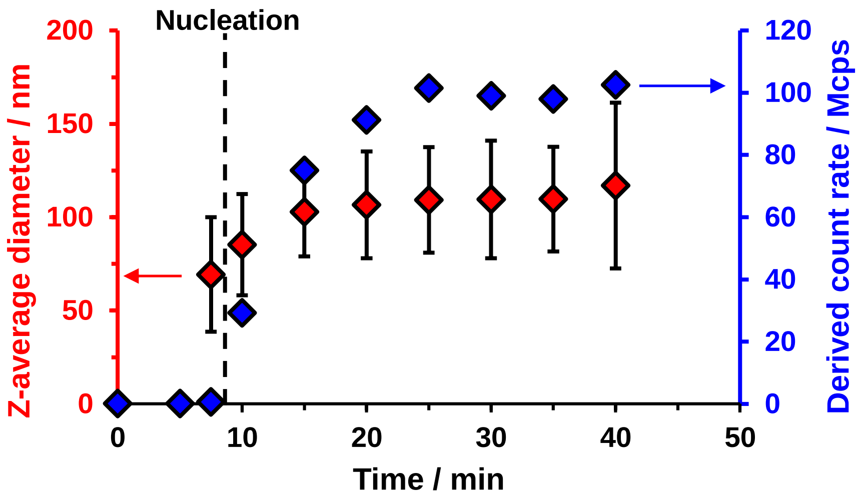

Figure 3.12. Evolution in *z*-average diameter and corresponding derived count rate (or scattered light intensity) over time as determined by DLS during the RAFT aqueous emulsion polymerisation of nBA at 30 °C and pH 3 when using a $PNAEP_{67}$ macro-CTA. Conditions: 20% w/w solids, $[PNAEP_{67}]/[Initiator] = 3.0$, target DP = 300. Note: The first two data points have been omitted owing to very low derived count rates (0.5 Mcps) and relatively large *z*-average diameters (> 500 nm), which are attributed to low concentrations of relatively large monomer droplets.

Reasonable RAFT control over this polymerisation was confirmed by chloroform GPC analysis, which revealed a linear relationship between M_n and monomer conversion. However, significantly broader MWDs ($M_w/M_n < 1.65$) were obtained compared to those observed for the styrene polymerisations (see Figure 3.11b). Similar observations have been reported for the RAFT aqueous emulsion polymerisation of nBA by other workers.[15,19,56] Moreover, the experimental M_n values were systematically higher than that expected. This can be partially attributed to the structural differences between the $PNAEP_{67}$–$PnBA_x$ diblock copolymers and the polystyrene standards used for GPC calibration. However, chain transfer to polymer is also likely to play a role here.[56]

Five $PNAEP_{67}$–$PnBA_x$ diblock compositions were targeted at 20% w/w solids via the RAFT aqueous emulsion polymerisation of nBA at 30 °C. At least 99% conversion was achieved within 1 h when targeting PnBA DPs of up to 750, as confirmed by ^1H NMR spectroscopy. However, only 72% conversion was achieved when targeting a PnBA DP of 1250. Chloroform GPC analysis indicated that relatively good RAFT control (M_w/M_n = 1.38) was achieved for a PnBA DP of 100 but relatively broad MWDs ($M_w/M_n > 1.50$) were obtained when targeting PnBA DPs above 250 (see Figure 3.13a). Furthermore, GPC analysis confirmed that the final diblock copolymer MWDs were contaminated with 5−10% residual PNAEP$_{67}$ precursor (Figure 3.13). Moreover, the similarity in the shape of both the RI (solid blue) and UV (dashed blue) curves indicates that even at 30 °C significant chain transfer to polymer is occurring and causing the molecular weight distributions to broaden (Figure 3.13b). This suggests slightly lower blocking efficiencies than those achieved for PNAEP$_{67}$−PS$_x$ nanoparticle syntheses (Figure 3.8).

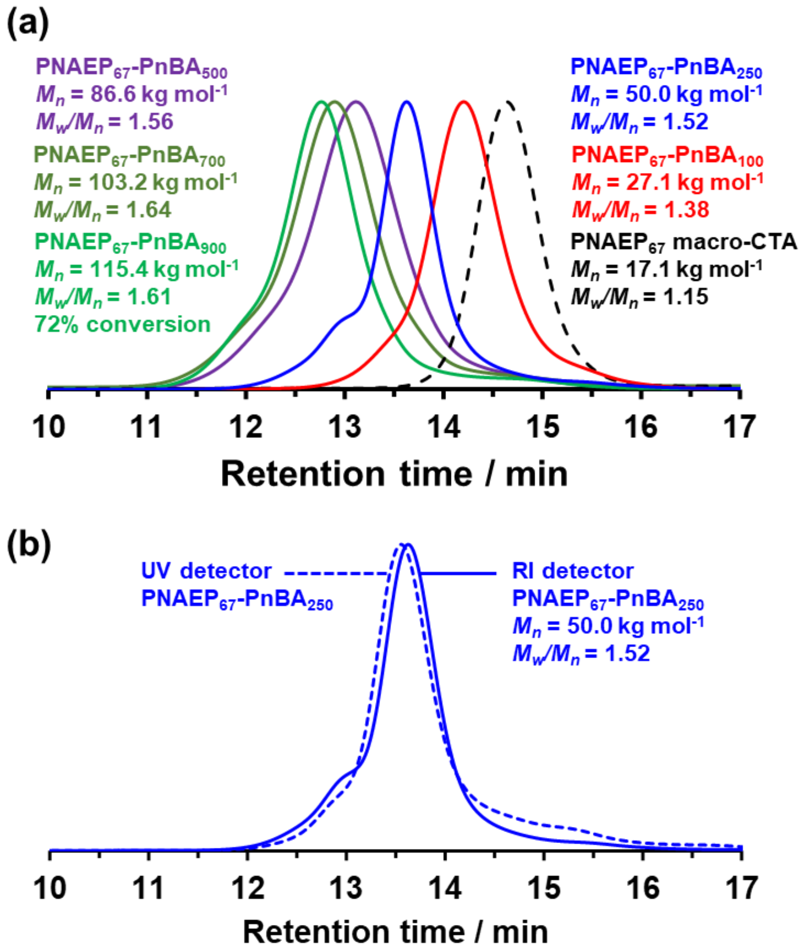

Figure 3.13. (a) Chloroform GPC curves recorded for PNAEP$_{67}$−PnBA$_x$ diblock copolymers (where x = 100, 250, 500, 700, or 900) prepared at 20% w/w solids via RAFT aqueous emulsion polymerisation of nBA at 30 °C using a refractive index (RI) detector. Molecular weight data are expressed relative to a series of near-monodisperse polystyrene calibration standards. (b) a comparison of the GPC curves recorded for a PNAEP$_{67}$-PnBA$_{250}$ diblock copolymer using either an RI detector (solid blue line) or a UV detector (dashed blue line). The apparent shift in retention time is simply because the UV detector is placed before the RI detector in the GPC set-up.

DLS analysis indicated that the mean sphere-equivalent nanoparticle diameter could be readily tuned from 45 to 141 nm simply by varying the target DP of the core-forming PnBA block from 100 to 700 for this PNAEP$_{67}$−PnBA$_x$ diblock copolymer series (Figure 3.14). Moreover, the relatively low DLS polydispersities are consistent with a kinetically-trapped spherical morphology. Unfortunately, the relatively low T_g of the PnBA homopolymer (–54 °C)[62] precluded meaningful TEM analysis of such nanoparticles.

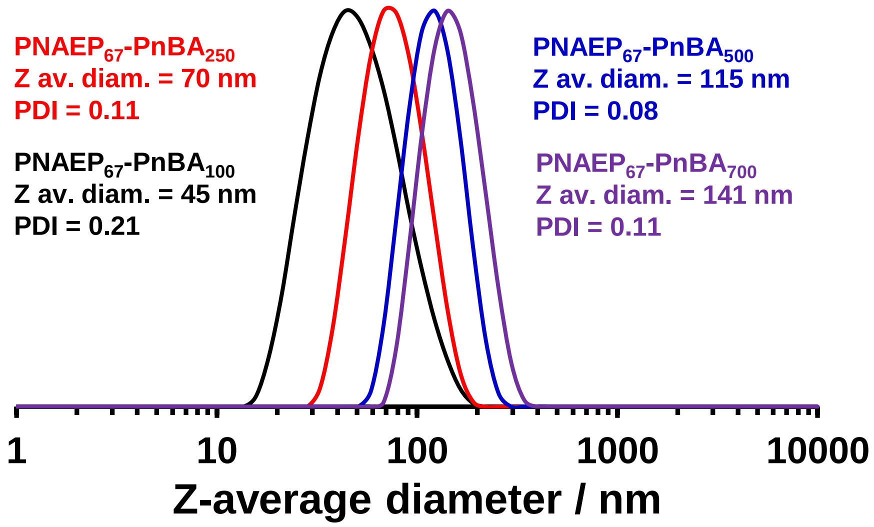

Figure 3.14. DLS particle size distributions recorded for four examples of PNAEP$_{67}$−PnBA$_x$ diblock copolymer nanoparticles (x = 100, 250, 500, and 700) prepared at 20% w/w solids via RAFT aqueous emulsion polymerisation of nBA at 30 °C.

3.3.3 Synthesis of PNAEP$_{67}$−P(S-*stat*-nBA)$_x$ Diblock Copolymer Nanoparticles via RAFT Aqueous Emulsion Polymerisation of styrene and nBA at 30 °C

Finally, PNAEP$_{67}$−P(S-*stat*-nBA)$_x$ diblock copolymer nanoparticles were synthesised via RAFT emulsion statistical copolymerisation of styrene (45 wt %) with nBA (55 wt %) at 20% w/w solids. Broad MWDs (M_w/M_n > 2.00) were observed when the synthesis of PNAEP$_{67}$−P(S-*stat*-nBA)$_x$ nanoparticles was attempted using the VA-044 initiator at 80 °C and pH 7, which correspond to the optimal conditions identified for the RAFT aqueous emulsion homopolymerisation of styrene (see Figure 3.15). This problem was attributed to the chain transfer to polymer at this relatively high reaction temperature. Moreover, some coagulum (>15%) was also observed for such high-temperature PISA syntheses. Thus, in order to ensure reasonable RAFT control and the formation of colloidally stable nanoparticles, the low-temperature redox initiator was utilised at pH 3 (see Scheme 3.4).

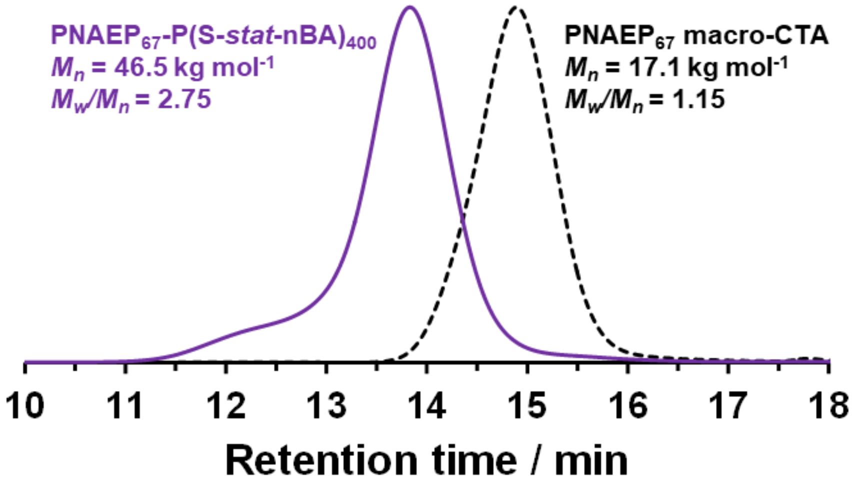

Figure 3.15. Chloroform GPC curves recorded for $PNAEP_{67}$-P(S-*stat*-nBA)$_{400}$ diblock copolymer nanoparticles prepared at 20% w/w solids *via* RAFT aqueous emulsion statistical copolymerisation of 45 wt.% styrene with 55 wt.% nBA at 80 °C using VA-044 initiator. Molecular weight data are expressed relative to a series of near-monodisperse polystyrene calibration standards.

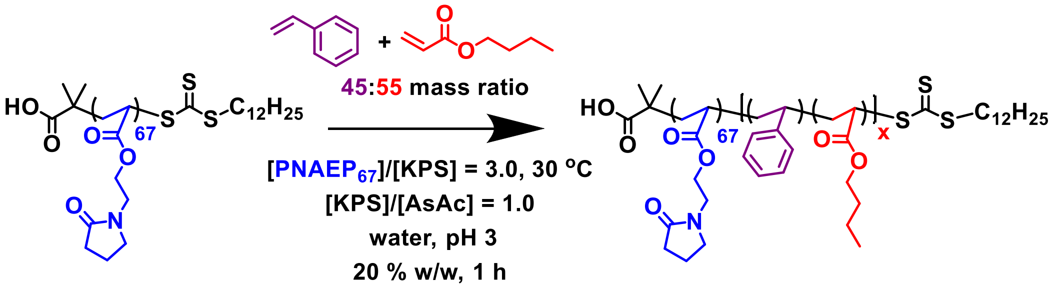

Scheme 3.4. Synthesis of $PNAEP_{67}$−P(S-*stat*-nBA)$_x$ diblock copolymer nanoparticles via RAFT aqueous emulsion statistical copolymerisation of styrene with nBA at 30 °C using a [$PNAEP_{67}$]/[KPS] molar ratio of 3.0 and a [KPS]/[AsAc] molar ratio of 1.0.

The kinetics for the RAFT aqueous emulsion statistical copolymerisation of styrene and nBA were monitored at 30 °C for a target $PNAEP_{67}$−P(S-*stat*-nBA)$_{100}$ diblock composition. Aliquots were taken at regular time intervals, and each reaction mixture was quenched by dilution and analysed in turn using ^{1}H NMR spectroscopy (Figure 3.16). A much longer induction period (95 min) was observed for this copolymerisation compared to those observed for the homopolymerisation of styrene (10 min) or nBA (5 min) using the same $PNAEP_{67}$ precursor (see Figures 3.4 and 3.11). This pronounced induction period has been reported in the literature and is attributed to styrene-terminated macroradicals, which exhibit much slower rates of addition compared to PBA-terminated radicals (as evidenced by the low styrene conversions obtained when polymerisations were attempted at 30 °C).[11,40,63]

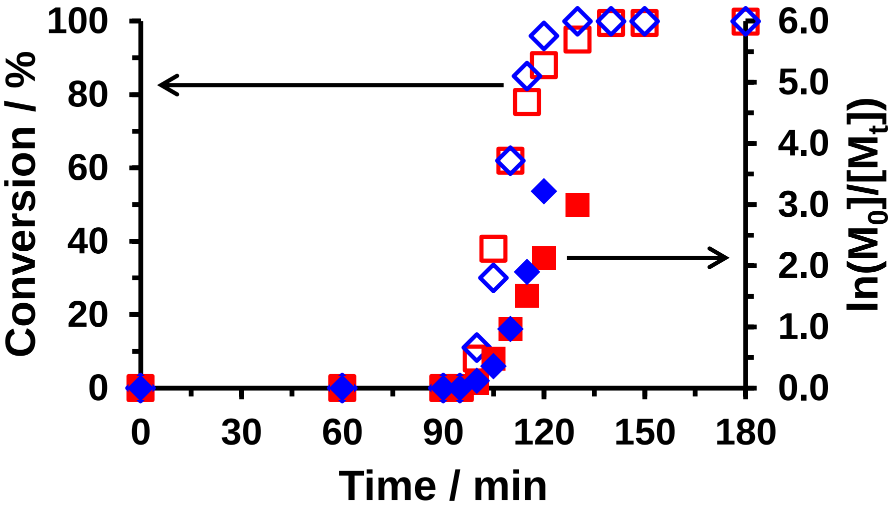

Figure 3.16. Conversion vs time curve (as determined by ^{1}H NMR spectroscopy) and the corresponding semilogarithmic plot obtained during the PISA synthesis of PNAEP$_{67}$−P(S-*stat*-nBA)$_{100}$ nanoparticles prepared at 20% w/w solids via RAFT aqueous emulsion statistical copolymerisation of 45 wt % styrene (open and filled red squares) with 55 wt % nBA (open and filled blue diamonds) at 30 °C using a [PNAEP$_{67}$]/[KPS] molar ratio of 3.0.

The vinyl signals for the two comonomers were readily distinguishable by ^{1}H NMR spectroscopy, which meant that their individual rates of reaction could be monitored (see Figure 3.17). After 105 min, the comonomer conversions were 11% for nBA and 8% for styrene: this is not unexpected given the significantly greater reactivity of the acrylic comonomer.[64] This time point appears to approximately correspond to the micellar nucleation event, with much greater rates of copolymerisation being observed thereafter. The initial gradients were calculated for each comonomer from their corresponding semilogarithmic plots: the initial rate of copolymerisation of nBA was 1.5 times faster than that of styrene. After 110 min, consumption of both comonomers reached 62%. However, nBA was fully consumed after 130 min, but only 95% styrene conversion had been achieved at this point. After 140 min, the styrene conversion reached 99%, indicating that very high final comonomer conversions can be achieved using the low-temperature redox initiator formulation. Two PNAEP$_{67}$−P(S-*stat*-nBA)$_x$ diblock copolymer formulations (where x = 100 or 400) were further investigated. ^{1}H NMR studies indicated that at least 99% comonomer conversion was achieved within 3 h in each case. Chloroform GPC analysis indicated that high blocking efficiencies and reasonable RAFT control (M_w/M_n < 1.55) were achieved (Figure 3.18). However, when an overall DP of 700 was targeted, only substantially incomplete conversion (67 and 46% conversions for nBA and styrene, respectively) was achieved under the same conditions.

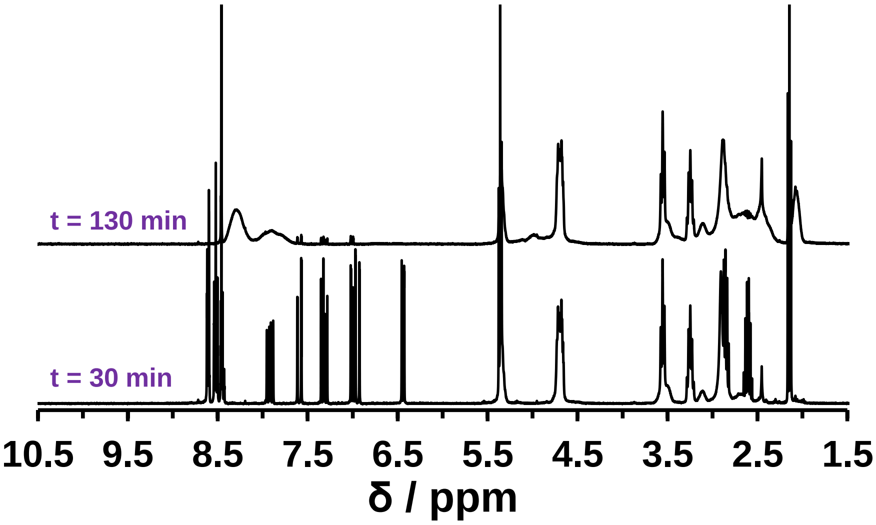

Figure 3.17. ^1H NMR spectra recorded in $CDCl_3$ after 30 min (lower spectrum) and 130 min (upper spectrum) during the synthesis of $PNAEP_{67}$-P(S-*stat*-nBA)$_{100}$ diblock copolymer nanoparticles prepared by RAFT aqueous emulsion statistical copolymerisation of 45 wt.% styrene with 55 wt.% nBA at 30 °C. Conditions: 1:1 KPS/AsAc low temperature initiator; 20% w/w solids.

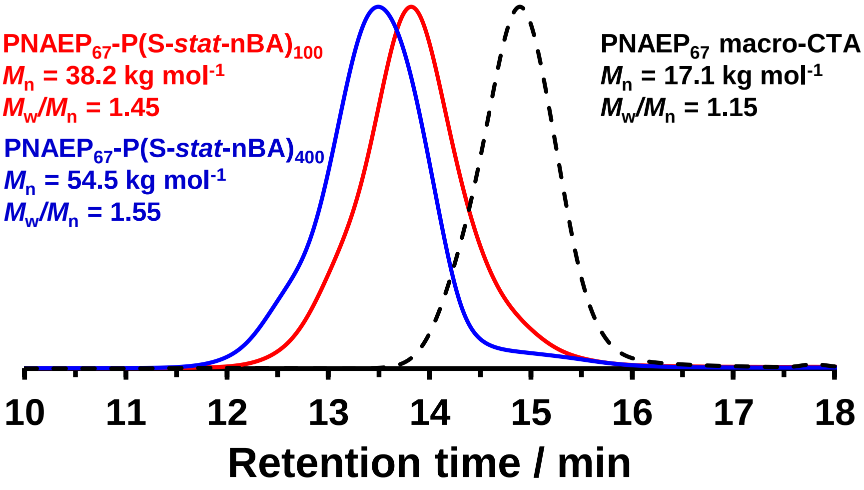

Figure 3.18. Chloroform GPC curves recorded for $PNAEP_{67}$−P(S-*stat*-nBA)$_x$ (where x = 100 or 400) diblock copolymer nanoparticles prepared at 20% w/w solids via RAFT aqueous emulsion statistical copolymerisation of 45 wt % styrene and 55 wt % nBA at 30 °C. Molecular weight data are expressed relative to a series of near-monodisperse PS calibration standards.

DLS and TEM studies on a 0.1% w/w dispersion of $PNAEP_{67}$−P(S-*stat*-nBA)$_{400}$ nanoparticles indicated that kinetically-trapped spheres with a mean hydrodynamic diameter of 99 nm and a relatively narrow particle size distribution (DLS polydispersity = 0.08) were obtained (Figure 3.19).

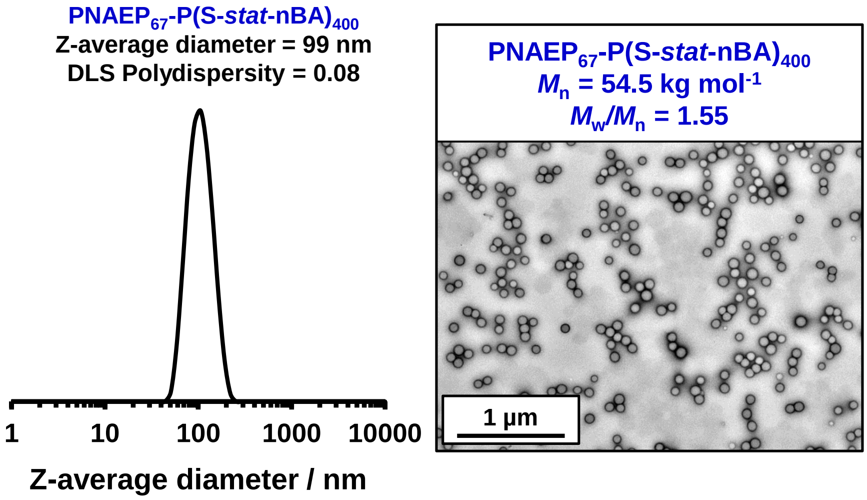

Figure 3.19. DLS particle size distribution and corresponding TEM image showing that well-defined, kinetically-trapped $PNAEP_{67}$-P(S-*stat*-nBA)$_{400}$ spheres are formed at 20% w/w solids via RAFT aqueous emulsion statistical copolymerisation of styrene and nBA at 30 °C.

3.3.4 Characterisation and Room Temperature Preparation of $PNAEP_{67}$-PS_x, $PNAEP_{67}$-$PnBA_x$ and $PNAEP_{67}$-P(S-*stat*-nBA)$_x$ Thin Films

DSC was used to determine T_g values for the $PNAEP_{67}$−$PnBA_{100}$, $PNAEP_{67}$−P(S-*stat*-nBA)$_{100}$, $PNAEP_{67}$−P(S-*stat*-nBA)$_{400}$, and $PNAEP_{67}$−PS_{100} diblock copolymers (Figure 3.20). Each diblock copolymer was dried from its 20% w/w aqueous dispersion in a vacuum oven at 30 °C for at least 24 h prior to analysis. DSC studies were performed using hermetically sealed aluminium pans at a heating rate of 10 °C min^{-1}. These DSC studies indicated that the $PNAEP_{67}$−$PnBA_{100}$ diblock copolymer had two distinct T_g values, indicating microphase separation between the hydrophilic and hydrophobic blocks (Figure 3.20). A lower T_g was observed at −46.9 °C, which is close to that reported for the PnBA homopolymer (−54 °C).[62] The second T_g occurred at 2.1 °C and is attributed to the $PNAEP_{67}$ block, because the T_g of the $PNAEP_{67}$ precursor is 4.2 °C. The DSC curve recorded for the $PNAEP_{67}$−PS_{100} diblock copolymer also exhibits two distinct T_g values at

1.3 and 81.1 °C, which correspond to the microphase-separated PNAEP and PS blocks, respectively.

According to Fox,[65] the T_g of a statistical copolymer can be calculated using Equation 3.5.

$$\frac{1}{T_g} = \frac{w_1}{T_{g1}} + \frac{w_2}{T_{g2}} \tag{3.5}$$

Here w_1 and w_2 are the weight fractions of the two comonomers, and T_{g1} and T_{g2} are the T_g values for their respective homopolymers. Using the experimental T_g values for the PS_{100} and $PnBA_{100}$ blocks obtained above, the theoretical T_g of the $PNAEP_{67}$−P(S-*stat*-nBA)$_{100}$ diblock copolymer was calculated to be 9 °C. This compares well with the experimental T_g value of 7.8 °C obtained from the corresponding DSC trace shown in Figure 3.20. However, the T_g of the $PNAEP_{67}$ block could not be observed because this thermal transition overlaps with that of the statistical copolymer block (Figure 3.20). Finally, increasing the DP from 100 to 400 raised the copolymer T_g from 7.8 to 18.0 °C, which was sufficient to enable the $PNAEP_{67}$ block T_g to be observed at approximately 1.3 °C.

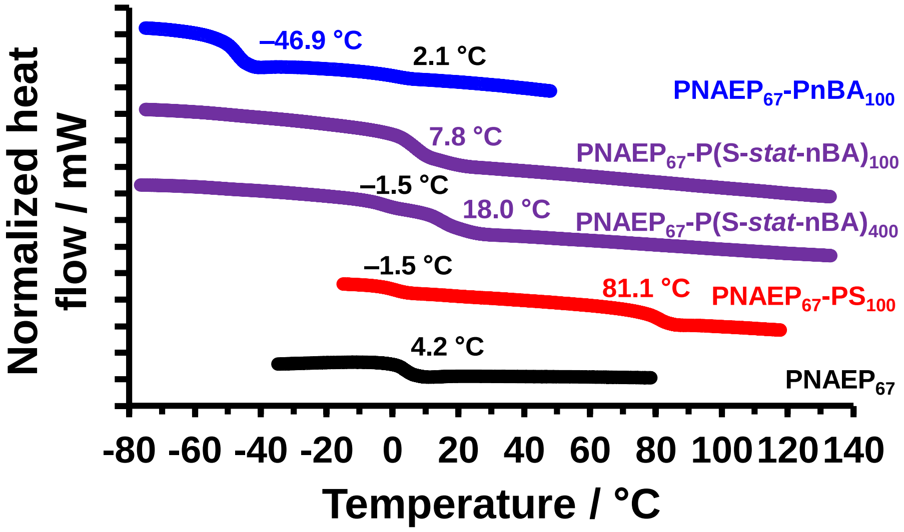

Figure 3.20. DSC curves recorded at a heating rate of 10 °C min^{-1} for $PNAEP_{67}$−$PnBA_{100}$, $PNAEP_{67}$−P(S-*stat*-nBA)$_{100}$, $PNAEP_{67}$−P(S-*stat*-nBA)$_{400}$, $PNAEP_{67}$−PS_{100}, and the $PNAEP_{67}$ macro-CTA. DSC curves are arbitrarily offset for the sake of clarity.

The optical transparency of $PNAEP_{67}-PS_{400}$, $PNAEP_{67}-PnBA_{400}$, and $PNAEP_{67}-P(S\text{-}stat\text{-}nBA)_{400}$ copolymer films prepared by spin-coating the corresponding aqueous dispersions onto glass slides was initially assessed by visual inspection. Unexpectedly, spin-coating $PNAEP_{67}-PS_{400}$ dispersions when targeting thin layers (<20 µm) produced relatively good-quality films despite the high T_g of the PS component. In this case, the PS cores do not undergo coalescence but are sufficiently small (<100 nm) that minimal light scattering occurs. However, increasing the film thickness led to embrittlement and a progressive reduction in transparency. Using $PNAEP_{67}-PnBA_{400}$ dispersions led to tacky, highly transparent films. Films prepared by spin-coating $PNAEP_{67}-P(S\text{-}stat\text{-}nBA)_{400}$ produced non-tacky, highly transparent films. Film transmittances were then assessed for three copolymer films of approximately the same mean thickness using visible absorption spectroscopy (see Figure 3.21). For 20 µm $PNAEP_{67}-PnBA_{400}$ and $PNAEP_{67}-P(S\text{-}stat\text{-}nBA)_{400}$ films, the transmission exceeded 95% over the entire range of wavelengths analysed (400−800 nm), with the pure $PNAEP_{67}-PnBA_{400}$ film being close to 100% transparent up to 600 nm. Conversely, films prepared from spin-coating a 20% w/w aqueous dispersion of $PNAEP_{67}-PS_{400}$ diblock copolymer nanoparticles remained below 85% transmittance. The films were less transparent at shorter wavelengths but still had a transmittance of more than 70% above 400 nm (Figure 3.21).

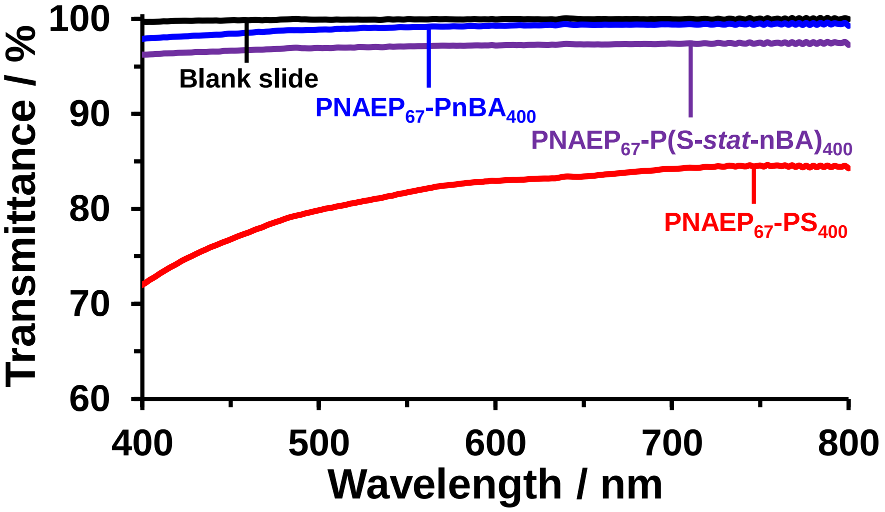

Figure 3.21. Transmission visible absorption spectra recorded for three copolymer films (mean film thickness = 20 µm) prepared via spin-coating 20% w/w aqueous dispersions of $PNAEP_{67}-PnBA_{400}$ (blue), $PNAEP_{67}-P(S\text{-}stat\text{-}nBA)_{400}$ (purple), and $PNAEP_{67}-PS_{400}$ (red) nanoparticles onto glass slides at 20 °C. The transmission spectrum (black) recorded for a blank glass slide is also shown as a reference.

3.4 Conclusions

A trithiocarbonate-based PNAEP macro-CTA with a degree of polymerisation of 67 ($PNAEP_{67}$) was used for the RAFT emulsion polymerisation of styrene, nBA, or statistical mixtures thereof. RAFT emulsion polymerisation of styrene using VA-044 initiator at 80 °C and pH 7 led to essentially full conversion within 40 min, with induction times as short as 10 min; GPC analysis indicated high blocking efficiencies and good control over the MWD ($M_w/M_n < 1.30$). DLS studies confirmed that systematically increasing the target DP from 100 to 700 enabled the *z*-average diameter of the resulting polystyrene−core spherical nanoparticles to be adjusted from 55 to 156 nm.

The same $PNAEP_{67}$ macro-CTA was then used for the RAFT emulsion polymerisation of nBA at 30 °C using a low-temperature redox initiator at pH 3, with essentially full conversion being achieved within 25 min. High blocking efficiencies were observed up to a PnBA target DP of 700 but relatively broad MWDs (M_w/M_n = 1.52−1.64) were obtained, presumably owing to side reactions such as chain transfer to polymer. DLS studies indicated that a series of $PNAEP_{67}$−$PnBA_x$ diblock copolymer spheres (where x = 100−700) exhibited *z*-average diameters ranging from 45 to 141 nm. Broad MWDs ($M_w/M_n > 2.00$) were observed when this synthesis was attempted using VA-044 initiator at 80 °C and pH 7, which correspond to the optimal conditions identified for the RAFT aqueous emulsion homopolymerisation of styrene. Moreover, significant coagulum (>15%) was observed for such high-temperature PISA syntheses.

Finally, the statistical copolymerisation of 45% styrene with 55% nBA was conducted with the low-temperature redox initiator at 30 °C using the $PNAEP_{67}$ macro-CTA. ^{1}H NMR analysis indicated a significantly longer induction period (95 min) compared to either homopolymerisation. Nevertheless, essentially full nBA conversion was achieved after 35 min, with all the styrene monomers being consumed within 45 min. DLS and TEM studies confirmed a well-defined spherical morphology for these relatively soft nanoparticles (*z*-average diameter = 99 nm, DLS polydispersity = 0.08). DSC analysis indicated that these styrene/nBA copolymers exhibited intermediate T_g values compared to the two respective homopolymers. Furthermore, these experimental data were in good agreement with theoretical values calculated using the Fox equation.

The film formation behaviour of selected diblock copolymer nanoparticles was explored using visible adsorption spectroscopy. The $PNAEP_{67}$−PS_{400} nanoparticles produced relatively good-quality particulate films despite the high T_g of the PS component. However, increasing the film thickness led to embrittlement and a reduction in transparency. The $PNAEP_{67}-PnBA_{400}$ films were found to be tacky and highly transparent. However, films prepared by spin-coating $PNAEP_{67}-P(S\text{-}\mathit{stat}\text{-}nBA)_{400}$ produced non-tacky, highly transparent films.

3.5 References

1 L. P. D. Ratcliffe, A. Blanazs, C. N. Williams, S. L. Brown and S. P. Armes, *Polym. Chem.*, 2014, **5**, 3643–3655.

2 J. Lesage de la Haye, I. Martin-Fabiani, M. Schulz, J. L. Keddie, F. D'Agosto and M. Lansalot, *Macromolecules*, 2017, **50**, 9315–9328.

3 S. Y. Khor, N. P. Truong, J. F. Quinn, M. R. Whittaker and T. P. Davis, *ACS Macro Lett.*, 2017, **6**, 1013–1019.

4 N. P. Truong, J. F. Quinn, A. Anastasaki, M. Rolland, M. N. Vu, D. M. Haddleton, M. R. Whittaker and T. P. Davis, *Polym. Chem.*, 2017, **8**, 1353–1363.

5 I. Martín-Fabiani, J. Lesage de la Haye, M. Schulz, Y. Liu, M. Lee, B. Duffy, F. D'Agosto, M. Lansalot and J. L. Keddie, *ACS Appl. Mater. Interfaces*, 2018, **10**, 11221–11232.

6 J. Zhou, H. Yao and J. Ma, *Polym. Chem.*, 2018, **9**, 2532–2561.

7 A. A. Cockram, R. D. Bradley, S. A. Lynch, P. C. D. Fleming, N. S. J. Williams, M. W. Murray, S. N. Emmett and S. P. Armes, *React. Chem. Eng.*, 2018, **3**, 645–657.

8 J. Tan, X. Dai, Y. Zhang, L. Yu, H. Sun and L. Zhang, *ACS Macro Lett.*, 2019, **8**, 205–212.

9 I. Martín-Fabiani, D. K. Makepeace, P. G. Richardson, J. Lesage de la Haye, D. A. Venero, S. E. Rogers, F. D'Agosto, M. Lansalot and J. L. Keddie, *Langmuir*, 2019, **35**, 3822–3831.

10 A. Guyot, *Curr. Opin. Colloid Interface Sci.*, 1996, **1**, 580–586.

11 I. Chaduc, M. Girod, R. Antoine, B. Charleux, F. D'Agosto and M. Lansalot, *Macromolecules*, 2012, **45**, 5881–5893.

12 W. Zhang, F. D'Agosto, P.-Y. Dugas, J. Rieger and B. Charleux, *Polymer*, 2013, **54**, 2011–2019.

13 X. Zhang, F. Boisson, O. Colombani, C. Chassenieux and B. Charleux, *Macromolecules*, 2014, **47**, 51–60.

14 I. Chaduc, A. Crepet, O. Boyron, B. Charleux, F. D'Agosto and M. Lansalot, *Macromolecules*, 2013, **46**, 6013–6023.

15 J. Rieger, G. Osterwinter, C. Bui, F. Stoffelbach and B. Charleux, *Macromolecules*, 2009, **42**, 5518–5525.

16 V. J. Cunningham, A. M. Alswieleh, K. L. Thompson, M. Williams, G. J. Leggett, S. P. Armes and O. M. Musa, *Macromolecules*, 2014, **47**, 5613–5623.

17 B. Akpinar, L. A. Fielding, V. J. Cunningham, Y. Ning, O. O. Mykhaylyk, P. W.

Fowler and S. P. Armes, *Macromolecules*, 2016, **49**, 5160–5171.

18 C. P. Jesson, V. J. Cunningham, M. J. Smallridge and S. P. Armes, *Macromolecules*, 2018, **51**, 3221–3232.

19 P. Gurnani, C. Sanchez-Cano, K. Abraham, H. Xandri-Monje, A. B. Cook, M. Hartlieb, F. Lévi, R. Dallmann and S. Perrier, *Macromol. Biosci.*, 2018, **18**, 1800213–1800222.

20 F. L. Hatton, A. M. Park, Y. Zhang, G. D. Fuchs, C. K. Ober and S. P. Armes, *Polym. Chem.*, 2019, **10**, 194–200.

21 P. J. Flory, *J. Chem. Phys.*, 1949, **17**, 1347–1348.

22 P. J. Flory and W. R. Krigbaum, *J. Chem. Phys.*, 1950, **18**, 1086–1094.

23 Z. Liu, H. Xiao, N. Wiseman and A. Zheng, *Colloid Polym. Sci.*, 2003, **281**, 815–822.

24 H. Tai, W. Wang and S. M. Howdle, *Polymer*, 2005, **46**, 10626–10636.

25 T. Tadros, *Colloids Surfaces A Physicochem. Eng. Asp.*, 2017, **519**, 11–19.

26 S. J. Byard, A. Blanazs, J. F. Miller and S. P. Armes, *Langmuir*, 2019, **35**, 14348–14357.

27 J. Xu, X. Xiao, Y. Zhang, W. Zhang and P. Sun, *J. Polym. Sci. Part A Polym. Chem.*, 2013, **51**, 1147–1161.

28 B. S. Tucker and B. S. Sumerlin, *Polym. Chem.*, 2014, **5**, 1566–1572.

29 N. J. Warren, O. O. Mykhaylyk, D. Mahmood, A. J. Ryan and S. P. Armes, *J. Am. Chem. Soc.*, 2014, **136**, 1023–1033.

30 N. P. Truong, M. V Dussert, M. R. Whittaker, J. F. Quinn and T. P. Davis, *Polym. Chem.*, 2015, **6**, 3865–3874.

31 S. J. Byard, M. Williams, B. E. McKenzie, A. Blanazs and S. P. Armes, *Macromolecules*, 2017, **50**, 1482–1493.

32 L. P. D. Ratcliffe, M. J. Derry, A. Ianiro, R. Tuinier and S. P. Armes, *Angew. Chemie Int. Ed.*, 2019, **58**, 18964–18970.

33 S. J. Byard, C. T. O'Brien, M. J. Derry, M. Williams, O. O. Mykhaylyk, A. Blanazs and S. P. Armes, *Chem. Sci.*, 2020, **11**, 396–402.

34 M. Lansalot and J. Rieger, *Macromol. Rapid Commun.*, 2019, **40**, 1800885.

35 M. Destarac and J. Wilson, WO/2013/113750, 2013.

36 S. Binauld, L. Delafresnaye, B. Charleux, F. D'Agosto and M. Lansalot, *Macromolecules*, 2014, **47**, 3461–3472.

37 A. Guinaudeau, O. Coutelier, A. Sandeau, S. Mazières, H. D. Nguyen Thi, V. Le Drogo, D. J. Wilson and M. Destarac, *Macromolecules*, 2014, **47**, 41–50.

38 V. J. Cunningham, M. J. Derry, L. A. Fielding, O. M. Musa and S. P. Armes, *Macromolecules*, 2016, **49**, 4520–4533.

39 R. R. Gibson, S. P. Armes, O. M. Musa and A. Fernyhough, *Polym. Chem.*, 2019, **10**, 1312–1323.

40 Y. Shi, G. Liu, H. Gao, L. Lu and Y. Cai, *Macromolecules*, 2009, **42**, 3917–3926.

41 W. Zhang, F. D'Agosto, O. Boyron, J. Rieger and B. Charleux, *Macromolecules*, 2012, **45**, 4075–4084.

42 W.-J. Zhang, C.-Y. Hong and C.-Y. Pan, *J. Mater. Chem. A*, 2014, **2**, 7819–7828.

43 B. T. T. Pham, D. Nguyen, V. T. Huynh, E. H. Pan, B. Shirodkar-Robinson, M. Carey, A. K. Serelis, G. G. Warr, T. Davey, C. H. Such and B. S. Hawkett, *Langmuir*, 2018, **34**, 4255–4263.

44 G. Carrot, S. Diamanti, M. Manuszak, B. Charleux and J.-P. Vairon, *J. Polym. Sci. Part A Polym. Chem.*, 2001, **39**, 4294–4301.

45 M. Chenal, C. Véchambre, J.-M. Chenal, L. Chazeau, V. Humblot, L. Bouteiller, C. Creton and J. Rieger, *Polymer*, 2017, **109**, 187–196.

46 C. Y. Kan, D. S. Liu, X. Z. Kong and X. L. Zhu, *J. Appl. Polym. Sci.*, 2001, **82**, 3194–3200.

47 Y. Lu, Y. Xia and R. C. Larock, *Prog. Org. Coatings*, 2011, **71**, 336–342.

48 G. Gody, T. Maschmeyer, P. B. Zetterlund and S. Perrier, *Macromolecules*, 2014, **47**, 3451–3460.

49 F. Stoffelbach, L. Tibiletti, J. Rieger and B. Charleux, *Macromolecules*, 2008, **41**, 7850–7856.

50 J. Bernard, M. Save, B. Arathoon and B. Charleux, *J. Polym. Sci. Part A Polym. Chem.*, 2008, **46**, 2845–2857.

51 A. Blanazs, J. Madsen, G. Battaglia, A. J. Ryan and S. P. Armes, *J. Am. Chem. Soc.*, 2011, **133**, 16581–16587.

52 W. H. Lane, *Ind. Eng. Chem. Anal. Ed.*, 1946, **18**, 295–296.

53 Y. Mai and A. Eisenberg, *Chem. Soc. Rev.*, 2012, **41**, 5969.

54 E. E. Brotherton, F. L. Hatton, A. A. Cockram, M. J. Derry, A. Czajka, E. J. Cornel, P. D. Topham, O. O. Mykhaylyk and S. P. Armes, *J. Am. Chem. Soc.*, 2019, **141**, 13664–13675.

55 J. Lesage de la Haye, X. Zhang, I. Chaduc, F. Brunel, M. Lansalot and F. D'Agosto, *Angew. Chemie Int. Ed.*, 2016, **55**, 3739–3743.

56 N. M. Ahmad, B. Charleux, C. Farcet, C. J. Ferguson, S. G. Gaynor, B. S. Hawkett, F. Heatley, B. Klumperman, D. Konkolewicz, P. A. Lovell, K. Matyjaszewski and R. Venkatesh, *Macromol. Rapid Commun.*, 2009, **30**, 2002–2021.

57 A. Agirre, J. I. Santos, A. Etxeberria, V. Sauerland and J. R. Leiza, *Polym. Chem.*, 2013, **4**, 2062–2079.

58 I. J. Johnson, E. Khosravi, O. M. Musa, R. E. Simnett and A. M. Eissa, *J. Polym. Sci. Part A Polym. Chem.*, 2015, **53**, 775–786.

59 G. S. Misra and C. V Gupta, *Die Makromol. Chemie*, 1973, **165**, 205–216.

60 H. Narain, S. M. Jagadale and N. D. Ghatge, *J. Polym. Sci. Polym. Chem. Ed.*, 1981, **19**, 1225–1238.

61 D. E. Cabelli and B. H. J. Bielski, *J. Phys. Chem.*, 1983, **87**, 1809–1812.

62 R. H. Wiley and G. M. Brauer, *J. Polym. Sci.*, 1948, **3**, 647–651.

63 T. R. Guimarães, M. Khan, R. P. Kuchel, I. C. Morrow, H. Minami, G. Moad, S. Perrier and P. B. Zetterlund, *Macromolecules*, 2019, **52**, 2965–2974.

64 R. A. Lyons, J. Hutovic, M. C. Piton, D. I. Christie, P. A. Clay, B. G. Manders, S. H. Kable and R. G. Gilbert, *Macromolecules*, 1996, **29**, 1918–1927.

65 T. G. Fox, *Bull. Am. Phys. Soc.*, 1956, **1**, 123.

Chapter 4

Synthesis and Characterisation of All-Acrylic Tetrablock Copolymer Nanoparticles via One-Pot RAFT Emulsion Polymerisation

4.1 Introduction

There are many RAFT-mediated PISA syntheses of diblock copolymer nanoparticles described in the literature that are prepared using either dispersion or emulsion polymerisation.[1–13] However, there are rather fewer examples of the synthesis of *multiblock copolymer nanoparticles*.[14–18] In 2013, Gody *et al*. reported the one-pot multistep sequential RAFT *solution* polymerisation of various acrylamides and acrylates (e.g. *N,N*-dimethylacrylamide (DMA), 4-acryloylmorpholine (NAM), *N,N*-diethylacrylamide (DEA) and *N*-isopropylacrylamide (NIPAM), acrylic acid (AA), poly(*n*-butyl acrylate) (PnBA) and 2-hydroxyethyl acrylate (HEA)) to prepare a wide range of multiblock copolymers at 65 or 70 °C using either AIBN or VA-044, repectively.[14] The synthesis of a hexablock, a dodecablock and finally an icosablock was used to highlight the versatility of this synthetic protocol, which provided access to relatively well-defined copolymer chains ($M_w/M_n < 1.40$) on a multi-gram scale. This pioneering study emphasised the importance of optimising the initiator concentration to control such RAFT solution polymerisations. More specifically, a relatively low initiator concentration was employed to minimise the formation of dead chains. Normally, this approach often leads to lower final monomer conversions. However, the relatively high propagation rate coefficients of acrylamides and acrylates enabled almost complete monomer conversion (> 99%) to be achieved for each block. One disadvantage of this study is that low block DPs were deliberately targeted to maximise RAFT control. This means that such multiblock copolymers are less likely to exhibit microphase separation in the solid state. Targeting significantly higher block DPs would lead to much more viscous copolymer solutions as well as reduced RAFT control. Furthermore, the formation of sterically-stabilised nanoparticles from such multiblock copolymers would most likely require tedious post-polymerisation processing using organic solvents.

It is well-documented that anionic polymerisation can be used to prepare well-defined ABA triblock copolymers where the outer A blocks are PS and the central B block is either PI or polybutadiene (PBD) to produce thermoplastic elastomers. Enthalpic incompatibility leads to microphase separation, with the PS blocks (T_g = 100 °C) forming hard, glassy domains at ambient temperature[19,20] embedded within a soft, rubbery matrix formed by the low T_g PI (or PBD) block.[21–23] The PS domains act as physical crosslinks and, if the soft central block is sufficiently long, this leads to a so-called synthetic rubber or thermoplastic elastomer. Such ABA triblock copolymers are highly flexible and extendable: the soft block chains uncoil when the material is stretched and the physical crosslinks ensure full elastic recovery once the applied stress is removed.[24] Importantly, this ABA block order is critical in order to achieve thermoplastic elastomeric properties as each end of the rubbery segment must be immobilised in the glassy domains to form a continuous network.[25] The microphase separation of block copolymers depends on the copolymer architecture, the relative block volume fractions and a sufficiently high χN parameter, where χ is the Flory-Huggins segmental interaction parameter and N is the mean degree of polymerisation.[26–29] It is well-known that high values of N favour strong segregation, while no microphase separation (or only weak segregation) is observed for relatively low N values.[30] Empirically, it is often observed that strong segregation usually occurs if $\chi N > 10$.[31] The ultimate mechanical properties of meth(acrylate)-based thermoplastic elastomers are relatively poor compared to the traditional styrenediene-based thermoplastic elastomers.[32–35] This is due to the much greater molecular weights between chain entanglements (M_e) required for (meth)acrylates (PnBA M_e = 28.0 kg mol^{-1})[35] compared to polydienes (PBD M_e = 1.7 kg mol^{-1} and PI M_e = 6.1 kg mol^{-1}).[36]

RAFT emulsion polymerisation offers an attractive route for the direct synthesis of high molecular weight multiblock copolymer nanoparticles in concentrated aqueous media.[16–18,37–39] This approach involves polymerising a water-immiscible monomer from one end of a water-soluble polymer precursor that acts as both a steric stabiliser and a RAFT agent. The growing hydrophobic block becomes insoluble at a relatively low critical DP, which leads to micellar nucleation. Unreacted monomer then diffuses into these nascent nanoparticles, which become monomer-swollen. The resulting high local monomer concentration leads to a significant increase in the rate of polymerisation.[40–43] This enables a relatively low initiator concentration to be employed, which maximises the pseudo-living character of the copolymer chains. The final latex enables a low-viscosity route to high molecular weight polymers that are more easily processed at an industrial scale. Nevertheless, there are surprisingly few literature reports of the synthesis of multiblock copolymer nanoparticles by RAFT emulsion polymerisation.[17,18,44]

Wang *et al.* used RAFT emulsion polymerisation to prepare well-defined, high molecular weight polystyrene-based nanoparticles.[45] The weak polyelectrolyte character of the poly(acrylic acid) precursor meant that the initial solution pH strongly influenced the ensuing styrene polymerisation. Thus, the RAFT emulsion polymerisation of styrene was initially performed at low pH to ensure good RAFT control. After micellar nucleation, the solution pH was raised to confer electrosteric stabilisation. This protocol afforded optimal RAFT control (M_n up to 544 kg mol^{-1}; $M_w/M_n < 1.26$). Subsequently, Luo *et al*. used this pH-switch method to prepare (PAA_{27}-PS_5)-PS_x-$PnBA_y$-PS_x tetrablock copolymer nanoparticles via sequential RAFT emulsion polymerisation of styrene (for 70 min), *n*-butyl acrylate (for 50 min) and styrene (for 85 min) under monomer-starved conditions (rate of monomer addition = 20 g per hour).[16] ^{1}H NMR studies indicated this was sufficient to reach more than 90% conversion for each block, which reduced the formation of gradient polymers at each stage. A series of relatively well-defined tetrablock copolymers (M_w/M_n = 1.41) were obtained when targeting an overall copolymer M_n of 86.1 kg mol^{-1} but significantly broader molecular weight distributions (M_w/M_n = 1.63-3.19) were observed when targeting higher molecular weights (M_n = 112 to 338 kg mol^{-1}). More specifically, the molecular weight distributions became broader for PnBA mass fractions of more than 60%. The mechanical properties of this series of thermoplastic elastomers were examined: tensile strengths of ~10 MPa and elongation at break values of 500% were obtained for PS contents of 40-50% by mass. The (PAA$_{27}$-PS$_5$)-PS$_x$-PnBA$_y$-PS$_x$ tetrablock copolymers were then isolated and subsequently solubilised as copolymer solutions in THF (10% w/w). Thermoplastic elastomer films were obtained by casting these solutions and allowing solvent evaporation over 3 days at room temperature. The films were dried to constant weight in a vacuum oven at 120 °C (above the T_g of PS) for 24 h. Preparing thermoplastic elastomer films directly from waterborne multiblock copolymer nanoparticles would avoid the use of such organic solvents and provide an industrially-relevant synthetic protocol.

A PAA$_{27}$-PS$_5$ precursor was later employed by Guimaraes *et al.* to prepare multiblock copolymers comprising four or more blocks via RAFT aqueous emulsion polymerisation.[17] A 'nonablock' PS homopolymer was prepared with at least 92% conversion being achieved within 3 h for each PS block (total reaction time = 9 x 3 = 27 h). However, after the sixth PS block the molecular weight distributions became broader (M_w/M_n = 1.4-1.7), suggesting a gradual loss of RAFT control. TEM and GPC studies were used to confirm that the mean contour length of the polymer chains is comparable to the particle radius. In principle, this means that one end of the polymer chain may be located at the surface of the particles while the other is located at the centre of the particle. In an attempt to prepare multiblock thermoplastic elastomers, the RAFT aqueous emulsion polymerisation of pure nBA was attempted. However, this only resulted in a relatively low monomer conversion despite employing a higher initiator concentration, longer polymerisation times and adjusting the solution pH. High nBA conversions could only be achieved if 10 wt.% styrene was added to the nBA monomer feed, with this statistical copolymerisation being performed over 18 h at 75 °C. This approach enabled the preparation of a P(AA$_{27}$-PS$_5$)-PS$_{200}$-P(BA-*stat*-S)$_{200}$-PS$_{200}$-P(BA-*stat*-S)$_{200}$-PS$_{200}$ hexablock copolymer, but GPC analysis indicated that the molecular weight distribution became significantly broader

(M_w/M_n > 1.5) after the third block. TEM studies of such copolymer particles were not possible owing to their film formation during TEM grid preparation. The nBA comonomer was then replaced with *n*-butyl methacrylate (BMA) and TEM studies confirmed that the resulting hexablock copolymer underwent microphase separation. This suggested the formation of a well-defined multi-layered onion-like structure within the nanoparticles. However, the statistical copolymerisation of styrene within the P(S-*stat*-BMA)$_{200}$ blocks must presumably result in poor mechanical properties (no data were reported by the authors) and the rather long polymerisation time (18 h) required to generate the P(S-*stat*-BMA)$_{200}$ block makes the synthesis of such multiblock copolymer nanoparticles unsuitable for industrial scale-up.

Herein we report the synthesis of new all-acrylic thermoplastic elastomer multiblock copolymer nanoparticles via sequential RAFT aqueous emulsion polymerisation of *n*BA and *t*-butyl acrylate (tBA) using PNAEP as a hydrophilic steric stabiliser block. It is well known that the propagation rate constants of acrylics are typically higher than that for the corresponding methacrylates (or styrene). Thus, this should enable high monomer conversions to be achieved for each block within relatively short polymerisation times. This should enable sufficient PnBA molecular weights to be reached affording high elasticity of the final tetrablock copolymer films (i.e. PnBA M_w > PnBA M_e). Despite tBA and nBA being structural isomers, ^{1}H NMR spectroscopy could be used to monitor the polymerisation kinetics. The T_g of PtBA homopolymer is sufficiently high (up to 50 °C)[46] compared to that of PnBA (T_g = –54 °C)[47–49] that thermoplastic elastomer films were anticipated when drying such tetrablock copolymer dispersions at ambient temperature. Moreover, the all-acrylic nature of this formulation should produce highly transparent films.

4.2 Experimental

4.2.1 Materials

NAEP was purified using the protocol outlined in Chapter 2. AsAc, KPS, DDMAT (98%), nBA, tBA, HCl and NaOH were purchased from Sigma-Aldrich (Dorset, UK). CD_3OD was purchased from Goss Scientific Instruments Ltd. (Cheshire, UK). All other solvents were purchased from Fisher Scientific (Loughborough, UK) and were used as received. Deionised water was used for all experiments and the solution pH was adjusted using either 1 M HCl or 1 M NaOH.

4.2.2 One-Pot Synthesis of $PNAEP_{85}$-$PtBA_{150}$-$PnBA_{x}$-$PtBA_{150}$ Tetrablock Copolymer Nanoparticles *via* Sequential RAFT Emulsion Polymerisation

A typical protocol used for the one-pot synthesis of $PNAEP_{85}$−P*t*BA_{150}-P*n*BA_{700}-P*t*BA_{150} tetrablock copolymer nanoparticles at 20% w/w solids was as follows: DDMAT RAFT agent (8.0 mg, 21.83 µmol) was added to NAEP (0.300 g, 1.64 mmol; target PNAEP DP = 75) and KPS (0.80 mg, 4.37 µmol; [DDMAT]/[KPS] molar ratio = 5.0) in a 28 mL glass vial charged with a magnetic flea (reaction solution 1). This vial was then placed in an ice bath and nitrogen was passed over the top of the solution for 30 min. Then the vial was immersed in an oil bath set at 30 °C. AsAc (1.20 mg, 4.37 µmol; [DDMAT]/[AsAc] molar ratio = 5.0; [KPS]/[AsAc] molar ratio = 1.0) and acidified deionised water (75.5 mg; pH 3; final solids concentration = 80% w/w) were combined and degassed before being added via a degassed syringe/needle to the glass vial containing reaction solution 1 under a nitrogen atmosphere. The ensuing NAEP polymerisation was allowed to proceed for 10 min prior to dilution of the viscous aqueous reaction solution via addition of degassed acidified water (2.62 g; pH 3; final target solids concentration = 20% w/w). The resulting reaction solution was then stirred magnetically for 2 min to ensure dissolution of the PNAEP homopolymer. A degassed syringe/needle was used to extract an aliquot for ^{1}H NMR spectroscopy analysis. The reduction in the monomer vinyl signals at 5.9 and 6.4 ppm relative to the integrated four ethyl protons at 3.4−3.8 ppm assigned to PNAEP indicated an NAEP conversion of 98%. The mean DP of this PNAEP precursor was calculated to be 85 as judged by ^{1}H NMR studies in CD_3OD [the integrated signal at 3.4-3.8 ppm (m, 4H) was compared to that at 0.86-0.96 ppm (t, 3H) assigned to the methyl RAFT chain-end]. DMF GPC analysis indicated an M_n of 15.5 kg mol^{-1} and an M_w/M_n of 1.15 compared to a series of ten near-monodisperse poly(methyl methacrylate) calibration standards. The reproducibility of this one-pot synthetic protocol is examined in Chapter 5. To generate the first PtBA block, degassed tBA (0.370 g, 2.92 mmol; PtBA target DP = 150) was added to the reaction solution. KPS (0.53 mg, 1.94 µmol; [$PNAEP_{85}$]/[KPS] molar ratio = 5.0) and AsAc (0.34 mg, 1.94 µmol; [$PNAEP_{85}$]/[AsAc] molar ratio = 5.0; [KPS]/[AsAc] molar ratio = 1.0) were added to the reaction mixture as dilute aqueous solutions (0.13 mM and 0.08 mM, respectively) using degassed syringe/needles. The tBA polymerisation was allowed to proceed for 30 min at 30 °C prior to dilution of the viscous aqueous reaction solution via addition of degassed acidified water (6.99 g; pH 3; final target solids concentration = 20% w/w). ^{1}H NMR spectroscopy studies indicated a final tBA conversion of 98%. The mean DP of the PtBA block was calculated to be 150 as judged by ^{1}H NMR spectroscopy analysis in CD_3OD [the integrated signal at 1.5 ppm (1350H) was compared to that assigned to two oxymethylene protons assigned to $PNAEP_{85}$ at 2.1-2.2 ppm (m, 170H)] (see Figure 4.3). DMF GPC analysis indicated an M_n of 27.9 kg mol^{-1} and an M_w/M_n of 1.31. To generate the PnBA block, degassed nBA (1.75 g, 13.62 mmol; PnBA target DP = 700) was added to the reaction solution. KPS (1.05 mg, 3.90 µmol; [$PNAEP_{85}$-$PtBA_{150}$]/[KPS] molar ratio = 10.0) and AsAc (0.69 mg, 3.90 µmol; [$PNAEP_{85}$-$PtBA_{150}$]/[AsAc] molar ratio = 10.0; [KPS]/[AsAc] molar ratio = 1.0) were added to the reaction mixture as dilute aqueous solutions (0.13 mM and 0.08 mM, respectively) using degassed syringe/needles. The nBA polymerisation was allowed to proceed for 40 min at 30 °C prior to dilution of the viscous aqueous reaction solution via addition of degassed acidified water (1.50 g; pH 3; final target solids concentration = 20% w/w). ^{1}H NMR studies indicated a final nBA conversion of 97%. The mean DP of the PtBA block was calculated to be 700 as judged by ^{1}H NMR analysis in CD_3OD [the integrated signal at 0.95 ppm (2100H) was compared to that assigned to four ethyl protons assigned to $PNAEP_{85}$ at 3.5-3.6 ppm (m, 340H)] (see Figure 4.3). DMF GPC analysis indicated an M_n of 114.6 kg mol^{-1} and an M_w/M_n of 1.54. To generate the second PtBA block, degassed tBA (0.370 g, 2.92 mmol; PtBA target DP = 150) was added to the reaction solution. KPS (0.53 mg, 1.94 µmol; [$PNAEP_{85}$-$PtBA_{150}$-$PnBA_{700}$]/[KPS] molar ratio = 5.0) and AsAc (0.34 mg, 1.94 µmol; [$PNAEP_{85}$-$PtBA_{150}$-$PnBA_{700}$]/[AsAc] molar ratio = 5.0; [KPS]/[AsAc] molar ratio = 1.0) were added to the reaction mixture as dilute aqueous solutions (0.13 mM and 0.08 mM, respectively) using degassed syringe/needles. The tBA polymerisation was allowed to proceed for 30 min at 30 °C before being quenched by exposing the reaction mixture to air and immersing the glass vial into an ice bath. ^{1}H NMR studies indicated a final tBA conversion of 99%. The mean DP of the PtBA block was calculated to be 150 as judged by ^{1}H NMR analysis in CD_3OD [the integrated signal at 1.5 ppm (total = 2700H, subtract 1350H from original $PtBA_{150}$ block = 1350H for second PtBA block) was compared with that assigned to four ethyl protons assigned to $PNAEP_{85}$ at 3.5-3.6 ppm (m, 340H)] (see Figure 4.3). DMF GPC analysis indicated an M_n of 131.5 kg mol^{-1} and an M_w/M_n of 1.59 when calibrated against a series of near-monodisperse PMMA standards. Other target tetrablock copolymer compositions were obtained by adjusting the [nBA]/[$PNAEP_{85}$-$PtBA_{150}$] molar ratio.

4.2.3 Copolymer Characterisation

^{1}H NMR Spectroscopy. Spectra were recorded in CD_3OD using a 400 MHz Bruker AVANCE-400 spectrometer with 64 scans being averaged per spectrum.

Gel Permeation Chromatography. Copolymer molecular weights and dispersities were determined using an Agilent 1260 Infinity GPC system equipped with both refractive index and UV−visible detectors. Two Agilent PLgel 5 μm Mixed-C columns and a guard column were connected in series and maintained at 60 °C. HPLC-grade DMF containing 10 mM LiBr was used as the eluent and the flow rate was set at 1.0 mL min^{-1}. A refractive index detector was used to calculate molecular weights and dispersities using a series of ten near-monodisperse poly(methyl methacrylate) calibration standards (with M_n values ranging from 370 to 2,520,000 g mol^{-1}).

Transmission Electron Microscopy. As-prepared copolymer dispersions were diluted at 20 °C using dilute aqueous HCl (pH 3) to generate 0.1% w/w aqueous dispersions. Copper/palladium TEM grids (Agar Scientific, UK) were coated in-house to produce thin films of amorphous carbon. These grids were then treated with a plasma glow discharge for 30 s to create a hydrophilic surface. One droplet of an aqueous copolymer dispersion (20 μL; 0.1% w/w) was placed on a freshly treated grid for 1 min and then blotted with a filter paper to remove excess solution. To stain the deposited nanoparticles, an aqueous solution of uranyl formate (10 μL; 0.75% w/w) was placed on the sample-loaded grid via micropipet for 45 s and then carefully blotted to remove excess stain. Each grid was then dried using a vacuum hose. Imaging was performed using a Philips CM100 instrument operating at 100 kV and equipped with a Gatan 1k CCD camera.

Dynamic Light Scattering. Measurements were conducted at 25 °C using a Malvern Instruments Zetasizer Nano ZS instrument equipped with a 4 mW He−Ne laser (λ = 633 nm) and an avalanche photodiode detector. Scattered light was detected at 173°. Copolymer dispersions were diluted to 0.10% w/w prior to analysis. Intensity-average hydrodynamic diameters were averaged over three runs and calculated using the Stokes−Einstein equation.

Differential scanning calorimetry. DSC studies were performed using a TA Instruments Discovery DSC instrument equipped with TZero low-mass aluminium pans and hermetically sealed lids. Copolymers were equilibrated above their T_g for 10 min before performing two consecutive thermal cycles at a rate of 10 °C min^{-1}. Two cycles were performed to minimize the thermal history of each sample.

Film Preparation. The as-prepared 20% w/w copolymer dispersions were allowed to dry on PTFE sheets in a 4 cm x 2 cm area at 20 °C in a fume cupboard for 24 h. The resulting films could be easily peeled off to produce free-standing films. The film thickness could be varied between 50 to 200 µm (± 10 µm) by drying larger volumes of the 20% w/w dispersion (1.0 ± 0.5 g to 5.0 ± 0.5 g, respectively).

Mechanical Properties. Preliminary tensile tests were performed by hand-stretching films, with digital photographs being recorded in their original relaxed state and at their maximum elongation before film rupture occurs. Changes in film length were measured using a ruler. After the stretched films were released, digital photographs were taken to ensure the films contracted to their original size.

Small Angle X-ray Scattering Studies. SAXS studies were conducted on 150 ± 10 µm $PNAEP_{85}$-$PtBA_{150}$-$PnBA_{400}$-$PtBA_{150}$ and $PNAEP_{85}$-$PtBA_{150}$-$PnBA_{700}$-$PtBA_{150}$ copolymer films using a Xeuss 2.0 (Xenocs) SAXS instrument equipped with a FOX 3D multilayered X-ray mirror, two sets of scatterless slits for collimation, a hybrid pixel area detector (Pilatus 1M, Dectris) and a liquid gallium MetalJet X-ray source (Excillum, λ = 1.34 Å). SAXS patterns were recorded at a sample-to-detector distance of approximately 1.20 m (calibrated using a silver behenate standard). 2D SAXS patterns were reduced to 1D plots by azimuthal integration within the Foxtrot software package.

SAXS patterns of 1.0% w/w aqueous tetrablock copolymer dispersions were collected at a synchrotron source (Diamond Light Source, station I22, Didcot, UK) using monochromatic X-ray radiation (wavelength, $\lambda = 0.124$ nm, with q ranging from 0.015 to 1.3 nm^{-1}, where $q = 4\pi \sin \theta/\lambda$ is the length of the scattering vector and θ is one-half of the scattering angle) and a 2D Pilatus 2M pixel detector (Dectris, Switzerland). Glass capillaries of 2.0 mm diameter were used as a sample holder. SAXS data were reduced (integration, normalization and absolute intensity calibration using SAXS patterns of deionized water assuming that the differential scattering cross-section of water is 0.0162 cm^{-1}) using Dawn software supplied by Diamond Light Source.[50]

4.3 Results and Discussion

4.3.1 Kinetic Study During the One-Pot Synthesis of PNAEP$_{85}$-PtBA$_{150}$-PnBA$_{x}$-PtBA$_{150}$ Tetrablock Copolymer Nanoparticles *via* Sequential RAFT Emulsion Polymerisation

The synthesis of block copolymer nanoparticles by RAFT aqueous emulsion polymerisation are typically afforded using a water-soluble precursor that acts as the steric stabiliser for the growing nanoparticles as well as the RAFT chain transfer agent.[43] Often this precursor is prepared by RAFT solution polymerisation in an organic solvent such as 1,4-dioxane. Such polymerisations are usually terminated at intermediate conversion to avoid monomer-starved conditions, which can lead to loss of RAFT chain-ends and hence lead to both homopolymer contamination and broadening of the final molecular weight distribution.[51] However, robust one-pot protocols have now been developed in which high conversion (>95%) is achieved for each block and the monomer for the subsequent block is added without any purification.[52,53] The synthesis of a 20% w/w aqueous dispersion of PNAEP$_{85}$-PtBA$_{150}$-PnBA$_{700}$-PtBA$_{150}$ tetrablock copolymer nanoparticles was attempted via initial RAFT aqueous solution polymerisation and subsequent sequential RAFT aqueous emulsion polymerisation using a four-step one-pot protocol at 30 °C (see Scheme 4.1). This redox couple and low polymerisation temperature was shown to be an appropriate initiator system for the RAFT emulsion polymerisation of nBA in Chapter 3. Moreover, the low temperature employed here should be sufficiently low to avoid ester hydrolysis of the tBA.[54] It was envisaged that the relatively high proportion of the soft PnBA block (62% by mass) should enable transparent elastomeric tetrablock copolymer films to be prepared via solution casting at ambient temperature.

First, a water-soluble PNAEP$_{85}$ precursor was prepared via RAFT aqueous solution polymerisation of NAEP (Scheme 4.1). ^{1}H NMR spectroscopy studies indicated that 98% NAEP conversion was achieved within 10 min. This relatively short timescale minimised premature loss of RAFT chain-ends owing to hydrolysis or other side-reactions.[55,56] This PNAEP$_{85}$ block was then chain-extended via RAFT aqueous emulsion polymerisation of tBA using the same low-temperature redox initiator ([PNAEP$_{85}$]/[KPS] molar ratio = 5.0) at 30 °C, see Scheme 4.1. Further initiator had to be added to ensure that a high monomer conversion was achieved, otherwise only 74% tBA conversion was obtained after 1 h at 30 °C (with no further increase in conversion being observed after 17 h at this temperature). DMF GPC studies performed on PNAEP$_{85}$-PtBA$_{150}$ diblock copolymers that had been synthesised at 350, 500 and 750 rpm indicated that the molecular weight distribution of the resulting PNAEP$_{85}$-PtBA$_{150}$ diblock copolymer was rather sensitive to the rate of stirring (see Figure 4.1).

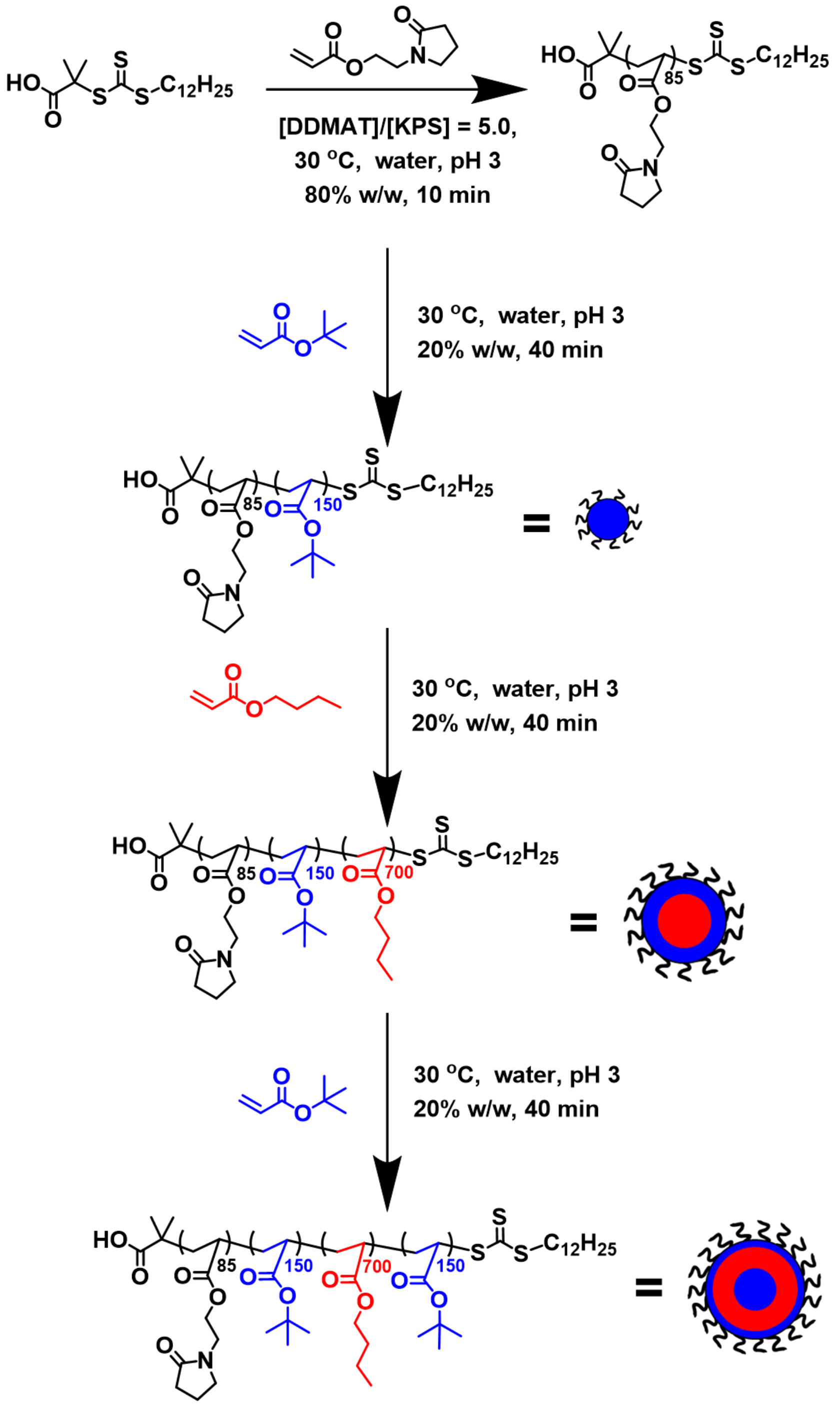

Scheme 4.1. Synthesis of PNAEP$_{85}$-PtBA$_{150}$-PnBA$_{700}$-PtBA$_{150}$ tetrablock copolymer nanoparticles via initial RAFT aqueous solution polymerisation and subsequent sequential RAFT aqueous emulsion polymerisation at 30 °C. Initiator was added with each monomer addition using a [KPS]/[AsAc] molar ratio of 1.0 and [trithiocarbonate]/[KPS] molar ratios of 5.0 for each tBA polymerisation and 10.0 for the NAEP and nBA polymerisations. Each

polymerisation was allowed to proceed until at least 95% conversion had been achieved prior to addition of the next monomer. Water was also added at each stage to maintain an overall copolymer concentration of 20% w/w.

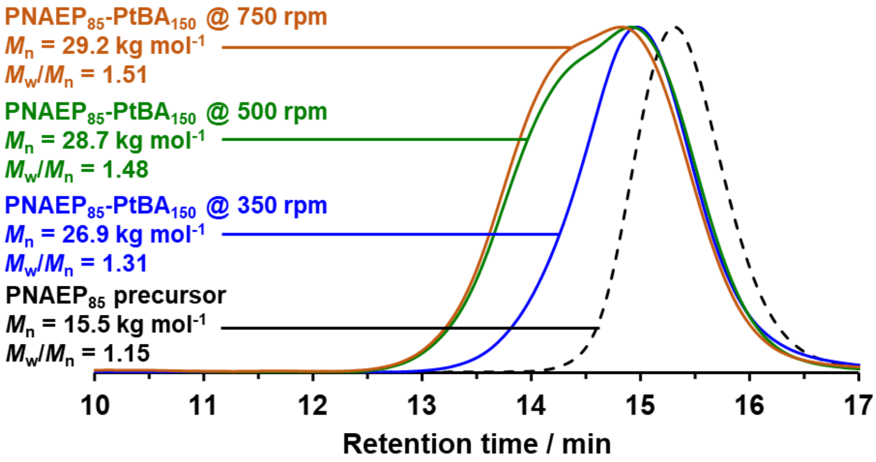

Figure 4.1. DMF GPC curves recorded for PNAEP$_{85}$-PtBA$_{150}$ diblock copolymers prepared using three different stirring rates (350, 500 or 750 rpm). Conducting the RAFT emulsion polymerisation of tBA at lower stirring rates resulted in substantially incomplete conversions. GPC data are expressed relative to a series of near-monodisperse poly(methyl methacrylate) calibration standards.

Interestingly, the *slowest* rate of stirring produced PNAEP$_{85}$-PtBA$_{150}$ diblock copolymers with a narrower molecular weight distribution (M_w/M_n = 1.31) compared to syntheses conducted using stirring rates of either 500 or 750 rpm (M_w/M_n = 1.48 or 1.51, respectively). However, attempting to perform the polymerisation at slower stirring rates merely resulted in incomplete conversion of the tBA monomer (e.g. only 87% tBA monomer conversion at 300 rpm). Thus, a stirring rate of 350 rpm was selected for all subsequent tetrablock copolymer syntheses. These findings are consistent with similar experiments conducted by Boissé *et al*., who reported that increasing the stirring rate from 100 to 750 rpm led to progressively broader molecular weight distributions (M_w/M_n values increased from 1.52 to 2.31, respectively) and faster rates of polymerisation.[57]

Presumably, faster stirring leads to smaller emulsion droplets, which leads to more efficient mass transport of the immiscible tBA monomer into the growing nanoparticles during RAFT emulsion polymerisation. Indeed, Perrier *et al.* recently published a series of papers investigating the importance of mass transport of monomer into the growing particles for such PISA formulations.[17,18,58,59] In particular, Richardson *et al.* reported that the diffusion-limited mass transport of BMA from monomer droplets into the growing polymer cores combined with the relatively high local concentration of RAFT chain-ends reduces the effective BMA/CTA molar ratio.[58] This reduces the number of monomer units added to each chain per activation/deactivation cycle (see RAFT mechanism in Figure XXX) and hence leads to narrow molecular weight distributions. However, the effect of varying the stirring rate was not examined. The curves shown in Figure 4.1 indicate that this can be an important parameter for RAFT aqueous emulsion polymerisation. This is consistent with the PISA literature for such heterogeneous formulations.[44,60]

^{1}H NMR spectroscopy was used to study the kinetics of the RAFT aqueous emulsion polymerisation of tBA (target DP = 150) at 30 °C using the PNAEP$_{85}$ precursor that was prepared *in situ*, see Figure 4.2. Periodic sampling of the reaction mixture involved dilution of each aliquot using CDCl$_3$, which was then dried using MgSO$_4$. ^{1}H NMR studies indicated an induction period of 5 min (see blue circles in Figure 4.2). After 15 min the tBA conversion was only 2.2%. This was attributed to the relatively low concentration of this water-immiscible monomer within the aqueous continuous phase. Thereafter, micellar nucleation produces nascent nanoparticles, which results in 24% tBA conversion after 20 min (i.e. just 5 min after nucleation). This polymerisation was allowed to continue for a further 10 min at 30 °C, which was sufficient to achieve 99% tBA conversion after 30 min, or an overall reaction time (including the RAFT solution polymerisation of NAEP) of 40 min (see Figure 4.2).

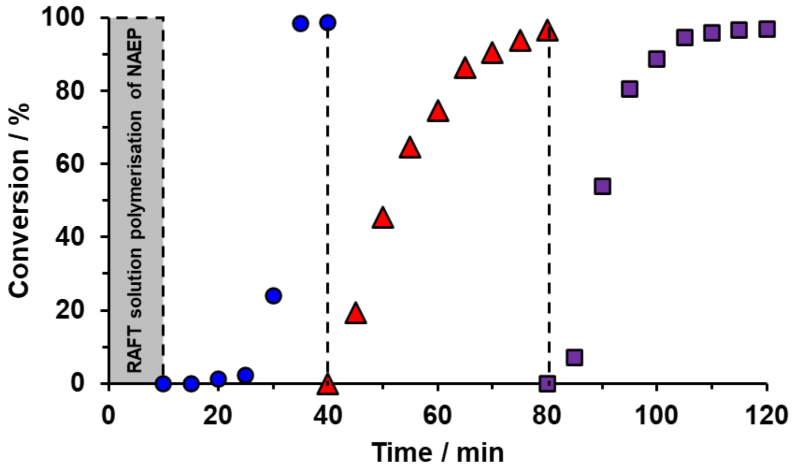

Figure 4.2. Conversion vs. time curves determined from ^{1}H NMR spectroscopy studies during the synthesis of PNAEP$_{85}$-PtBA$_{150}$-PnBA$_{700}$-PtBA$_{150}$ tetrablock copolymer nanoparticles at 30 °C via the one-pot sequential RAFT emulsion polymerisation of tBA (blue circles), nBA (red triangles) and tBA (purple squares) using a PNAEP$_{85}$ precursor that was synthesised *in situ* by RAFT aqueous solution polymerisation of NAEP at 80% w/w solids within 10 min (see grey region; kinetic data not shown). Target degrees of polymerisation were 150, 700 and 150 for the first PtBA block, the PnBA block and the second PtBA block, respectively. A [trithiocarbonate]/KPS molar ratio of 5.0 was used to prepare the two tBA blocks whereas a [trithiocarbonate]/KPS molar ratio of 10.0 was

employed for the polymerisation of nBA and NAEP. Vertical dashed lines indicate the injection times for the tBA, nBA and tBA monomers during this PISA synthesis.

After 30 min, the nBA and the KPS/AsAc initiator dissolved in dilute aqueous HCl (pH 3) were added to the reaction mixture under a nitrogen atmosphere. Although tBA and nBA are structural isomers, unique ^{1}H NMR signals for each block could be identified for the two corresponding homopolymers, see Figure 4.3. More specifically, tertiary methyl protons *c* assigned to PtBA and pendent methyl protons *d* assigned to PnBA were used to calculate instantaneous monomer conversions - and hence block DPs - throughout the polymerisation. ^{1}H NMR analysis indicated that 20% nBA conversion was achieved within 5 min at 30 °C. This step was allowed to proceed for 40 min to ensure a high final nBA conversion (>95%; see red triangles in Figure 4.2) prior to the final step. To complete the tetrablock copolymer synthesis, tBA monomer and further redox initiator dissolved in dilute aqueous HCl (pH 3) were added after 70 min. In this case, no induction period was observed and ^{1}H NMR analysis indicated a high final monomer conversion was achieved within 40 min (see purple squares in Figure 4.2). These kinetic studies confirm that PNAEP$_{85}$-PtBA$_{150}$-PnBA$_{700}$-PtBA$_{150}$ tetrablock copolymer nanoparticles can be prepared within 2 h at 30 °C using a convenient one-pot sequential RAFT emulsion polymerisation protocol. It is perhaps worth emphasising that this overall timescale is much shorter than that observed for various literature syntheses of multiblock copolymer nanoparticles, which typically require 3 to 18 h per block.[16–18]

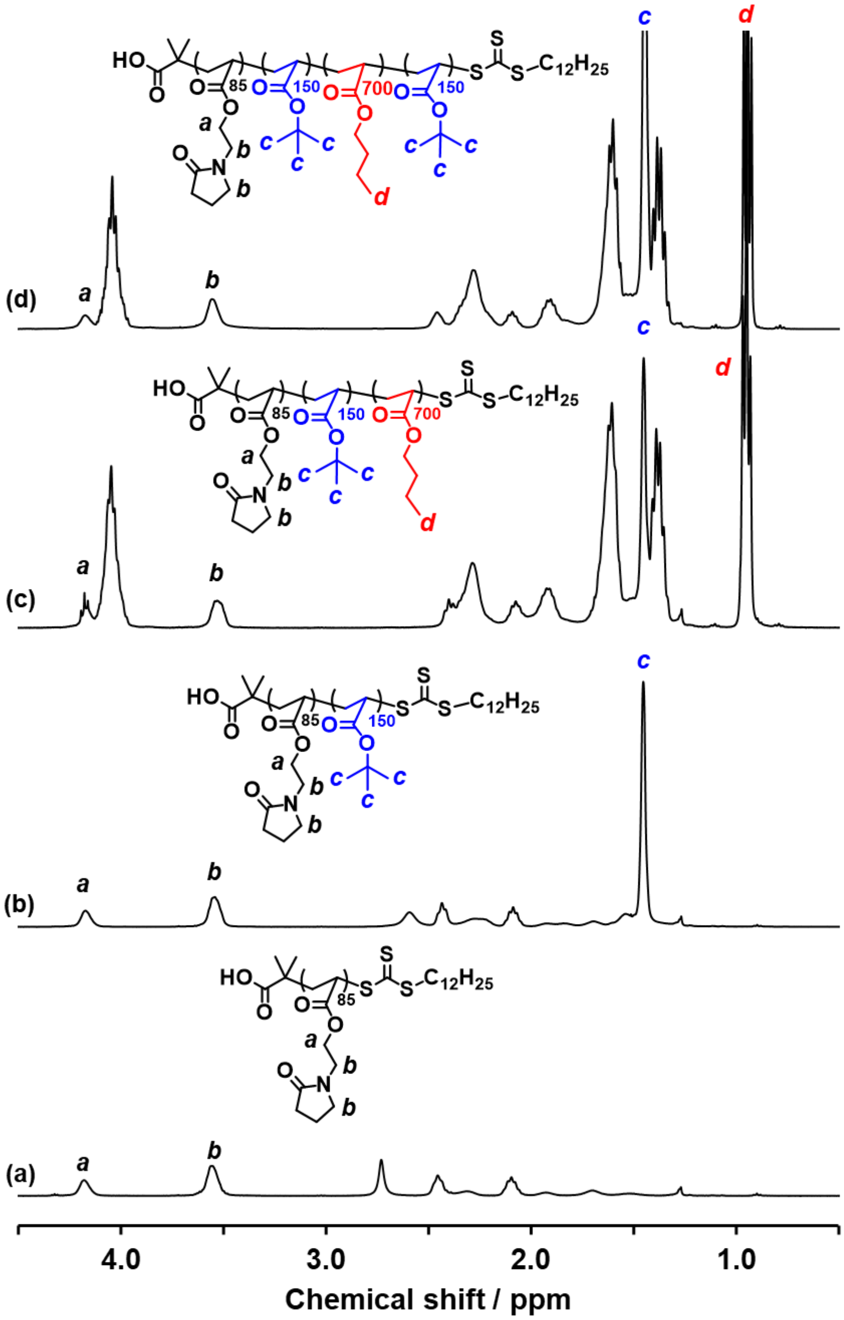

Figure 4.3. Partially assigned ^1H NMR spectra recorded in $CDCl_3$ for each stage of the sequential RAFT aqueous emulsion polymerisation synthesis outlined in Scheme 4.1: (a) the initial $PNAEP_{85}$ precursor, (b) the $PNAEP_{85}$-$PtBA_{150}$ diblock copolymer, (c) the intermediate $PNAEP_{85}$-$PtBA_{150}$-$PnBA_{700}$ triblock copolymer and (d) the final $PNAEP_{85}$-$PtBA_{150}$-$PnBA_{700}$-$PtBA_{150}$ tetrablock copolymer. In each spectrum, the protons associated with the growing block could be identified and did not overlap with the proton signals assigned to the PNAEP stabiliser block.

Each of the aliquots extracted during the ^1H NMR kinetics study were also analysed by DMF GPC to monitor the evolution in the copolymer molecular weight distribution (see Figure 4.4). A linear increase in M_n with monomer conversion was observed during each stage of this synthesis (Figure 4.4a). As expected, a relatively large increase in molecular weight (86.7 kg mol^{-1}) was observed for the synthesis of the PnBA$_{700}$ block, whereas two rather smaller increases in molecular weight (12.4 kg mol^{-1} and 16.9 kg mol^{-1}, respectively) for the synthesis of each PtBA$_{150}$ block. The latter difference is attributed to the fact that the PNAEP$_{85}$ precursor has a significant influence over the M_n observed for the PNAEP$_{85}$-PnBA$_{150}$ diblock copolymer but barely affects the M_n observed for the final tetrablock copolymer chains. Moreover, all such M_n data are apparent values that are expressed relative to poly(methyl methacrylate) calibration standards. The copolymer molecular weight distribution gradually broadened during the polymerisation (Figure 4.4b), with an M_w/M_n of 1.59 being observed for the final tetrablock copolymer. This is significantly higher than that expected for a well-controlled RAFT polymerisation (M_w/M_n << 1.50).[61–63] However, it compares quite well to GPC data reported in the literature for multiblock copolymer nanoparticles prepared by sequential RAFT aqueous emulsion polymerisation.[17,18,44] GPC curves obtained using either an RI detector (solid purple line in Figure 4.5) or a UV detector (dashed purple line in Figure 4.5) had comparable shapes, which suggests that the relatively broad final molecular weight distribution is simply the result of chain transfer to polymer. This is a well-documented side-reaction for acrylic polymers and is more readily observed for higher molecular weight chains[64–66] It is perhaps worth emphasizing that the higher observed dispersities indicate a significant increase in M_w relative to M_n, which may well be beneficial in terms of the mechanical properties ($M_w >> M_e$) exhibited by the corresponding tetrablock copolymer films (see below).

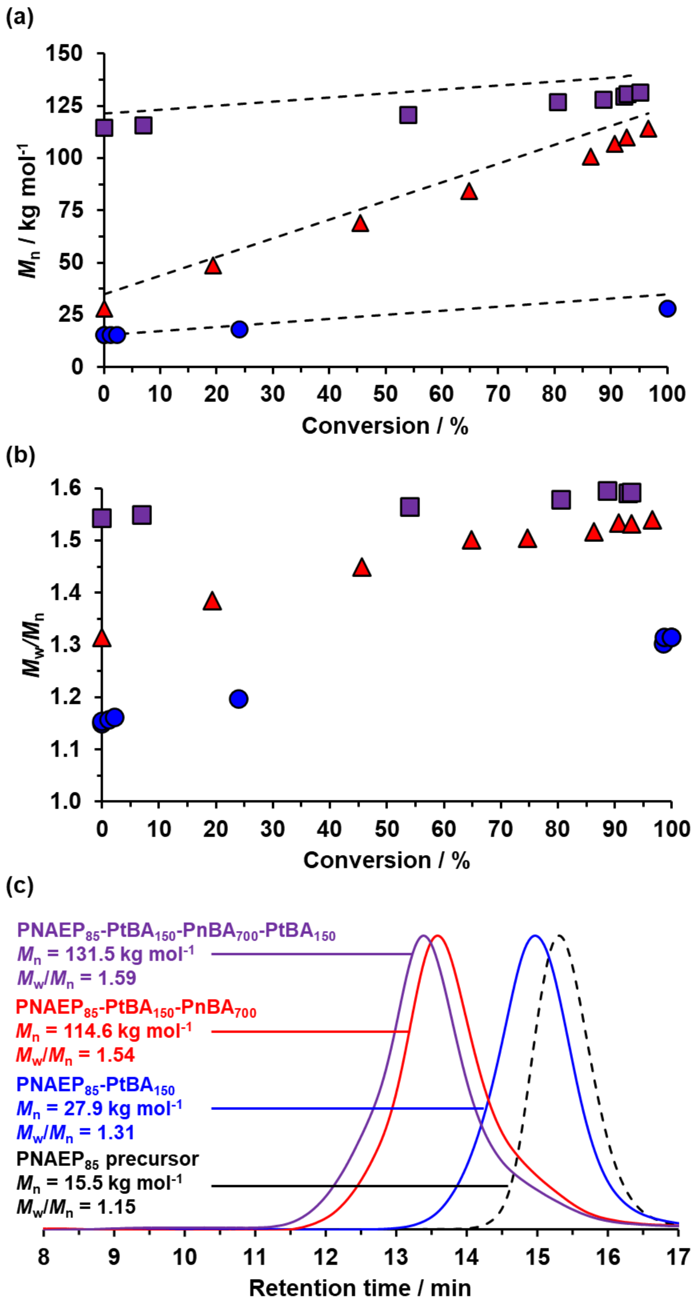

Figure 4.4. DMF GPC data illustrating the evolution in (a) M_n and (b) M_w/M_n vs. monomer conversion for growth of the first PtBA block (blue circles), the PnBA block (red triangles), and the second PtBA block (purple squares) during the synthesis of PNAEP$_{85}$-PtBA$_{150}$-PnBA$_{700}$-PtBA$_{150}$ tetrablock copolymer nanoparticles *via* one-pot RAFT aqueous emulsion polymerisation at 30 °C. In part (a), the dashed lines represent the theoretical M_n values for each block. (c) GPC curves recorded during the synthesis of the PNAEP$_{85}$-PtBA$_{150}$-PnBA$_{700}$-PtBA$_{150}$ tetrablock copolymer chains after more than 95% monomer conversion had been observed for each individual block (see Figure 4.2). GPC data are expressed relative to a series of near-monodisperse poly(methyl methacrylate) calibration standards).

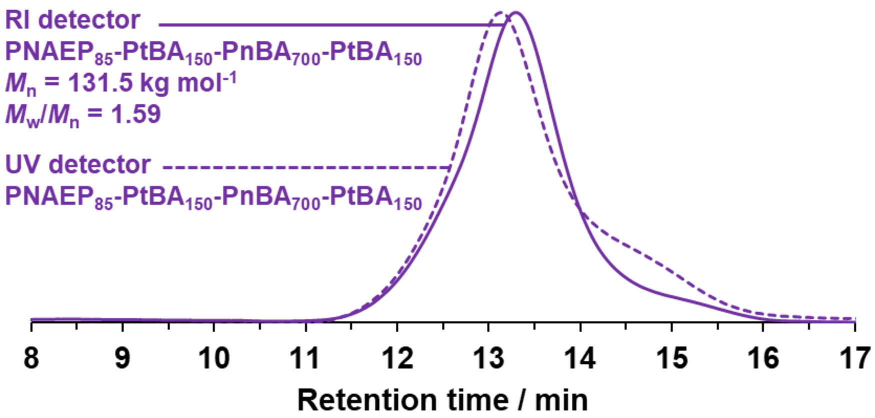

Figure 4.5. GPC curves recorded for a PNAEP$_{85}$-PtBA$_{150}$-PnBA$_{700}$-PtBA$_{150}$ tetrablock copolymer using either an RI detector (solid purple line) or a UV detector (dashed purple line). The apparent shift in retention time is simply because the UV detector is placed before the RI detector in the GPC set-up.

In principle, the isomeric nature of PtBA and PnBA might be expected to lead to only weak (or perhaps no) segregation between these two hydrophobic blocks in the solid state.[30] However, the T_g values for PnBA homopolymer (–54 °C)[47–49] and PtBA (29-50 °C)[46] differ significantly, which should promote microphase separation. According to Perrier and co-workers, hydrophobic RAFT Z-groups (such as that originating from DDMAT) should be located within the centre of the growing nanoparticles.[18] This should afford multi-layered 'onion-like' nanoparticles (see Scheme 4.1 and Figure 4.6a). However, it is not impossible for the central PnBA block to displace the PtBA chains from the copolymer/water interface.[67] One prerequisite for such engulfment is that the reaction temperature should be above the T_g of the engulfing polymer (i.e. the PnBA block). Since these syntheses are performed at 30 °C, this process could in principle occur.

DLS studies of aliquots extracted from the reaction mixture during the RAFT aqueous emulsion polymerisation of tBA confirmed the formation of well-defined nanoparticles, with a significant increase in the scattered light intensity (or derived count rates) indicating that micellar nucleation occurred within 25 min (Figure 4.6a). Well-defined PNAEP$_{85}$-PtBA$_{150}$ nanoparticles with a z-average diameter of 68 nm and a DLS polydispersity of 0.09 were formed within 40 min, with this timescale corresponding to the end of the tBA polymerisation (see Figure 4.6b). TEM analysis revealed the presence of spherical nanoparticles with a number-average diameter of 43 ± 6 nm (see Figure 4.6c). The significant discrepancy between the diameter obtained from DLS (68 nm) and TEM (43 nm) analysis is expected and arises due to the latter technique being used to determine the diameter of dehydrated cores whilst the former obtains the size of the particle from the hydrated shell surrounding the particles in motion. Furthermore, DLS is significantly more statistically robust than TEM with measurements averaged of many particles compared to the few spheres that are captured and subsequently measured in Figure 4.6c. Subsequent addition of nBA monomer led to an increase in the z-average diameter and DLS polydispersity within 5 min, which is ascribed to the formation of monomer-swollen nanoparticles (Figure 4.6a). This is consistent with the fact that no induction period was observed for this second-stage polymerisation (see Figure 4.2). A gradual increase in z-average diameter and reduction in DLS polydispersity was observed during the nBA polymerisation, resulting in the formation of relatively large, well-defined PNAEP$_{85}$-PtBA$_{150}$-PnBA$_{700}$ triblock copolymer nanoparticles (final z-average diameter = 123 nm, DLS polydispersity = 0.11; see Figures 4.6a and 4.6b). Close inspection of the TEM image shown in Figure 4.6c indicates the presence of partially fused aggregates comprising multiple spherical nanoparticles (apparent number-average diameter = 141 ± 18 nm). This artifact is simply the result of the relatively low T_g of the PnBA block, which comprises 72% of the triblock copolymer chains by mass. This leads to significant nanoparticle deformation during TEM grid preparation. Nevertheless, the presence of the high T_g PtBA component enabled representative TEM images to be recorded for these nanoparticles. Only a modest increase in z-average diameter and DLS polydispersity was observed after the synthesis of the second PtBA block (Figure 4.6a). However, this is not unexpected bearing in mind the relatively small DP difference between the intermediate triblock and the final tetrablock. After 120 min, the final PNAEP$_{85}$-PtBA$_{150}$-PnBA$_{700}$-PtBA$_{150}$ nanoparticles exhibited a z-average diameter of 138 nm and a DLS polydispersity = 0.11 (see Figure 4.6a and Figure 4.6b). TEM analysis confirmed a kinetically-trapped spherical morphology (Figure 4.6c), which is often observed for such RAFT aqueous emulsion polymerisation formulations.[17,42,68] As expected, targeting nanoparticles with a higher PtBA content minimised film formation during TEM grid preparation. In this case, TEM studies indicated a number-average diameter of 102 ± 10 nm, which is consistent with the z-average diameter of 138 nm reported by DLS.

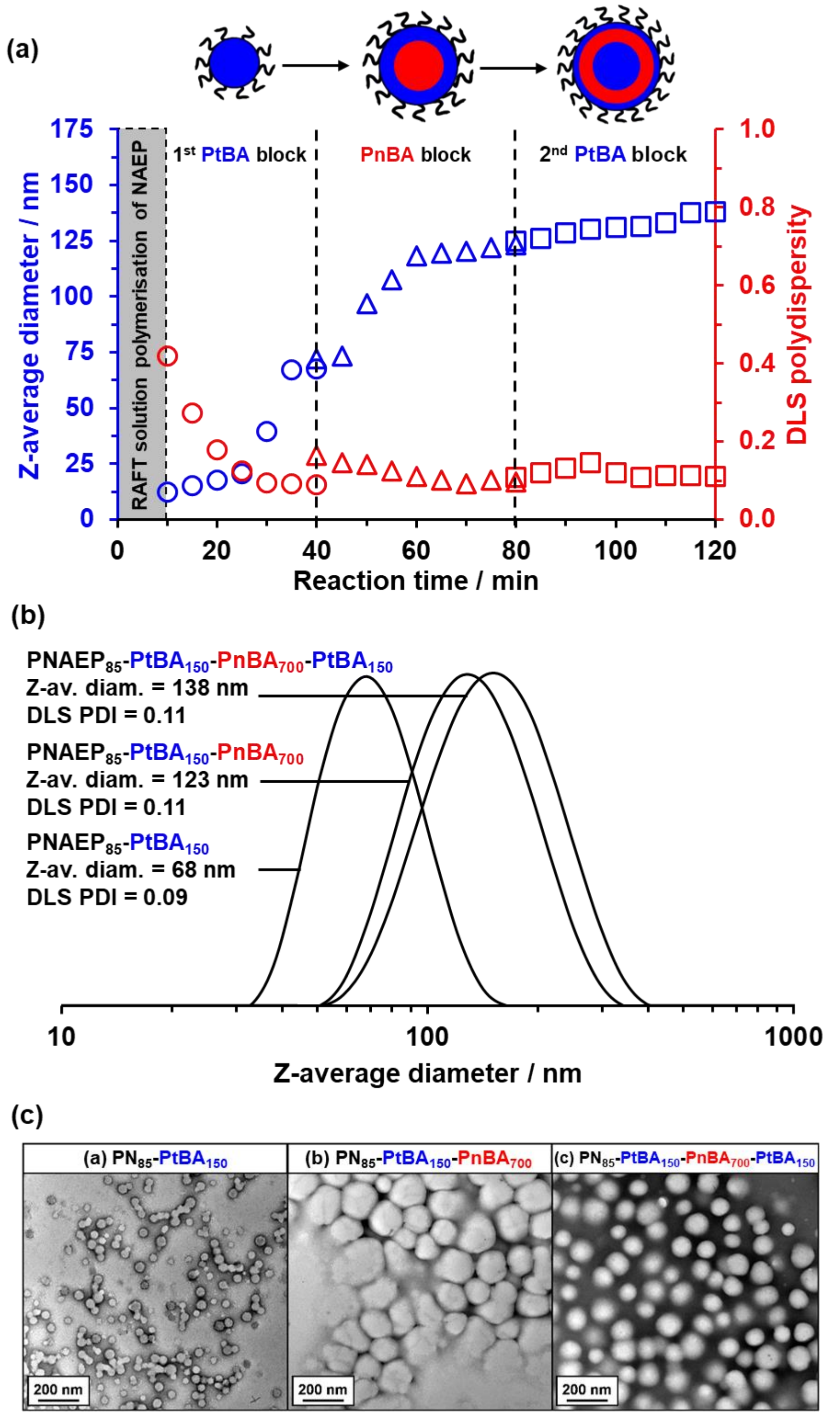

Figure 4.6. (a) Evolution of z-average diameter and polydispersity during the synthesis of PNAEP$_{85}$-PtBA$_{150}$-PnBA$_{700}$-PtBA$_{150}$ tetrablock copolymer nanoparticles *via* sequential RAFT emulsion polymerisation as indicated by DLS studies. Vertical dashed lines indicate the time at which each monomer was added to the reaction mixture. (b) DLS particle size distributions recorded for the diblock, triblock and tetrablock copolymer nanoparticles formed after each stage of this sequential RAFT aqueous emulsion polymerisation (>95% monomer conversion was achieved in each case). (c) Corresponding TEM images recorded for (a) the initial PNAEP$_{85}$-PtBA$_{150}$ spheres, (b) the intermediate PNAEP$_{85}$-PtBA$_{150}$-PnBA$_{700}$ spheres and (c) the final PNAEP$_{85}$-PtBA$_{150}$-PnBA$_{700}$-PtBA$_{150}$ spheres.

4.3.2 Synthesis and SAXS analysis of PNAEP$_{85}$-PtBA$_{150}$-PnBA$_x$-PtBA$_{150}$ Tetrablock Copolymer Nanoparticles

The DP of the soft PnBA block was systematically varied from 200 to 700 to prepare three examples of tetrablock copolymers. GPC studies indicated that the M_n increased linearly with the target PnBA DP (see Table 4.1). DLS experiments confirmed a monotonic increase in the final z-average diameter. However, attempts to target PnBA DPs above 800 invariably resulted in substantially incomplete comonomer conversions despite increasing the initiator concentration and extending the reaction time allowed for each block. It is perhaps also worth noting that the initial PNAEP$_{85}$-PtBA$_{150}$ diblock copolymer nanoparticles/chains obtained for these three syntheses exhibited remarkably similar GPC and DLS data, which indicates rather good reproducibility for this PISA protocol.

Table 4.1. Summary of GPC and DLS data obtained during the synthesis of three examples of PNAEP$_{85}$-PtBA$_{150}$-PnBA$_x$-PtBA$_{150}$ tetrablock copolymer nanoparticles (x = 200, 400 or 700) synthesised by sequential RAFT aqueous emulsion polymerisation at 30 °C.

	DMF GPC^a		DLS	
Polymer Composition	**M_n / kg mol^{-1}**	**M_w/M_n**	**Z-average diameter / nm**	**Polydispersity**
PNAEP$_{85}$-PtBA$_{150}$	26.3	1.36	66	0.11
PNAEP$_{85}$-PtBA$_{150}$-PnBA$_{200}$	57.5	1.46	89	0.10
PNAEP$_{85}$-PtBA$_{150}$-PnBA$_{200}$-PtBA$_{150}$	70.4	1.58	101	0.07
PNAEP$_{85}$-PtBA$_{150}$	26.2	1.34	66	0.08
PNAEP$_{85}$-PtBA$_{150}$-PnBA$_{400}$	76.1	1.48	102	0.09
PNAEP$_{85}$-PtBA$_{150}$-PnBA$_{400}$-PtBA$_{150}$	92.5	1.60	118	0.11
PNAEP$_{85}$-PtBA$_{150}$	27.9	1.31	68	0.09
PNAEP$_{85}$-PtBA$_{150}$-PnBA$_{700}$	114.6	1.54	123	0.11
PNAEP$_{85}$-PtBA$_{150}$-PnBA$_{700}$-PtBA$_{150}$	131.5	1.59	138	0.11

^{a}Refractive detector, DMF eluent, PMMA calibration standards

SAXS studies were conducted on 1.0% w/w aqueous dispersions of PNAEP$_{85}$-PtBA$_{150}$-PnBA$_{400}$-PtBA$_{150}$ and PNAEP$_{85}$-PtBA$_{150}$-PnBA$_{700}$-PtBA$_{150}$ tetrablock copolymer nanoparticles (Fig. 4.6). The low *q* gradient in an *I*(*q*) vs. q plot (where *I*(*q*) is the scattering intensity and *q* is the scattering vector) is characteristic of the predominant copolymer morphology. For both SAXS patterns shown in Figure 4.7 this gradient tends towards zero, which is consistent with the presence of spherical nanoparticles.[69,70] Moreover, the position of the first minimum (see d_1* in Figure 4.7) can be used to estimate the nanoparticle core radius (*r*) using Equation 4.1.[71]

$$r = \frac{4.49}{q} \tag{4.1}$$

This analysis indicated that the core diameter (or 2*r*) increased from 92 nm to 104 nm when the target PnBA DP was raised from 400 to 700. This agrees well with the increase in z-average diameter from 118 to 138 nm reported by DLS studies (see Table 4.1). However, the two SAXS patterns shown in Figure 4.6 could not be satisfactorily fitted using a well-known spherical micelle model,[72] with significant deviations between the model fit and the experimental data being observed in the low *q* region. In principle, this discrepancy could be related to the anticipated onion-like internal structure of these nanoparticles or incipient nanoparticle aggregation to form spherical dimers and trimers having similar low *q* gradients.[69] It should be noted that these two aqueous dispersions were transported via Royal Mail to Diamond Light Source for remote analysis and their thermal history is not known. In this context, it is perhaps noteworthy that conducting a freeze-thaw cycle led to discernible incipient nanoparticle aggregation, as indicated by a significant increase in DLS polydispersity from 0.11 to 0.42.

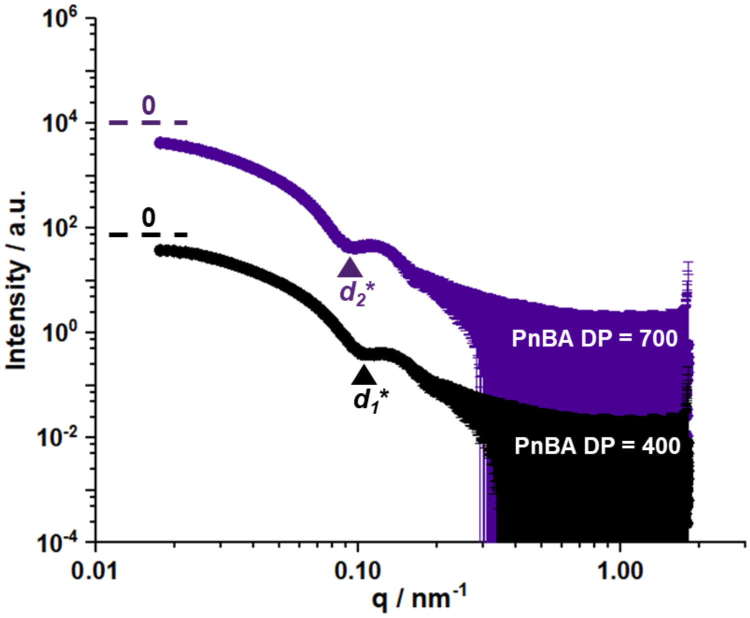

Figure 4.7. SAXS patterns recorded for 1.0% w/w aqueous dispersions of PNAEP$_{85}$-PtBA$_{150}$-PnBA$_{400}$-PtBA$_{150}$ and PNAEP$_{85}$-PtBA$_{150}$-PnBA$_{700}$-PtBA$_{150}$ tetrablock copolymers prepared by sequential RAFT aqueous emulsion polymerisation. The dashed lines at low *q* represent zero gradients. The volume-average nanoparticle radius was estimated from the position of the first minimum (see d_1* for PnBA DP = 400 and d_2* for PnBA DP = 700).

4.3.3 Preparation and Characterisation of PNAEP$_{85}$-PtBA$_{150}$-PnBA$_{x}$-PtBA$_{150}$ Tetrablock Copolymer Thermoplastic Elastomeric Films

DSC was used to determine T_g values for PNAEP$_{85}$-PtBA$_{150}$, PNAEP$_{85}$-PtBA$_{150}$-PnBA$_{700}$ and PNAEP$_{85}$-PtBA$_{150}$-PnBA$_{700}$-PtBA$_{150}$ (Figure 4.8). These studies indicated that PNAEP$_{85}$-PtBA$_{150}$ exhibited two distinct T_g values, indicating microphase separation between the hydrophilic and hydrophobic blocks. The T_g observed at −3.9 °C was assigned to the PNAEP$_{85}$ precursor (see Chapter 3). The T_g at 43.2 °C was attributed to the PtBA$_{150}$ block and is close to that reported[46] for PtBA homopolymers (PtBA T_g = 30-50 °C). The DSC curve recorded for PNAEP$_{85}$-PtBA$_{150}$-PnBA$_{700}$ indicated three distinct T_g values. The prominent T_g at –46.8 °C is close to the literature value for PnBA homopolymer and reflects the relatively high mass fraction of 72% for this component.[47–49] Two weaker features corresponding to T_g transitions for the PNAEP$_{85}$ and PtBA$_{150}$ blocks were also discernible. The T_g observed for the PtBA block was reduced from 43.2 °C to 39.4 °C, which most likely reflects the fact that it is attached to the more mobile PnBA block.[44,45] Three distinct T_g values were observed for PNAEP$_{85}$-PtBA$_{150}$-PnBA$_{700}$-PtBA$_{150}$ owing to its higher PtBA content. However, the PtBA T_g was further lowered to 34.2 °C, which may indicate partial miscibility of the two PtBA blocks with the longer PnBA block. ^{1}H NMR spectroscopy studies of these DSC samples indicated no residual monomer. Nevertheless, this final DSC trace indicates a 93 °C difference between the T_g values for the hard and soft blocks, which should be sufficient to produce thermoplastic elastomer properties.

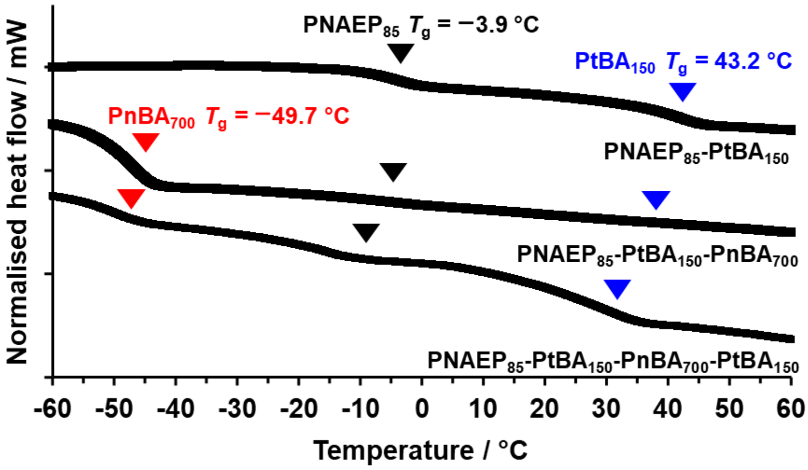

Figure 4.8. DSC curves recorded at a heating rate of 10 °C min^{-1} for PNAEP$_{85}$, PNAEP$_{85}$-PtBA$_{150}$, PNAEP$_{85}$-PtBA$_{150}$-PnBA$_{700}$ and PNAEP$_{85}$-PtBA$_{150}$-PnBA$_{700}$-PtBA$_{150}$. Inverted triangles indicate the T_g values for PNAEP (black), PtBA (blue) and PnBA (red) homopolymers. These DSC curves are arbitrarily offset for the sake of clarity.

$PNAEP_{85}$-$PtBA_{150}$-$PnBA_{200}$-$PtBA_{150}$, $PNAEP_{85}$-$PtBA_{150}$-$PnBA_{400}$-$PtBA_{150}$ and $PNAEP_{85}$-$PtBA_{150}$-$PnBA_{700}$-$PtBA_{150}$ copolymer films were prepared by drying the respective 20% w/w aqueous dispersions at 20 °C in a fume cupboard for 24 h. The film thickness could be varied between 50 to 200 µm (± 10 µm) by drying larger volumes of the 20% w/w dispersion (1.0 ± 0.5 g to 5.0 ± 0.5 g, respectively). A 150 µm $PNAEP_{85}$-$PtBA_{150}$-$PnBA_{200}$-$PtBA_{150}$ film displayed no thermoplastic elastomer behaviour owing to its PtBA-rich content and hence was not studied further. Similar observations were made by Zhu and co-workers for PS-rich PS-PnBA-PS triblock copolymer films.[16] Digital photographs of the copolymer films are shown in Figure 4.9. The $PNAEP_{85}$-$PtBA_{150}$-$PnBA_{400}$-$PtBA_{150}$ film was significantly more coloured owing to its lower overall DP and therefore higher concentration of trithiocarbonate end-groups, while the $PNAEP_{85}$-$PtBA_{150}$-$PnBA_{700}$-$PtBA_{150}$ film has the highest transparency. Preliminary tensile tests were performed by simply hand-stretching these films, with digital photographs being recorded in their original relaxed state (see Figures 4.9a and 4.9c) and at their maximum elongation before film rupture occurs (see Figures 4.9b and 4.9d). After the stretched films are released, they contracted to their original size (see Figure 4.9e). The elongation at break was calculated using Equation 4.2. Increasing the PnBA DP from 400 to 700 resulted in an increase in the elongation at break from 145% to 400%. Thus, reducing the glassy PtBA content results in more elastic films.

$$Elongation\ at\ break = \left(\frac{Final\ length}{Initial\ length}\right) \times 100 \qquad (4.2)$$

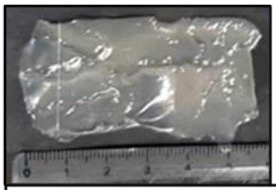

(a) $PNAEP_{85}$-$PtBA_{150}$-$PnBA_{400}$-$PtBA_{150}$ "Relaxed"

(b) $PNAEP_{85}$-$PtBA_{150}$-$PnBA_{400}$-$PtBA_{150}$ "Elongation at break"

(c) $PNAEP_{85}$-$PtBA_{150}$-$PnBA_{700}$-$PtBA_{150}$ "Relaxed"

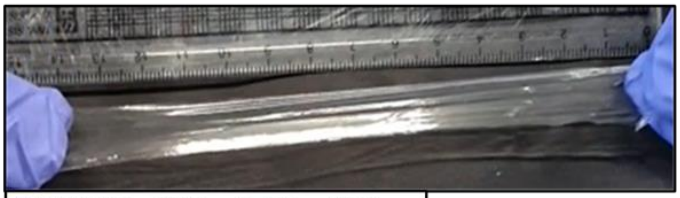

(d) $PNAEP_{85}$-$PtBA_{150}$-$PnBA_{700}$-$PtBA_{150}$ "Elongation at break"

(e) Returning to original size after stretching

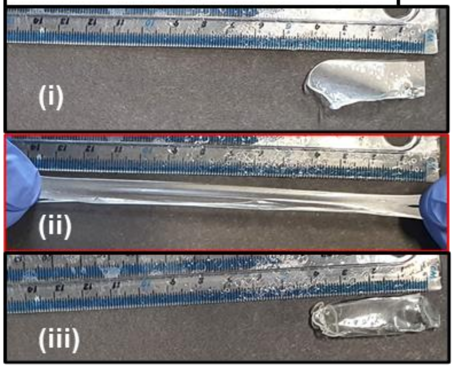

Figure 4.9. Digital photographs recorded during preliminary tensile tests on $PNAEP_{85}$-$PtBA_{150}$-$PnBA_{400}$-$PtBA_{150}$ [(a) and (b)] and $PNAEP_{85}$-$PtBA_{150}$-$PnBA_{700}$-$PtBA_{150}$ [(c) and (d)] films (mean film thickness = 150 ± 10 µm). (e) Images recorded (i) prior to stretching a $PNAEP_{85}$-$PtBA_{150}$-$PnBA_{700}$-$PtBA_{150}$ film (ii) the same film at its maximum elongation before break and (iii) the same film after returning to its original 4 cm length. These tetrablock copolymer films were prepared by drying the corresponding 20% w/w aqueous dispersions on PTFE sheets at 20 °C for 24 h.

SAXS measurements were used to characterise the microphase-separated structure of PNAEP$_{85}$-PtBA$_{150}$-PnBA$_{200}$-PtBA$_{150}$ (black trace in Figure 4.9), PNAEP$_{85}$-PtBA$_{150}$-PnBA$_{400}$-PtBA$_{150}$ (green trace in Figure 4.10) and PNAEP$_{85}$-PtBA$_{150}$-PnBA$_{700}$-PtBA$_{150}$ (blue trace in Figure 4.10) tetrablock copolymer films after drying at 20 °C. In each case, a relatively broad principal scattering peak was identified (see Bragg reflections labelled q^* in Figure 4.10). This feature can be used to calculate the mean domain size d within the microphase-separated films using Equation 4.3. Analysis indicated that d increased from 57 Å to 64 Å on increasing the PnBA DP from 200 to 700.

$$d = \frac{2\pi}{q*} \tag{4.3}$$

The two SAXS patterns recorded for PnBA DP = 400 and 700 exhibit three higher order structure peaks at q^*, $2q^*$ and $3q^*$, which is consistent with a lamellar structure[73] (Figure 4.10). The pattern obtained for the PnBA DP = 400 film had broader features than that for the PnBA DP = 700 film, indicating weaker microphase separation. This correlates well with the poor elastomeric properties identified in Figure 4.9. The SAXS pattern recorded for the PnBA DP = 200 film has a very weak second order peak and no discernible third order peak. Its lack of long-range translational order is typically observed when χ is low and is consistent with the inferior elastomeric properties observed for this film.[27] According to the literature, lamellar phases usually lead to poor thermoplastic properties, with film failure occurring at relatively low elongation at break values.[21,74–77] Typically, optimum thermoplastic elastomer performance is obtained when either spherical or cylindrical hard block domains are uniformly distributed within a continuous soft block matrix.[73,78] This suggests that stronger, more resilient thermoplastic elastomers (compared to that shown in Figure 4.9) should be feasible if such morphologies can be produced. This clearly warrants further examination but unfortunately time constraints do not allow further experiments to be conducted.

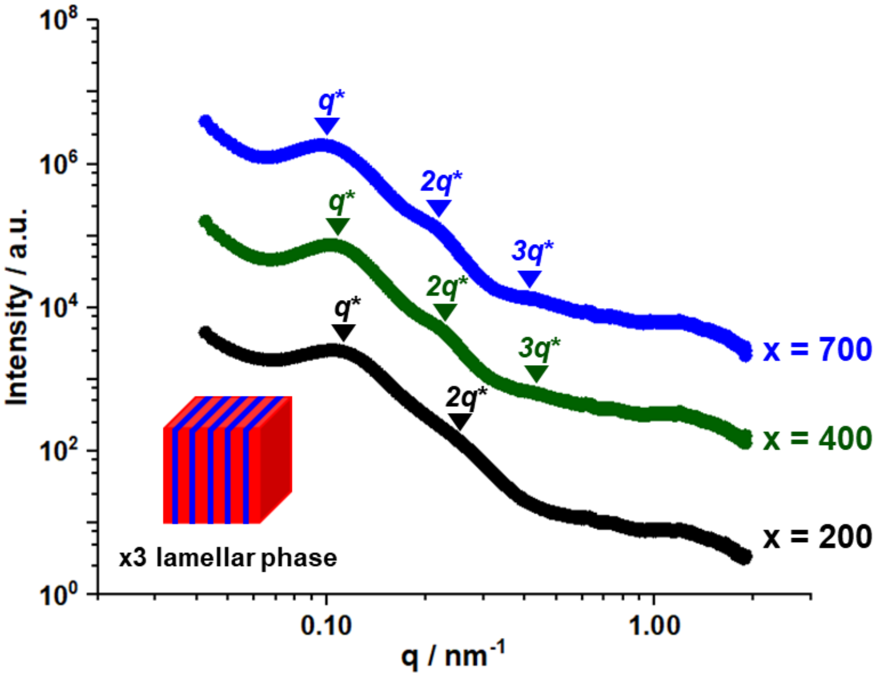

Figure 4.10. SAXS patterns recorded for $PNAEP_{85}$-$PtBA_{150}$-$PnBA_{200}$-$PtBA_{150}$ (black), $PNAEP_{85}$-$PtBA_{150}$-$PnBA_{400}$-$PtBA_{150}$ (green) and $PNAEP_{85}$-$PtBA_{150}$-$PnBA_{700}$-$PtBA_{150}$ (blue) tetrablock copolymer films dried at 20 °C without annealing. Higher order scattering peaks are labelled relative to the principal scattering peaks (*q**). The inset schematic cartoon shows the lamellar phase morphology for each of these three tetrablock copolymers (red = PnBA and blue = PtBA) suggested by such SAXS data.

4.4 Conclusions

Thermoplastic elastomers based on two structural isomers, *t*-butyl acrylate and *n*-butyl acrylate, were prepared by a four-step one-pot protocol involving RAFT aqueous emulsion polymerisation at 30 °C. This enabled high molecular weight tetrablock copolymers to be synthesised in relatively short time periods and via a low-viscosity route (compared to similar polymers being synthesised via solution polymerisation). ^1H NMR kinetic studies indicated that the synthesis of a 20% w/w aqueous dispersion of $PNAEP_{85}$-$PtBA_{150}$-$PnBA_{700}$-$PtBA_{150}$ tetrablock copolymer nanoparticles was complete within 120 min and confirmed high conversions (98%) were achieved for each polymerisation stage. GPC analysis of aliquots taken during such kinetic studies indicated gradual broadening of the molecular weight distribution (final $M_n = 131.5$ kg mol^{-1}, final $M_w/M_n = 1.60$). However, this is not unexpected given that chain transfer to polymer is well-known for acrylic polymers, even for polymerisations conducted under relatively mild conditions.[79] After a 25 min induction period, DLS and TEM studies confirmed the formation of spherical PNAEP$_{85}$-PtBA$_{150}$ nanoparticles during the RAFT emulsion polymerisation of tBA. Such nanoparticles acted as a seed for the subsequent polymerisation of nBA. The initial addition of nBA produced monomer-swollen seed particles (as indicated by an increase in z-average diameter and higher DLS polydispersity) and there was no discernible induction period for this polymerisation stage. Moreover, the z-average diameter increased significantly during the polymerisation of nBA, which is consistent with the much higher molecular weight indicated by DMF GPC analysis. Despite the relatively low glass transition temperature of the PnBA block the onion-like structure of these PnBA-rich nanoparticles enabled TEM studies to be conducted. DLS analysis indicated that the final PNAEP$_{85}$-PtBA$_{150}$-PnBA$_{700}$ spherical nanoparticles became swollen on addition of tBA monomer and the final PNAEP$_{85}$-PtBA$_{150}$-PnBA$_{700}$-PtBA$_{150}$ tetrablock nanoparticles exhibited a z-average diameter of 138 nm. TEM analysis confirmed that such nanoparticles did not undergo film formation when drying from dilute aqueous solution. The kinetically-trapped spherical morphology observed for this PISA formulation is consistent with the relatively long PNAEP stabiliser chains, which also bear a terminal anionic carboxylate group.[80–82]

Three examples of PNAEP$_{85}$-PtBA$_{150}$-PnBA$_{x}$-PtBA$_{150}$ tetrablock copolymers (where x = 200, 400 or 700) were analysed by GPC, DLS, DSC and SAXS. A linear increase in M_n with conversion of each block was observed indicating living character was maintained throughout the polymerisation. The nanoparticle diameter increased with time and corresponded well with the monomer conversion and overall molecular weight of each block, as expected. DSC studies of PNAEP$_{85}$-PtBA$_{150}$, PNAEP$_{85}$-PtBA$_{150}$-PnBA$_{700}$ and PNAEP$_{85}$-PtBA$_{150}$-PnBA$_{700}$-PtBA$_{150}$ indicated that the T_g difference between the hard and soft blocks was approximately 93 °C. Their all-acrylic nature enabled the three tetrablock copolymer dispersions to form transparent films when dried at room temperature. However, the PNAEP$_{85}$-PtBA$_{150}$-PnBA$_{200}$-PtBA$_{150}$ film displayed no elastomeric properties owing to the relatively short PnBA block. For the two other tetrablock copolymer films, The elongation at break increased from 145% (PnBA DP = 400) to 400% (PnBA DP = 700), which suggests that these materials do indeed act as good-quality thermoplastic elastomers.

Finally, SAXS was used to characterise the extent of phase separation within these three tetrablock copolymer films. Each film exhibited a lamellar structure, with higher degrees of phase separation being observed for higher molecular weight copolymers. Literature precedent suggests that if tetrablock copolymer films comprising spherical or cylindrical domains could be prepared then even better elastomeric properties might be obtained.[73]

4.5 References

1 A. B. Lowe and C. L. McCormick, *Prog. Polym. Sci.*, 2007, **32**, 283–351.

2 B. Charleux, G. Delaittre, J. Rieger and F. D'Agosto, *Macromolecules*, 2012, **45**, 6753–6765.

3 J. Tan, H. Sun, M. Yu, B. S. Sumerlin and L. Zhang, *ACS Macro Lett.*, 2015, **4**, 1249–1253.

4 C. A. Figg, A. Simula, K. A. Gebre, B. S. Tucker, D. M. Haddleton and B. S. Sumerlin, *Chem. Sci.*, 2015, **6**, 1230–1236.

5 S. L. Canning, G. N. Smith and S. P. Armes, *Macromolecules*, 2016, **49**, 1985–2001.

6 M. J. Derry, L. A. Fielding and S. P. Armes, *Prog. Polym. Sci.*, 2016, **52**, 1–18.

7 S. Chen, P. Shi and W. Zhang, *Chinese J. Polym. Sci.*, 2017, **35**, 455–479.

8 X. Wang and Z. An, *Macromol. Rapid Commun.*, 2019, **40**, 1800325.

9 J. M. G. Cowie, *Polymers: Chemistry and Physics of Modern Materials*, Nelson Thornes, Cheltenham, 2002.

10 A. Blanazs, A. J. Ryan and S. P. Armes, *Macromolecules*, 2012, **45**, 5099–5107.

11 B. Karagoz, L. Esser, H. T. Duong, J. S. Basuki, C. Boyer and T. P. Davis, *Polym. Chem.*, 2014, **5**, 350–355.

12 N. J. Warren and S. P. Armes, *J. Am. Chem. Soc.*, 2014, **136**, 10174–10185.

13 J. Rieger, *Macromol. Rapid Commun.*, 2015, **36**, 1458–1471.

14 G. Gody, T. Maschmeyer, P. B. Zetterlund and S. Perrier, *Nat. Commun.*, 2013, **4**, 1–9.

15 G. Gody, T. Maschmeyer, P. B. Zetterlund and S. Perrier, *Macromolecules*, 2014, **47**, 3451–3460.

16 Y. Luo, X. Wang, Y. Zhu, B.-G. Li and S. Zhu, *Macromolecules*, 2010, **43**, 7472–7481.

17 T. R. Guimarães, M. Khan, R. P. Kuchel, I. C. Morrow, H. Minami, G. Moad, S. Perrier and P. B. Zetterlund, *Macromolecules*, 2019, **52**, 2965–2974.

18 G. K. K. Clothier, T. R. Guimarães, M. Khan, G. Moad, S. Perrier and P. B. Zetterlund, *ACS Macro Lett.*, 2019, **8**, 989–995.

19 B. Wunderlieh, *Thermal Analysis*, Academic Press, NY, 1990.

20 J. Rieger, *J. Therm. Anal.*, 1996, **46**, 965–972.

21 M. Morton, J. E. McGrath and P. C. Juliano, *J. Polym. Sci. Part C Polym. Symp.*,

2007, **26**, 99–115.

22 F. S. Bates, M. A. Hillmyer, T. P. Lodge, C. M. Bates, K. T. Delaney and G. H. Fredrickson, *Science*, 2012, **336**, 434–440.

23 H. Feng, X. Lu, W. Wang, N.-G. Kang and J. Mays, *Polymers*, 2017, **9**, 494–525.

24 A. M. Diciccio and G. W. Coates, *J. Am. Chem. Soc.*, 2011, **133**, 10724–10727.

25 G. Holden, E. T. Bishop and N. R. Legge, *J. Polym. Sci. Part C Polym. Symp.*, 2007, **26**, 37–57.

26 P. C. Hiemenz and T. P. Lodge, *Polymer Chemistry - 2nd Edition*, CRC Press, New York, 2007.

27 C. Sinturel, F. S. Bates and M. A. Hillmyer, *ACS Macro Lett.*, 2015, 4, 1044–1050.

28 Z. Sun, W. Zhang, S. Hong, Z. Chen, X. Liu, S. Xiao, E. B. Coughlin and T. P. Russell, *Polymer*, 2017, **121**, 297–303.

29 J. Jennings, E. J. Cornel, M. J. Derry, D. L. Beattie, M. J. Rymaruk, O. J. Deane, A. J. Ryan and S. P. Armes, *Angew. Chemie*, 2020, **132**, 10940–10945.

30 F. S. Bates and G. H. Fredrickson, *Phys. Today*, 1999, **52**, 32–38.

31 F. S. Bates, *Science*, 1991, **251**, 898–905.

32 L. N. Venkateshwaran, G. A. York, C. D. DePorter, J. E. McGrath and G. L. Wilkes, *Polymer*, 1992, **33**, 2277–2286.

33 E. Ihara, M. Morimoto and H. Yasuda, *Macromolecules*, 1995, **28**, 7886–7892.

34 R. Jerome, P. Bayard, R. Fayt, C. Jacobs, S. Varshney and P. Teyssie, Hanser, Munich, 1996, p. 521.

35 J.-D. Tong and R. Jerôme, *Macromolecules*, 2000, **33**, 1479–1481.

36 G. Holden and N. R. Legge, Hanser, Munich, 1996, p. 47.

37 P. B. Zetterlund, Y. Kagawa and M. Okubo, *Chem. Rev.*, 2008, **108**, 3747–3794.

38 H. Tobita, *Macromol. Symp.*, 2008, **261**, 36–45.

39 P. B. Zetterlund, *Polym. Chem.*, 2011, **2**, 534–549.

40 M. Chenal, L. Bouteiller and J. Rieger, *Polym. Chem.*, 2013, **4**, 752–762.

41 G. Delaittre and B. Charleux, *Macromolecules*, 2008, **41**, 2361–2367.

42 V. J. Cunningham, A. M. Alswieleh, K. L. Thompson, M. Williams, G. J. Leggett, S. P. Armes and O. M. Musa, *Macromolecules*, 2014, **47**, 5613–5623.

43 J. Jennings, G. He, S. M. Howdle and P. B. Zetterlund, *Chem. Soc. Rev.*, 2016, **45**, 5055–5084.

44 Y. Luo, X. Wang, B.-G. Li and S. Zhu, *Macromolecules*, 2011, **44**, 221–229.

45 X. Wang, Y. Luo, B. Li and S. Zhu, *Macromolecules*, 2009, **42**, 6414–6421.

46 W. Liu, T. Nakano and Y. Okamoto, *Polymer*, 2000, **41**, 4467–4472.

47 G. Carrot, S. Diamanti, M. Manuszak, B. Charleux and J.-P. Vairon, *J. Polym. Sci.*

Part A Polym. Chem., 2001, **39**, 4294–4301.

48 M. Chenal, C. Véchambre, J.-M. Chenal, L. Chazeau, V. Humblot, L. Bouteiller, C. Creton and J. Rieger, *Polymer*, 2017, **109**, 187–196.

49 P. Gurnani, C. Sanchez-Cano, K. Abraham, H. Xandri-Monje, A. B. Cook, M. Hartlieb, F. Lévi, R. Dallmann and S. Perrier, *Macromol. Biosci.*, 2018, **18**, 1800213–1800222.

50 M. Basham, J. Filik, M. T. Wharmby, P. C. Y. Chang, B. El Kassaby, M. Gerring, J. Aishima, K. Levik, B. C. A. Pulford, I. Sikharulidze, D. Sneddon, M. Webber, S. S. Dhesi, F. Maccherozzi, O. Svensson, S. Brockhauser, G. Náray and A. W. Ashton, *J. Synchrotron Radiat.*, 2015, **22**, 853–858.

51 J. F. Quinn, L. Barner, C. Barner-Kowollik, E. Rizzardo and T. P. Davis, *Macromolecules*, 2002, **35**, 7620–7627.

52 I. Chaduc, W. Zhang, J. Rieger, M. Lansalot, F. D'Agosto and B. Charleux, *Macromol. Rapid Commun.*, 2011, **32**, 1270–1276.

53 S. J. Byard, M. Williams, B. E. McKenzie, A. Blanazs and S. P. Armes, *Macromolecules*, 2017, **50**, 1482–1493.

54 G. A. Al-Muntasheri, H. A. Nasr-El-Din, J. A. Peters and P. L. J. Zitha, *Eur. Polym. J.*, 2008, **44**, 1225–1237.

55 D. B. Thomas, A. J. Convertine, R. D. Hester, A. B. Lowe and C. L. McCormick, *Macromolecules*, 2004, **37**, 1735–1741.

56 M. Mertoglu, A. Laschewsky, K. Skrabania and C. Wieland, *Macromolecules*, 2005, **38**, 3601–3614.

57 S. Boissé, J. Rieger, G. Pembouong, P. Beaunier and B. Charleux, *J. Polym. Sci. Part A Polym. Chem.*, 2011, **49**, 3346–3354.

58 R. A. E. Richardson, T. R. Guimaraes, M. Khan, G. Moad, P. B. Zetterlund and S. Perrier, *Macromolecules*, 2020, **53**, 7672–7683.

59 M. Khan, T. R. Guimarã, K. Choong, G. Moad, S. Perrier and P. B. Zetterlund, , DOI:10.1021/acs.macromol.0c02415.

60 J. Božović-Vukić, H. T. Mañon, J. Meuldijk, C. Koning and B. Klumperman, *Macromolecules*, 2007, **40**, 7132–7139.

61 G. Moad, E. Rizzardo and S. H. Thang, *Aust. J. Chem.*, 2012, **65**, 985–1076.

62 D. J. Keddie, *Chem. Soc. Rev.*, 2014, **43**, 496–505.

63 S. Perrier, *Macromolecules*, 2017, **50**, 7433–7447.

64 N. M. Ahmad, F. Heatley and P. A. Lovell, *Macromolecules*, 1998, **31**, 2822–2827.

65 F. Heatley, P. A. Lovell and T. Yamashita, *Macromolecules*, 2001, **34**, 7636–7641.

66 N. M. Ahmad, B. Charleux, C. Farcet, C. J. Ferguson, S. G. Gaynor, B. S. Hawkett, F. Heatley, B. Klumperman, D. Konkolewicz, P. A. Lovell, K. Matyjaszewski and R. Venkatesh, *Macromol. Rapid Commun.*, 2009, **30**, 2002–2021.

67 R. H. Ottewill, A. B. Schofield and J. A. Waters, *Colloid Polym. Sci.*, 1996, **274**, 763–771.

68 N. P. Truong, M. V Dussert, M. R. Whittaker, J. F. Quinn and T. P. Davis, *Polym. Chem.*, 2015, **6**, 3865–3874.

69 N. J. Warren, O. O. Mykhaylyk, D. Mahmood, A. J. Ryan and S. P. Armes, *J. Am. Chem. Soc.*, 2014, **136**, 1023–1033.

70 S. J. Byard, C. T. O’Brien, M. J. Derry, M. Williams, O. O. Mykhaylyk, A. Blanazs and S. P. Armes, *Chem. Sci.*, 2020, **11**, 396–402.

71 M. Li, Y. Liu, H. Nie, R. Bansil and M. Steinhart, *Macromolecules*, 2007, **40**, 9491–9502.

72 J. S. Pedersen, *J. Appl. Crystallogr.*, 2000, **33**, 637–640.

73 G. L. Gregory, G. S. Sulley, L. P. Carrodeguas, T. T. D. Chen, A. Santmarti, N. J. Terrill, K.-Y. Lee and C. K. Williams, *Chem. Sci.*, 2020, **11**, 6567–6581.

74 J. E. Puskas, P. Antony, M. El Fray and V. Altstädt, *Eur. Polym. J.*, 2003, **39**, 2041–2049.

75 J. G. Drobny, *Handbook of Thermoplastic Elastomers*, William Andrew Publishing, Norwich, NY, 2007.

76 R. Shanks and I. Kong, in *Thermoplastic Elastomers*, InTech, Melbourne, 2012.

77 W. Wang, W. Lu, A. Goodwin, H. Wang, P. Yin, N.-G. Kang, K. Hong and J. W. Mays, *Prog. Polym. Sci.*, 2019, **95**, 1–31.

78 P. D. Topham, J. R. Howse, O. O. Mykhaylyk, S. P. Armes, R. A. L. Jones and A. J. Ryan, *Macromolecules*, 2006, **39**, 5573–5576.

79 M. El-Aasser and P. A. Lovell, *Emulsion polymerization and emulsion polymers*, John Wiley and Sons, Chichester, 1998.

80 S. Y. Khor, N. P. Truong, J. F. Quinn, M. R. Whittaker and T. P. Davis, *ACS Macro Lett.*, 2017, **6**, 1013–1019.

81 N. J. Warren, M. J. Derry, O. O. Mykhaylyk, J. R. Lovett, L. P. D. D. Ratcliffe, V. Ladmiral, A. Blanazs, L. A. Fielding and S. P. Armes, *Macromolecules*, 2018, **51**, 8357–8371.

82 R. R. Gibson, S. P. Armes, O. M. Musa and A. Fernyhough, *Polym. Chem.*, 2019, **10**, 1312–1323.

Chapter 5

Synthesis and Aqueous Solution Properties of Shape-Shifting Stimulus-Responsive Diblock Copolymer Nano-Objects

5.1 Introduction

It is well-known that AB diblock copolymers can self-assemble in solution to form a range of sterically-stabilised nanoparticles.[1–4] Depending on the relative volume fractions of the two blocks[1], the copolymer morphology can be spheres[1], worms[4,5] or vesicles[6]. However, traditional post-polymerisation processing routes to such nano-objects usually require co-solvents and are invariably conducted in dilute solution.[1,5,7,8] These are important constraints that have severely limited potential commercial applications. In contrast, PISA enables the efficient synthesis of block copolymer nano-objects of controllable size, morphology and surface composition directly in the form of concentrated dispersions in a wide range of polar[4,9–11] or non-polar[12,13] solvents. PISA involves chain extension of a soluble homopolymer precursor using a suitable second monomer in an appropriate solvent, with the latter being chosen so that the growing second block becomes insoluble at some critical chain length, thus leading to the formation of diblock copolymer nano-objects. This approach has enabled the facile preparation of spheres, worms or vesicles, with highly convenient one-pot protocols being developed for some formulations.[14–16] In principle, such nanoparticles offer a wide range of potential applications, including new biocompatible hydrogels for cell culture and long-term storage,[10,17,18] microencapsulation of proteins and enzymes within vesicles,[19–23] bespoke Pickering emulsifiers,[24] novel flocculants,[25] and new lubricants for the formulation of ultralow-viscosity automotive engine oils[26]. The majority of the PISA literature utilises RAFT polymerisation.[27–35] This is an example of controlled/living radical polymerisation based on the principle of rapid reversible chain transfer: an organosulfur-based CTA is utilised to prepare well-defined functional block copolymers with low dispersities and predictable mean DPs.[36–38]

Recently, we reported the convenient PISA synthesis of two examples of a new class of thermoresponsive diblock copolymer of *fixed composition* that can form spheres, worms or vesicles in aqueous solution simply by adjusting the solution temperature.[16,39] In both cases, spheres are formed at sub-ambient temperature, worms are produced at around ambient temperature and vesicles are generated above ambient temperature. Variable temperature ^{1}H NMR spectroscopy studies indicate that in each case this remarkable behaviour is the result of the variable degree of hydration of the weakly hydrophobic structure-directing block, which was either PHPMA[18] or PHBA.[40] Importantly, the significantly lower T_g – and hence greater chain mobility – exhibited by the acrylic PHBA block led to much thermoreversible sphere/worm and worm/vesicle morphological transitions than those observed for the methacrylic PHPMA block. Unfortunately, this relatively low T_g also led to film formation, which made it impossible to determine copolymer morphologies via TEM. In principle, this technical issue can be addressed by using cryo-TEM.[41–43] However, the weakly hydrophobic nature of the PHBA chains leads to a relatively high degree of hydration, which minimises electron contrast with the frozen aqueous phase and leads to poor-quality images. Thus, Byard and co-workers addressed this problem by statistically copolymerising HBA with a crosslinkable comonomer DAAM.[16] This approach was ultimately successful, but incorporating just 20 mol% DAAM comonomer reduced the thermoresponsive behaviour exhibited by the HBA-rich structure-directing block. In principle, identifying a suitable crosslinking protocol for *pure* PHBA-based nanoparticles should raise the T_g of this block sufficiently to ensure that copolymer morphologies can be readily assigned by conventional TEM analysis. This is one of the main objectives of the present study.

Glutaraldehyde (GA) is a linear water-soluble dialdehyde (see (I) in Figure 5.1) that is widely used as a crosslinker for various biomedical applications,[44,45] including the covalent stabilisation of proteins to facilitate their characterisation by electron microscopy.[46–48] It has also been used to crosslink various water-soluble polymers.[49–54] However, as far as we are aware, this reagent has not been previously used to crosslink thermoresponsive diblock copolymer nanoparticles.

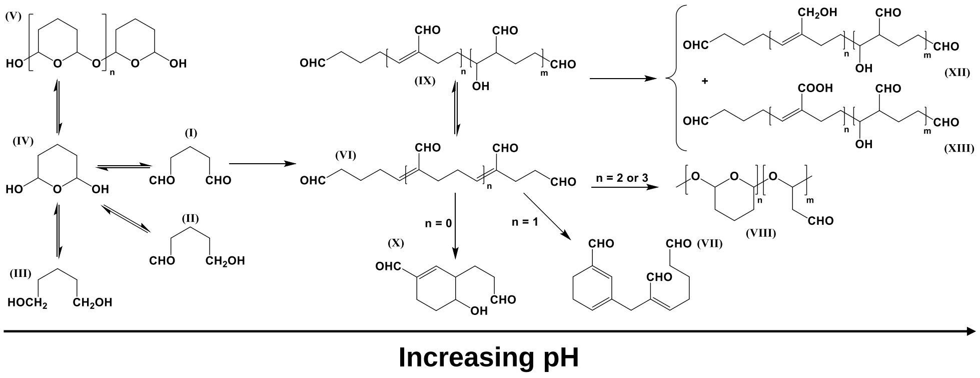

Figure 5.1. Suggested chemical structures derived from glutaraldehyde (GA) in aqueous solution on adjusting the solution pH (which increases from left to right).

GA can undergo a remarkable range of reactions in aqueous solution (see Figure 5.1).[45–48,55–59] This rich chemistry can produce a complex mixture of monomeric GA, unsaturated polymeric GA [see structures (VI), (IX) and (XIII)] and cyclic GA species [e.g. structures (IV), (V), (VII), (X) and (XI)]. The major species depends on both the initial GA concentration and the solution pH (Figure 5.1).[44] The crosslinking of proteins using GA is not fully understood but is believed to occur via various mechanisms, including nucleophilic attack of the aldehyde groups on GA by pendent amine groups on the protein to form imine bonds[55,59] and Michael addition of protein amino groups of α,β-unsaturated aldehydes formed by aldol condensation of GA[56,57] [see (VI) in Figure 5.1]. GA has been shown to favour intra-molecular crosslinks over inter-molecular crosslinks when reacting with proteins.[47,58] However, the relative amounts of these two types of crosslinks depends on both the GA and protein concentrations.[47,58] GA has also been widely investigated as a crosslinker for the acid-catalysed synthesis of water-insoluble PVA membranes.[49–54] FT-IR spectroscopy studies indicated that the major product formed during the reaction between PVA and GA contained an acetal ring group formed from the reaction between two pairs of neighbouring secondary hydroxyl groups on the PVA chains with the two aldehyde groups on GA (Figure 5.2a).[60] Other major products shown in Figure 5.2 have also been reported.[50] Given this literature precedent, we postulated that GA should be able to act as an effective crosslinker for PHBA-based nanoparticles in aqueous solution.

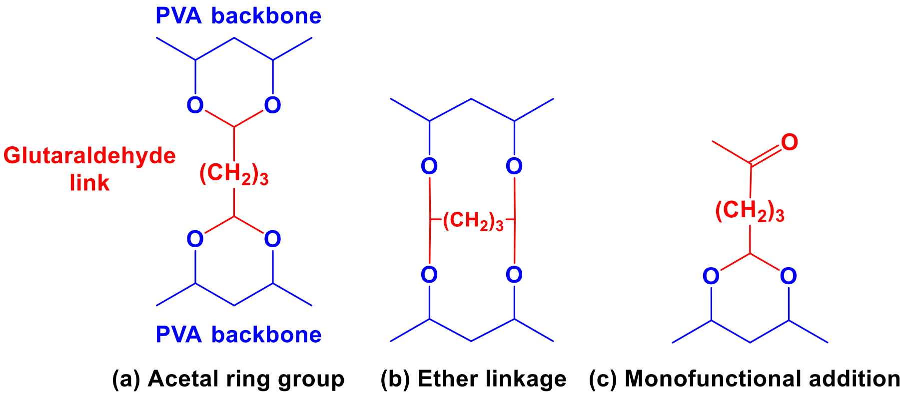

Figure 5.2. Typical species formed after the reaction between poly(vinyl alcohol) and glutaraldehyde in aqueous solution: (a) crosslinked major product containing an acetal ring group, (b) formation of an ether linkage in a crosslinked minor product and (c) the monofunctional pendent aldehyde formed after reaction between a pair of neighbouring hydroxyl groups with one of the aldehyde groups on GA.[50,58]

Herein we report the synthesis of a range of new thermoresponsive pyrrolidone-functional diblock copolymer nano-objects *via* RAFT aqueous dispersion polymerisation of HBA using PNAEP as a non-ionic hydrophilic steric stabiliser block (see Scheme 5.1 and Chapters 2-4).[61,62] Optimised conditions for the covalent stabilisation of PNAEP-PHBA nanoparticles with GA crosslinker are established and TEM is then used to assign copolymer morphologies. We demonstrate that the critical temperature for the local maximum in dispersion viscosity owing to worm formation can be tuned over a wide range of temperatures by systematic variation of the diblock copolymer composition. Moreover, we also show that adjusting the dispersion pH induces a vesicle-to-sphere transition owing to a subtle change in the degree of hydration of the structure-directing PHBA block caused by ionisation of a carboxylic acid group located at the end of the PNAEP stabiliser chains.

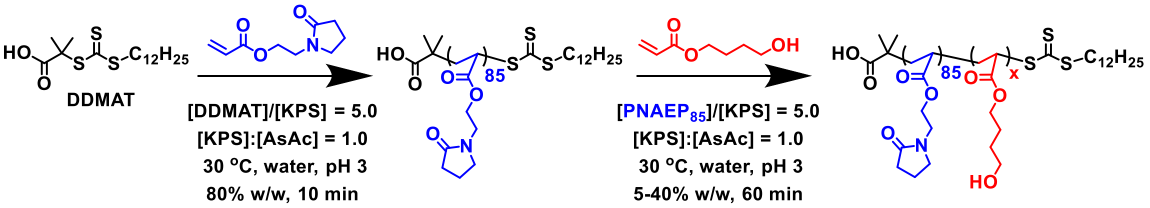

Scheme 5.1. One-pot synthesis of PNAEP$_{85}$-PHBA$_x$ diblock copolymer nano-objects *via* RAFT aqueous dispersion polymerisation of HBA at 30 °C using a [PNAEP$_{85}$]/[KPS] molar ratio of 5.0 and a [KPS]/[AsAc] molar ratio of 1.0. The RAFT solution polymerisation of NAEP is essentially complete within 10 min at 30 °C, while the RAFT aqueous dispersion polymerisation of HBA only requires a further 60 min at this temperature.

5.2 Experimental

5.2.1 Materials

NAEP was purified using the sample protocol outline in Chapter 2. HBA was kindly donated by Scott Bader Ltd. (Wollaston, UK) and was purified *via* extraction using *n*-hexane (twenty times) to remove diacrylate impurities. All chemicals used for NAEP and HBA purification were purchased from Sigma-Aldrich (Dorset, UK) and were used as received. AsAc, KPS, N,N,N′,N′-tetramethylethylenediamine (TMEDA), 3-(trimethylsilyl)-1-propanesulfonic acid sodium salt (DSS), glutaraldehyde solution (GA; 50% w/w in water) and DDMAT were purchased from Sigma-Aldrich (Dorset, UK). CD_3OD and D_2O were purchased from Goss Scientific Instruments Ltd. (Cheshire, UK). All other solvents were purchased from Fisher Scientific (Loughborough, UK) and were used as received. Deionised water was used for all experiments.

5.2.2 One-Pot Synthesis of $PNAEP_{85}$-$PHBA_x$ Diblock Copolymer Nano-Objects via RAFT Aqueous Dispersion Polymerisation

A typical protocol used for the one-pot synthesis of $PNAEP_{85}$−$PHBA_{435}$ diblock copolymer nano-objects at 20% w/w solids was as follows: DDMAT RAFT agent (5.3 mg, 14.56 µmol) was added to NAEP (0.2 g, 1.09 mmol; target PNAEP DP = 75) and KPS (0.8 mg, 2.91 µmol; [DDMAT]/[KPS] molar ratio = 5.0) were weighed into a 28 mL glass vial charged with a magnetic flea (reaction solution 1). Reaction solution 1 was then placed in an ice bath and nitrogen was passed over the top of the solution for 30 min. After 30 min, the vial containing reaction solution 1 was immersed in an oil bath set at 30 °C. AsAc (0.5 mg, 2.91 µmol; [DDMAT]/[AsAc] molar ratio = 5.0; [KPS]/[AsAc] molar ratio = 1.0) and acidic deionised water (57.0 mg; pH 3; final solids concentration = 78% w/w) were combined and degassed before being added via a degassed syringe/needle to reaction solution 1 under a nitrogen atmosphere. The NAEP polymerisation was allowed to proceed for 10 min prior to dilution of the viscous aqueous reaction solution via addition of degassed acidic water (5.85 g; pH 3; final target solids concentration = 20% w/w). The resulting reaction solution was stirred magnetically for 2 min to ensure the PNAEP homopolymer became fully solubilised. A degassed syringe/needle was used to extract an aliquot for ^{1}H NMR spectroscopy analysis. The disappearance of vinyl signals at 5.9 and 6.4 ppm relative to the integrated four ethyl protons at 3.4−3.8 ppm assigned to PNAEP indicated a monomer conversion of 98%. Its mean DP was calculated to be 86 (DDMAT RAFT efficiency = 87%) as judged by ^{1}H NMR studies in CD_3OD [the integrated signal at 3.4-3.8 ppm (m, 4H) was compared with that assigned to the methyl RAFT chain-end at 0.86-0.96 ppm (t, 3H)]. DMF GPC analysis indicated an M_n of 19.2 kg mol^{-1} and an M_w/M_n of 1.16 compared to a series of ten near-monodisperse poly(methyl methacrylate) calibrants. To perform the chain extension, degassed HBA (1.19 g, 8.29 mmol; PHBA target DP = 435) was added to the reaction solution. KPS (1.03 mg, 3.80 µmol; [PNAEP]/[KPS] molar ratio = 5.0) and AsAc (0.67 mg, 3.80 µmol; [PNAEP]/[AsAc] molar ratio = 5.0; [KPS]/[AsAc] molar ratio = 1.0) were added to the reaction as dilute solutions (0.13 mM and 0.08 mM, respectively) using degassed syringe/needles. The HBA polymerisation was allowed to proceed for 1 h at 30 °C (N.B. polymerisations targeting 5% w/w solids were left for 2 h at 30 °C) before being quenched by exposing the reaction mixture to air and immersing the glass vial into an ice bath. The extent of polymerisation was determined by ^{1}H NMR spectroscopy: comparison of the integrated residual monomer vinyl proton signals at 5.8 and 6.5 ppm relative to the integrated two oxymethylene protons at 4.2−4.3 ppm assigned to PHBA indicated a final HBA conversion of 98%. The mean DP of the PHBA block was calculated to be 435 as judged by ^{1}H NMR spectroscopy analysis in CD_3OD (the integrated signal at 3.6-3.8 ppm (t, 870H) was compared with that assigned to two oxymethylene protons assigned to $PNAEP_{85}$ at 2.1-2.2 ppm (m, 170H)). DMF GPC analysis indicated an M_n of 64.5 kg mol^{-1} and an M_w/M_n of 1.31 relative to a series of near-monodisperse PMMA calibration standards. The volume of water was adjusted to afford the desired final solids concentrations. Other target diblock copolymer compositions were obtained by adjusting the [HBA]/[$PNAEP_{85}$] molar ratio.

5.2.3 Covalent Stabilisation of Diblock Copolymer Nano-objects Using Glutaraldehyde

A typical protocol used for crosslinking $PNAEP_{85}$−$PHBA_{255}$ spheres is as follows. A 5% w/w acidic aqueous dispersion of $PNAEP_{85}$−$PHBA_{255}$ spheres (0.5 g; PHBA = 121 µmol) and glutaraldehyde (GA; 8.0 mg, 80 µmol, GA/PHBA molar ratio = 0.66) were added to a 7 mL vial. The ~5% w/w acidic reaction mixture was stirred at 25 °C for 16 h. Then an aliquot (0.01 g) was extracted and diluted with water (4.99 g; final target solids concentration = 0.05% w/w) and stirred for 24 h prior to preparation of the corresponding TEM grid (see below for further details). Crosslinking of $PNAEP_{85}$−$PHBA_{340-375}$ worms and $PNAEP_{85}$-$PHBA_{435-565}$ vesicles was also performed at 5% w/w; in the former case, this copolymer concentration was sufficiently low to avoid gelation during crosslinking. To crosslink $PNAEP_{85}$-$PHBA_x$ diblock copolymer nano-objects at a particular temperature or pH, 5% w/w dispersions were either equilibrated at the desired reaction temperature for 1 h or after an appropriate amount of 1 M NaOH or HCl was added prior to GA addition and then allowed to crosslink for 16 h before dilution with water (final target solids concentration = 0.05% w/w) that had been pre-equilibrated at either the same temperature or pH.

5.2.4 Copolymer Characterisation

^{1}H NMR Spectroscopy. Spectra were recorded in either CD_3OD or D_2O using a 400 MHz Bruker AVANCE-400 spectrometer with 64 scans being averaged per spectrum.

Gel Permeation Chromatography. Copolymer molecular weights and dispersities were determined using an Agilent 1260 Infinity GPC system equipped with both refractive index and UV−visible detectors. Two Agilent PLgel 5 μm Mixed-C columns and a guard column were connected in series and maintained at 60 °C. HPLC-grade DMF containing 10 mM LiBr was used as the eluent and the flow rate was set at 1.0 mL min^{-1}. Refractive index detection was used for calculation of molecular weights and dispersities by calibration against a series of ten near-monodisperse PMMA standards (with M_n values ranging from 370 to 2,520,000 g mol^{-1}).

Transmission Electron Microscopy. Unless stated otherwise, as-prepared copolymer dispersions were diluted at 20 °C using acidified deionised water (pH 3) to generate 0.05% w/w aqueous dispersions. Copper/palladium TEM grids (Agar Scientific, UK) were coated in-house to produce thin films of amorphous carbon. These grids were then treated with a plasma glow discharge for 30 s to create a hydrophilic surface. One droplet of an aqueous copolymer dispersion (20 μL; 0.05% w/w) was placed on a freshly-treated grid for 1 min and then blotted with a filter paper to remove excess solution. To stain the deposited nanoparticles, an aqueous solution of uranyl formate (10 μL; 0.75% w/w) was placed on the sample-loaded grid via micropipet for 45 s and then carefully blotted to remove excess stain. Each grid was then dried using a vacuum hose. Imaging was performed using a Philips CM100 instrument operating at 100 kV and equipped with a Gatan 1k CCD camera.

Dynamic Light Scattering. Measurements were conducted at 25 °C (unless stated otherwise) using a Malvern Instruments Zetasizer Nano ZS instrument equipped with a 4 mW He−Ne laser ($\lambda = 633$ nm) and an avalanche photodiode detector. Scattered light was detected at 173°. Copolymer dispersions were diluted to 0.10% w/w prior to analysis. Intensity-average hydrodynamic diameters were averaged over three runs and calculated using the Stokes−Einstein equation. Variable temperature studies were performed by heating the cuvette from 5°C to 42°C, followed by cooling from 42°C to 5°C at 2°C intervals. Between each measurement, 5 min was allowed for thermal equilibration.

Aqueous Electrophoresis. Zeta potential measurements were performed on 0.1% w/w aqueous copolymer dispersions at 20 °C in the presence of 1 mM KCl using the same Malvern Zetasizer Nano ZS instrument. The initial copolymer dispersion pH was pH 2.5 and was adjusted by addition of small amounts of aqueous 0.1 M NaOH, with 10 min being allowed for equilibrium at each pH. Zeta potentials were calculated from the Henry equation using the Smoluchowski approximation. Hydrodynamic DLS diameters were also recorded during these pH sweep experiments. All data were averaged over three consecutive runs.

Rheology. An AR-G2 rheometer equipped with a variable temperature Peltier plate and a 40 mL 2° aluminium cone was used for all experiments. The dispersion viscosity, loss modulus and storage modulus were measured as a function of applied strain, angular frequency, and temperature to assess the gel strength, gel viscosity and critical gelation temperature. Percentage strain sweeps were conducted at 25 °C using a constant angular frequency of 1.0 rad s^{-1}. Angular frequency sweeps were conducted at the critical gelation temperature corresponding to the maximum complex viscosity using an applied strain of 1.0%. Temperature sweeps were conducted using 20% w/w copolymer dispersions at an applied strain of 1.0% and an angular frequency of 1.0 rad s^{-1}. In these latter experiments, the copolymer dispersion was subjected to a single thermal cycle (heating up to 60 °C, followed by cooling to 1 °C), and then equilibrated at 1 °C for 15 min prior to measurements. The temperature was adjusted at 2 °C intervals, allowing a thermal equilibration time of 60 s between each measurement.

Small Angle X-ray Scattering Studies. SAXS patterns of 1.0% w/w aqueous tetrablock copolymer dispersions were collected at either a synchrotron source (Diamond Light Source, station I22, Didcot, UK) using monochromatic X-ray radiation (wavelength, $\lambda = 0.124$ nm, with q ranging from 0.015 to 1.3 nm^{-1}, where $q = 4\pi \sin \theta/\lambda$ is the length of the scattering vector and θ is one-half of the scattering angle) and a 2D Pilatus 2M pixel detector (Dectris, Switzerland) or using a Xeuss 2.0 (Xenocs) SAXS instrument equipped with a FOX 3D multilayered X-ray mirror, two sets of scatterless slits for collimation, a hybrid pixel area detector (Pilatus 1M, Dectris) and a liquid gallium MetalJet X-ray source (Excillum, $\lambda = 1.34$ Å). SAXS patterns were recorded at a sample-to-detector distance of approximately 1.20 m (calibrated using a silver behenate standard). Glass capillaries of 2.0 mm diameter were used as a sample holder. SAXS data were reduced (integration, normalization and absolute intensity calibration using SAXS patterns of deionized water assuming that the differential scattering cross-section of water is 0.0162 cm^{-1}) using Dawn software supplied by Diamond Light Source.[49] The temperature was adjusted and a thermal equilibration time of 10 min between each measurement was allowed.

5.3 Results and Discussion

5.3.1 Synthesis of PNAEP$_x$-PHBA$_y$ Diblock Copolymer Nano-objects via RAFT Aqueous Dispersion Polymerisation

Various research groups have demonstrated that RAFT-mediated aqueous dispersion polymerisation offers an efficient, reproducible route to synthesise a wide range of sterically-stabilised nanoparticles.[10,63–68] Moreover, this versatile approach usually provides access to spheres, worms and vesicles, whereas many RAFT-mediated aqueous emulsion polymerisation formulations are restricted to kinetically-trapped spheres.[62,69–71] Furthermore, the weakly hydrophobic character of the structure-directing block means that RAFT aqueous dispersion polymerisation often produces *stimulus-responsive* block copolymer nano-objects.[18,72,73] Herein, we explore an atom-efficient, industrially-relevant one-pot route in which the synthesis of a water-soluble precursor is taken to high conversion (95-97%) and immediately chain extended without further purification.[14–16] Preliminary studies indicated that PNAEP DPs below 65 only afforded macroscopic precipitates when targeting highly asymmetric PHBA-rich diblock copolymers under the stated reaction conditions (see Figure 5.3). Accordingly, several longer PNAEP$_{85}$ precursors were prepared via RAFT aqueous solution polymerisation of NAEP at pH 3.0 using DDMAT at 30 °C. To minimise the well-known problem of chain transfer to polymer during acrylic polymerisations,[74] a low-temperature redox initiator based on KPS and AsAc[75–77] was employed at a [DDMAT]/[KPS] molar ratio of 5.0. ^{1}H NMR studies confirmed good reproducibility for this first step: the PNAEP precursor had a mean DP of 85 ± 1 and 96 ± 1% NAEP conversion was achieved within just 10 min at 30 °C; these data are averaged over the thirty PNAEP precursors that were used to construct the pseudo-phase diagram (see later).

Figure 5.3. Digital image showing macroscopic phase separation when targeting PNAEP$_{35}$-PHBA$_{115}$ diblock copolymer nano-objects at 20% w/w solution and pH 3. Fortunately, much better colloidal stability was achieved by increasing the PNAEP DP up to 85.

DMF GPC analysis of the same aliquots extracted for ^{1}H NMR analysis confirmed good reproducibility for the target M_n of the thirty PNAEP$_{85}$ precursors prepared via RAFT aqueous solution polymerisation (19.1 ± 0.4 kg mol^{-1}; Figure 5.4). Moreover, each precursor had a relatively narrow molecular weight distribution ($M_w/M_n < 1.20$; Figure 5.4). These results compare well with those reported by Rubens *et al.* for various homopolymers (prepared using methyl (meth)acrylate, ethyl (meth)acrylate, butyl (meth)acrylate or styrene) synthesised using an autonomous self-optimising flow reactor, for which the variation in the target molecular weight was ± 2.5%.[78]

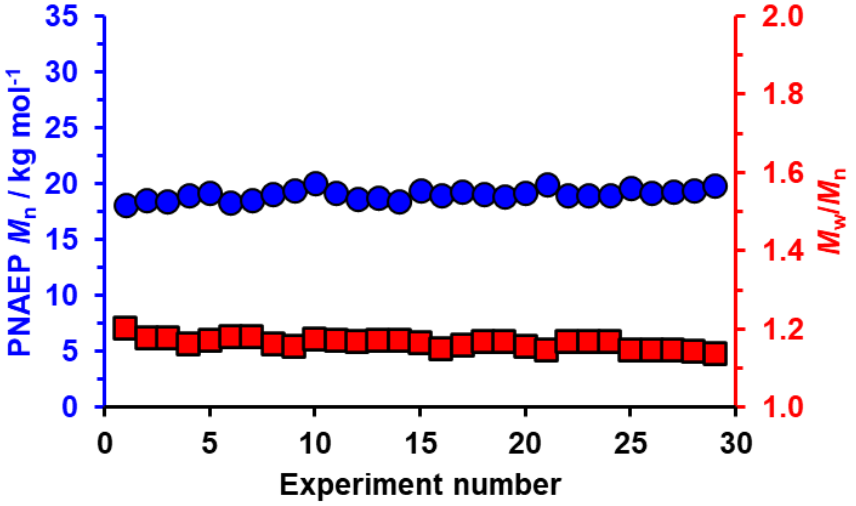

Figure 5.4. Reproducibility of M_n and M_w/M_n data indicated by DMF GPC analysis for each PNAEP$_{85}$ precursor (mean M_n = 19.1 ± 0.4 kg mol^{-1} and M_w/M_n = 1.16 ± 0.02) prepared by RAFT aqueous solution polymerisation of NAEP at pH 3 and 30 °C. In each case, this was the first step in the one-pot synthesis of PNAEP$_{85}$–PHBA$_x$ diblock copolymer nano-objects.

5.3.2 Kinetic Study During the One-Pot Synthesis of PNAEP$_{85}$-PHBA$_x$ Diblock Copolymer Nano-objects via RAFT Aqueous Dispersion Polymerisation at pH 3 or pH 7

The kinetics for the subsequent RAFT aqueous dispersion polymerisation of HBA at 30 °C were determined when targeting a PNAEP$_{85}$−PHBA$_{435}$ diblock composition (see circles in Figure 5.5). Importantly, the pH of the aqueous dispersion was adjusted to pH 3, which is well below the pK_a of approximately 5.25 for the carboxylic acid group located at the end of each PNAEP$_{85}$ stabiliser block (see Chapter 3). This precaution ensures that there is essentially no terminal anionic charge, which has been shown to prevent the formation of higher order morphologies such as worms and vesicles for analogous methacrylic formulations.[79] ^{1}H NMR studies were used to monitor the disappearance of vinyl signals at 5.8 and 6.4 ppm relative to the integrated two oxymethylene protons at 4.2−4.3 ppm assigned to the growing PHBA block (see Figure 5.6). This approach indicated that more than 95% conversion was achieved within 60 min at 30 °C when targeting 20% w/w solids. There is no discernible inhibition period, and the rate of polymerisation appears to remain constant (see semi-logarithmic plot; red circles in Figure 5.5a). The lack of any rate enhancement following micellar nucleation (observed after ~6 min or 25% conversion, which corresponds to a critical DP of 109; see Figure 5.7a) is perhaps surprising, because Blanazs *et al.* reported a marked rate enhancement associated with this event during the RAFT aqueous dispersion polymerisation of HPMA, which is an isomer of HBA.[63] This unexpected observation is attributed to the significantly higher aqueous solubility of HBA (which is miscible with water in all proportions) compared to that of HPMA (aqueous solubility ~130 g dm^{-3} at 25 °C); this means that monomer partitioning into the growing micelles is much less pronounced in the former case.[63]

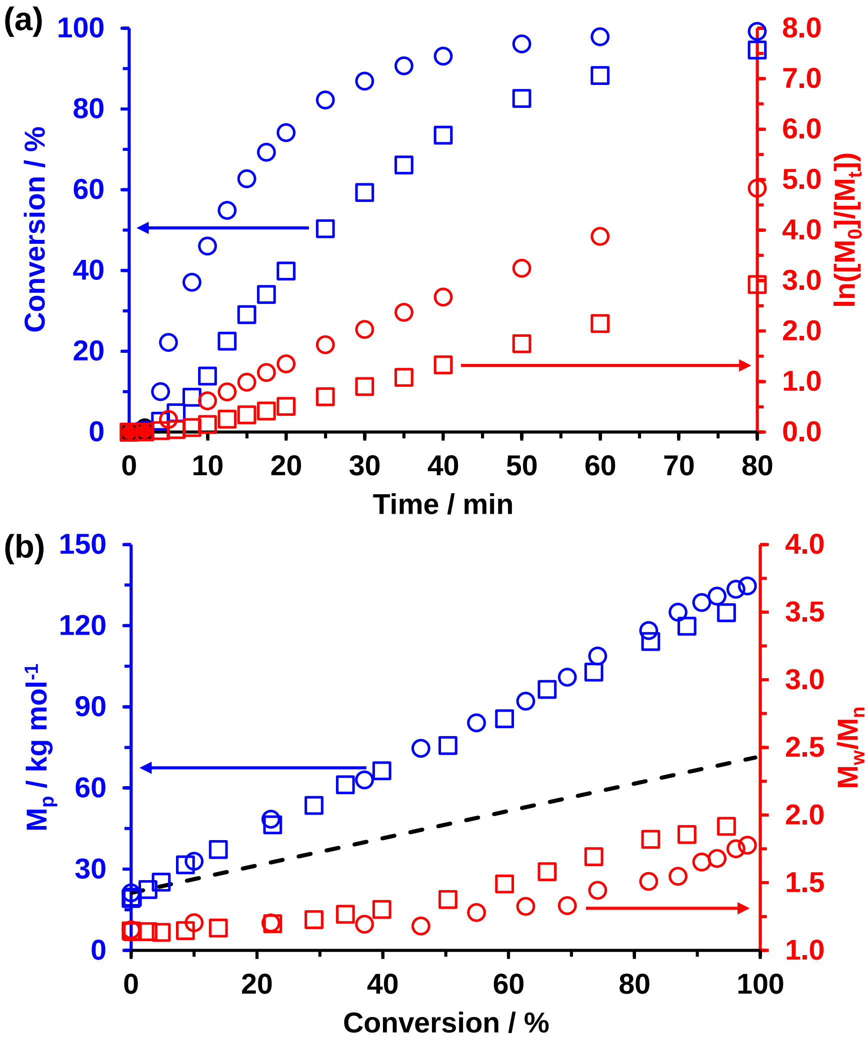

Figure 5.5. (a) Conversion *vs* time curves and the corresponding semilogarithmic plots determined by ^{1}H NMR spectroscopy during the RAFT aqueous dispersion polymerisation of HBA at 30 °C when targeting PNAEP$_{85}$-PHBA$_{435}$ diblock copolymer nanoparticles at either pH 3.0 (circles) or pH 7.0 (squares). Conditions: 20% w/w solids, [PNAEP$_{85}$]/[KPS] molar ratio = 5.0. (b) Evolution of M_n and M_w/M_n against conversion at either pH 3.0 (open circles) or pH 7.0 (open squares) determined by DMF GPC using a series of near-monodisperse PMMA calibration standards. The dashed line indicates the corresponding theoretical M_n values.

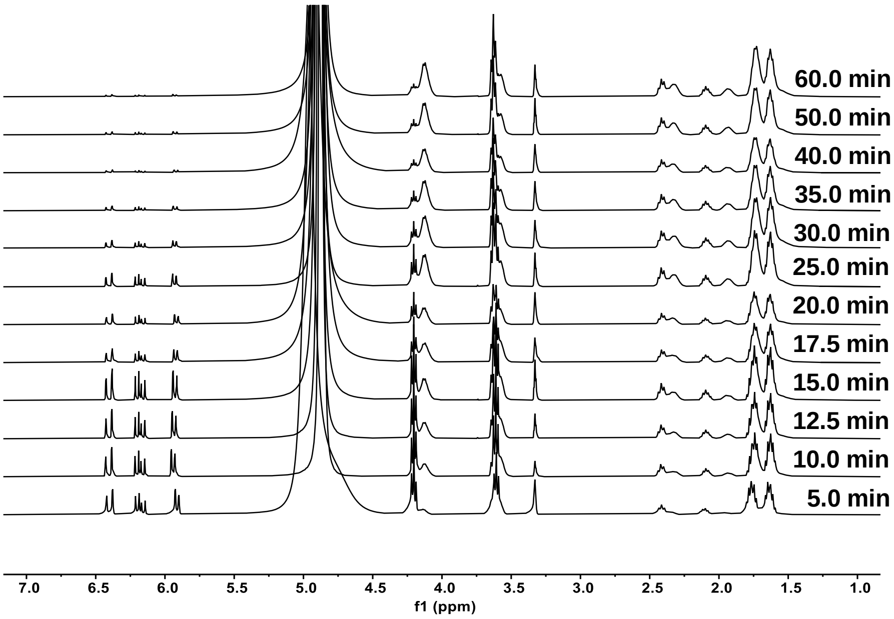

Figure 5.6. ^{1}H NMR spectra illustrating the gradual disappearance of the vinyl proton signals (between 5.8 and 6.5 ppm) during the RAFT aqueous dispersion polymerisation of HBA at 30 °C using a PNAEP$_{85}$ precursor at pH 3. Conditions: 20% w/w solids, [PNAEP$_{85}$]/[KPS] = 5.0, target PHBA DP = 435. Essentially full conversion (> 99%) is achieved within 60 min under these conditions.

DLS and aqueous electrophoresis studies of a PNAEP$_{35}$-PHBA$_{115}$ diblock copolymer indicated that the z-average diameter could be reduced from 585 nm to 32 nm by raising the dispersion pH from 4.8 to 5.9, i.e. above the *p*K$_a$ of the carboxylic acid end-group (see Figure 5.8). Accordingly, the synthesis of PNAEP$_{85}$-PHBA$_{435}$ diblock copolymers *via* RAFT aqueous dispersion polymerisation of HBA at 30 °C was attempted at pH 7.0. In this case, the low-temperature redox initiator system was based on KPS and N,N,N',N'-tetramethylethylenediamine (TMEDA), which is known to be effective at neutral pH.[80,81]

^{1}H NMR studies indicated an induction period of 4 min and a somewhat slower rate of polymerisation compared to the analogous synthesis at pH 3.0 when using a [PNAEP$_{85}$]/[KPS] molar ratio of 5.0 and a [TMEDA]/[KPS] molar ratio of 1.0 (see blue squares in Figure 5.5b). DLS studies indicated that particle nucleation occurred after 20.0 min (see Figure 5.7b). This corresponds to a HBA conversion of 40% and a critical PHBA DP of 174, which is significantly higher than that required at pH 3 (at pH 3, the critical PHBA DP = 109). This suggests that the anionic carboxylate group located at the end of each PNAEP$_{85}$ stabiliser chain is sufficient to delay the micellar nucleation of the growing PNAEP$_{85}$-PHBA$_x$ diblock copolymer chains compared to PNAEP$_{85}$ stabiliser chains containing a unionised carboxylic acid group. Nevertheless, 99% HBA conversion was achieved within 120 min (see blue squares in Figure 5.5b). DLS analysis indicated significantly different particle evolution during the RAFT dispersion of HBA depending on the dispersion pH (Figure 5.9).

(a) pH 3

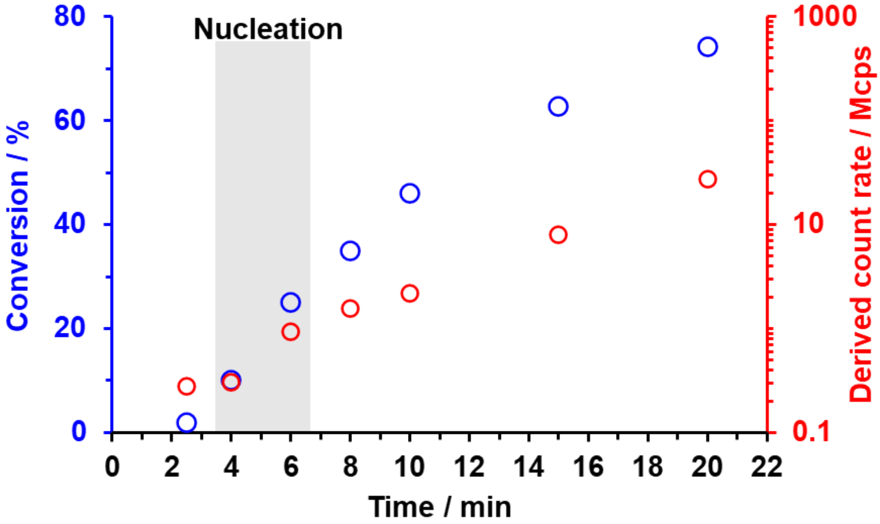

(b) pH 7

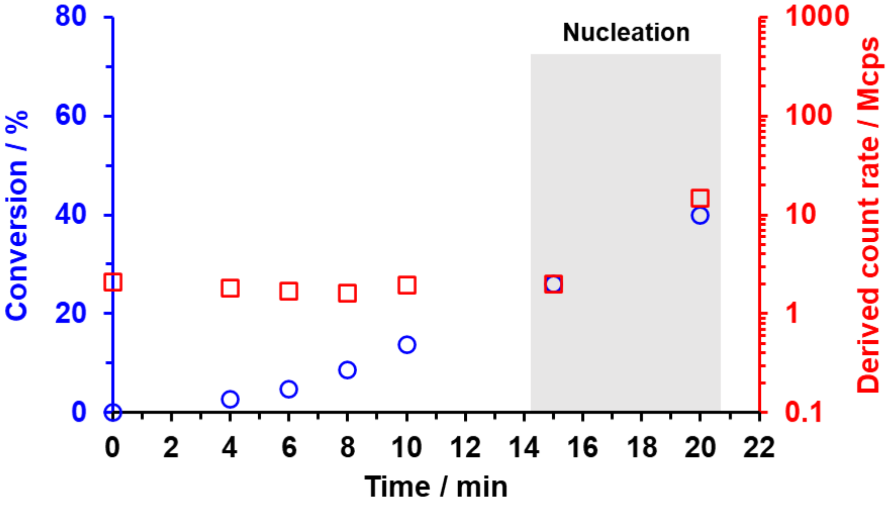

Figure 5.7. Evolution in monomer conversion and corresponding scattered light intensity (derived count rate) over time during the RAFT aqueous dispersion polymerisation of HBA at 30 °C when using a $PNAEP_{85}$ precursor: (a) pH 3 and (b) pH 7 Conditions: 20% w/w solids, $[PNAEP_{85}]/[KPS] = 3.0$, target PHBA DP = 435.

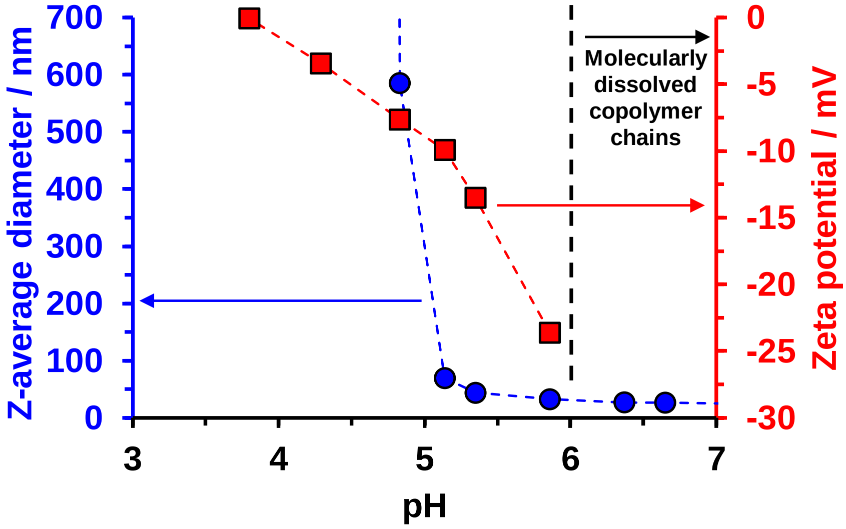

Figure 5.8. Z-average DLS diameter (blue circles) and zeta potential (red squares) vs. dispersion pH curves recorded for PNAEP$_{35}$-PHBA$_{115}$ diblock copolymer nanoparticles. Clearly, the steric stabilisation afforded by the PNAEP$_{35}$ stabiliser chains is not sufficient to prevent aggregation if the dispersion pH falls below the *p*K$_a$ of the carboxylic acid end-group.

At pH 3 four distinct morphology regions were identified (Figure 5.9a). At HBA conversions below 25%, the growing diblock copolymer chains are simply molecularly dissolved. Once nucleation has occurred, uniform spherical nanoparticles (DLS PDI < 0.10) grow in size from 30 nm to 47 nm as the HBA conversion increases from 25% to 63%. At higher HBA conversions, the z-average diameter increases significantly up to 1120 nm and the particle size distribution is much broader (DLS PDI = 1.0). Similar DLS data have been reported for pure worm phases.[82,83] Finally, as the HBA polymerisation nears completion, the z-average diameter is reduced to 837 nm (DLS PDI = 0.52), suggesting that a worm-to-vesicle transition has occurred. This sequence of copolymer morphologies is well-established for RAFT aqueous dispersion polymerisation formulations in the literature.[63]

In striking contrast, DLS analysis of a series of aliquots periodically extracted during the RAFT dispersion polymerisation of HBA at pH 7 indicated that this formulation only produced spherical nanoparticles (Figure 5.9b). After nucleation (40% HBA conversion), the z-average diameter for these spheres increased monotonically from 26 nm to 43 nm throughout the rest of the polymerisation. This was attributed to the terminal anionic charge on the PNAEP stabiliser chains, which is sufficient to prevent 1D sphere-sphere fusion and hence ensures the formation of kinetically-trapped spheres (Figure 5.9 and Scheme 5.2).

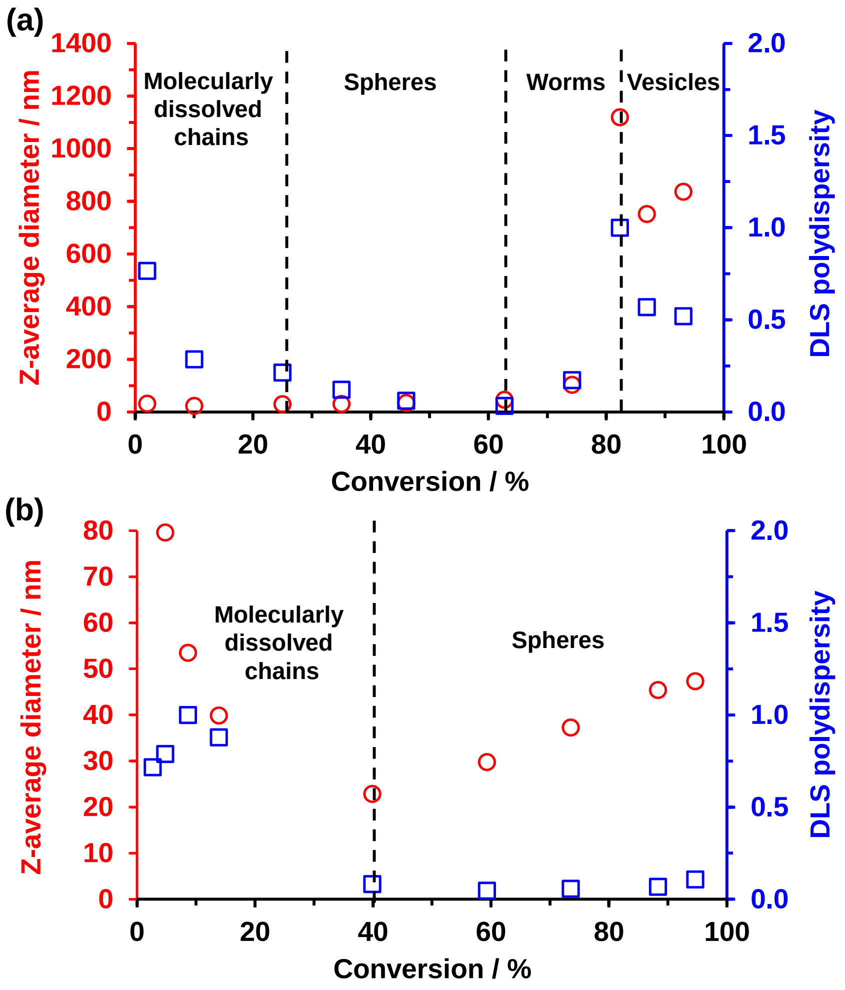

Figure 5.9. Evolution in DLS z-average diameter (red circles) and DLS polydispersity (blue squares) with monomer conversion during the RAFT aqueous dispersion polymerisation of HBA at (a) pH 3 (upper data set) and (b) pH 7 (lower data set). Conditions: 20% w/w solids, target PHBA DP = 435, [PNAEP$_{85}$]/[KPS] molar ratio = 5.0.

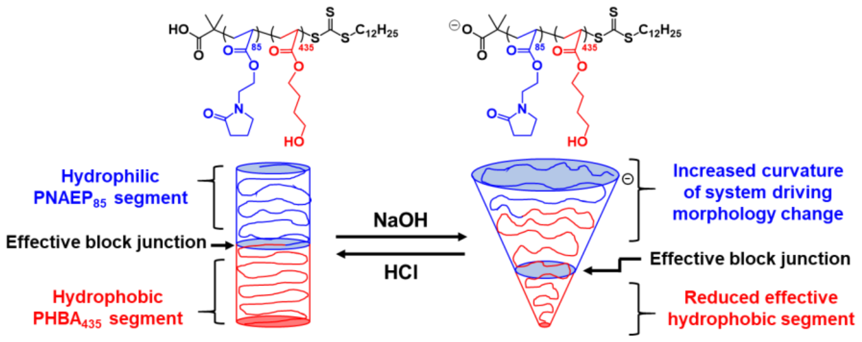

Scheme 5.2. Schematic cartoon to illustrate the effect of introducing terminal anionic charge via ionisation of the carboxylic acid group located at the end of each PNAEP$_{85}$ stabiliser chain of a PNAEP$_{85}$-PHBA$_{435}$ diblock copolymer. This is achieved by raising the dispersion pH from 3.0 to 7.0, which in turn drives a change in the copolymer morphology.

DMF GPC analysis indicated a linear evolution in molecular weight for HBA polymerisations performed at both pH 3 and 7 (Figure 5.5b). The final dispersity of the $PNAEP_{85}$-$PHBA_{435}$ diblock copolymer prepared at pH 7 (M_w/M_n = 1.91) was marginally higher than that obtained at pH 3 (M_w/M_n = 1.78). This difference was attributed to a slightly lower blocking efficiency which inevitably leads to homopolymer contamination: ~10% of the $PNAEP_{85}$ precursor did not undergo chain extension at pH 7 compared to ~5% for the same HBA polymerisation performed at pH 3, see Figure 5.10.

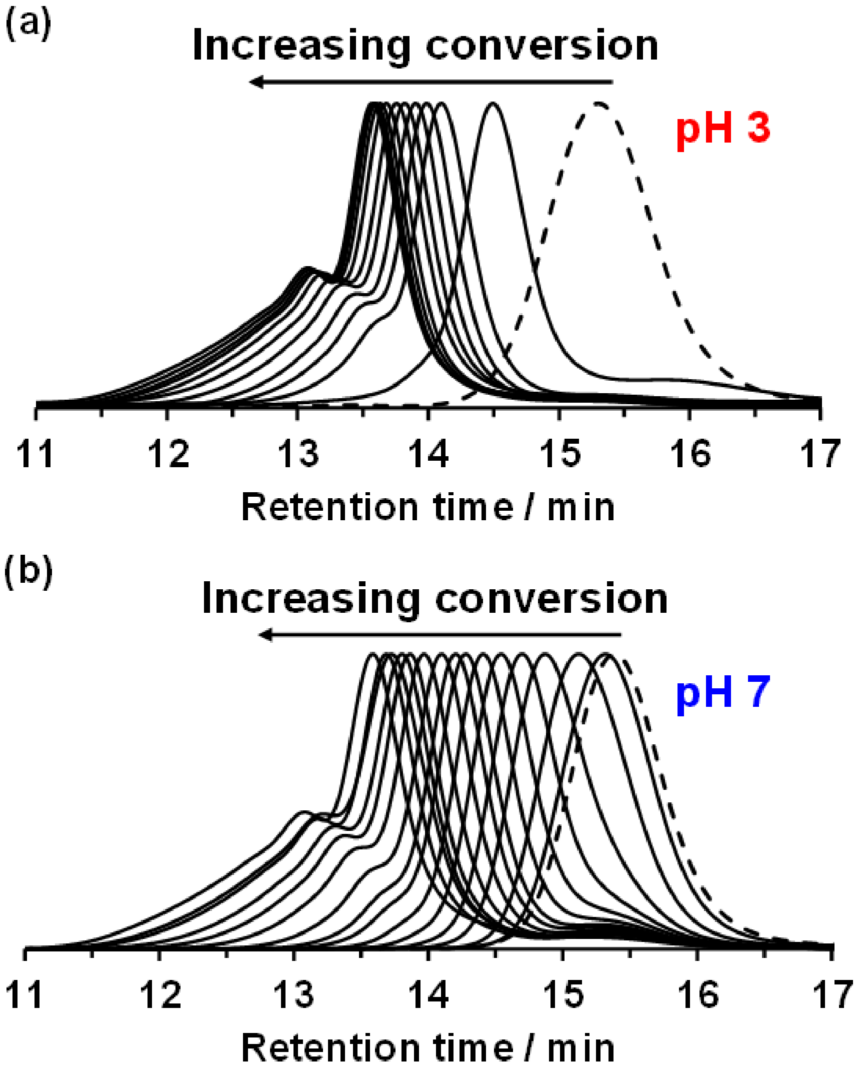

Figure 5.10. GPC traces recorded for the RAFT aqueous dispersion polymerisation of HBA conducted at (a) pH 3 (upper data set) and (b) pH 7 (lower data set). Dashed lines represent the unpurified $PNAEP_{85}$ precursor prepared via RAFT aqueous solution polymerisation of NAEP during the first step of this one-pot synthetic protocol.

Various copolymer morphologies were targeted at pH 3 by systematically varying the DP of the core-forming PHBA block between 100 and 550 while adjusting the copolymer concentration between 5% w/w and 40% w/w. ^{1}H NMR studies indicated that at least 90% conversion was achieved within 2 h at 5% w/w solids and more than 99% conversion within 1 h at 10% w/w or higher (see Table 5.1).

Table 5.1. Summary of the target diblock compositions, HBA conversions, molecular weight data, DLS particle diameters and DLS polydispersities and TEM assignments for all the PNAEP$_{85}$-PHBA$_x$ diblock copolymer nano-objects prepared in this study. [N.B. TEM assignments were made for glutaraldehyde-crosslinked nano-objects in all cases].

	^{1}H NMR		DMF GPC			DLS		TEM
Polymer concentration / % w/w	**PHBA DP**	**Conversion / %**	**M_n / kg mol^{-1}**	**M_p / kg mol^{-1}**	**M_w/M_n**	**Z-average diameter / nm**	**PDI**	**Assigned morphology**
5	125	90	43.2	48.1	1.20	31	0.14	Spheres
5	240	90	64.5	76.1	1.31	46	0.01	Spheres
5	315	90	83.4	96.5	1.30	133	0.22	Spheres+worms
5	370	90	92.6	105.8	1.37	328	0.43	Spheres+worms
5	530	90	132.1	141.2	1.51	600	0.27	Vesicles
10	170	98	60.2	63.5	1.26	38	0.02	Spheres
10	265	97	80.6	85.7	1.34	74	0.21	Spheres+worms
10	350	97	102.4	104.8	1.44	371	0.61	Spheres+worms
10	445	97	123.7	127.4	1.72	523	0.28	Worms+Vesicles
10	525	97	149.1	149.4	2.00	1854	0.24	Vesicles
15	140	99	56.2	57.0	1.21	32	0.06	Spheres
15	260	99	86.7	84.9	1.37	84	0.15	Spheres+worms
15	295	98	99.1	93.0	1.30	149	0.31	Spheres+worms
15	350	99	120.1	109.4	1.32	951	0.35	Worms
15	435	99	150.3	128.6	1.56	874	0.45	Vesicles
15	540	99	183.6	143.9	1.74	1630	0.30	Vesicles
20	115	99	54.6	56.0	1.21	30	0.08	Spheres
20	245	99	80.5	79.6	1.36	71	0.12	Spheres+worms
20	340	99	113.3	102.0	1.41	1037	0.48	Worms
20	435	99	148.6	122.7	1.65	1374	0.38	Vesicles
20	545	99	193.4	145.2	2.01	6071	0.17	Vesicles
30	140	99	59.1	59.1	1.17	34	0.03	Spheres
30	250	99	82.1	76.1	1.29	143	0.26	Spheres+worms
30	375	99	125.3	113.9	1.40	1303	0.40	Worms
30	565	99	198.9	152.2	1.87	4874	0.26	Vesicles
40	120	99	55.1	55.5	1.21	33	0.07	Spheres
40	245	99	86.2	81.1	1.32	119	0.19	Spheres+worms
40	355	99	126.2	107.8	1.45	1072	0.56	Worms
40	515	99	173.8	133.5	2.07	5410	0.31	Vesicles

DMF GPC analysis of the final PNAEP$_{85}$-PHBA$_x$ diblock copolymers indicated a strong linear correlation between the PHBA DP (as determined by end-group analysis using ^{1}H NMR spectroscopy) and the M_p of the final diblock copolymer (see Figure 5.11). For this comparison, the peak molecular weight M_p was preferred to M_n owing to the gradual development of a high molecular weight shoulder for PHBA DPs greater than 350. This feature resulted in progressive broadening of the molecular weight distribution

(M_w/M_n > 1.35) and thus greater deviation from theoretical M_n values calculated on the basis of ^{1}H NMR studies using end-group analysis (see Figure 5.12).

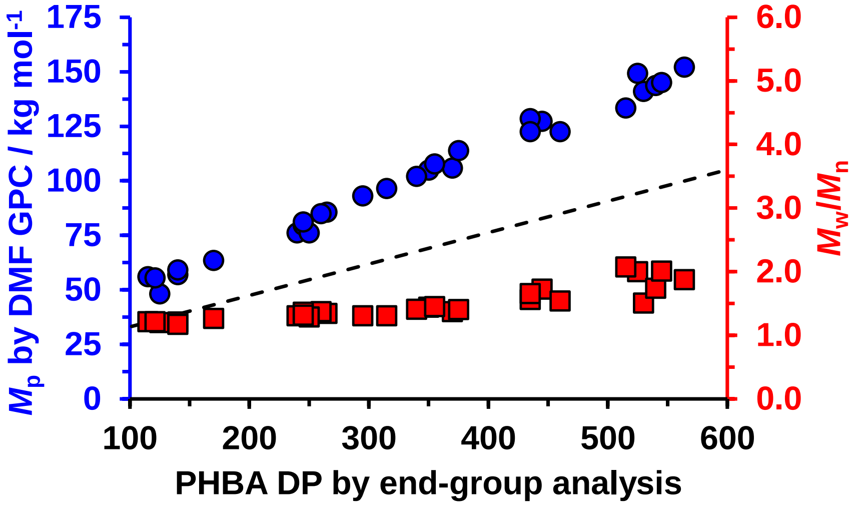

Figure 5.11. Relationship between the peak molecular weight (M_p) (determined by DMF GPC using a series of PMMA calibration standards) and PHBA DP (determined *via* ^{1}H NMR spectroscopy using end-group analysis). The corresponding dispersity data (M_w/M_n) are also shown for this copolymer series while the dashed line indicates the corresponding theoretical number-average molecular weight.

Similar observations reported for other PISA formulations[28,84] have been attributed to low levels (< 0.3 mol%) of dimethacrylate impurity; the incorporation of such bifunctional comonomers inevitably leads to branching as longer chains are targeted.[85] However, the HBA monomer used in the present study was purified by exhaustive extraction with *n*-hexane to remove any diacrylate impurities prior to its polymerisation.[16] Although we cannot exclude the possibility that a small amount of diacrylate impurity still remains after such purification, it is also well-documented that acrylic polymerisations suffer from chain transfer to polymer, which leads to long-chain branching.[74] GPC analysis of a $PNAEP_{85}$-$PHBA_{245}$ diblock copolymer using either a refractive index (RI) detector or a UV detector indicated the presence of a high molecular weight shoulder in each case (see Figure 5.13). This is consistent with chain transfer to polymer during the RAFT acidic aqueous dispersion polymerization of HBA, even though such syntheses were conducted at 30 °C. Indeed, there is literature precedent to suggest that this side reaction still occurs even during polymerizations conducted at 30 °C Indeed, there is literature precedent to suggest that this side reaction still occurs even during polymerisations conducted at 30 °C.[74,86,87]

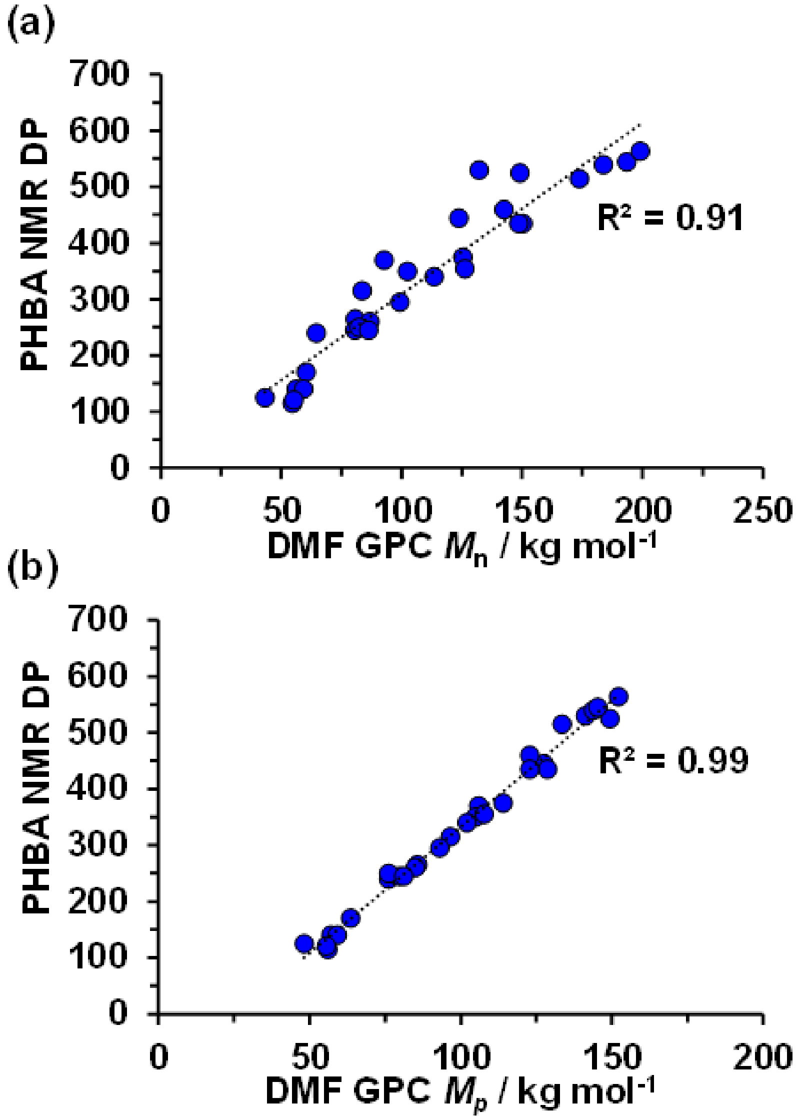

Figure 5.12. PHBA DPs calculated by end-group analysis using ^{1}H NMR spectroscopy plotted against (a) M_n (top) and (b) M_p (bottom) data obtained by DMF GPC analysis (vs. a series of PMMA calibration standards). R^2 values are included to highlight the more linear relationship obtained for the M_p data set compared to the M_n data set. This difference is attributed to a high molecular weight shoulder that appears when targeting PHBA DPs above 350; the latter feature is most likely the result of chain transfer to polymer.

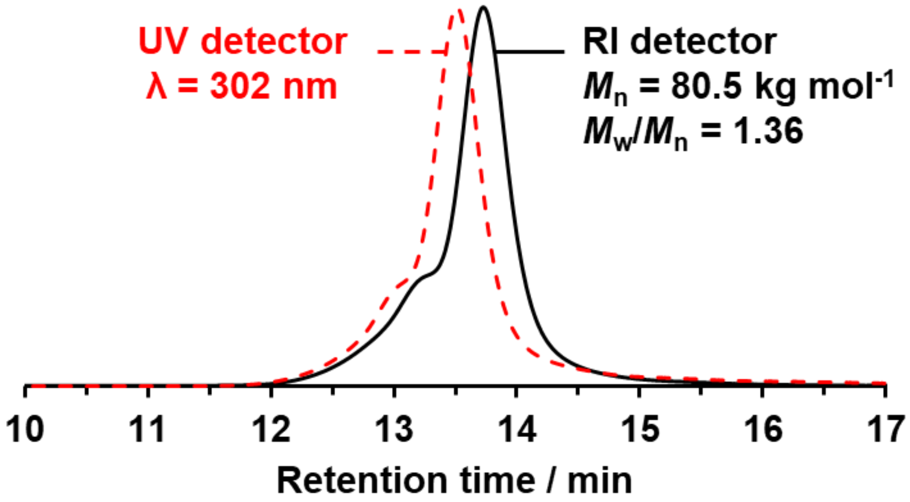

Figure 5.13. GPC curves recorded for a PNAEP$_{85}$-PHBA$_{245}$ diblock copolymer using either a RI detector (black solid trace) or a UV detector (λ = 302 nm; red dashed trace). The apparent shift in retention time is simply because the UV detector is placed before the RI detector in the GPC set-up.

5.3.3 Covalent Stabilisation of Diblock Copolymer Nano-objects Using Glutaraldehyde

TEM was employed to assess the morphology of the PNAEP$_{85}$-PHBA$_x$ diblock copolymer nano-objects formed at 22 °C and pH 3. In our experience, TEM characterisation of such nano-objects is extremely challenging because the PHBA block has a relatively low T_g, as indicated by its soft gum-like appearance at ambient temperature and confirmed by DSC of a PHBA$_{300}$ homopolymer (see Figure 5.14). As far as we are aware, there are no other T_g values reported for PHBA in the literature. Five PNAEP$_{85}$-PHBA$_x$ diblock copolymers prepared via RAFT aqueous dispersion polymerisation were then analysed by DSC. Two heating cycles were performed between –80 °C and 60 °C. The T_g observed for the PHBA block was reduced from –14.3 °C to –40.5 °C on increasing its DP (x) from 125 to 525 (Figure 5.15). This trend is contrary to that expected according to the Flory-Fox equation.[88] However, this relationship assumes that there are no specific interactions between the comonomer repeat units, whereas hydrogen bonding between the pyrrolidone rings within the PNAEP block and the hydroxyl groups on the HBA repeat units almost certainly occurs in the solid state.

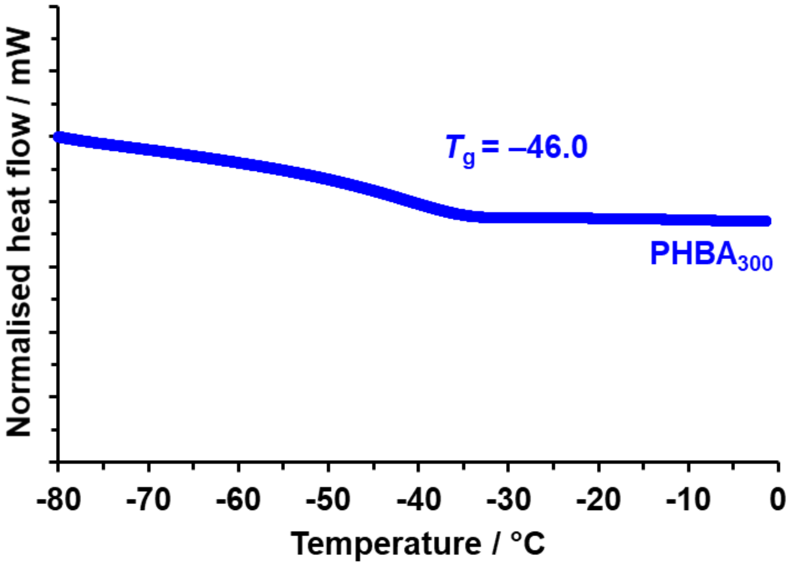

Figure 5.14. DSC curve recorded at a heating rate of 10 °C min^{-1} for a PHBA$_{300}$ homopolymer prepared *via* RAFT solution dispersion polymerisation of HBA in methanol at 44 °C. The calculated T_g is stated above the corresponding DSC curve.

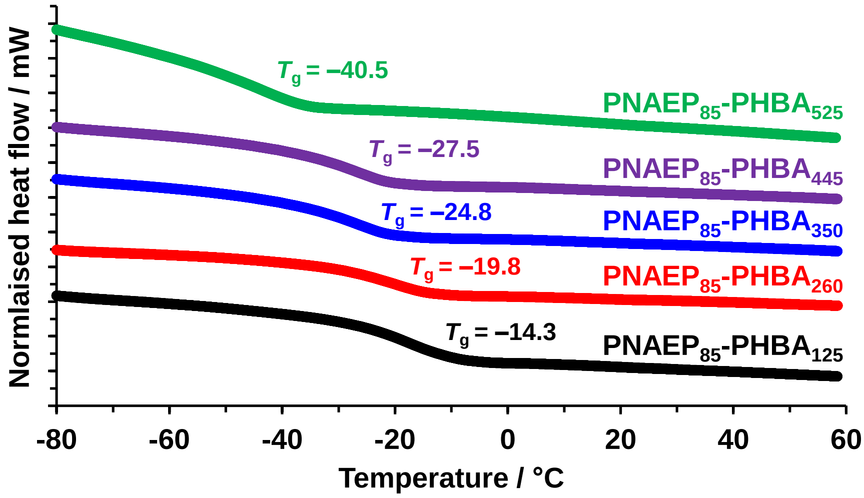

Figure 5.15. DSC curves recorded at a heating rate of 10 °C min^{-1} for PNAEP$_{85}$–PHBA$_{125}$, PNAEP$_{85}$–PHBA$_{260}$, PNAEP$_{85}$–PHBA$_{350}$, PNAEP$_{85}$–PHBA$_{445}$ and PNAEP$_{85}$–PHBA$_{525}$ diblock copolymers prepared *via* one-pot RAFT aqueous dispersion polymerisation of HBA. The T_g determined for each PHBA block is stated above the corresponding DSC curve. Each DSC curve is arbitrarily offset for the sake of clarity.

The low T_g values recorded for the PHBA block (Figures 5.14 and 5.15) invariably lead to film formation on the TEM grid (Figure 5.16a), which makes the original copolymer morphology impossible to assess. In the present study, crosslinking between the weakly hydrophobic PHBA chains is achieved using GA, which forms acetal linkages with pendent hydroxyl groups in aqueous solution (Scheme 5.3).[44] In principle, one GA molecule can react with four PHBA hydroxy groups to form two stable acetal linkages. This suggests that a GA/HBA molar ratio of 0.25 should be sufficient to afford covalently-stabilised nanoparticles that do not undergo film formation during TEM grid preparation. However, it was found empirically that a GA/HBA molar ratio of 0.66 was required to ensure that good-quality TEM images were obtained (see Figure 5.16). Attempts to monitor the rate of this crosslinking reaction through ^{1}H NMR and FTIR studies were unsuccessful (data not shown). No doubt this is the result of the complex chemistry exhibited by GA in aqueous solution, for which many side reactions are known.[45–48,55–59] However, when GA was added to 20% w/w PNAEP$_{85}$-PHBA$_x$ nano-objects (PNAEP$_{85}$-PHBA$_x$ spheres, worms and vesicles; GA/HBA molar ratio = 0.66) the dispersion gelled within 5 min. This indicated that crosslinking occurs rapidly at this relatively high copolymer concentration. To avoid gelation, all crosslinking was conducted at 5% w/w and the GA reaction was allowed to proceed for 16 h (Scheme 5.3).

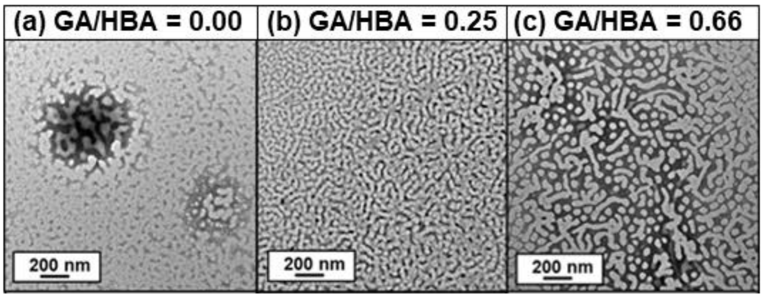

Figure 5.16. Representative TEM images recorded for (a) linear PNAEP$_{85}$-PHBA$_{265}$ and covalently-stabilised PNAEP$_{85}$-PHBA$_{265}$ diblock copolymers using (b) GA crosslinker (5% w/w, GA/HBA molar ratio = 0.35, pH 3) and (c) GA crosslinker (5% w/w, GA/HBA molar ratio = 0.66, pH 3). In each case, the nano-objects were reacted with GA for 24 h at 22 °C prior to dilution to 0.05% w/w for TEM analysis.

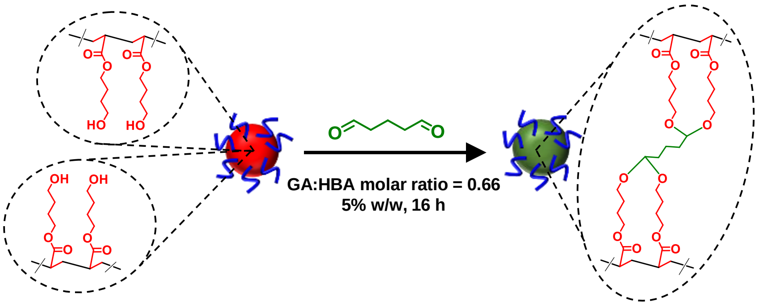

Scheme 5.3. Intermolecular crosslinking of the PHBA chains within PNAEP$_{85}$-PHBA$_x$ diblock copolymer nano-objects (in this case, spheres) via acid-catalysed nucleophilic attack of pendent hydroxyl groups by glutaraldehyde (GA). This enabled a range of PNAEP$_{85}$-PHBA$_x$ diblock copolymer nano-objects to be crosslinked under a variety of conditions (dispersion pH between 3 and 7 and dispersion temperatures between 11 °C and 41 °C.

5.3.4 Construction of a phase diagram for $PNAEP_{85}$-$PHBA_x$ Nano-Objects

This approach enabled reproducible covalent stabilisation of the various nano-objects. Importantly, the concomitant increase in T_g allowed conventional TEM analysis, see Figure 5.17. Moreover, DSC analysis confirmed that GA crosslinking increased the T_g of the PHBA block from less than –14 °C to more than 100 °C while retaining the original T_g for the PNAEP block (Figure 5.17f). DLS studies indicated that such crosslinking also eliminated the stimulus-responsive behaviour exhibited by some of these nano-objects, hence preserving the preferred copolymer morphology at any desired temperature or pH (Figure 5.18a and Figure 5.18b). The TEM-assigned morphologies were used to construct a phase diagram (Figure 5.19a). Finally, SAXS studies of $PNAEP_{85}$-$PHBA_{110}$, $PNAEP_{85}$-$PHBA_{350}$ and $PNAEP_{85}$-$PHBA_{450}$ nano-objects were used to confirm pure phases of spheres, worms, and vesicles, respectively (Figure 5.19b).

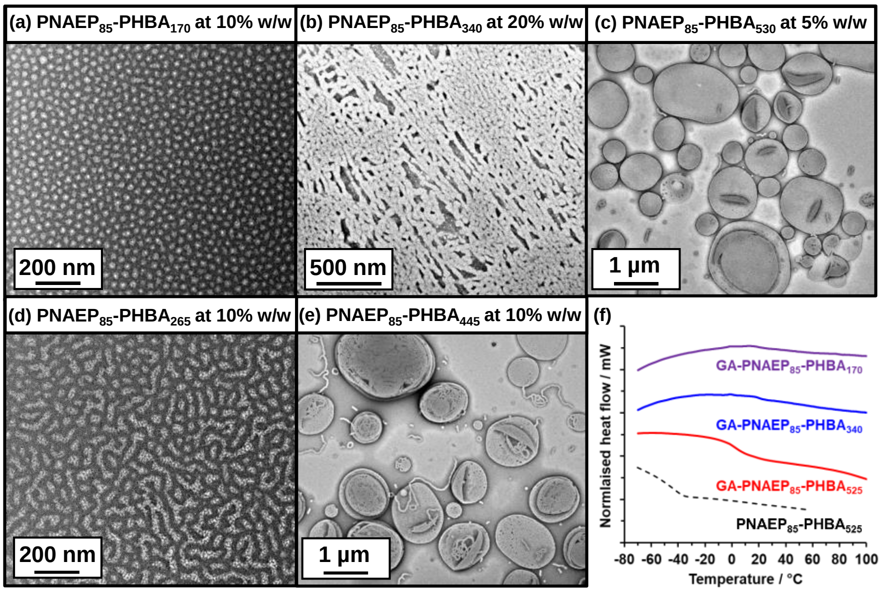

Figure 5.17. Representative TEM images recorded for: (a) $PNAEP_{85}$-$PHBA_{170}$ spheres prepared at 10% w/w; (b) $PNAEP_{85}$-$PHBA_{340}$ worms prepared at 20% w/w; (c) $PNAEP_{85}$-$PHBA_{530}$ vesicles prepared at 5% w/w; (d) a $PNAEP_{85}$-$PHBA_{265}$ mixed phase comprising spheres and short worms prepared at 10% w/w; (e) a $PNAEP_{85}$-$PHBA_{455}$ mixed phase comprising worms and vesicles prepared at 10% w/w; (f) DSC traces recorded for a linear $PNAEP_{85}$-$PHBA_{525}$ diblock copolymer (dashed black) and three GA-crosslinked $PNAEP_{85}$-$PHBA_x$ diblock copolymer nano-objects (where x = 170, 340 or 525). In each case, the nano-objects were covalently stabilised using GA crosslinker (5% w/w, GA/HBA molar ratio = 0.66, pH 3) for 24 h at 22 °C prior to dilution to 0.05% w/w for TEM analysis.

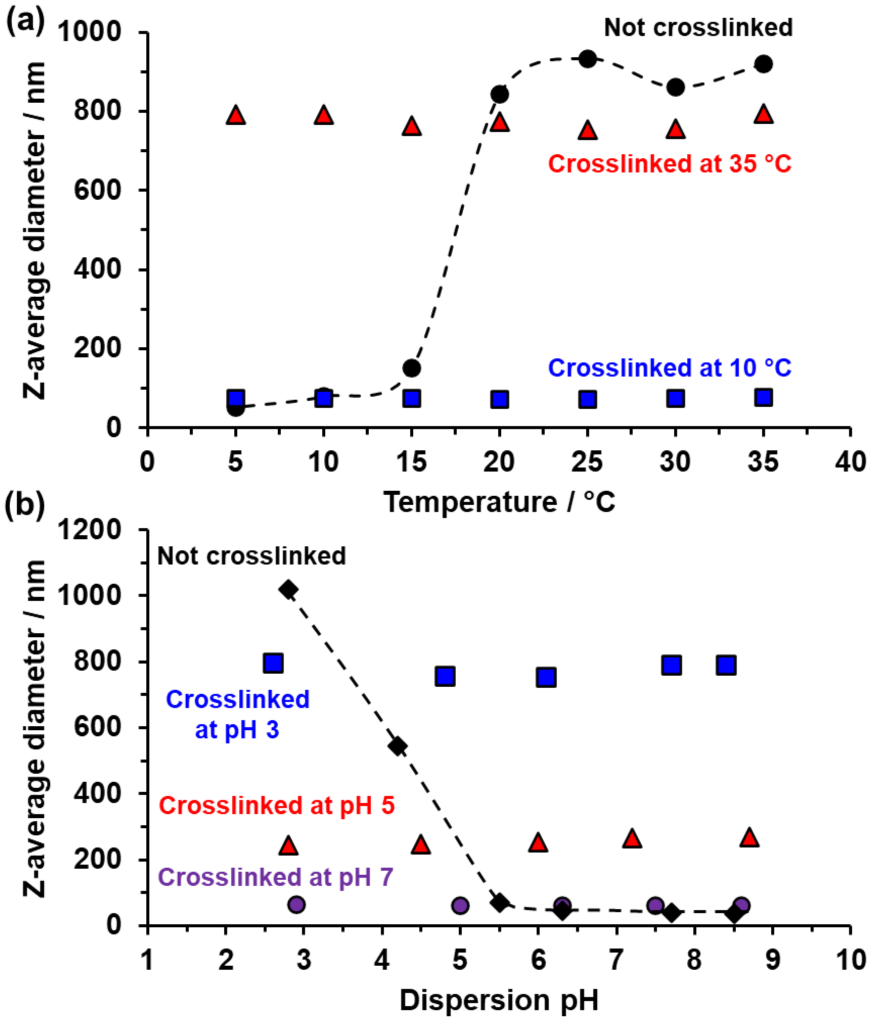

Figure 5.18. (a) Variable temperature DLS studies of 0.1% PNAEP$_{85}$-PHBA$_{435}$ diblock copolymer nano-objects prior to crosslinking (black circles; dashed lined added for as a guide for the eye), crosslinked for 24 h using 5% w/w glutaraldehyde at either 10 °C (blue squares) or at 35 °C (red triangles). (b) DLS data obtained as a function of dispersion pH for aqueous dispersions of 0.1% PNAEP$_{85}$-PHBA$_{545}$ diblock copolymer nano-objects prior to crosslinking (black diamonds; dashed lined added for as a guide for the eye), crosslinked at 22 °C for 24 h using 5% w/w glutaraldehyde at pH 3 (blue squares), pH 5 (red triangles), and pH 7 (purple circles).

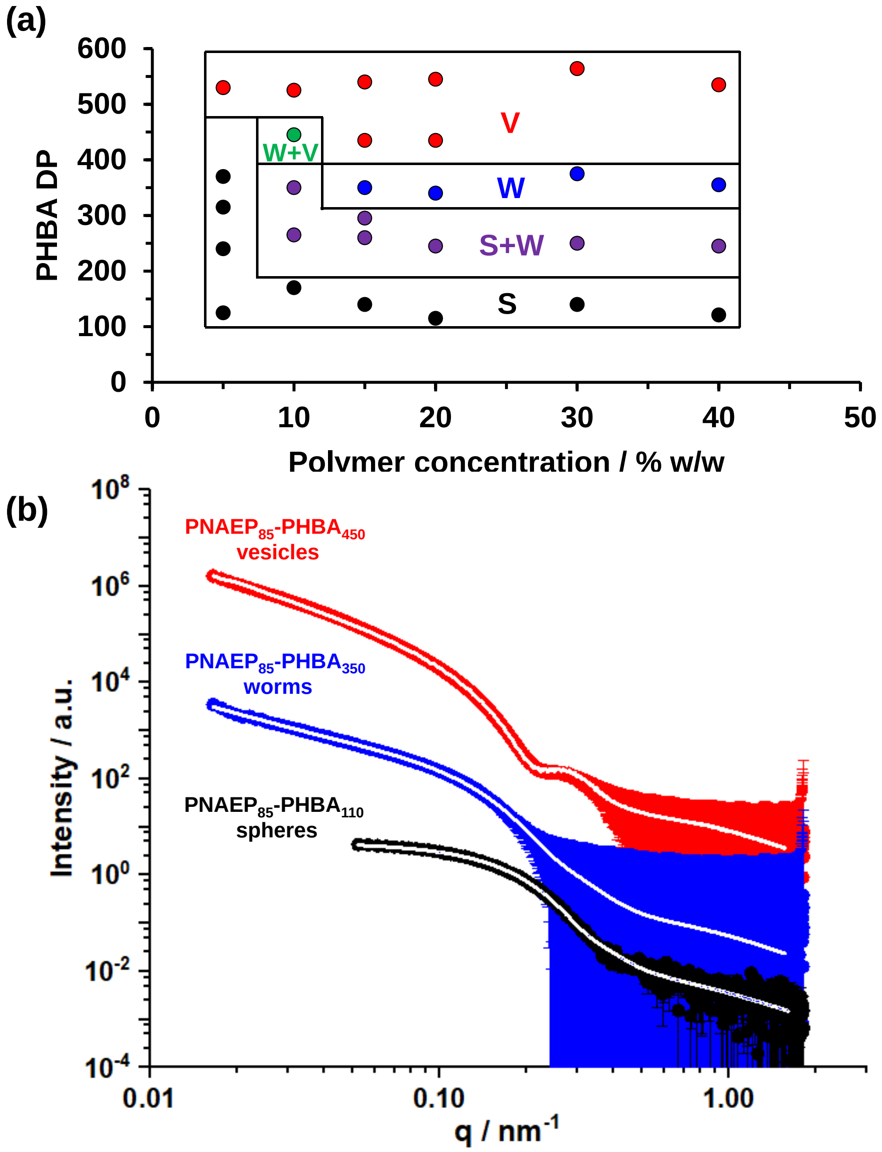

Figure 5.19. (a) Phase diagram constructed for PNAEP$_{85}$-PHBA$_x$ diblock copolymer nano-objects. **S** = pure spheres; **S + W** = a mixed phase comprising spheres & worms; **W** = pure worms; **W + V** = a mixed phase comprising worms & vesicles; **V** = pure vesicles. Each copolymer morphology was assigned on the basis of TEM analysis of covalently-stabilised nano-objects prepared using glutaraldehyde as a crosslinker at pH 3 and 22 °C (GA/HBA molar ratio = 0.66). Corresponding TEM images are shown in Figure 5.20. (b) SAXS patterns (black, blue and red symbols) and corresponding data fits (solid white lines) obtained for 1.0% w/w aqueous copolymer dispersions of *linear* PNAEP$_{85}$-PHBA$_{110}$ spheres, PNAEP$_{85}$-PHBA$_{350}$ worms and PNAEP$_{85}$-PHBA$_{450}$ vesicles (each of these nano-objects was synthesised at 20 % w/w solids).

At the lowest concentration investigated (5% w/w), relatively transparent dispersions of free-flowing, kinetically-trapped spheres were obtained when targeting PHBA DPs ranging from 125 to 240. For this series of spheres, the z-average diameter recorded by DLS studies at 22 °C increased linearly from 31 nm to 46 nm with increasing

PHBA DP (see Table 5.1 and Figure 5.20). When the target PHBA DP was increased up to either 315 or 370, the final copolymer dispersion remained free-flowing. However, DLS analysis (see Table 5.1) indicated a significant increase in the z-average particle diameter (up to 133 nm and 328 nm, respectively) and substantially broader particle size distributions (DLS polydispersities were 0.22 and 0.43, respectively). TEM analysis of the corresponding GA-crosslinked nano-objects indicated the presence of a minor population of relatively short worms (Figure 5.20). The final copolymer dispersion became turbid when further increasing the PHBA DP to 530; DLS analysis indicated large, relatively polydisperse particles (z-average diameter = 600 nm, DLS polydispersity = 0.27), suggesting vesicle formation. Indeed, TEM studies confirmed the presence of highly polydisperse, unilamellar vesicles of 1-2 µm diameter (see Figure 5.20). Obtaining pure phases of higher order morphologies at such low copolymer concentrations is relatively rare owing to the reduced probability of sphere-sphere fusion under such conditions.[10] Presumably, the high degree of hydration and relatively low T_g of the structure-directing PHBA chains results in sufficiently high mobility to facilitate the evolution in copolymer morphology during PISA.[28]

For $PNAEP_{85}$-$PHBA_x$ dispersions prepared at 10% w/w solids, TEM analysis of covalently-stabilised nano-objects (crosslinked at 22 °C and pH 3) indicated pure spheres for x = 170 (z-average diameter = 38 nm), a mixed phase of spheres & worms for x = 265 and 350 (z-average diameter = 74 nm and 371 nm, respectively) and a mixed phase comprising worms & vesicles for x = 445 (z-average diameter = 523 nm; see Table 5.1 and Figure 5.20). The latter dispersion was both highly turbid (owing to strong light scattering by the vesicles) and also formed a free-standing gel (owing to multiple worm-to-worm contacts[89]). On increasing the PHBA DP up to 525, DLS and TEM studies indicated the formation of a pure vesicle phase (z-average diameter = 1864 nm), as expected. At 15% w/w solids (or higher), pure worms could be obtained for x = 340–375, resulting in the formation of highly transparent free-standing gels at 22 °C and pH 3 (Figure 5.20). This suggests that the greater mobility of the PHBA chains leads to a relatively broad DP range for a pure worm phase compared to other diblock copolymer systems. For example, Byard *et al.* reported that a pure worm phase could be obtained at only a *single* core-forming block DP for an all-acrylamide formulation when investigating a range of steric stabiliser block DPs.[66] Similarly, pure worm phases are only observed for x = 200–220 for PEG_{113}-$PHPMA_x$ diblock copolymers or for x = 115–140 for $PGMA_{47}$-$PHPMA_x$ diblock copolymers, respectively.[63,82] It is perhaps also worth emphasising that $PNAEP_{85}$-$PHBA_x$ worms require much higher x values compared to the aforementioned systems. This reduces the RAFT agent content of the diblock copolymer, which makes such formulations more cost-effective and also less likely to lead to toxicity problems.[90] These advantages augur well for potential cell biology applications.[91–93] Finally, DLS and TEM analysis of the vesicles formed when x = 435–565 confirmed that higher copolymer concentrations promote the formation of oligolamellar vesicles (see Table 5.1 and Figure 5.20).[10]

SAXS patterns recorded for 1.0% w/w aqueous dispersions of linear $PNAEP_{85}$-$PHBA_{110}$, $PNAEP_{85}$-$PHBA_{350}$ and $PNAEP_{85}$-$PHBA_{450}$ nano-objects at pH 3 are shown in Figure 5.20b. Unlike TEM, the SAXS data are averaged over many millions of nanoparticles, so the latter technique is expected to provide much more statistically robust information. Moreover, SAXS studies are conducted on aqueous dispersions, so GA crosslinking is not required to stabilise the copolymer morphology. The low q gradient for the $PNAEP_{85}$-$PHBA_{110}$ SAXS pattern is close to zero, which indicates the presence of spheres, as expected.[94] In contrast, the low q gradient of the SAXS pattern obtained for the $PNAEP_{85}$-$PHBA_{350}$ dispersion is close to –1, suggesting highly anisotropic worms.[16,82] Finally, a low q gradient of –2 was observed for the $PNAEP_{85}$-$PHBA_{350}$ SAXS pattern, which is characteristic of vesicles (or bilayers).[16,82]

As expected based on the corresponding TEM images, such SAXS patterns could be satisfactorily fitted using well-known scattering models developed for spheres, worms and vesicles, respectively (see Table 5.2 for a summary of the nano-object dimensions obtained when using such models).[95,96] Analysis of the SAXS data shown in Figure 5.20b indicated a core diameter of 29 nm for the $PNAEP_{85}$-$PHBA_{110}$ spheres, which is consistent with a hydrodynamic DLS diameter of 30 nm and also a TEM diameter of 28 nm for the crosslinked spheres. A core cross-section diameter of 34 nm was determined for $PNAEP_{85}$-$PHBA_{350}$ worms; this is somewhat smaller than that suggested with TEM studies (45 nm), perhaps suggesting that the PHBA cores remain deformable after GA crosslinking.[14] An overall volume-average diameter of 749 nm was determined by SAXS for the $PNAEP_{85}$-$PHBA_{450}$ vesicles (DLS diameter = 874 nm and TEM diameter = 734 nm). Interestingly, the mean vesicle membrane thickness of 23.2 nm suggests significant interdigitation of the PHBA chains.[16,97] These data are generally self-consistent, indicating that using the GA crosslinker enables effective covalent stabilisation of nano-objects without significantly perturbing their dimensions.

Table 5.2. Summary of z-average diameters (and corresponding DLS polydispersities, or PDI), structural parameters obtained from SAXS analysis and number-average TEM diameters estimated for $PNAEP_{85}$-$PHBA_x$ nano-objects at 20 °C. DLS studies were conducted using 0.1% w/w aqueous dispersions. SAXS studies were performed on 1.0% w/w aqueous dispersions using well-known sphere, worm or vesicle models to fit the data (see the SAXS models section in Chapter 7 for more information). TEM analysis was conducted using 0.05% w/w aqueous dispersions of GA-crosslinked $PNAEP_{85}$-$PHBA_x$ nano-objects (crosslinking conditions: 5% w/w, GA/HBA molar ratio = 0.66, pH 3).

		DLS	SAXS					TEM
PHBA DP	**Assigned morphology**	**Diameter / nm (PDI)**	**Diameter / nm**	**Width / nm**	**Length / nm**	**Kuhn length / nm**	**Membrane thickness / nm**	**Diameter / nm**
110	**Spheres**	**30 (0.08)**	**29 ± 4**	**--**	**--**	**--**	**--**	**28 ± 4**
350	**Worms**	**371 (0.61)**	**--**	**34 ± 4**	**>1000**	**101**	**--**	**45 ± 7**
450	**Vesicles**	**874 (0.45)**	**749 ± 112**	**--**	**--**	**--**	**23 ± 3**	**734 ± 110**

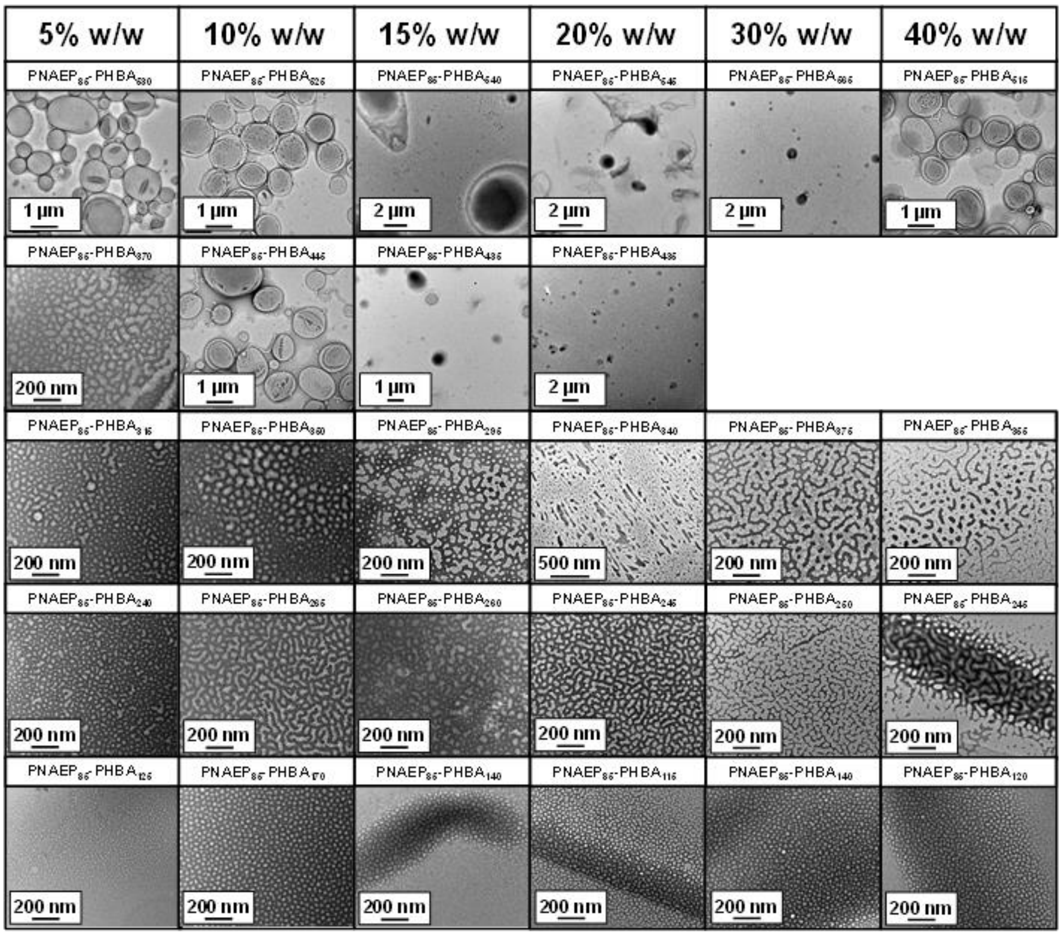

Figure 5.20. TEM images recorded for all the glutaraldehyde-crosslinked $PNAEP_{85}$-$PHBA_x$ diblock copolymer nano-objects prepared in this study. These images were used to assign the copolymer morphology and hence construct the phase diagram shown in Figure 5.19.

5.3.5 Analysis of the pH-dependence of $PNAEP_{85}$-$PHBA_x$ Nano-Objects

Lovett and co-workers reported that ionisation of a single carboxylic acid end-group increased the degree of hydration of the stabiliser block of $PGMA_{56}$-$PHPMA_{155}$ worms sufficiently to induce a worm-to-sphere transition.[72] This pH-induced change in the packing parameter, *P*, proved to be reversible and could be prevented by addition of salt. Furthermore, gradual addition of 1 M NaOH to $PGMA_{43}$-$PHPMA_{200}$ vesicles lead to the *irreversible* formation of a free-standing worm gel. To examine whether ionisation of terminal carboxylic acid groups also induced a change in copolymer morphology for $PNAEP_{85}$-$PHBA_{545}$ diblock copolymer nano-objects, GA crosslinking was conducted at pH 3, pH 5 and pH 7 prior to TEM analysis (Figure 5.21a).

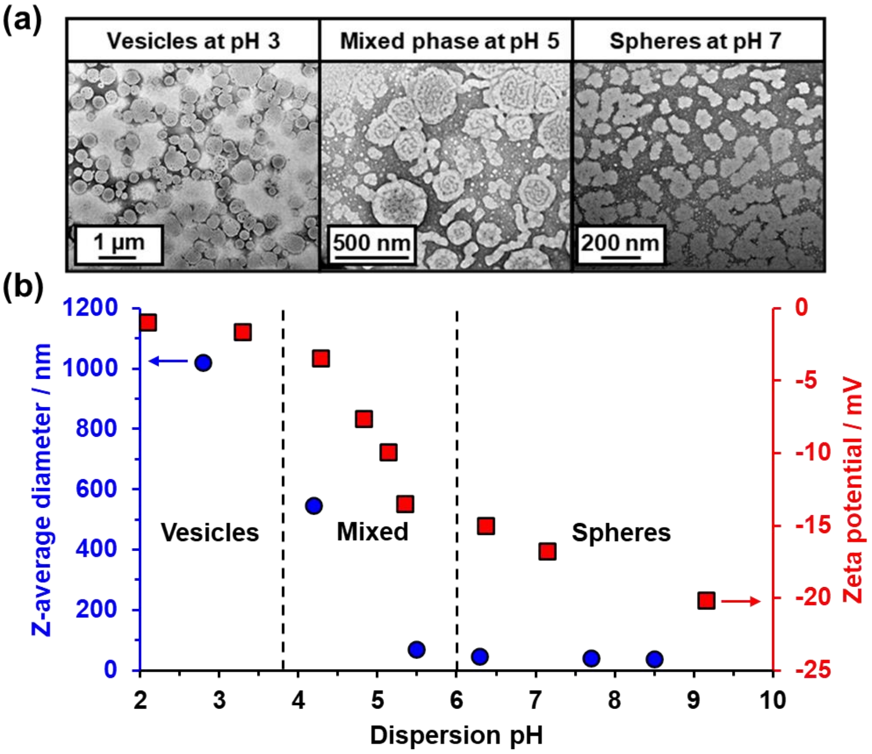

Figure 5.21. (a) TEM images recorded for $PNAEP_{85}$-$PHBA_{545}$ diblock copolymer nano-objects crosslinked using glutaraldehyde at 22 °C for 24 h at pH 7, pH 5 or pH 3. (b) Z-average diameter (blue squares) and zeta potential (red squares) as a function of dispersion pH recorded for the same $PNAEP_{85}$-$PHBA_{545}$ nano-objects, where the anionic character observed above pH 4 is attributed to ionisation of the carboxylic acid group located at the end of each PNAEP stabiliser chain.

The carboxylic acid end-groups are protonated at pH 3 and polydisperse vesicles are obtained under such conditions (z-average diameter = 1020 nm; TEM diameter = 690 ± 260 nm; see Figure 5.21). The dispersion pH was adjusted to pH 5 by addition of NaOH and TEM studies indicated the formation of a mixed phase comprising vesicles and worms. DLS analysis indicated that a concomitant reduction in z-average diameter occurred during this partial phase transition from vesicles to mixed vesicles/worms (Figure 5.21). Further NaOH addition produced somewhat ill-defined, pseudo-spherical nano-objects at pH 7 (z-average diameter = 38 nm; TEM diameter = 87 ± 18 nm; Figure 5.21). This suggests that ionisation of the carboxylic acid end-group at the end of each PNAEP stabiliser chain is sufficient to drive a vesicle-to-sphere transition. This interpretation is supported by aqueous electrophoresis data (see Figure 5.21b). Furthermore, this pH-induced transition proved to be both rapid and reversible, as evidenced by digital photographs and DLS studies (see Figure 5.22). It is perhaps also noteworthy that the vesicles formed at pH 3 exhibit a distinctive ‘brain coral’ type morphology; Penfold *et al.* reported similar observations for a related aqueous PISA formulation.[98]

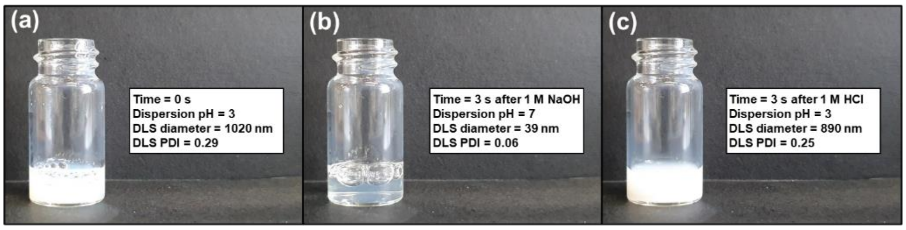

Figure 5.22. Digital photographs illustrating the reversible vesicle-to-sphere transition exhibited by a 5% w/w aqueous dispersion of $PNAEP_{85}$-$PHBA_{530}$ nano-objects. This morphology cycle was performed by adjusting the dispersion pH from pH 3 [(a) 1020 nm vesicles] to pH 7 [(b) 39 nm spheres] and then switching the dispersion pH back to pH 3 [(c) 890 nm vesicles] at 21 °C.

Variable temperature ^{1}H NMR spectroscopy has been used to monitor the relative degree of hydration of weakly hydrophobic blocks within diblock copolymer nano-objects.[16,18,61,99–101] More specifically, Byard *et al.* recently reported that heating linear $PDMAC_{56}$-P(HBA-*stat*-DAAM)$_{264}$ nano-objects from 0 to 70 °C resulted in a remarkable evolution in copolymer morphology from spheres to worms to vesicles to lamellae, with the apparent degree of hydration of the HBA-rich core increasing from 62% to 83%. Herein, we conducted ^{1}H NMR studies of linear $PNAEP_{85}$-$PHBA_x$ diblock copolymer nano-objects to determine the apparent degree of hydration of the structure-directing PHBA block *as a function of dispersion pH* (Figure 5.23). This involved comparing the integrated

-C$\underline{H}_2$OH signals assigned to the partially hydrated PHBA chains to integrated methylene signals assigned to the pendent pyrrolidone rings on the PNAEP chains. For PNAEP$_{85}$-PHBA$_{545}$ vesicles, adjusting the dispersion pH from pH 3 to pH 7 leads to an increase in the mean degree of hydration of the PHBA block from 31% to 65% (Figure 5.23), which accounts for the associated vesicle-to-sphere transition that is observed by TEM (Figure 5.22a). Surprisingly, more hydrated HBA repeat units were observed on both heating at pH 3[16] and ionisation of the terminal carboxylic acid at 20 °C, yet the former increases the packing parameter, whereas the latter leads to its reduction. This contrasting behaviour can be rationalised by appreciating the difference between *uniform* and *surface* plasticisation of the structure-directing block. Heating PHBA-rich chains leads to a higher degree of hydration (i.e. UCST-like behaviour). If such plasticisation is *uniform*, the relative volume fraction of this structure-directing block increases relative to the stabiliser block, thus leading to a higher packing parameter. This drives the evolution in morphology from spheres (P = 1/3) to worms (1/3 < P ≤ 1/2) to vesicles (1/2 < P ≤ 1) to lamellae (P > 1). However, when the PHBA block becomes more hydrated via ionisation of the carboxylic acid end-group on the stabiliser chains, this induces *surface* plasticisation of the nano-objects such that the HBA repeat units located nearest to the block junction become solvated. This results in an effective increase in the volume fraction of the stabiliser block relative to that of the core block and hence a concomitant reduction in the packing parameter, causing the vesicles that are present at pH 3 to form spheres at pH 7.

^{1}H NMR studies of PNAEP$_{85}$-PHBA$_{340}$ worms prepared at pH 3 also indicated a higher degree of hydration for the PHBA chains on switching to pH 7, which causes a worm-to-sphere transition. However, in this case the mean degree of hydration was somewhat higher than that observed for the PNAEP$_{85}$-PHBA$_{545}$ diblock copolymer vesicles (42% vs 29%, respectively). Presumably, this is because the shorter structure-directing block is less hydrophobic.[102] Perhaps surprisingly, ^{1}H NMR studies of PNAEP$_{85}$-PHBA$_{140}$ spheres indicated *minimal change* in the degree of hydration of the PHBA block (from 65% to 70%) when switching from pH 2 to pH 8. In this case, no change in copolymer morphology was observed (nor did molecular dissolution occur). This suggests that introducing a *single* anionic charge at the end of the PNAEP$_{85}$ stabiliser chains leads to an upper limit degree of hydration of approximately 70% for the PHBA block (see Figure 5.23d), regardless of the PHBA DP.

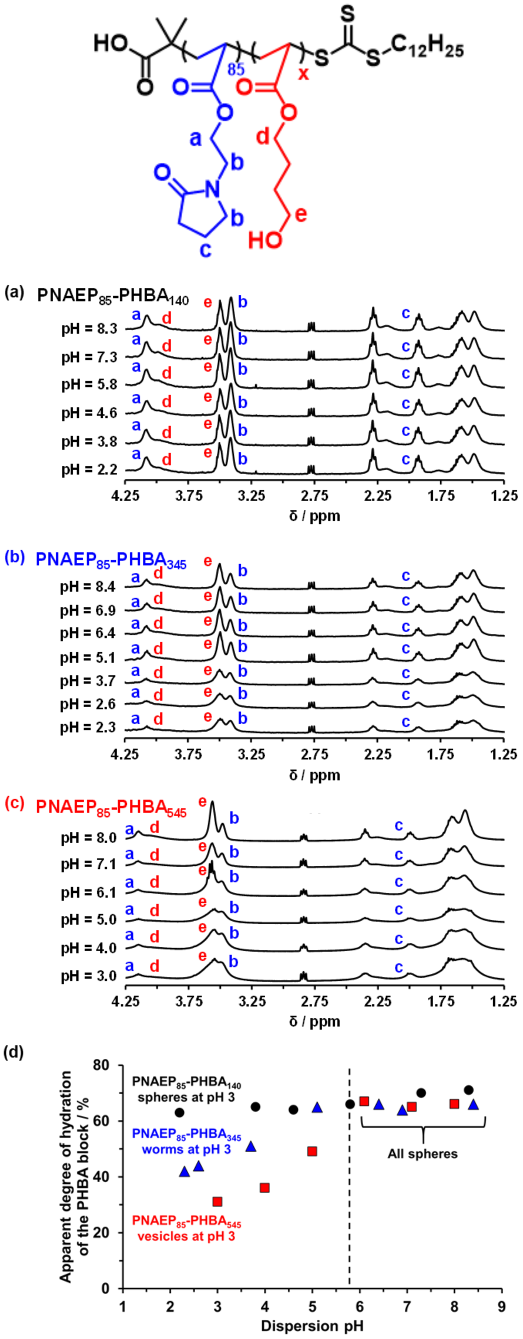

Figure 5.23. Partially assigned ^{1}H NMR spectra recorded for 5% w/w dispersion of (a) PNAEP$_{85}$-PHBA$_{140}$ spheres, (b) PNAEP$_{85}$-PHBA$_{345}$ worms, (c) PNAEP$_{85}$-PHBA$_{545}$ vesicles originally prepared at pH 3. (d) Apparent degree of hydration of the structure-directing PHBA block as a function of dispersion pH for linear PNAEP$_{85}$–PHBA$_{x}$ nano-objects at 20 °C. The 2.77 ppm signal is assigned to the two C$\underline{H}_2$-SO$_3^-$ protons present in DSS which serves as an external standard. Adjusting the dispersion pH leads to ionisation of the carboxylic acid end-group and a concomitant change in the relative degree of hydration of the weakly hydrophobic PHBA block in the case of the PNAEP$_{85}$-PHBA$_{345}$ worms and PNAEP$_{85}$-PHBA$_{545}$ vesicles, but not for the PNAEP$_{85}$-PHBA$_{140}$ spheres. [N.B.100% hydration corresponds to the actual DP of the PHBA block, as calculated by ^{1}H NMR studies of molecularly-dissolved copolymer chains in CD$_3$OD (see Figure 5.24)].

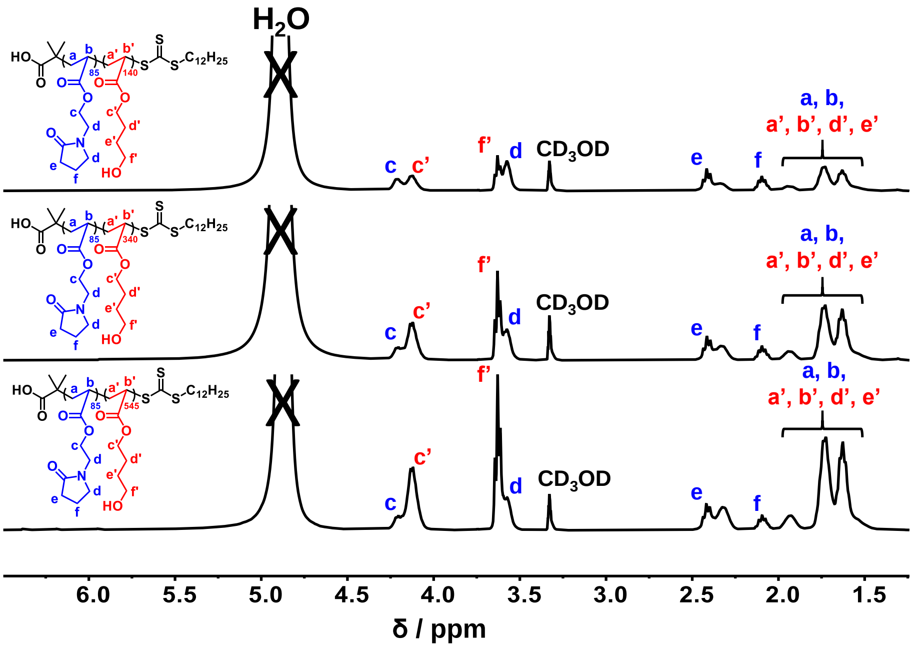

Figure 5.24. ^{1}H NMR spectra recorded for molecularly-dissolved PNAEP$_{85}$–PHBA$_x$ diblock copolymer chains in CD$_3$OD; x = 140 (top), 340 (middle) and 545 (bottom).

5.3.6 Analysis of the Thermoresponse of PNAEP$_{85}$-PHBA$_x$ Nano-Objects

To explore the thermoresponsive nature of PHBA-based nano-objects, variable temperature DLS experiments were conducted on dilute aqueous dispersions of PNAEP$_{85}$-PHBA$_{295}$ nano-objects (0.10% w/w and 0.05% w/w, respectively) while rheology studies were performed on 20% w/w aqueous dispersions of the same nano-objects as a function of temperature (Figure 5.25). DLS studies indicated that relatively small spheres were formed between 5 °C and 13 °C. TEM analysis of GA-crosslinked PNAEP$_{85}$-PHBA$_{295}$ nanoparticles prepared at 11 °C (see point (a) in Figure 5.25) indicates the presence of mainly spheres with a minor population of short worms. Warming from 13 °C to 23 °C leads to a larger z-average diameter and a higher complex viscosity (|η*|); a maximum |η*| is observed at 22 °C, which corresponds to the formation of a soft, transparent free-standing gel. This is consistent with the formation of highly anisotropic worms, with a 3D gel network being formed via multiple inter-worm contacts.[77] We have recently reported that the maximum |η*| should correspond to the presence of highly linear worms.[4] Indeed, TEM studies of the GA-crosslinked nano-objects prepared at 23 °C indicate a pure worm phase with minimal branching (see point (b) in Figure 5.25). Further heating led to a significant reduction in |η*| owing to the formation of vesicles (see point (c) in Figure 5.25). Heating the turbid, free-flowing vesicular dispersion above 36 °C led to a second increase in |η*|, with TEM analysis suggesting the formation of lamellae (see point (d) in Figure 5.25). The relatively soft nature of these PNAEP$_{85}$-PHBA$_{x}$ worm gels (G' ~ 24 to 28 Pa) is likely to be related to the highly hydrated PHBA block. Moreover, variable temperature SAXS studies conducted on a 1.0% w/w aqueous dispersion of PNAEP$_{85}$–PHBA$_{295}$ nano-objects enabled patterns to be recorded at 5 °C, 23 °C and 34 °C (Figure 5.25c). Such patterns could be satisfactorily fitted using well-known scattering models developed for spheres, worms or vesicles respectively, providing further evidence of the remarkable thermoresponsive behavior conferred by the PHBA block.[95,96] In each case, the nano-object dimensions calculated from the SAXS fits were consistent with those determined by DLS and estimated by TEM (see Table 5.3). SAXS analysis enabled the sphere diameter to be determined at 5 °C. GA crosslinking proved to be unsuccessful at such a low temperature, with TEM images only possible for spheres/dimers at 11 °C. An additional SAXS pattern was recorded at 41 °C. In this case, the mean distance (*d*) between the stacked lamellae sheets was calculated to be 43 nm (using $d = 2\pi/q$ where q is the maximum value of the broad diffraction peak at 0.16 nm^{-1}, as indicated by the red triangle in Figure 5.25c).[103,104]

Table 5.3. Summary of z-average diameters (and corresponding DLS polydispersities, or PDI), structural parameters obtained from SAXS analysis and number-average TEM diameters estimated for an aqueous dispersion of PNAEP$_{85}$-PHBA$_{295}$ nano-objects at 5 °C, 23 °C, 34 °C and 41 °C. DLS studies were conducted using 0.1% w/w aqueous dispersions. SAXS studies were performed on 1.0% w/w aqueous dispersions using well-known sphere, worm or vesicle models for data fits (see the SAXS models section in Chapter 7 for more information). TEM analysis was conducted on 0.05% w/w aqueous dispersions of GA-crosslinked PNAEP$_{85}$-PHBA$_{295}$ nano-objects (crosslinking conditions: 5% w/w, GA/HBA molar ratio = 0.66, pH 3, equilibrated for 1 h before GA addition).

		DLS	**SAXS**						**TEM**
Temperature / °C	**Assigned morphology**	**Diameter / nm (PDI)**	**Diameter / nm**	**Width / nm**	**Length / nm**	**Kuhn length / nm**	**Membrane thickness / nm**	**Lamellae stacking / nm**	**Diameter / nm**
5	**Spheres**	**50 (0.03)**	**36 ± 4**	**--**	**--**	**--**	**--**	**--**	**63 ± 17 (11 °C)**
23	**Worms**	**630 (0.47)**	**--**	**35 ± 4**	**>9000**	**700**	**--**	**--**	**42 ± 8**
34	**Vesicles**	**486 (0.28)**	**426 ± 82**	**--**	**--**	**--**	**16 ± 3**	**--**	**342 ± 110**
41	**Lamellae**	**560 (0.52)**	**--**	**--**	**--**	**--**	**--**	**43**	**6100 ± 2600**

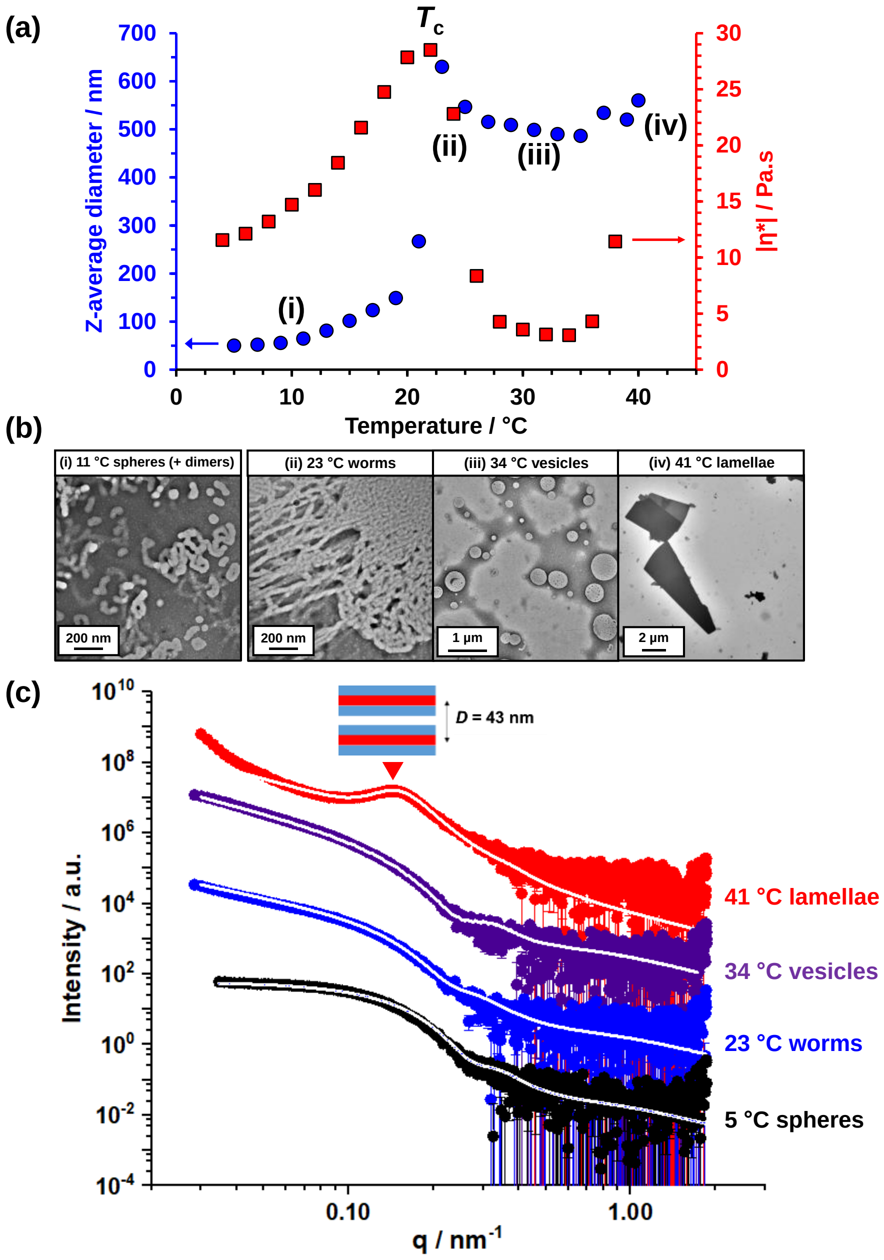

Figure 5.25. (a) Variation in z-average diameter (blue circles) and complex viscosity (red squares) with temperature for an aqueous dispersion of linear PNAEP$_{85}$-PHBA$_{295}$ diblock copolymer nanoparticles. DLS studies were conducted on 0.1% w/w aqueous dispersions while rheological measurements were performed on a 10% w/w aqueous dispersion at an applied strain of 1.0% and an angular frequency of 1.0 rad s^{-1} during a heating cycle starting at 1 °C (15 min was allowed for thermal equilibration at this initial temperature prior to heating). (b) For TEM analysis, 5% w/w aqueous dispersions of PNAEP$_{85}$-PHBA$_{295}$ nanoparticles were reacted with glutaraldehyde crosslinker for 24 h at (i) 11 °C, (ii) 23 °C, (iii) 34 °C or (iv) 41 °C. (c) Small-angle X-ray scattering patterns recorded for a 1.0% w/w aqueous dispersion of linear thermoresponsive PNAEP$_{85}$–PHBA$_{295}$ nano-objects at 5 °C (black data), 23 °C (blue data), 34 °C (purple data) and 41 °C (red data; red triangle indicates the diffraction peak used to calculate *d*). The white lines indicate the data fits obtained using appropriate scattering models (see Chapter 7 for further details).

The same 20% w/w $PNAEP_{85}$-$PHBA_{295}$ nano-objects were subjected to rheological studies during a thermal cycle to assess the thermoreversibility of the various morphology transitions (the red circles and blue squares shown in Figure 5.26 indicate data obtained during the heating and cooling stages of this experiment). The rheology profile for $PNAEP_{85}$-$PHBA_{295}$ nano-objects is similar to that reported by Byard *et al.* for $PDMAC_{56}$-$P(HBA)_{218-269}$ nano-objects.[40] However, the various morphology transitions observed herein occur within a narrower temperature range (2 °C to 45 °C for the present study compared to 1 °C to 70 °C). This suggests that incorporation of 20 mol% DAAM comonomer within the structure-directing HBA-rich block reduces the thermoresponsive character of the nano-objects.

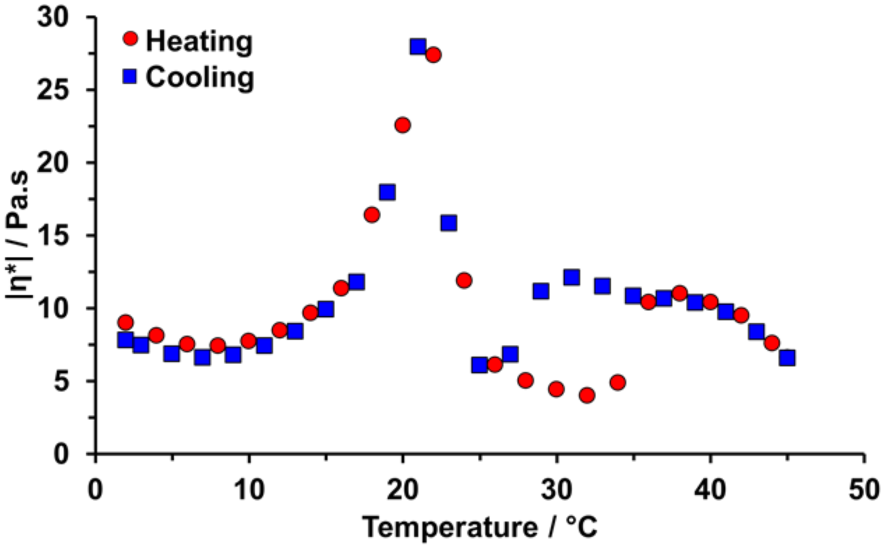

Figure 5.26. Variable temperature complex viscosity measurements for a 20% w/w aqueous dispersion of linear $PNAEP_{85}$-$PHBA_{295}$ nano-objects conducted at pH 3 using an applied strain of 1.0% and an angular frequency of 1.0 rad s^{-1} during a heating cycle (red circles) and a cooling cycle (blue squares). 15 min was allowed for thermal equilibration at the initial temperature of 2 °C prior to heating.

Significant hysteresis was observed for the lamellae-to-vesicle transition when cooling $PNAEP_{85}$-$PHBA_{295}$ lamellae from 45 °C. More specifically, vesicles were not formed until reaching 27 °C, despite being present at up to 34 °C during the heating run (see Figure 5.25 and Figure 5.26). Moreover, the lamellae-to-vesicle transition observed on cooling occurs at the same temperature at which the worm-to-vesicle transition is complete on heating (27 °C in Figure 5.26). However, further cooling indicates little or no hysteresis during the vesicle-to-worm transition with essentially the maximum |η*| being achieved at comparable temperatures (27.4 Pa.s at 22 °C on heating and 27.8 Pa.s at 21

°C on cooling). Similarly, no evidence hysteresis was observed for the worm-to-sphere transition when cooling from 21 °C to 0 °C with almost identical $|\eta^*|$ data sets being recorded for the heating and cooling cycles. This indicates that the associative sphere-to-worm-to-vesicle transitions and dissociative vesicle-worm-to-sphere transitions can each occur within the experimental timeframe of 55 min allowed for the heating (and cooling) run. In principle, the associative pathway should be slower than the dissociative pathway because the former requires co-operative events (e.g. the stochastic 1D fusion of multiple spheres during the sphere-to-worm transition[105]). This suggests that the highly mobile nature of the PHBA chains enable morphology transitions to occur within relatively short time scales (5-10 min).

In principle, systematic variation of the PHBA DP should enable the critical temperature at which such morphology transitions occur to be tuned.[102] This important point is illustrated in Figure 5.27, which shows the rheological behaviour observed for five different PNAEP$_{85}$-PHBA$_{x}$ nano-objects (where x = 110, 200, 295, 380 or 475). In particular, a large increase in $|\eta^*|$ occurs when these thermoresponsive nano-objects undergo a sphere-to-worm transition (see Figures 5.27a-d).[16,85] For a PHBA DP of 110, the critical temperature, T_c, for this transition is around 50 °C (see Figure 5.27a). However, longer PHBA blocks exhibit lower T_c values (see Figures 5.27b-d). It is also noteworthy that heating the PNAEP$_{85}$-PHBA$_{110}$ nano-objects up to 60 °C resulted in no further morphological transitions being observed. In striking contrast, the rheology data obtained for PNAEP$_{85}$-PHBA$_{200}$ suggests the formation of spheres between 10 and 20 °C, worms at around 37 °C, vesicles at approximately 40 °C and lamellae at 50 °C. Interestingly, these worms exhibit a maximum $|\eta^*|$ at around physiological temperature. In principle, this may be useful for potential biomedical applications, e.g. long-term cell culture within a wholly synthetic 3D matrix[91] or stasis induction studies.[92,93] However, these rheological experiments were conducted at pH 3. Nevertheless, it should be feasible to similarly tune the critical temperature required for maximum $|\eta^*|$ (i.e., for the formation of highly linear worms) at physiological pH in the presence of a suitable cell culture medium (e.g., PBS or *Nutristem*). Clearly, such optimisation would require using an alternative RAFT agent that did not contain a carboxylic acid group, unless the added salt was sufficient to screen the electrostatics.[106] Returning to Figure 5.27, increasing the PHBA DP changes the preferred copolymer morphology at 20 °C from spheres (x = 110 or 200) to worms (x = 295 or 380) to vesicles (x = 475). In the latter case, the copolymer dispersion had to be *cooled* to 2 °C to partially dehydrate the PHBA block and hence induce a vesicle-to-worm transition. It is perhaps worth emphasising here that PHPMA-based nano-objects with

DPs greater than 220 exhibited no thermoresponsive behaviour owing to the significantly greater hydrophobic character of this block.[82,107] Finally, an inverse linear correlation is observed between T_c and the PHBA DP over a wide temperature range (2 °C to 50 °C), see Figure 5.27f. In principle, this relationship can be used to predict the T_c for other diblock copolymer compositions by interpolating between x values.

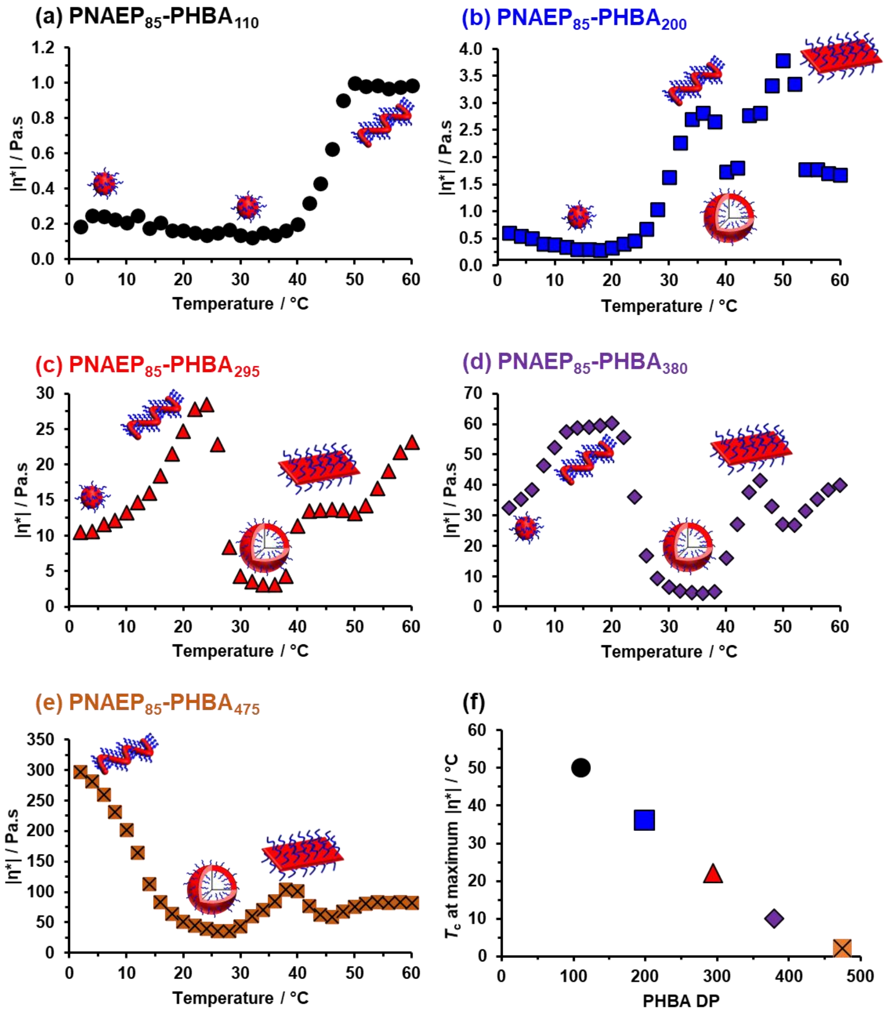

Figure 5.27. Variable temperature complex viscosity measurements for 20% w/w aqueous dispersions of PNAEP$_{85}$-PHBA$_x$ nano-objects at pH 3 for an applied strain of 1.0% and an angular frequency of 1.0 rad s^{-1}: (a) x = 110, (b) x = 200, (c) x = 295, (d) x = 380 and (e) x = 475. Schematic cartoons of spheres, worms, vesicles, and lamellae indicate the likely copolymer morphology at specific temperatures. These assignments are based on the data shown in Figure 5.25 and are consistent with a recent study by Byard *et al*.[16] (f) Relationship between the critical temperature (T_c) corresponding to the maximum |η*| and the PHBA DP for the same five aqueous dispersions of PNAEP$_{85}$-PHBA$_x$ nano-objects.

5.3.7 Using the PNAEP$_{85}$-PHBA$_x$ phase diagram to Target “Thick” Worms

The phase diagram (Figure 5.19) indicated that pure PNAEP$_x$-PHBA$_y$ worms can be obtained if the y:x ratio is maintained between 4.2 and 4.8. Furthermore, the maximum complex viscosity (which indicates worm formation) shown in Figure 5.27 is reduced from 300 Pa.s to 1 Pa.s when lowering the PHBA DP from 475 to 110. This suggests that the DP of the PHBA block must be increased to achieve stronger free-standing gels over a broader temperature range. If a y:x ratio of ~4.5 is to be maintained, this would require higher PNAEP stabiliser DPs to be targeted. However, according to the PISA literature this approach is normally problematic: increasing the stabiliser block DP typically results in kinetically-trapped spheres rather than worm formation because the stochastic 1D fusion of multiple spheres is inhibited.[64] However, for the present diblock copolymer formulation it was postulated that the high chain mobility of the PHBA block (see Figure 5.14 and Figure 5.15) might enable the stabiliser block DP to be increased significantly while still enabling access to a pure worm morphology. Accordingly, four PNAEP$_x$-PHBA$_y$ diblock copolymers were synthesised *via* RAFT aqueous dispersion polymerisation of HBA using a one-pot protocol at pH 3 targeting x = 65, 80, 105 or 276 at a constant y:x ratio of 4.0. The final 20% w/w diblock copolymer dispersions formed free-standing gels that became increasingly turbid when targeting higher PHBA DPs. After crosslinking with glutaraldehyde, TEM studies confirmed that a pure worm morphology had been achieved in each case despite the relatively long PNAEP stabiliser block (Figure 5.28). The mean worm width estimated by TEM measurements increased from 30 nm to 100 nm on increasing the PHBA DP from 245 to 920.

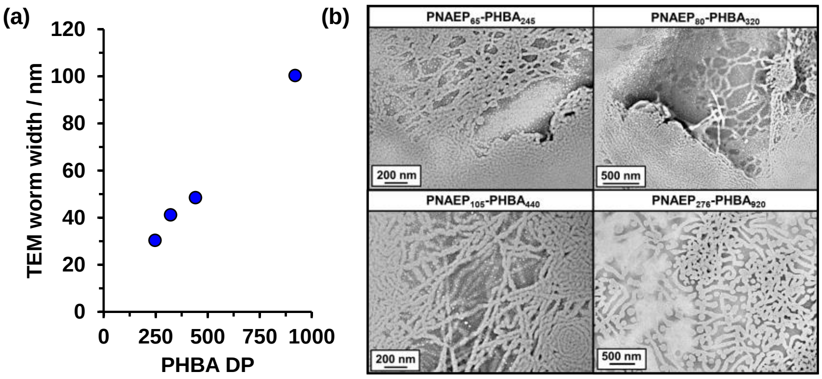

Figure 5.28. Relationship between mean worm width (as estimated from TEM studies) and PHBA DP for a series of PNAEP$_x$-PHBA$_y$ worms prepared *via* RAFT aqueous dispersion polymerisation at pH 3 targeting 20% w/w solids in each case. Representative TEM images recorded for the corresponding crosslinked diblock copolymer worms are also shown.

Three PNAEP$_x$-PHBA$_y$ diblock copolymers were then prepared using the phase diagram in Figure 5.19 to target spheres (i.e., by employing a y:x ratio of ~1.3). DLS analysis suggested that these three PNAEP$_x$-PHBA$_y$ dispersions comprised spherical nanoparticles with z-average diameters of 35 nm (PNAEP$_{100}$-PHBA$_{130}$), 72 nm (PNAEP$_{200}$-PHBA$_{260}$) and 96 nm (PNAEP$_{300}$-PHBA$_{360}$) at 20 °C (see Figure 5.29), with DLS polydispersities always lying below 0.10. Despite the relatively high PNAEP stabiliser DP, variable temperature DLS studies revealed that a pronounced upturn in apparent particle diameter – indicating a sphere-to-worm transition – occurred at a critical temperature (T_{crit}) in each case. Moreover, T_{crit} increased from 40 °C to 70 °C as the PNAEP stabiliser block DP was adjusted from 100 to 300. Thus, this suggests that both the critical temperature and maximum complex viscosity of PNAEP$_x$-PHBA$_y$ diblock copolymer nano-objects can be precisely tuned according to the specific requirements for a given application.

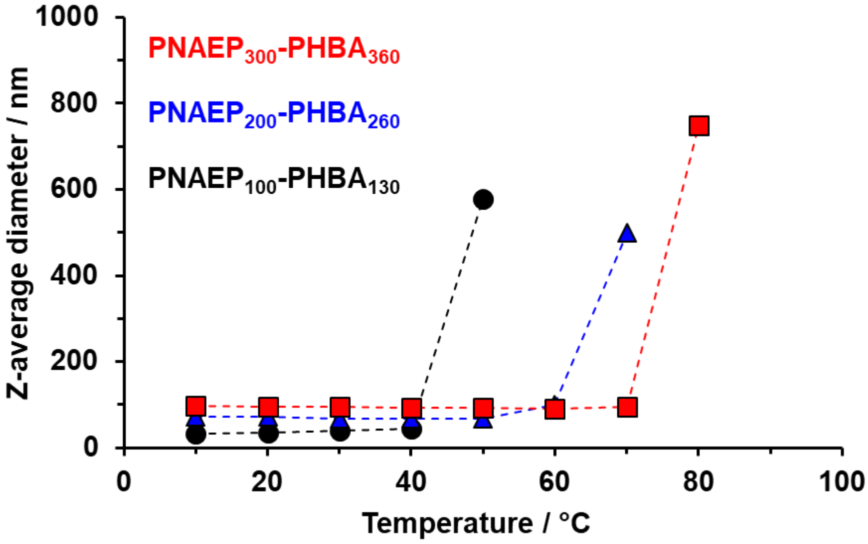

Figure 5.29. Variable temperature DLS data obtained for three PNAEP$_x$-PHBA$_y$ diblock copolymer spheres where x = 100, 200 and 300 and y = 130, 260 and 360, respectively. The pronounced upturn in z-average diameter at critical temperatures (e.g., approximately 40 °C, 60 °C and 70 °C) suggests that each of these spherical nanoparticles can undergo sphere-to-worm transitions despite their relatively long PNAEP stabiliser blocks.

5.4 Conclusions

A series of PNAEP$_{85}$-PHBA$_x$ diblock copolymer nano-objects have been prepared via redox-initiated RAFT aqueous dispersion polymerisation of HBA at 30 °C using a highly convenient and reproducible one-pot protocol. Unusually, there is no discernible rate enhancement following micellar nucleation, which is attributed to the relatively high aqueous solubility of HBA compared to its isomeric methacrylic analogue (HPMA). Nevertheless, high HBA conversions could be achieved within 60 min at pH 3 and within 120 min at pH 7. In both cases, DMF GPC analysis indicated a linear evolution in copolymer molecular weight with conversion, as expected for a well-controlled RAFT polymerisation. However, relatively broad molecular weight distributions (M_w/M_n ~ 1.7-2.1) were obtained, particularly when targeting higher PHBA DPs. This is attributed to chain transfer to polymer, which is well-documented for acrylic monomers even at relatively low reaction temperatures.[74,86,108] DLS and aqueous electrophoresis studies indicated that introducing anionic charge at the end of the PNAEP steric stabiliser chains by raising the dispersion pH above the pK_a of the terminal carboxylic acid group was sufficient to drive a vesicle-to-sphere transition.

To enable assignment of copolymer morphologies, $PNAEP_{85}$-$PHBA_x$ nano-objects were crosslinked using glutaraldehyde, which forms acetal linkages between pendent hydroxyl groups on the PHBA chains and hence raises their T_g (as confirmed by DSC studies). TEM studies of such covalently-stabilised nano-objects confirmed that pure spheres, worms, and vesicles could be obtained at 20 °C and pH 3 by adjusting the target diblock copolymer composition. This approach enabled the construction of a pseudo-phase diagram by systematically varying the PHBA DP between 100 and 550 while targeting copolymer concentrations of 5 to 40% w/w.

Using glutaraldehyde to crosslink $PNAEP_{85}$-$PHBA_{545}$ nano-objects while varying the dispersion pH at 20 °C indicated that the copolymer morphology was pure vesicles at pH 3, a mixed phase comprising spheres, worms, and vesicles at pH 5 and pure spheres at pH 7. ^{1}H NMR studies of linear $PNAEP_{85}$-$PHBA_x$ nano-objects suggest that this shift in copolymer morphology is driven by *surface plasticisation* of the PHBA cores, which occurs on raising the dispersion pH above the pK_a of the carboxylic acid group located at the end of each $PNAEP_{85}$ stabiliser chain. This leads to an overall reduction in the fractional packing parameter despite the greater degree of (partial) hydration of the PHBA block. On the other hand, *uniform* plasticisation of the PHBA chains occurs on heating, which increases the fractional packing parameter and hence drives sphere-to-worm, worm-to-vesicle, and vesicle-to-lamellae transitions.

Rheology, DLS and TEM studies were conducted on aqueous dispersions of five examples of $PNAEP_{85}$-$PHBA_x$ nano-objects as a function of temperature. This series of experiments indicated that the critical temperature required for the maximum complex viscosity (|η*|) – which corresponds to the formation of highly linear worms – could be tuned by systematically varying the PHBA DP. Furthermore, |η*| could be adjusted from 1 to 297 Pa.s. Finally, an inverse linear relationship was observed between this critical temperature and the PHBA DP over a relatively wide temperature range (2 to 50 °C). Increasing the PNAEP DP (length of the stabiliser block) required targeting higher PHBA DPs to achieve nanoparticles. However, the PNAEP:PHBA DP ratios identified by the phase diagram were still predictive and were used to target spheres and worms. TEM analysis indicated that worm diameter increased linearly with PNAEP DP whilst temperature variable DLS indicated these particles were still thermoresponsive despite their large stabiliser blocks.

Given their anticipated biocompatibility, we envisage that next-generation $PNAEP_x$-$PHBA_y$ worm gels comprising ester- or amide-capped end-groups are likely to offer new opportunities as wholly synthetic 3D matrices for long-term cell culture studies[91] or possibly for inducing stasis in embryonic human stem cells.[92,93] However, for this potential to be realised, it will be necessary to develop PISA formulations that produce free-standing thermoresponsive worm gels at pH 7, rather than in acidic solution.

5.5 References

1 L. Zhang and A. Eisenberg, *Science*, 1995, **268**, 1728–1731.

2 S. Abbas, Z. Li, H. Hassan and T. P. Lodge, *Macromolecules*, 2007, **40**, 4048–4052.

3 S. Y. Kim, K. E. Lee, S. S. Han and B. Jeong, *J. Phys. Chem. B*, 2008, **112**, 7420–7423.

4 R. Verber, A. Blanazs and S. P. Armes, *Soft Matter*, 2012, **8**, 9915–9922.

5 Y.-Y. Won, H. T. Davis and F. S. Bates, *Science*, 1999, **283**, 960–963.

6 B. M. Discher, *Science*, 1999, **284**, 1143–1146.

7 X. Wang, G. Guerin, H. Wang, Y. Wang, I. Manners and M. A. Winnik, *Science*, 2007, **317**, 644–647.

8 J. B. Gilroy, T. Gädt, G. R. Whittell, L. Chabanne, J. M. Mitchels, R. M. Richardson, M. A. Winnik and I. Manners, *Nat. Chem.*, 2010, **2**, 566–570.

9 B. Charleux, G. Delaittre, J. Rieger and F. D'Agosto, *Macromolecules*, 2012, **45**,

6753–6765.

10 N. J. Warren and S. P. Armes, *J. Am. Chem. Soc.*, 2014, **136**, 10174–10185.

11 J. Rieger, *Macromol. Rapid Commun.*, 2015, **36**, 1458–1471.

12 M. J. Derry, L. A. Fielding and S. P. Armes, *Prog. Polym. Sci.*, 2016, **52**, 1–18.

13 C. E. Boott, J. Gwyther, R. L. Harniman, D. W. Hayward and I. Manners, *Nat. Chem.*, 2017, **9**, 785–792.

14 I. Chaduc, W. Zhang, J. Rieger, M. Lansalot, F. D'Agosto and B. Charleux, *Macromol. Rapid Commun.*, 2011, **32**, 1270–1276.

15 G. Gody, T. Maschmeyer, P. B. Zetterlund and S. Perrier, *Macromolecules*, 2014, **47**, 3451–3460.

16 S. J. Byard, C. T. O'Brien, M. J. Derry, M. Williams, O. O. Mykhaylyk, A. Blanazs and S. P. Armes, *Chem. Sci.*, 2020, **11**, 396–402.

17 L. G. Griffith and M. A. Swartz, *Nat. Rev. Mol. Cell Biol.*, 2006, **7**, 211–224.

18 A. Blanazs, R. Verber, O. O. Mykhaylyk, A. J. Ryan, J. Z. Heath, C. W. I. Douglas and S. P. Armes, *J. Am. Chem. Soc.*, 2012, **134**, 9741–9748.

19 K. Kataoka, A. Harada and Y. Nagasaki, *Adv. Drug Deliv. Rev.*, 2001, **47**, 113–131.

20 A. V. Kabanov, E. V. Batrakova and V. Y. Alakhov, *J. Control. Release*, 2002, **82**, 189–212.

21 J. Rodriguez-Hernandez, F. Checot, Y. Gnanou and S. Lecommandoux, *Prog. Polym. Sci.*, 2005, **30**, 691–724.

22 D. Roy, J. N. Cambre and B. S. Sumerlin, *Prog. Polym. Sci.*, 2010, **35**, 278–301.

23 R. P. Brinkhuis, F. P. J. T. Rutjes and J. C. M. van Hest, *Polym. Chem.*, 2011, **2**, 1449–1462.

24 D. J. Growney, O. O. Mykhaylyk and S. P. Armes, *Langmuir*, 2014, **30**, 6047–6056.

25 N. J. W. Penfold, Y. Ning, P. Verstraete, J. Smets and S. P. Armes, *Chem. Sci.*, 2016, **7**, 6894–6904.

26 M. J. Derry, L. A. Fielding and S. P. Armes, *Polym. Chem.*, 2015, **6**, 3054–3062.

27 S. Perrier and P. Takolpuckdee, *J. Polym. Sci. Part A Polym. Chem.*, 2005, **43**,

5347–5393.

28 S. Sugihara, A. Blanazs, S. P. Armes, A. J. Ryan and A. L. Lewis, *J. Am. Chem. Soc.*, 2011, **133**, 15707–15713.

29 X. Zhang, S. Boissé, W. Zhang, P. Beaunier, F. D'Agosto, J. Rieger and B. Charleux, *Macromolecules*, 2011, **44**, 4149–4158.

30 B. Karagoz, L. Esser, H. T. Duong, J. S. Basuki, C. Boyer and T. P. Davis, *Polym. Chem.*, 2014, **5**, 350–355.

31 J. Tan, H. Sun, M. Yu, B. S. Sumerlin and L. Zhang, *ACS Macro Lett.*, 2015, **4**, 1249–1253.

32 Y. Jiang, N. Xu, J. Han, Q. Yu, L. Guo, P. Gao, X. Lu and Y. Cai, *Polym. Chem.*, 2015, **6**, 4955–4965.

33 D. Zhou, S. Dong, R. P. Kuchel, S. Perrier and P. B. Zetterlund, *Polym. Chem.*, 2017, **8**, 3082–3089.

34 S. Perrier, *Macromolecules*, 2017, **50**, 7433–7447.

35 S. Y. Khor, J. F. Quinn, M. R. Whittaker, N. P. Truong and T. P. Davis, *Macromol. Rapid Commun.*, 2019, **40**, 1800438.

36 G. Moad, E. Rizzardo and S. H. Thang, *Aust. J. Chem.*, 2006, **59**, 669.

37 G. Moad, E. Rizzardo and S. H. Thang, *Aust. J. Chem.*, 2009, **62**, 1402–1472.

38 G. Moad, E. Rizzardo and S. H. Thang, *Aust. J. Chem.*, 2012, **65**, 985.

39 L. P. D. Ratcliffe, M. J. Derry, A. Ianiro, R. Tuinier and S. P. Armes, *Angew. Chemie Int. Ed.*, 2019, **58**, 18964–18970.

40 S. J. Wilson, *Synthesis and Characterisation of Stimulus-responsive Diblock Copolymer Nano-objects Prepared by RAFT Aqueous Dispersion Polymerisation*, PhD Thesis, University of Sheffield, Sheffield, UK, 2019.

41 N. Petzetakis, A. P. Dove and R. K. O'Reilly, *Chem. Sci.*, 2011, **2**, 955–960.

42 W. Zhao, G. Gody, S. Dong, P. B. Zetterlund and S. Perrier, *Polym. Chem.*, 2014, **5**, 6990–7003.

43 C. J. Mable, R. R. Gibson, S. Prevost, B. E. McKenzie, O. O. Mykhaylyk and S. P. Armes, *J. Am. Chem. Soc.*, 2015, **137**, 16098–16108.

44 I. Migneault, C. Dartiguenave, M. J. Bertrand and K. C. Waldron, *Biotechniques*, 2004, **37**, 790–802.

45 D. D. Sabatini, K. Bensch and R. J. Barrnett, *J. Cell Biol.*, 1963, **17**, 19–58.

46 M. A. Hayat, *Fixation for Electron Microscopy*, Acedemic Press, New York, USA, 1981.

47 M. A. Hayat, *Micron Microsc. Acta*, 1986, **17**, 115–135.

48 J. A. Kiernan, *Micros. Today*, 2000, **8**, 8–13.

49 K.-J. Kim, S.-B. Lee and N. W. Han, *Polym. J.*, 1993, **25**, 1295–1302.

50 C.-K. Yeom and K.-H. Lee, *J. Memb. Sci.*, 1996, **109**, 257–265.

51 S. Kurihara, S. Sakamaki, S. Mogi, T. Ogata and T. Nonaka, *Polymer.*, 1996, **37**, 1123–1128.

52 P. S. Rao, S. Sridhar, M. Y. Wey and A. Krishnaiah, *Polym. Bull.*, 2007, **59**, 289–298.

53 B. Bolto, T. Tran, M. Hoang and Z. Xie, *Prog. Polym. Sci.*, 2009, **34**, 969–981.

54 J.-B. Fan, Y. Song, S. Wang, J. Meng, G. Yang, X. Guo, L. Feng and L. Jiang, *Adv. Funct. Mater.*, 2015, **25**, 5368–5375.

55 A. F. S. A. Habeeb and R. Hiramoto, *Arch. Biochem. Biophys.*, 1968, **126**, 16–26.

56 F. M. Richards and J. R. Knowles, *J. Mol. Biol.*, 1968, **37**, 231–233.

57 K. Peters and F. M. Richards, *Annu. Rev. Biochem.*, 1977, **46**, 523–551.

58 D. T. Cheung, N. Perelman, E. C. Ko and M. E. Nimni, *Connect. Tissue Res.*, 1985, **13**, 109–115.

59 K. Okuda, I. Urabe, Y. Yamada and H. Okada, *J. Ferment. Bioeng.*, 1991, **71**, 100–105.

60 H. S. Mansur, C. M. Sadahira, A. N. Souza and A. A. P. Mansur, *Mater. Sci. Eng. C*, 2008, **28**, 539–548.

61 O. J. Deane, J. R. Lovett, O. M. Musa, A. Fernyhough and S. P. Armes, *Macromolecules*, 2018, **51**, 7756–7766.

62 O. J. Deane, O. M. Musa, A. Fernyhough and S. P. Armes, *Macromolecules*, 2020,

53, 1422–1434.

63 A. Blanazs, J. Madsen, G. Battaglia, A. J. Ryan and S. P. Armes, *J. Am. Chem. Soc.*, 2011, **133**, 16581–16587.

64 A. Blanazs, A. J. Ryan and S. P. Armes, *Macromolecules*, 2012, **45**, 5099–5107.

65 S. Sugihara, A. H. Ma'Radzi, S. Ida, S. Irie, T. Kikukawa and Y. Maeda, *Polymer*, 2015, **76**, 17–24.

66 S. J. Byard, M. Williams, B. E. McKenzie, A. Blanazs and S. P. Armes, *Macromolecules*, 2017, **50**, 1482–1493.

67 J. C. Foster, S. Varlas, B. Couturaud, J. R. Jones, R. Keogh, R. T. Mathers and R. K. O'Reilly, *Angew. Chemie Int. Ed.*, 2018, **57**, 15733–15737.

68 F. D'Agosto, J. Rieger and M. Lansalot, *Angew. Chemie Int. Ed.*, 2020, **132**, 2 – 29.

69 I. Chaduc, A. Crepet, O. Boyron, B. Charleux, F. D'Agosto and M. Lansalot, *Macromolecules*, 2013, **46**, 6013–6023.

70 V. J. Cunningham, A. M. Alswieleh, K. L. Thompson, M. Williams, G. J. Leggett, S. P. Armes and O. M. Musa, *Macromolecules*, 2014, **47**, 5613–5623.

71 N. P. Truong, M. V Dussert, M. R. Whittaker, J. F. Quinn and T. P. Davis, *Polym. Chem.*, 2015, **6**, 3865–3874.

72 J. R. Lovett, N. J. Warren, L. P. D. Ratcliffe, M. K. Kocik and S. P. Armes, *Angew. Chemie Int. Ed.*, 2015, **54**, 1279–1283.

73 R. Deng, M. J. Derry, C. J. Mable, Y. Ning and S. P. Armes, *J. Am. Chem. Soc.*, 2017, **139**, 7616–7623.

74 N. M. Ahmad, B. Charleux, C. Farcet, C. J. Ferguson, S. G. Gaynor, B. S. Hawkett, F. Heatley, B. Klumperman, D. Konkolewicz, P. A. Lovell, K. Matyjaszewski and R. Venkatesh, *Macromol. Rapid Commun.*, 2009, **30**, 2002–2021.

75 G. S. Misra and C. V Gupta, *Die Makromol. Chemie*, 1973, **165**, 205–216.

76 H. Narain, S. M. Jagadale and N. D. Ghatge, *J. Polym. Sci. Polym. Chem. Ed.*, 1981, **19**, 1225–1238.

77 D. E. Cabelli and B. H. J. Bielski, *J. Phys. Chem.*, 1983, **87**, 1809–1812.

78 M. Rubens, J. H. Vrijsen, J. Laun and T. Junkers, *Angew. Chemie - Int. Ed.*, 2019, **58**, 3183–3187.

79 N. J. W. Penfold, J. R. Lovett, N. J. Warren, P. Verstraete, J. Smets and S. P. Armes, *Polym. Chem.*, 2016, **7**, 79–88.

80 X. De Feng, X. Q. Guo and K. Y. Qiu, *Die Makromol. Chemie*, 1988, **189**, 77–83.

81 N. Kohut-Svelko, R. Pirri, J. M. Asua and J. R. Leiza, *J. Polym. Sci. Part A Polym. Chem.*, 2009, **47**, 2917–2927.

82 N. J. Warren, O. O. Mykhaylyk, D. Mahmood, A. J. Ryan and S. P. Armes, *J. Am. Chem. Soc.*, 2014, **136**, 1023–1033.

83 E. E. Brotherton, F. L. Hatton, A. A. Cockram, M. J. Derry, A. Czajka, E. J. Cornel, P. D. Topham, O. O. Mykhaylyk and S. P. Armes, *J. Am. Chem. Soc.*, 2019, **141**, 13664–13675.

84 Y. Li and S. P. Armes, *Angew. Chemie Int. Ed.*, 2010, **49**, 4042–4046.

85 I. Bannister, N. C. Billingham, S. P. Armes, S. P. Rannard and P. Findlay, *Macromolecules*, 2006, **39**, 7483–7492.

86 N. M. Ahmad, F. Heatley and P. A. Lovell, *Macromolecules*, 1998, **31**, 2822–2827.

87 A. Agirre, J. I. Santos, A. Etxeberria, V. Sauerland and J. R. Leiza, *Polym. Chem.*, 2013, **4**, 2062–2079.

88 T. G. Fox, *Bull. Am. Phys. Soc.*, 1956, **1**, 123.

89 J. R. Lovett, M. J. Derry, P. Yang, F. L. Hatton, N. J. Warren, P. W. Fowler and S. P. Armes, *Chem. Sci.*, 2018, **9**, 7138–7144.

90 D. Pissuwan, C. Boyer, K. Gunasekaran, T. P. Davis and V. Bulmus, *Biomacromolecules*, 2010, **11**, 412–420.

91 K. A. Simon, N. J. Warren, B. Mosadegh, M. R. Mohammady, G. M. Whitesides and S. P. Armes, *Biomacromolecules*, 2015, **16**, 3952–3958.

92 I. Canton, N. J. Warren, A. Chahal, K. Amps, A. Wood, R. Weightman, E. Wang, H. Moore and S. P. Armes, *ACS Cent. Sci.*, 2016, **2**, 65–74.

93 M. Sponchioni, C. T. O'Brien, C. Borchers, E. Wang, M. N. Rivolta, N. J. W. Penfold, I. Canton and S. P. Armes, *Chem. Sci.*, 2020, **11**, 232–240.

94 O. Glatter and O. Kratky, *Small Angle X-ray Scattering,* London, Vol. 130., 1982.

95 J. S. Pedersen, *J. Appl. Crystallogr.*, 2000, **33**, 637–640.

96 J. Bang, S. Jain, Z. Li, T. P. Lodge, J. S. Pedersen, E. Kesselman and Y. Talmon, *Macromolecules*, 2006, **3**, 1199–1208.

97 G. Battaglia and A. J. Ryan, *J. Am. Chem. Soc.*, 2005, **127**, 8757–8764.

98 N. J. W. Penfold, J. R. Lovett, P. Verstraete, J. Smets and S. P. Armes, *Polym. Chem.*, 2017, **8**, 272–282.

99 F. Zeng, Z. Tong and H. Feng, *Polymer*, 1997, **38**, 5539–5544.

100 M. V. Deshmukh, A. A. Vaidya, M. G. Kulkarni, P. R. Rajamohanan and S. Ganapathy, *Polymer*, 2000, **41**, 7951–7960.

101 P. J. Roth, T. P. Davis and A. B. Lowe, *Macromolecules*, 2012, **45**, 3221–3230.

102 N. J. Warren, M. J. Derry, O. O. Mykhaylyk, J. R. Lovett, L. P. D. Ratcliffe, V. Ladmiral, A. Blanazs, L. A. Fielding and S. P. Armes, *Macromolecules*, 2018, **51**, 8357–8371.

103 M. Li, Y. Liu, H. Nie, R. Bansil and M. Steinhart, *Macromolecules*, 2007, **40**, 9491–9502.

104 R. R. Gibson, E. J. Cornel, O. M. Musa, A. Fernyhough and S. P. Armes, *Polym. Chem.*, 2020, **11**, 1785–1796.

105 A. Czajka and S. P. Armes, *Chem. Sci.*, 2020, **11**, 11443–11454.

106 R. R. Gibson, S. P. Armes, O. M. Musa and A. Fernyhough, *Polym. Chem.*, 2019, **10**, 1312–1323.

107 N. J. W. Penfold, J. R. Whatley and S. P. Armes, *Macromolecules*, 2019, **52**, 1653–1662.

108 S. L. Canning, V. J. Cunningham, L. P. D. Ratcliffe and S. P. Armes, *Polym. Chem.*, 2017, **8**, 4811–4821.

Chapter 6

Conclusions and Outlook

6.1 Conclusions and Outlook

Ashland Global Specialty Chemicals Inc is an American company that industrially manufactures PNVP which is a water-soluble polymer with various attractive properties, such as its non-ionic character, strong dipole moment, film-forming ability and biocompatibility.[1,2] However, the preparation of pyrrolidone-based block copolymers by RAFT aqueous polymerisation has been restricted owing to NVP's poor copolymerisability[3–6] and its side-reactions with either water[7] or xanthates.[8,9] This limitation was partially circumvented by Cunningham and co-workers using NMEP, which is a methacrylic analogue of NVP.[10,11] However, PNMEP exhibits LCST behaviour, which prevents its use as a stabiliser block in PISA syntheses.[12] More recently, Gibson *et al.* reported that ionisation of carboxylic acid end-groups enables the use of PNMEP precursors as stabilisers for RAFT aqueous dispersion and emulsion polymerisations. However, such PISA formulations only resulted in kinetically-trapped spheres, which became flocculated in the presence of relatively low concentrations of added salt.[13]

In this Thesis, aqueous PISA syntheses have been conducted using NAEP, which is significantly more hydrophilic than NMEP. NAEP is not yet manufactured on an industrial scale and, prior to this Thesis, there was only one literature report of the RAFT polymerisation of NAEP.[14] This was an early example of a photoinitiated RAFT aqueous solution polymerisation and substantially incomplete monomer conversions were obtained. In this Thesis, the RAFT polymerisation of NAEP is optimised to enable the synthesis of well-defined, high molecular weight homopolymers and block copolymers. This was achieved using RAFT aqueous solution polymerisation (Chapter 2), RAFT aqueous emulsion polymerisation (Chapters 3 and 4), RAFT aqueous dispersion polymerisation (Chapter 5).

Chapter 2 is focused on examining the physical properties of PNAEP homopolymers and the synthesis of well-defined PNAEP-based diblock copolymers. A series of well-defined PNAEP_x homopolymers with mean DPs varying from 40 to 400 were prepared by RAFT aqueous solution polymerisation at 30 °C. In principle, the synthesis of PNAEP homopolymers with higher DPs should reduce the concentration of RAFT chain-ends, which minimises their colour, cost and malodour. However, targeting DPs of 500 or more resulted in substantially lower NAEP conversions (< 80%) even after 24 h. This was attributed to the very low initiator concentration required to prepare well-defined, high molecular weight PNAEP homopolymers, and perhaps also their associated increase in solution viscosity (which inhibits efficient stirring). The solids concentration employed in these polymerisations was necessarily high (60-80% w/w) to ensure that the hydrophobic

DDMAT was fully soluble in the reaction mixture. In principle, NAEP could be chain-extended from a water-soluble PNAEP macro-CTA at lower solids concentrations. This should facilitate efficient stirring throughout the synthesis and may enable the production of cost-effective high molecular weight polymers. DSC analysis indicated that PNAEP homopolymers with DPs of up to 400 exhibited T_g values below ambient temperature. This suggests that PNAEP exhibits better film-forming properties compared to PNMEP. On the other hand, the former films are rather tacky compared to those obtained when using PNVP. Importantly, such PNAEP$_{40\text{-}400}$ homopolymers remained water-soluble up to 90 °C, confirming their greater hydrophilic character compared to PNMEP.[13] Thus PNAEP was expected to confer effective steric stabilisation during either RAFT aqueous emulsion or RAFT aqueous dispersion polymerisation. The pseudo-living character of the RAFT aqueous solution polymerisation of NAEP was confirmed by subsequent efficient chain extension using HEA, OEGA or NIPAM to produce well-defined all-acrylic double-hydrophilic diblock copolymer chains. Moreover, the PNAEP-PNIPAM diblock copolymer proved to be thermoresponsive, forming PNIPAM-core micelles on heating above the LCST of the PNIPAM block. Prior to the formation of well-defined PNIPAM-core micelles, DLS studies indicated the presence of relatively large, non-micellar aggregates between 32 and 39 °C. Similar observations have been reported in the literature[15–18] and it is possible that PNIPAM homopolymer contamination produces such aggregates.[18] On the other hand, GPC analysis indicated high blocking efficiencies and monomodal traces. To further explore such ‘anomalous’ micellisation, centrifugation could be conducted at 32-39°C to isolate the relatively large aggregates prior to their analysis by ^{1}H NMR spectroscopy and UV GPC. The former technique should confirm whether such aggregates contained a higher proportion of PNIPAM than that indicated by the mean diblock copolymer composition, while the latter technique should indicate whether all the chains contain an active RAFT chain-end. Finally, a new pH-responsive diblock copolymer was prepared by chain extension of a PDEA precursor via RAFT aqueous solution polymerisation of NAEP at low pH. Recently, zwitterionic PDMA-PMAA diblock copolymers have been demonstrated to act as an effective pigment dispersant.[19] The strong dipole moment of the pyrrolidone ring in PNVP enables sequestration of many fugitive dyes and is therefore used as anti-dye transfer agents in laundry formulations.[20,21] In principle, the highly polar nature of PNAEP-based double-hydrophilic diblock copolymers (such as those synthesised in Chapter 2) may well confer good pigment dispersant performance. This hypothesis warrants further exploration. ^{1}H NMR spectroscopy studies of the pH-responsive PDEA$_{99}$−PNAEP$_y$ diblock copolymers indicated the formation of PDEA-core spherical micelles on adjusting the solution pH from pH 2 to pH 10. DLS analysis indicated that increasing the PNAEP DP led to a significant reduction in the *z*-average diameter for this series of $PDEA_{99}-PNAEP_x$ spheres. According to the literature, if a suitable PDEA-rich diblock composition is targeted, then the formation of pyrrolidone-functional pH-responsive worms and vesicles should be feasible.[22,23] The findings presented in this Chapter indicated that PNAEP precursors should act as a non-ionic stabiliser block for aqueous PISA synthesises.

Accordingly, Chapter 3 focused on the RAFT emulsion polymerisation of styrene, nBA, or statistical mixtures thereof using a trithiocarbonate-based $PNAEP_{67}$ precursor. ^1H NMR, GPC and DLS studies indicated that the RAFT aqueous emulsion polymerisation of styrene at 80 °C led to 99% conversion within 40 min at pH 7. Similarly, the RAFT aqueous emulsion polymerisation of nBA at 30 °C led to 99% conversion within 25 min at pH 3. In each case, DLS confirmed that well-defined spherical nanoparticles (with z-average diameters ranging from 55 to 156 nm for PS-based nanoparticles and 45 to 141 nm for PnBA-based nanoparticles) could be prepared when the core-forming block DP was systematically varied from 100 to 700. Furthermore, such nanoparticles remained colloidally stable between pH 3 and pH 8. However, attempting the RAFT emulsion polymerisation of nBA under the conditions employed for the polymerisation of styrene (80 °C, pH 7) only resulted in broad molecular weight distributions ($M_w/M_n > 3.00$) and significant coagulum. This loss of RAFT control is attributed to chain transfer to polymer, which is well-documented for acrylic monomers even at relatively low reaction temperatures.[24–26]

The low T_g of PNAEP (as evidenced by DSC studies in Chapter 2) unexpectedly enabled good-quality $PNAEP_{67}-PS_{400}$ films to be prepared by spin-coating dispersions at room temperature despite the high T_g of the PS cores. However, such films remained particulate in nature and increasing the film thickness (> 20 µm) led to embrittlement and a concomitant reduction in transparency. In contrast, spin-coating aqueous dispersions of $PNAEP_{67}-PnBA_{400}$ nanoparticles produced highly transparent copolymer films with complete loss of the original copolymer morphology. However, such films were rather tacky owing to the low T_g of the PnBA component. To prepare non-tacky transparent films, the statistical copolymerisation of 45% styrene with 55% nBA was conducted at 30 °C using the low-temperature redox initiator. As expected, DSC analysis indicated that these styrene/nBA copolymers exhibited intermediate T_g values compared to the two respective homopolymers. These pyrrolidone-functional films may be worth evaluating as anti-bacterial surfaces. Such films could also be characterised by surface zeta potential measurements to confirm their non-ionic nature.[27]

In principle, the preparation of worms and vesicles by RAFT aqueous emulsion polymerisation using a PNAEP precursor as a steric stabiliser block should be of considerable academic interest. However, such PISA formulations often lead to kinetically-trapped morphologies.[28–30] To overcome this limitation, steric stabilisers composed of statistical mixtures of AA with OEGA have been used to access higher order morphologies for PS-based diblock copolymers.[31–34] However, despite its undoubted success, this empirical approach is not well-understood. Thus, targeting $P(NAEP_x\text{-}\textit{stat}\text{-}AA_y)_z$ or $P(NAEP_x\text{-}\textit{stat}\text{-}OEGA_y)_z$ statistical copolymer precursors for the RAFT aqueous emulsion polymerisation of styrene while systematically varying 'x' and 'z' may provide useful insights if any such precursors enable the formation of higher order morphologies.

Chapter 4 utilises RAFT aqueous emulsion polymerisation to prepare waterborne multiblock copolymer nanoparticles with desirable mechanical properties. In 2010, Luo *et al*. reported the synthesis of PS-PnBA-PS thermoplastic elastomers by RAFT emulsion polymerisation at 70 °C.[35] However, this relatively high reaction temperature resulted in broad molecular weight distributions for the final copolymers ($M_w/M_n > 2.0$), particularly when targeting high PnBA contents. This agrees well with the results reported in Chapter 3 whereby a significantly lower reaction temperature (30 °C) was required to produce relatively well-defined $PNAEP_{85}\text{-}PnBA_x$ diblock copolymers. Thus, all-acrylic $PNAEP_{85}\text{-}PtBA_{150}\text{-}PnBA_x\text{-}PtBA_{150}$ tetrablock copolymer spheres were synthesised at 30 °C via sequential monomer addition using a four-step one-pot protocol. Here PtBA blocks were preferred to PS blocks as their acrylic nature should ensure high blocking efficiencies while also enabling high conversions to be achieved within relatively short timescales. ^1H NMR, GPC and DLS studies confirmed the synthesis of onion-like $PNAEP_{85}\text{-}PtBA_{150}\text{-}PnBA_{700}\text{-}PtBA_{150}$ tetrablock copolymer nanoparticles within 120 min, with high monomer conversions (> 98%) being achieved for each block. TEM analysis confirmed that such nanoparticles did not undergo significant film formation when drying from dilute aqueous solution. In principle, cryo-TEM studies could provide further evidence for their onion-like internal structure. Alternatively, ultrathin cross-sections of such nanoparticles may enable their internal morphology to be observed by conventional TEM studies.[36] DSC studies confirmed that the T_g of PtBA homopolymer is above ambient temperature. Thus it can act as the hard block, while the PnBA acts as the soft block. Despite their isomeric nature, these two hydrophobic blocks undergo microphase separation when films are cast at ambient temperature.

Three examples of transparent $PNAEP_{85}\text{-}PtBA_{150}\text{-}PnBA_x\text{-}PtBA_{150}$ tetrablock copolymer films (where x = 200, 400 or 700) were cast from 20% w/w aqueous dispersions at room temperature. One drawback of RAFT polymerisation is the colour that is imparted by the RAFT agent in the final copolymer. In principle, increasing the DP of these tetrablock copolymers further should result in almost completely colourless films as the RAFT agent concentration becomes negligible. Moreover, the cost and malodour of these films will be minimised, which augurs well for potential industrial scale-up. As expected, the $PNAEP_{85}$-$PtBA_{150}$-$PnBA_{200}$-$PtBA_{150}$ film displayed poor elastomeric properties owing to the relatively short PnBA block. For the two other tetrablock copolymer films, the elongation at break increased from 145% (PnBA DP = 400) to 400% (PnBA DP = 700), which indicates that such copolymers can behave as a thermoplastic elastomer (or synthetic rubber). Despite the similar x-ray scattering densities (ξ) observed for the two isomeric blocks ($\xi_{\mathrm{PtBA}} = 9.47 \times 10^{10}$ cm^{-2} and $\xi_{\mathrm{PnBA}} = 10.01 \times 10^{10}$ cm^{-2}), SAXS studies indicated that this elasticity is the result of microphase separation of the PtBA and PnBA blocks to form lamellar structures, with more defined domains being observed for the higher molecular weight copolymer. Further optimisation of the copolymer composition should afford films with various internal morphologies.[37] In particular, tetrablock copolymer films comprising either spherical or cylindrical PtBA domains should be accessible at lower PtBA volume fractions and such morphologies are expected to afford thermoplastic elastomers with greater toughness and elasticity.[38] Chapter 4 demonstrated that RAFT aqueous emulsion polymerisation was an efficient protocol to produce tetrablock copolymer nanoparticles at 20% w/w solids. In order for these syntheses to be comparable to those used to produce industrial latex formulations, even higher final copolymer concentrations would be required.[39] However, initial attempts to increase the copolymer concentration above 20% w/w solids resulted in macroscopic precipitation. In principle, this problem could be avoided by performing these polymerisations at pH 7 by substituting the KPS/AsAC initiator system for the KPS/TMEDA initiator system (see Chapter 5). At this pH deprotonation of the terminal carboxylic acid group should confer additional electrosteric stabilisation and hence prevent macroscopic precipitation.

Most of the work presented in this Thesis is focused on using PNAEP as a water-soluble precursor for the synthesis of sterically-stabilised spheres via RAFT aqueous emulsion polymerisation. In the case of the tetrablock copolymer nanoparticles, this kinetically-trapped morphology is actually preferred because it ensures minimal dispersion viscosity. Unlike RAFT aqueous emulsion polymerisation, RAFT aqueous dispersion polymerisation normally provides a reliable route to higher order morphologies such as worms and vesicles.[40] However, relatively few water-miscible monomers are suitable for such PISA formulations. Recently, O'Reilly *et al*.[41] and Byard *et al*.[42,43] prepared diblock copolymer spheres, worms or vesicles by the RAFT aqueous dispersion polymerisation of HBA. However, in both cases the low T_g of the PHBA block prevented conventional TEM studies. O'Reilly and co-workers overcame this limitation by using cryo-TEM. However, the relatively high degree of hydration of the PHBA block led to relatively poor electron contrast.[41] Instead, Byard *et al*. statistically copolymerised HBA with a crosslinkable monomer (DAAM). The pendent ketone group on the DAAM comonomer units was subsequently reacted with adipic acid dihydrazide: this approach enabled the covalent stabilisation of the nano-objects and allowed good-quality TEM images to be obtained. However, comparing the rheological behaviour of linear PDMAC-PHBA and PDMAC-P(HBA-*stat*-DAAM) nano-objects suggested that incorporation of the DAAM comonomer limited the thermoresponsive behaviour exhibited by the HBA-rich structure-directing block, thus reducing the reversibility of the vesicle-to-worm transition.[43]

In view of this literature precedent, Chapter 5 was focused on the synthesis of PNAEP$_{85}$-PHBA$_x$ diblock copolymer nano-objects at 30 °C using a highly convenient and reproducible one-pot RAFT aqueous dispersion polymerisation protocol. To enable TEM assignment of copolymer morphologies, PNAEP$_{85}$-PHBA$_x$ nano-objects were crosslinked using a water-soluble bisaldehyde, GA. This approach proved successful and enabled the construction of a pseudo-phase diagram by systematically varying the PHBA DP between 100 and 550 while targeting copolymer concentrations of 5 to 40% w/w. The thermoresponsive behaviour of linear PNAEP$_{85}$-PHBA$_{295}$ nano-objects was investigated by variable temperature rheology and DLS studies. Sphere-to-worm, worm-to-vesicle and vesicle-to-lamellae morphology transitions were observed on raising the temperature from 5 °C to 50 °C. Further evidence for these morphology transitions was provided by TEM studies of nano-objects that had been crosslinked at specific temperatures and variable temperature SAXS studies of the linear nano-objects. On cooling, significant hysteresis was observed for the lamellar-to-vesicle transition. This was also observed by Byard *et al*. for PDMAC$_{54}$-PHBA$_{218\text{-}269}$ diblock copolymer nano-objects.[43] In principle, using the GA crosslinking protocol outlined in this Chapter to trap the intermediate nano-objects formed during cooling should provide useful mechanistic insights regarding the true nature of this morphological transition.

Increasing the PNAEP DP up to 276 while maintaining a PNAEP/PHBA molar ratio of ~3.8 enabled the preparation of a series of PNAEP$_x$-PHBA$_y$ worms. TEM analysis indicated that their mean cross-sectional diameter increased linearly with PNAEP DP while variable temperature DLS studies confirmed that thermoresponsive behaviour was maintained, even for the longest PHBA block. In principle, the thickest worms may be sufficiently large to enable their visualisation by fluorescence microscopy (if tagged with an appropriate dye label). Warren *et al*. reported a series of PEG$_{113}$-PHPMA$_x$ nano-objects that displayed irreversible thermoresponsive behaviour.[44] This was attributed to the relatively high DP of the PEG_{113} block inhibiting the sphere-sphere fusion required to reform the worms on heating. The ability of the relatively thick $PNAEP_x$-$PHBA_y$ worms to retain their thermoreversibility suggests that the more weakly hydrophobic PHBA block may enable the limits observed for PHPMA-based PISA formulations to be surpassed. However, the PNAEP stabiliser block should be replaced with PEG_{113} for an unequivocal comparison. This would also facilitate variable temperature ^{1}H NMR spectroscopy studies of the differing degrees of hydration of the isomeric PHPMA and PHBA blocks. According to the literature,[42,45] the former becomes more hydrated on cooling (LCST-like behaviour) whereas the latter becomes more hydrated on heating (UCST-like behaviour) so markedly different behaviour is anticipated.

DLS and aqueous electrophoresis studies indicated that introducing anionic charge at the end of the PNAEP stabiliser chains by raising the dispersion pH above the pK_a of the terminal carboxylic acid group was sufficient to drive a rapid, reversible vesicle-to-sphere transition. Lovett *et al*. reported that ionisation of carboxylic acid end-groups increased the effective volume fraction of the *stabiliser block* of $PGMA_{56}$-$PHPMA_{155}$ worms sufficiently to induce a worm-to-sphere transition.[46] However, ^{1}H NMR studies of linear $PNAEP_{85}$-$PHBA_x$ nano-objects conducted at various dispersion pH suggest that the worm-to-sphere transition observed for this system is instead driven by surface plasticisation of the *core-forming PHBA block*. This pH-dependence most likely prevents the use of these nano-objects for biomedical applications. However, methylation of the pendent carboxylic acid group should enable the design of pH-insensitive thermoresponsive PNAEP-PHBA worm gels. Given their anticipated biocompatibility, such gels are likely to offer new opportunities as wholly synthetic 3D matrices for long-term cell culture studies[47] or possibly for inducing stasis in embryonic human stem cells.[48,49]

6.2 References

1 F. Haaf, A. Sanner and F. Straub, *Polym. J.*, 1985, **17**, 143–152.

2 M. Teodorescu and M. Bercea, *Polym. Plast. Technol. Eng.*, 2015, **54**, 923–943.

3 T. P. Davis and M. B. Huglin, *Polymer*, 1990, **31**, 513–519.

4 G. Moad, E. Rizzardo and S. H. Thang, *Aust. J. Chem.*, 2006, **59**, 669–692.

5 G. Moad, E. Rizzardo and S. H. Thang, *Aust. J. Chem.*, 2009, **62**, 1402–1472.

6 G. Moad, E. Rizzardo and S. H. Thang, *Aust. J. Chem.*, 2012, **65**, 985–1076.

7 J. W. Breitenbach, *J. Polym. Sci.*, 1957, **23**, 949–953.

8 D. B. Thomas, A. J. Convertine, L. J. Myrick, C. W. Scales, A. E. Smith, A. B. Lowe, Y. A. Vasilieva, N. Ayres and C. L. McCormick, *Macromolecules*, 2004, **37**, 8941–8950.

9 D. B. Thomas, A. J. Convertine, R. D. Hester, A. B. Lowe and C. L. McCormick, *Macromolecules*, 2004, **37**, 1735–1741.

10 V. J. Cunningham, S. P. Armes and O. M. Musa, *Polym. Chem.*, 2016, **7**, 1882–1891.

11 V. J. Cunningham, Y. Ning, S. P. Armes and O. M. Musa, *Polymer*, 2016, **106**, 189–199.

12 V. J. Cunningham, M. J. Derry, L. A. Fielding, O. M. Musa and S. P. Armes, *Macromolecules*, 2016, **49**, 4520–4533.

13 R. R. Gibson, S. P. Armes, O. M. Musa and A. Fernyhough, *Polym. Chem.*, 2019, **10**, 1312–1323.

14 Y. Shi, G. Liu, H. Gao, L. Lu and Y. Cai, *Macromolecules*, 2009, **42**, 3917–3926.

15 T. Zdeněk, S. Antonín, P. Vladimír and K. Pavel, *Die Makromol. Chemie*, 1977, **178**, 2743–2746.

16 Z. Zhou and B. Chu, *Macromolecules*, 1987, **20**, 3089–3091.

17 Y. Fukumine, K. Inomata, A. Takano and T. Nose, *Polymer.*, 2000, **41**, 5367–5374.

18 T. P. Lodge, J. Bang, K. J. Hanley, J. Krocak, S. Dahlquist, B. Sujan and J. Ott, *Langmuir*, 2003, **19**, 2103–2109.

19 S. M. North and S. P. Armes, *Green Chem.*, , DOI:10.1039/d0gc04271d.

20 H. Einaga and M. Harada, *Langmuir*, 2005, **21**, 2578–2584.

21 H. Tsunoyama, H. Sakurai, Y. Negishi and T. Tsukuda, *J. Am. Chem. Soc.*, 2005, **127**, 9374–9375.

22 A. Blanazs, J. Madsen, G. Battaglia, A. J. Ryan and S. P. Armes, *J. Am. Chem. Soc.*, 2011, **133**, 16581–16587.

23 N. J. Warren, M. J. Derry, O. O. Mykhaylyk, J. R. Lovett, L. P. D. D. Ratcliffe, V. Ladmiral, A. Blanazs, L. A. Fielding and S. P. Armes, *Macromolecules*, 2018, **51**, 8357–8371.

24 N. M. Ahmad, F. Heatley and P. A. Lovell, *Macromolecules*, 1998, **31**, 2822–2827.

25 N. M. Ahmad, B. Charleux, C. Farcet, C. J. Ferguson, S. G. Gaynor, B. S. Hawkett, F. Heatley, B. Klumperman, D. Konkolewicz, P. A. Lovell, K. Matyjaszewski and R. Venkatesh, *Macromol. Rapid Commun.*, 2009, **30**, 2002–2021.

26 S. L. Canning, V. J. Cunningham, L. P. D. Ratcliffe and S. P. Armes, *Polym. Chem.*, 2017, **8**, 4811–4821.

27 N. J. W. Penfold, A. J. Parnell, M. Molina, P. Verstraete, J. Smets and S. P. Armes, *Langmuir*, 2017, **33**, 14425–14436.

28 V. J. Cunningham, A. M. Alswieleh, K. L. Thompson, M. Williams, G. J. Leggett, S. P. Armes and O. M. Musa, *Macromolecules*, 2014, **47**, 5613–5623.

29 N. P. Truong, M. V Dussert, M. R. Whittaker, J. F. Quinn and T. P. Davis, *Polym. Chem.*, 2015, **6**, 3865–3874.

30 J. Jennings, G. He, S. M. Howdle and P. B. Zetterlund, *Chem. Soc. Rev.*, 2016, **45**, 5055–5084.

31 W. Zhang, F. D'Agosto, O. Boyron, J. Rieger and B. Charleux, *Macromolecules*, 2012, **45**, 4075–4084.

32 X. Zhang, F. Boisson, O. Colombani, C. Chassenieux and B. Charleux, *Macromolecules*, 2014, **47**, 51–60.

33 J. Lesage de la Haye, X. Zhang, I. Chaduc, F. Brunel, M. Lansalot and F. D'Agosto, *Angew. Chemie Int. Ed.*, 2016, **55**, 3739–3743.

34 S. Y. Khor, N. P. Truong, J. F. Quinn, M. R. Whittaker and T. P. Davis, *ACS Macro Lett.*, 2017, **6**, 1013–1019.

35 Y. Luo, X. Wang, Y. Zhu, B.-G. Li and S. Zhu, *Macromolecules*, 2010, **43**, 7472–7481.

36 T. R. Guimarães, M. Khan, R. P. Kuchel, I. C. Morrow, H. Minami, G. Moad, S. Perrier and P. B. Zetterlund, *Macromolecules*, 2019, **52**, 2965–2974.

37 A. K. Ghose, V. N. Viswanadhan and J. J. Wendoloski, *J. Phys. Chem. A*, 1998, **102**, 3762–3772.

38 G. L. Gregory, G. S. Sulley, L. P. Carrodeguas, T. T. D. Chen, A. Santmarti, N. J. Terrill, K.-Y. Lee and C. K. Williams, *Chem. Sci.*, 2020, **11**, 6567–6581.

39 A. A. Cockram, R. D. Bradley, S. A. Lynch, P. C. D. Fleming, N. S. J. Williams, M. W. Murray, S. N. Emmett and S. P. Armes, *React. Chem. Eng.*, 2018, **3**, 645–657.

40 N. J. Warren and S. P. Armes, *J. Am. Chem. Soc.*, 2014, **136**, 10174–10185.

41 J. C. Foster, S. Varlas, B. Couturaud, J. R. Jones, R. Keogh, R. T. Mathers and R. K. O'Reilly, *Angew. Chemie Int. Ed.*, 2018, **57**, 15733–15737.

42 S. J. Byard, C. T. O'Brien, M. J. Derry, M. Williams, O. O. Mykhaylyk, A. Blanazs and S. P. Armes, *Chem. Sci.*, 2020, **11**, 396–402.

43 S. J. Wilson, *Synthesis and Characterisation of Stimulus-responsive Diblock Copolymer Nano-objects Prepared by RAFT Aqueous Dispersion Polymerisation*, PhD Thesis, University of Sheffield, Sheffield, UK, 2019.

44 N. J. Warren, O. O. Mykhaylyk, D. Mahmood, A. J. Ryan and S. P. Armes, *J. Am. Chem. Soc.*, 2014, **136**, 1023–1033.

45 A. Blanazs, R. Verber, O. O. Mykhaylyk, A. J. Ryan, J. Z. Heath, C. W. I. Douglas and S. P. Armes, *J. Am. Chem. Soc.*, 2012, **134**, 9741–9748.

46 J. R. Lovett, N. J. Warren, L. P. D. Ratcliffe, M. K. Kocik and S. P. Armes, *Angew. Chemie Int. Ed.*, 2015, **54**, 1279–1283.

47 K. A. Simon, N. J. Warren, B. Mosadegh, M. R. Mohammady, G. M. Whitesides and S. P. Armes, *Biomacromolecules*, 2015, **16**, 3952–3958.

48 I. Canton, N. J. Warren, A. Chahal, K. Amps, A. Wood, R. Weightman, E. Wang, H. Moore and S. P. Armes, *ACS Cent. Sci.*, 2016, **2**, 65–74.

49 M. Sponchioni, C. T. O'Brien, C. Borchers, E. Wang, M. N. Rivolta, N. J. W. Penfold, I. Canton and S. P. Armes, *Chem. Sci.*, 2020, **11**, 232–240.

Chapter 7

Appendix

7.1 Small Angle X-ray Scattering (SAXS) Models

In general, the intensity of X-rays scattered by a dispersion of nano-objects [usually represented by the scattering cross section per unit sample volume, $\frac{d\Sigma}{d\Omega}(q)$ can be expressed as:

$$\frac{d\Sigma}{d\Omega}(q) = NS(q)\int_0^\infty \dots \int_0^\infty F(q, r_1, \dots, r_k)^2 \Psi(r_1, \dots, r_k) dr_1 \dots dr_k \tag{7.1}$$

where $F(q, r_1, \dots, r_k)$ is the form factor, $r_1, \dots, r_k$ is a set of *k* parameters describing the structural morphology, $\Psi(r_1, \dots, r_k)$ is the distribution function, S(*q*) is the structure factor and *N* is the nano-object number density per unit volume expressed as:

$$N = \frac{\varphi}{\int_0^\infty \dots \int_0^\infty V(r_1, \dots, r_k)\Psi(r_1, \dots, r_k) dr_1 \dots dr_k} \tag{7.2}$$

where $V(r_1, \dots, r_k)$ is volume of the nano-object and φ is their volume fraction in the dispersion. For all SAXS experiments conducted herein, a dilute copolymer concentration of 1.0 % w/w was utilised. As such, for all analysis and modelling it was assumed that s(q) = 1.

Sphere model. The spherical micelle form factor equation for Equation 7.1 is given by[2]:

$$F_{sph}(q) = N_s^2 \beta_s^2 A_s^2(q, R_s) + N_s \beta_c^2 F_c(q, R_g) + (q) \tag{7.3}$$

Where R_s is the core radius of the spherical micelle, R_g, is the radius of gyration of the PNAEP$_{85}$ corona block. The core block and the corona block X-ray scattering length contrast is given by $\beta_s = V_s(\xi_s - \xi_{sol})$ and $\beta_s = V_c(\xi_c - \xi_{sol})$, respectively. Here ξ_s, ξ_c and ξ_{sol} are the X-ray scattering length densities of the core-forming block ($\xi_{PHBA} = 10.65 \times 10^{10}$ cm^{-2}), the coronal stabilizer block ($\xi_{PNAEP} = 11.46 \times 10^{10}$ cm^{-2}; this was calculated using the density of the PNAEP$_{85}$ homopolymer as measured by densitometry, see Chapter 7.2) and the solvent ($\xi_{sol} = 9.42 \times 10^{10}$ cm^{-2}). V_s and V_c are the volumes of the core-forming block and the coronal stabilizer block, respectively. Using the molecular weights of the PHBA and PEG$_{113}$ blocks and their respective mass densities ($\rho_{PHBA} = 1.16$ g cm^{-3} and $\rho_{PNAEP} = 1.26$ g cm^{-3}; see below), the individual block volumes can be calculated from $V = \frac{M_{n,pol}}{N_A \rho}$, where M$_{n,pol}$ corresponds to the number-average molecular weight of the block determined by ^{1}H NMR spectroscopy. The sphere form factor amplitude is used for the amplitude of the core self-term:

$$A_c(q, R_s) = \Phi(qR_s)\exp\left(-\frac{q^2\sigma^2}{2}\right) \tag{7.4}$$

Where $\Phi(qR_s) = \frac{3[\sin(qR_s) - qR_s\cos(qR_s)]}{(qR_s)^3}$. A sigmoidal interface between the two blocks was assumed for the spherical micelle form factor (equation 7.4). This is described by the exponent term with a width σ accounting for a decaying scattering length density at the micellar interface. This σ value was fixed at 2.2 during fitting. The form factor amplitude of the spherical micelle corona is:

$$A_c(q) = \frac{\int_{R_s}^{R_s+2s} \mu_c(r)\frac{sin(qr)}{qr}r^2dr}{\int_{R_s}^{R_s+2s} \mu_c(r)r^2dr} exp\left(-\frac{q^2\sigma^2}{2}\right) \tag{7.5}$$

The radial profile, $\mu_c(r)$, can be expressed by a linear combination of two cubic b splines, with two fitting parameters *s* and *a* corresponding to the width of the profile and the weight coefficient, respectively. This information can be found elsewhere,[3,4] as can the approximate integrated form of Equation 7.5. The self-correlation term for the corona block is given by the Debye function:

$$F_c(q,R_g) = \frac{2[\exp(-q^2R_g^2)-1+q^2R_g^2]}{q^4R_g^2} \tag{7.6}$$

Where R_g is the radius of gyration of the PNAEP$_{85}$ coronal block. The R_g obtained of the PNAEP$_{85}$ coronal block of 2.6 nm is comparable to the estimated value of 2.4 nm and fixed throughout the study. The latter can be calculated from the total contour length of the PNAEP$_{85}$ block, L$_{PNAEP85}$ = 85 × 0.255 nm = 28.8 nm (since the projected contour length per PEG repeat unit is defined by two C-C bonds adopting an *all-trans* conformation, 0.255 nm) and the Kuhn length of 1.53 nm based on the known literature value for PMMA results in an approximate R_g of $(28.8 \times 1.53/6)^{0.5}$ = 24 nm. The aggregation number of the spherical micelle is:

$$N_s = (1 - x_{sol})\frac{\frac{4}{3}\pi R_s^3}{V_s} \tag{7.7}$$

Where x_{sol} is the volume fraction of solvent in the PHBA micelle core. An effective structure factor expression proposed for interacting spherical micelles[5] has been used in equation 7.1:

$$S_s(q) = 1 + \frac{A_{s\_mic}^{av}(q)^2[S_{PY}(q,R_{PY},f_{PY})-1]}{F_{s\_mic}(q)} \tag{7.8}$$

Herein the form factor of the average radial scattering length density distribution of micelles is used as $A_{s\_mic}^{av}(q) = N_s[\beta_s A_s(q,R_s) + \beta_c A_c(q)]$ and $S_{PY}(q,R_{PY},f_{PY})$ is a hard-sphere interaction structure factor based on the Percus-Yevick approximation,[5] where R_{PY} is the interaction radius and f_{PY} is the hard-sphere volume fraction. A polydispersity for one parameter (R_s) is assumed for the micelle model which is described by a Gaussian distribution. Thus, the polydispersity function in Equation 7.1 can be replaced as:

$$\Psi(r_1) = \frac{1}{\sqrt{2\pi\sigma_{R_s}^2}} exp\left(-\frac{(r_1-R_s)^2}{2\sigma_{R_s}^2}\right) \tag{7.9}$$

Where σ_{R_s} is the standard deviation for R_s. In accordance with equation 7.2, the number density per unit volume for the micelle model is expressed as:

$$N = \frac{\varphi}{\int_0^{\infty} V(r_1)\Psi(r_1)dr_1} \tag{7.10}$$

where φ is the total volume fraction of copolymer in the spherical micelles and $V(r_1)$ is the total *volume* of copolymer in a spherical micelle $[V(r_1) = (V_s + V_c)N_s(r_1)]$.

Worm-like micelle model

The worm-like micelle form factor in Equation 7.1 is expressed as[2]:

$$F_{w_{mic}}(q) \ = \ N_w^2\beta_s^2\, F_w^2(q) + N_w\beta_c^2F_c(q,R_g) + N_w(N_w - 1)\beta_c^2S_{cc}(q) + 2N_w^2\beta_s\beta_cS_{sc}(q) \tag{7.11}$$

where all the parameters are the same as in the spherical micelles model (Equation 7.3). The self-correlation time for the worm-like micelle core or radius is:

$$F_w(q) \ = \ F_{worm}(q, L_w, b_w)A_{csworm}^2\,(q, R_w) \tag{7.12}$$

where

$$A_{csworm}^2(q, R_w) = \left[2\frac{J_1(qR_w)}{qR_w}\right]^2 \tag{7.13}$$

and J_1 is the first-order Bessel function of the first kind, and a form factor $F_{worm}(q, L_w, b_w)$ for self-avoiding semi-flexible chains represent the worm-like micelle, where b_w is the worm Kuhn length and L_w is the mean worm contour length. A complete expression for the chain form factor can be found elsewhere.[6] The self-correlation term for the corona block is given by the Debye function shown in Equation 7.6. The mean aggregation number of the worm-like micelle is given by:

$$N_w \ = \ (1 - x_{sol})\frac{\pi R_w^2L_w}{V_s} \tag{7.14}$$

where x_{sol} is the volume fraction of solvent within the worm-like micelle core. Possible semi-spherical caps at the ends of each worm are not considered in this form factor.

Vesicle model

The vesicle form factor in Equation 7.1 is expressed as:

$$F_{ves}(q) = \ N_v^2\beta_m^2A_m^2(q) + N_v\beta_{vc}^2F_c(q, R_g) + N_v(N_v - 1)\beta_{vc}^2A_{vc}^2(q) + 2N_v^2\beta_m\beta_{vc}A_m(q)A_{vc}(q) \tag{7.15}$$

The X-ray scattering length contrast for the membrane-forming block (PHBA) and the coronal stabilizer block (PEG_{113}) is given by $\beta_m = V_m(\xi_m - \xi_{sol})$ and $\beta_{vc} = V_{vc}\ (\xi_{vc} - \xi_{sol})$, respectively, where ξ_m, ξ_{vc} and ξ_{sol} are the X-ray scattering length densities of the membrane-forming block ($\xi_{PHBA} = 10.65 \times 10^{10}$ cm^{-2}), the coronal stabilizer block ($\xi_{PNAEP} = 11.46 \times 10^{10}$ cm^{-2}) and the solvent ($\xi_{sol} = 9.42 \times 10^{10}$ cm^{-2}). V_m and V_{vc} are the volumes of the membrane-forming block and the coronal stabilizer block, respectively. Using the molecular weights of the PHBA and $PNAEP_{85}$ blocks and their respective mass densities

(ρ_{PHBA} = 1.16 g cm^{-3} and ρ_{PNAEP} = 1.26 g cm^{-3}), the individual block volumes can be calculated from $V = \frac{M_{n,pol}}{N_A\rho}$, where $M_{n,pol}$ corresponds to the number-average molecular weight of the block determined by ^{1}H NMR spectroscopy. The amplitude of the membrane self-term is:

$$A_m(q) = \frac{V_{out}\varphi(qR_{out}) - V_{in}\varphi(qR_{in})}{V_{out} - V_{in}} e^{\left(-\frac{q^2\sigma_{in}^2}{2}\right)} \tag{7.16}$$

where $R_{in} = R_m - \frac{1}{2}T_m$ is the inner radius of the membrane, $R_{out} = R_m + \frac{1}{2}T_m$ is the outer radius of the membrane, $V_{in} = \frac{4}{3}\pi R_{in}^3$, $V_{out} = \frac{4}{3}\pi R_{out}^3$. It should be noted that Equation 7.16 differs from that reported in the original work. More specifically, the exponent term in Equation 7.16 represents a sigmoidal interface between the blocks, with a width σ_{in} accounting for a decaying scattering length density at the membrane surface. The numerical value of σ_{in} was fixed at 2.2. The mean vesicle aggregation number, N_v, is given by:

$$N_v = (1 - x_{sol})\frac{V_{out} - V_{in}}{V_m} \tag{7.17}$$

where x_{sol} is the solvent (i.e. water) volume fraction within the vesicle membrane. A simpler expression for the corona self-term of the vesicle model than that used for the spherical micelle corona self-term was preferred because the contribution to the scattering intensity from the corona block is much less than that from the membrane block in this case. Assuming that there is no penetration of the solvophilic coronal blocks into the solvophobic membrane, the amplitude of the vesicle corona self-term is expressed as:

$$A_{vc}(q) = \Psi(qR_g)\frac{1}{2}\left[\frac{\sin[q(R_{out}+R_g)]}{q(R_{out}+R_g)} + \frac{sin[q(R_{in}-R_g)]}{q(R_{in}-R_g)}\right] \tag{7.18}$$

where the term outside the square brackets is the factor amplitude of the corona block copolymer chain such that:

$$\Psi(qR_g) = \frac{1 - exp^{(-qR_g)}}{(qR_g)^2} \tag{7.19}$$

For the vesicle model, it was assumed that two parameters are polydisperse: the overall radius of the vesicles and the membrane thickness (R_m and T_m, respectively). Each is assumed to have a Gaussian distribution, so the polydispersity function in Equation (7.1) can be expressed as:

$$\Psi(r_1, r_2) = \frac{1}{\sqrt{2\pi\sigma_{Rm}^2}} exp^{\left(-\frac{(r_1 - R_m)^2}{2\sigma_{Rm}^2}\right)} \frac{1}{\sqrt{2\pi\sigma_{Tm}^2}} exp^{\left(-\frac{(r_1 - T_m)^2}{2\sigma_{Tm}^2}\right)} \tag{7.20}$$

where σ_{Rm} and σ_{Tm} are the standard deviations for R_m and T_m, respectively. Following Equation 7.2, the number density per unit volume for the vesicle model is expressed as:

$$N = \frac{\varphi}{\int_0^\infty \int_0^\infty V(r_1,r_2)\Psi(r_1,r_2)dr_1dr_2} \quad (7.21)$$

where φ is the total volume fraction of copolymer in the vesicles and $V(r_1, r_2)$ is the total volume of copolymers in a vesicle $[V(r_1, r_2) = (V_m + V_{vc})N_v (r_1, r_2)]$. Programming tools within the Irena SAS Igor Pro macros were used to implement the scattering models.[7]

7.2 Measurement of PNAEP$_{85}$ Density

Densitometry measurements were conducted at 20 °C on aqueous solutions of PNAEP$_{85}$ using an Anton Paar DMA 5000 M density meter to produce a linear calibration curve.

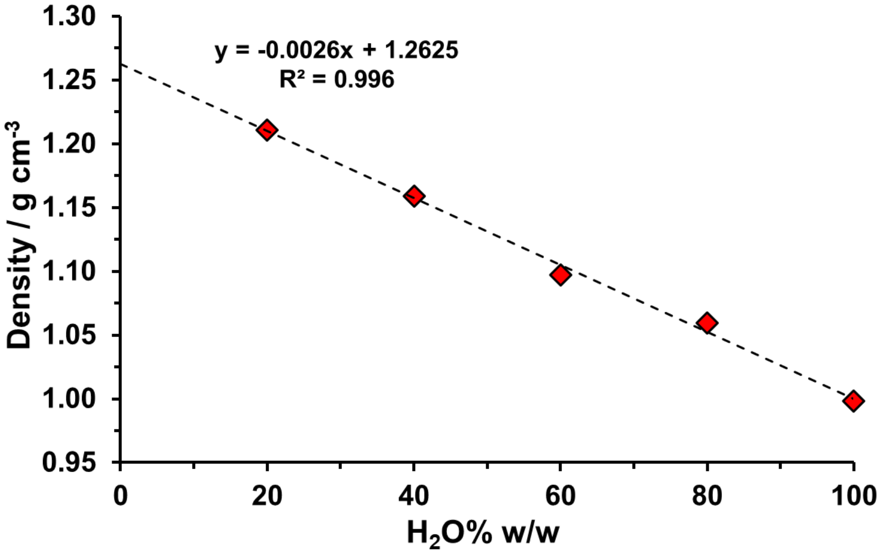

Figure 7.1. Linear calibration curve obtained by densitometry measurements conducted at 20 °C on aqueous solution of PNAEP$_{85}$ prepared at various concentrations (20-80% w/w). The density of PNAEP$_{85}$ (i.e. at 0% H$_2$O w/w) was calculated as the y-intercept that was obtained using the straight line equation.